

**Design of an Original Methodology for the Efficient and Economic  
Appraisal of Existing and New Technologies in Form Grinding  
Processes including Helical**

PHILIP WILLIAM HART

A thesis submitted in partial fulfilment of the requirements of Liverpool John Moores  
University for the degree of Master of Philosophy

This research programme was carried out  
in collaboration with the PTG Holroyd Precision and 3M

July 2018

## **Abstract**

The purpose of this research was to create and design a methodology for new product evaluation with an interest in the affects that they could have on form and helical grinding. The design uses a relatively small and commonly available grinding machine so that testing could be done without need for an expensive helical grinding machine typical of that utilised in industry. The contact conditions of the helical grinding process were considered, and the workpiece geometry was designed to closely replicate the form and entry and exit conditions found in helical form grinding of screw compressor rotors. The equipment design allows the grinding forces to be measured in axial, normal and tangential planes. This will allow the variation in axial forces to be explored and allow any variation in hydrodynamic forces to be investigated during the entry and exit regions.

Grinding trials showed the importance of the need to measure the true depth of cut for a grinding pass. A novel method of measuring the depth of cut was designed that will allow an accurate measurement of the form position before and after a grinding pass. Replication methods for the workpiece and grinding wheel form were designed to allow capture on the grinding machine to facilitate an economic appraisal method that allows testing to be carried out in a short period of time.

A 3D printed coolant nozzle was designed with an air scraper to overcome the air barrier around the periphery of the grinding. The aim of the design was to reduce the need for a high pressure grinding fluid jet and allowing less turbulent flow to enter the grinding nip at lower pressures.

A preliminary cost model was created with inputs that relate to form grinding and allow the user to investigate different process parameters and arrive at a cost per part.

## **Acknowledgements**

I would like to thank PTG Holroyd Precision for sponsoring and providing the opportunity to carry out this research. I also extend my thanks to my director of studies, Professor Michael Morgan for his support and guidance during this work.

Gratitude is also due to Professor Chris Holmes and Dr Andre Batako whose encouragement and practical help throughout the project has been vital to the author.

Acknowledgements are extended to the collaborating partner 3M for the support, advice and guidance.

I would also like to thank the technical staff, particular thanks go to Mr Peter Moran and Mr Paul Wright for their support throughout my time at AMTReL.

Finally, I would like to thank my friends and family who have provided critical support and guidance throughout the course of this endeavour.

## Nomenclature

Symbol	Meaning	S.I. Units
$a$	Applied depth of cut or set depth of cut	m
$a_e$	Real/actual/effective depth of cut	m
$a_d$	Dressing depth	m
$a_n$	Depth of cut normal to the surface	m
$a_{sw}$	Wheel wear depth	m
$a_t$	Thermal expansion of the workpiece	m
$b_{cu}$	Uncut chip width	m
$b_d$	Effective contact width of dresser	m
$\overline{b_{cu}}$	Mean uncut chip width	m
$b_{cu.max}$	Maximum uncut chip width	m
$b_s$	Wheel width	m
$b_w$	Contact/workpiece width	m
$d$	Pitch diameter	m
$d_{cu}$	Unloaded cut diameter	m
$d_e$	Effective wheel diameter	m
$d_{ef}$	Effective diameter when cutting	m
$d_s$	Wheel diameter/wheel diameter at a point on a form	m
$f_d$	Dressing lead	m
$f_{rd}$	Radial feed	m
$G$	Grinding ratio (G-ratio)	-
$h_{cu}$	Uncut chip thickness	m
$\overline{h_{cu}}$	Mean uncut chip thickness	m
$h_{cu.max}$	Maximum uncut chip thickness	m

$k_a$	Stiffness of grinding wheel and workpiece contact	N/m
$k_e$	Overall grinding system stiffness	N/m
$k_m$	Machine stiffness	N/m
$k_{ms}$	Machine stiffness of wheel head and column	N/m
$k_{mw}$	Machine stiffness of table and fixturing	N/m
$k_{ss}$	Grinding wheel stiffness	N/m
$k_{ws}$	Workpiece stiffness	N/m
$l_c$	Contact length	m
$L_e$	Rotor Lead	m
$l_f$	Deformation contact length	m
$l_g$	Geometric contact length	m
$l_k$	Kinematic contact length	m
$L$	Cutting edges spacing in the cutting direction	m
$L_w$	Workpiece length	m
$n_s$	Number of grinding wheel rotations per second	-
$p_p$	Point on a profile	-
$q_d$	Speed ratio	-
$Q_w$	Volumetric removal rate	m <sup>3</sup> /s
$Q'_w$	Specific removal rate per unit of contact width	m <sup>2</sup> /s
$r$	Dresser tip radius	m
$r_{cu}$	Uncut chip aspect ratio	-
$r_{max}$	Maximum wheel radius on form	m
$r_{min}$	Minimum wheel radius on form	m
$r_p$	Wheel radius to a point on the wheel form	m
$r_{pmin}$	Minimum wheel radius to a point on the wheel form	m
$s$	Feed per cutting edge	m

$U_d$	Overlap ratio	-
$\overline{V_{cu}}$	Mean uncut chip volume	$m^3$
$v_{fd}$	Dressing feedrate	m/min
$v_s$	Wheel surface speed	m/s
$v_{sd}$	Dressing wheel speed	m/s
$V_s$	Volume of tool wear	$m^3$
$v_w$	Workpiece surface speed	m/s
$V_w$	Volume of material removed from workpiece	$m^3$
$y_{max}$	Maximum radius of a grinding wheel form from the axis of rotation	m
$\alpha$	Profile angle	degrees
$\delta$	System deflections	m
$\theta$	Helix angle	degrees
$\theta_s$	Angle of geometric contact	degrees
$\theta'_s$	Angle of contact for maximum chip thickness	degrees
$\pi$	Pi mathematical constant	-

## Abbreviations

ABS	Acrylonitrile Butadiene Styrene
AMTReL	Advanced Manufacturing Technology Research Laboratory
ANOVA	Analysis of variance
BSPP	British Standard Pipe Parallel
CBN	Cubic Boron Nitride
CMM	Coordinate Measuring Machine
CNC	Computer Numerically Control
CVD	Chemical Vapor Deposition
DAQ	Data Acquisition
DoC	Depth of Cut
DRO	Digital readout
DTI	Dial Test Indicator
FDM	Fused Deposition Modelling
HEDG	High Efficiency Deep Grinding
LVDT	Linear Variable Differential Transformer
MCD	Monocrystalline Diamond
ND	Natural Diamond
OD	Overall Diameter
PCD	Polycrystalline Diamond
PCD	Pitch Circle Diameter
PLA	Polylactic Acid
PMM	Precision Measuring Machine
PSI	Pounds per Square Inch
RMS	Root Mean Square
SD	Synthetic Diamond

SME	Small and Medium-sized Enterprises
VI	Virtual Instrument

## Contents

<b>Abstract</b>	<b>I</b>
<b>Acknowledgements</b>	<b>II</b>
<b>Nomenclature</b>	<b>III</b>
<b>Abbreviations</b>	<b>VI</b>
<b>Contents</b>	<b>VIII</b>
<b>List of figures</b>	<b>XVI</b>
<b>List of tables</b>	<b>XIX</b>
<b>1 Introduction</b>	<b>1</b>
1.1 Background to the investigation	1
1.2 Research aim and objectives	5
1.2.1 Research aim	5
1.2.2 Objectives	5
<b>2 Introduction to grinding processes</b>	<b>6</b>
2.1 Material removal rate	7
2.1.1 Surface grinding	8
2.2 Contact lengths	11
2.2.1 Surface grinding geometric contact length	11
2.2.2 Surface grinding kinematic contact length	13

2.2.3	Surface grinding chip thickness and aspect ratio	13
2.2.4	Surface form grinding contact length	15
2.2.5	Helical form grinding contact length	19
2.3	Contact mechanics	21
2.3.1	Contact length	21
2.3.2	Contact length due to deflections	22
2.3.3	Contact length due to depth of cut	22
2.3.4	Contact length due to deflections and DoC	22
2.3.5	Contact area	24
2.4	Helical form grinding	25
<b>3</b>	<b>Introduction to grinding/process fluids</b>	<b>34</b>
3.1	Types of grinding fluids	36
3.2	Grinding fluid lubrication	37
3.3	Grinding fluid application	37
3.3.1	Useful flow	39
3.3.2	Coherent jet	40
3.3.3	Auxiliary nozzles	40
3.3.4	Coolant applications aids	40
<b>4</b>	<b>Introduction to conditioning of grinding wheels</b>	<b>41</b>
4.1	Dressing	42
4.2	Conditioning methods	42

4.3	The main conventional dressing methods	42
4.3.1	Rotary dressing	42
4.3.1.1	Profile dressers	43
4.3.1.2	Form dressers	43
4.3.2	Traverse dressing	44
4.3.3	Fixed dressing	45
4.3.4	Continuous dressing	45
4.4	Tool materials	46
<b>5</b>	<b>Preliminary grinding trials</b>	<b>47</b>
5.1	Introduction	47
5.2	Aim	47
5.3	Objectives	47
5.4	Theory	47
5.4.1	Grinding Fluids	51
5.5	Apparatus	51
5.6	Method	54
5.7	Results and calculations	57
5.8	Discussion of results	58
5.9	Conclusions	60
<b>6</b>	<b>System and equipment design</b>	<b>61</b>
6.1	Fixture design	63

6.2	Nozzle design	63
6.3	Grinding wheel form capture	64
6.4	Workpiece design	65
6.5	Abwood series 5020 surface grinding machine	69
6.6	On machine DoC measurement	70
6.7	Grinding fluid system	72
6.7.1	Pressure gauge	73
6.7.2	Flow meter	74
6.8	Form replication	75
6.8.1	Introduction	75
6.8.2	Plastiform MD-3P RT-001	78
6.8.3	Best product for the application	82
6.9	Data acquisition systems	83
6.10	Virtual instrument design	84
<b>7</b>	<b>System calibration</b>	<b>87</b>
7.1	Tesatronic LVDT gauge equipment initial testing	87
7.1.1	Introduction	87
7.1.2	Tests conducted on granite surface plate	88
7.1.2.1	Repeatability test	88
7.1.2.1.1	Aim	88
7.1.2.1.2	Conclusion	88

7.1.2.2	Accuracy test (linearity and bias) using gauge blocks	89
7.1.2.2.1	Aim	89
7.1.2.2.2	Conclusion	89
7.2	Tesatronic LVDT tests conducted on Abwood 5025 surface grinder	89
7.2.1	Basic linearity test using movement of the Z axis	89
7.2.1.1	Aim	89
7.2.1.2	Conclusion	90
7.2.2	Repeatability test between two points on the same surface by moving the Z axis	90
7.2.2.1	Aim	90
7.2.2.2	Conclusion	90
7.2.3	Repeatability test between two surfaces by moving the Z axis	90
7.2.3.1	Aim	90
7.2.3.2	Conclusion	90
7.2.4	Repeatability test between two points on the same surface by moving the X axis.	91
7.2.4.1	Aim	91
7.2.4.2	Conclusion	91
7.2.5	Repeatability test between two surfaces by moving the X axis.	91
7.2.5.1	Aim	91
7.2.5.2	Conclusion	91

7.2.6	Repeatability test between two points on the same surface moving the Z axis using two LVDT probes	91
7.2.6.1	Aim	91
7.2.6.2	Conclusion	92
7.2.7	Repeatability between two surfaces moving the Z axis using two LVDT probes.	92
7.2.7.1	Conclusion	93
7.3	Dynamometer calibration	94
7.3.1	Aim	94
7.3.2	Objective	94
7.4	Conclusion	94
7.5	Flowmeter calibration tests	95
7.5.1	Aim	95
7.5.2	Objective	95
7.6	Conclusion	95
7.7	Omega pressure gauge calibration tests	96
7.7.1	Aim	96
7.7.2	Objective	96
7.8	Conclusion	96
<b>8</b>	<b>Grinding fluid nozzle trials</b>	<b>97</b>
8.1	Introduction	97
8.2	Aim	97

8.3	Objectives	98
8.4	Theory	98
8.5	Conclusions	98
<b>9</b>	<b>Cost model</b>	<b>99</b>
9.1	Additional considerations for form dressing	99
<b>10</b>	<b>Conclusions</b>	<b>104</b>
<b>11</b>	<b>Further work</b>	<b>105</b>
	<b>References</b>	<b>107</b>
	Appendix A - Discussion of other Plastiform products tested	112
	Appendix B - Supplementary information for LVDT repeatability test	116
	Appendix C - Supplementary information for LVDT Accuracy test	121
	Appendix D - Supplementary information for linearity test using Z axis	125
	Appendix E - Supplementary information for 2 position repeatability test on the same surface by moving the Z axis	128
	Appendix F - Supplementary information for repeatability test between two surfaces by moving the Z axis	132
	Appendix G - Supplementary information for repeatability test between two points on the same surface by moving the X axis	136
	Appendix H - Supplementary information for repeatability test between two surfaces by moving the X axis	140

Appendix I - Supplementary information for repeatability test between two points on the same surface moving the Z axis using two LVDT probes	144
Appendix J - Supplementary information for repeatability between two surfaces moving the Z axis using two LVDT probes	151
Appendix K - Supplementary information for dynamometer calibration	158
Appendix L - Supplementary information on flow meter calibration	172
Appendix M - Supplementary information for Omega pressure gauge calibration test	179
Appendix N - Supplementary information for grinding fluid nozzle tests	187
Appendix O - The preliminary cost model presented at ICMR 2017	194
Appendix P - Workpiece Fixture Design	200
Appendix Q - Workpiece Design	201
Appendix R - Coolant nozzle drawing	202
Appendix S - Graphite sheet holder	203
Appendix T - Graphite sheet holder clamp plate	204

## List of figures

Figure 1-1 example of small screw compressor rotors.

Figure 1-2 example of large screw compressor rotors.

Figure 2-1 Idealised uncut chip mean and maximum width and thickness.

Figure 2-2 Volume of material removed in one grinding pass.

Figure 2-3 Straight surface grinding geometric contact length.

Figure 2-4 Surface grinding geometric and kinematic contact lengths.

Figure 2-5 Maximum uncut chip thickness in surface grinding.

Figure 2-6 Surface form grinding.

Figure 2-7 Straight surface form grinding. Section B-B shows a section and projected view showing the process to be similar to straight surface grinding.

Figure 2-8 a) and b) are an example of a form ground slot. a) shows the full length of the slot and b) shows the apparent contact area viewed from directly above. The green area is the nascent surface created by the grinding wheel, the blue area is the apparent area of contact between the grinding wheel and the workpiece and the red area is existing surface that will be removed as the grinding wheel advances through the workpiece.

Figure 2-9 Coordinate frame for the tool and workpiece (Sheth and Malkin, 1990).

Figure 2-10 Contact arc due to depth of cut and deflections (Rowe et al., 1993). Where  $d_3$  is the contact curve during loading,  $d_2$  is undeformed diameter of the contact curve, and  $d_s$  is the undeformed wheel diameter.

Figure 2-11 Example of apparent contact area for a surface form grinding workpiece.

Figure 2-12 Principle axes, transverse and normal planes. The normal plane is perpendicular to two points on the profile at the pitch diameter.

Figure 2-13 Male and female helical compressor rotor transverse profiles.

Figure 2-14 Depth of cut variation around a female profile.

Figure 2-15 Variation of feedrate around a profile for different grinding processes.

Figure 2-16 Variation of geometric contact length for surface grinding a form.

Figure 2-17 Change in helical length with diameter.

Figure 2-18 Burn on the end face of a compressor rotor where the edge angles are small.

Figure 2-19 Relationship of rotor geometry to lead, and the result of a push off error on a fitted lead result.

Figure 2-20 Examples of lead errors.

Figure 3-1 Air barrier holding back the coolant (Ebbrell et al., 2000).

Figure 5-1 Schematic of surface grinding machine with horizontal wheel spindle and reciprocating table, adapted from BSO (2014).

Figure 5-2 Diagram of grinding system stiffness.

Figure 5-3 Abwood 5025 surface grinder.

Figure 5-4 Magnetic base and finger dial test indicator mounted on a ground parallel.

Figure 5-5 Single point dresser in holder.

Figure 5-6 DoC trial results using the corrected measurement values.

Figure 5-7 Depth of material removed for measurement number 4 after spark-out passes.

Figure 5-8 Finger dial test indicator angle to workpiece surface.

Figure 6-1 Abwood 5025 surface grinder.

Figure 6-2 Grinding machine arrangement with metrology station.

Figure 6-3 Coolant nozzle with integrated adjustable air scraper.

Figure 6-4 3D printed version of the grinding fluid nozzle with adjustable air scraper.

Figure 6-5 Holder for graphite sheet used to capture grinding wheel form. Shown with 3D printed example of what the grinding wheel form would look like.

Figure 6-6 A large pair of screw compressor rotors.

Figure 6-7 Comparison of form in workpiece with typical male and female profiles found in helical screw compressor rotors. Male form in green, female form in red and the workpiece form in black.

Figure 6-8 Parallelogram workpiece design with angled ends and asymmetric form.

Figure 6-9 workpiece and workpiece fixture located on the Kistler force dynamometer.

Figure 6-10 workpiece with LVDT datum guides.

Figure 6-11 workpiece with LVDT datum guides and LVDT and grinding fluid guides. The LVDT and grinding fluid guides are shown in cyan and orange colours.

Figure 6-12 GT21 LVDT probe.

Figure 6-13 TESA R2M-1 rack with two M4P-2 modules installed and power supply underneath.

Figure 6-14 LVDT probe arrangement on workpiece.

Figure 6-15 Grinding fluid delivery system.

Figure 6-16 Omega PG-5000 1000PSI pressure gauge with 0-5V output.

Figure 6-17 Model number spec and pinout details for pressure gauge.

Figure 6-18 Omega Flow meter.

Figure 6-19 Sample moulding using Plastiform MD-3P RT-001. a) view of positive moulding of workpiece. b) view of the surface roughness replicated by moulding. c) Positive moulding inside the moulding using Plastiform D.A.V CA-001. d) The positive and negative moulds separated.

Figure 6-20 MD-3P mould used with AC-020.

Figure 6-21 MD-3P moulding applied directly to workpiece without AC-020.

Figure 6-22 Damage seen to moulding at the radius between the flat and round sides of the profile.

Figure 6-23 Graph of surface finish measurements on MD-3P mouldings.

Figure 6-24 Arrangement used to measure surface roughness of the workpiece and moulds. The angle vice was adjusted so that the flat side surface of the form was parallel to the movement of the Surtronic stylus.

Figure 6-25 NI6250 data acquisition system diagram used to capture dynamometer readings.

Figure 6-26 LabVIEW Virtual instrument for simultaneous encoder and 10 analogue input data capture.

Figure 6-27 Front panel of LabVIEW Virtual instrument for simultaneous encoder and 10 analogue input data capture.

Figure 7-1 Axis configuration of surface grinder, adapted from Singh (2015).

Figure 9-1 Cost model inputs tab.

Figure 9-2 Cost model calculation tab.

## **List of tables**

Table 3-1 Grinding fluid characteristics (1= worst, 4 =best) (Webster, 1995).

Table 5-1 Abwood 5025 surface grinder specification

Table 5-2 Depth of cut trial result no grinding fluid

Table 5-3 Depth of cut trial results with grinding fluid

Table 6-1 Abwood series 5020 surface grinding machine specification.

Table 6-2 FTB792 specification.

Table 6-3 Summary of Plastiform product characteristics.

Table 6-4 Surface roughness measurement results for workpiece and MD-3P mouldings.

# **1 Introduction**

## **1.1 Background to the investigation**

Within industry it can be hard to find the time, money or resources to perform thorough evaluation of the variables of a grinding process. Grinding of helical parts can often be the bottle neck of a manufacturing line and is usually one of the last operations to be performed on components. Figure 1-1 and Figure 1-2 show examples of small and large helical screw compressor rotors respectively.

It can be hard for manufacturers to suspend production to conduct new product evaluations. This can be due to grinding often being one of the last operations that is done to a workpiece and can mean that the tests are done on workpieces that are in a high value added condition. Altering process parameters during testing can result in workpieces being scrapped due to thermal damage, surface finish or geometric errors, the value of these scrapped parts can be significant. Large manufacturers may be able to invest in such research; however, small and medium enterprises (SME's) can find it hard to undertake appraisals on a regular basis as new production technologies come to market.

Often suppliers of grinding process consumables will bring new products to market that claim to be better than the competition, more productive, cheaper than other products, for example, grinding wheels, grinding oils, and coolant nozzles. To change the coolant that is used in a large grinding machine that needs 6000 litres or more can cost several thousand pounds. There is a strong financial disincentive to take an expensive machine tool out of production for careful experimentation, and even then, it can be difficult to arrange testing under the same conditions and using the same component type or material used previously. This makes it hard to compare and draw conclusions from the results. A test rig design that allows evaluation of new products at low cost and an economic model that can then be used to demonstrate the financial benefits of the new product will overcome these major obstacles.



Figure 1-1 example of small screw compressor rotors.



Figure 1-2 example of large screw compressor rotors.

There would be real benefit to industry should an efficient and economic appraisal methodology be established that can be carried out on a standard and relatively small grinding machine, suitably instrumented, that would allow independent assessment of grinding process variables and provide industrial users with the data that they need for process improvements or design.

Precision helical form (profile) grinding brings additional issues which needed to be considered when setting the experimental strategy of the research, namely, the asymmetric grinding forces and contact geometry between the wheel and workpiece. A common problem when grinding helical compressor rotors is the lead errors at the ends of the workpiece. This is often referred to as 'push off' and it is suggested that the grinding action causes deflection of the workpiece and work holding arrangement. In addition, it may also

result in elastic deflections of the grinding wheel (Malkin, 1989, Yamada et al., 2012, Yamada et al., 2011), including the wheel mounting and bearing assembly.

When grinding helical parts the grinding forces can be acting axially on one side of the wheel as it starts to enter the workpiece, and as the wheel progresses through the part the wheel comes into full engagement with the part. The axial forces on the grinding wheel at this point are thought to depend upon the form that the grinding wheel is grinding. As the wheel exits the workpiece the axial forces change to the opposite direction to those when the wheel entered the workpiece. The change in these forces is thought to be one cause of lead errors on helical parts. However, it is also observed that coolant application conditions can be different during entry and exit of the grinding wheel for the component. It could be that the variation in the coolant application through the grinding pass causes the grinding conditions to change, affecting the hydrodynamic forces created between the grinding wheel and the workpiece and consequently the material removal rate throughout the grinding pass. A workpiece holding apparatus has been designed that closely replicates the varying entry and exit conditions and provides the facility to grind the workpiece with or without coolant guides. The designed apparatus could be used to evaluate the effect of coolant guides which may be used to effectively extend the workpiece and help balance the grinding forces or create more consistent coolant application through the grinding pass for a helical part.

Furthermore, machining helical parts creates a situation that each point of the cutting tool traverses a different contact length between the tool and the workpiece (Stosic, 2006). This can create non-uniform tool wear along the form/profile of the tool. Malkin (1989) and Rowe (2009) have each showed the relationship between grinding wheel wear and the grinding forces. When using plated Cubic Boron Nitride (CBN) grinding wheels that are not dressed to give fresh abrasive the forces can change over a long period of time (equivalent to thousands of workpieces), which may equate to several months production. The change in forces as the grinding wheel wears can result in a need for grinding process changes throughout its life as the wheel wears (Morgan et al., 2007).

Further exploration of the grinding forces during the entry and exit of the grinding wheel to the workpiece as a grinding wheel wears would help to understand the process and stiffness requirements of the workpiece holding, machine axis tuning parameters and the machine structure. Two possible methods to create similar conditions to those seen in helical grinding on a creep feed grinder are (i) having a parallelogram sectioned workpiece

and (ii) traversing through a rectangular workpiece at an angle. These two approaches could give the similar grinding wheel entry and exit condition to/from the workpiece to those seen in helical grinding.

A methodology has been established that has potential to accommodate evaluation of the performance of a range of new technologies on a machine tool more commonly available in research laboratories.

The methodology is a statistical approach using a combination of Taguchi methods to find the factors that have the greatest effect on the responses of interest, and response surface methodology using a limited series of tests to model the response behaviour. A review of the literature, for example (Chomsamutr and Jongprasithporn, 2012, Kilickap, 2010, DOJA, 2012, Bagherian Azhiri et al., 2014, Dhavlikar et al., 2003, Jamal et al., 2017), shows that statistical based approaches support this approach. In general Taguchi methods can be used when first assessing a new product and can be useful to understand which process factor affect the responses that are of interest. After identifying the factors that have the main effect on the response, a response surface methodology design can be made using only these factors. The response surface methodology design is a fractional factorial design giving a limited series of tests. A second-order polynomial mathematical relationship can then be established for the factors and test responses. The mathematical relationships can be used to generate surface plots that help to visualise the process responses and can aid in finding process optimum conditions as well as predicting process outcomes.

The apparatus design also accommodates the possibility to investigate the effect of varying contact conditions on grinding forces for a pseudo-helical grind.

Before selecting a methodology and designing the test equipment it was necessary to understand grinding process theories to appreciate how helical grinding differed from other grinding processes. The theories of removal rate, contact lengths and contact mechanics are covered in chapter 2. It was expected that the test arrangement would require grinding fluid application and it was necessary to understand the theories of grinding fluids and the application requirements so that they could be catered for in the test arrangement, the theories are discussed within chapter 3. The apparatus would need to use dressable grinding wheels that are widely used within industry. Several different dressing and conditioning methods are available, it was necessary to understand the differences between them, the

associated parameters and limitations of the methods when selecting the method to use. The conditioning of the grinding wheels is discussed in chapter 4.

## **1.2 Research aim and objectives**

### **1.2.1 Research aim**

To conceive and design a novel methodology for new product evaluation in relation to form grinding processes using a relatively small, non-specialist machine tool by simulating in part the contact conditions found in helical form grinding.

### **1.2.2 Objectives**

1. to design an experimental machining arrangement to allow:
  - the study of grinding forces in the helical profile grinding process by simulating in part the contact conditions
  - measurement of wear rates of the grinding wheel relative to the amount of workpiece material removed
  - process measurements that will allow specific grinding energy to be calculated
2. to develop a preliminary economic model for production cost that can be used in cooperation with the statistical methodology

## **2 Introduction to grinding processes**

Grinding is a complex process that requires knowledge of a number of subject areas such as solid and fluid mechanics, thermodynamics, metallurgy, tribology, mechanical design and metrology, in order to understand the process and its outcomes.

Grinding is an abrasive manufacturing process that uses hard particles to alter the surface of materials. The hard particles are referred to as grits or grains. Grinding processes use fixed abrasive grits typically in a belt or wheel form to remove material from the workpiece in a similar manner to milling and turning (macro) but on a smaller (micro) level.

The grinding process involves removal of material from a workpiece through the action of abrasive grits interacting with the work. The process generates swarf from the workpiece, wheel debris and heat. Fluid is frequently employed to help lower temperature and to aid removal of swarf and debris. Some processes however, do not use a grinding fluid though in such cases larger frictional losses occur and risk of thermal damage is increased. Dry grinding generally occurs with materials reactive to fluid or where the presence of fluid can be detrimental to safety. In wet processes the fluid is used to lubricate the grinding process reducing friction, cool the part and flush away swarf.

An abrasive wheel is made up of the grits, bonds that hold the grits in place and porosity. The most common abrasive grit materials used are aluminium oxide, silicon carbide, cubic boron nitride (CBN) and diamond. The grit bond material is softer than the grits allowing for a self-sharpening action, examples are vitrified, resin or metal. An effective abrasive grit will be harder than the workpiece material throughout its contact with the workpiece. When the grit is in sliding contact with the workpiece high temperatures are created and the grit must remain harder than the workpiece material at these high temperatures else the grit will be rapidly worn away.

The interaction between the grit and work lies in a branch of material science referred to as tribology. The contact between an abrasive grit and workpiece is related to the machining parameters, geometry of wheel and workpiece and materials employed. The differences result in varying kinematics for the process. A good level of understanding of the kinematics and contact mechanics of abrasives grits has been reached by previous research with focus being given to the most common operations: surface and cylindrical grinding. A good description of the tribology of a grinding process has been given by Marinescu et al. (2012).

## 2.1 Material removal rate

The grinding process removes material from the workpiece and invariably also from the grinding wheel. Removal rates can provide a useful measure of how the process is performing. When the removal rate and the machining power are known the specific grinding energy can be calculated. An inefficient grinding processes has high specific grinding energy and an efficient process has low specific grinding energy. The efficiency of different grinding technologies, processes and settings can be appraised by calculating the specific grinding energy.

Helical form grinding has kinematics that are neither the same as surface or cylindrical grinding but somewhere between depending upon the helix angle of the workpiece. For a part with a helix angle of  $0^\circ$  the process is the same a surface form grinding and for a helix angle of  $90^\circ$  the process is the same as cylindrical plunge form grinding.

The material removal process creates grinding swarf as a by-product, that is made up largely of individual chips of the workpiece material. The chips have a process related width, thickness and length. The length of the chips can be many times greater than the thickness of the chip. When studying the kinematics of the abrasive grit and how it forms, one uses an idealised chip, the thickness and width of the chip are usually referred to as the uncut chip thickness  $h_{cu}$  and uncut chip width  $b_{cu}$ . Both of these parameters vary along the chip length from 0 to  $h_{cu.max}$  and 0 to  $b_{cu.max}$  respectively. Figure 2-1 shows the idealised chip maximum and mean widths and thicknesses. The mean chip width  $\overline{b_{cu}}$  and thickness  $\overline{h_{cu}}$  occur when the volume is equally divided in two to give the mean volume  $\overline{V_{cu}} = V_1 = V_2$ .

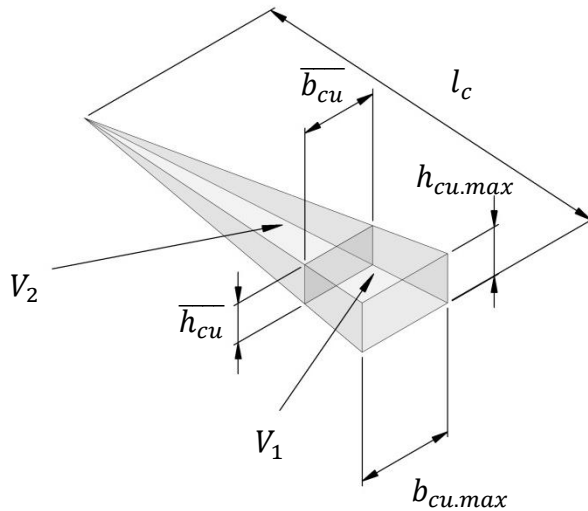


Figure 2-1 Idealised uncut chip mean and maximum width and thickness.

### 2.1.1 Surface grinding

Understanding the volume removed from the workpiece and the grinding wheel can aid the evaluation of the performance of a grinding process. The values calculated can be used in calculation of consumable costs per part ground.

The volume of material removed for surface grinding in one pass is shown in Figure 2-2 and is given by

$$V_w = b_w \cdot a_e \cdot L_w \quad (1)$$

Where  $b_w$  is the width of the workpiece,  $a_e$  is the effective depth of cut and  $L_w$  is the workpiece length.

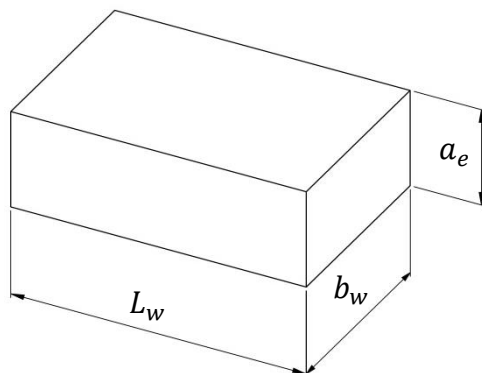


Figure 2-2 Volume of material removed in one grinding pass.

Example

$$600 \text{ mm}^3 = 100\text{mm} \times 0.01\text{mm} \times 600\text{mm} \quad (2)$$

Lots of chip volumes make up the volume removed from the workpiece.

Volume of tool wear is given by

$$V_s = b_w \cdot a_{sw} \cdot \pi \cdot d_s \quad (3)$$

Where  $a_{sw}$  is the depth of wheel wear and  $d_s$  is the wheel diameter.

Example

$$78.5398\text{mm}^3 = 100\text{mm} \times 0.0005\text{mm} \times \pi \times 500\text{mm} \quad (4)$$

Grinding ratio  $G$  (sometimes referred to as G-ratio) is the ratio of material removed from the workpiece to the volume of material removed from the wheel.

$$G = \frac{V_w}{V_s} \quad (5)$$

Grinding ratio can be used to evaluate the wear rate of the grinding wheel and can aid the assessment of the suitability of the grinding wheel for the process. G-ratio is a measure of a grinding wheel's capability to remove material by resisting wear. Low G-ratio values indicate that the wheel is not resisting wear. High G-ratios indicate that the wheel is resisting wear and is able to remove a large amount of material in comparison to the volume of grinding wheel wear. The G-ratio can vary considerably for different grinding wheel types.

Example

$$7.639 = \frac{600\text{mm}^3}{78.5398\text{mm}^3} \quad (6)$$

For surface grinding the volume removal rate  $Q_w$  is given by:

$$Q_w = b_w \cdot a_e \cdot v_w \quad (7)$$

Where  $b_w$  is the width of the workpiece,  $a_e$  is the effective depth of cut and  $v_w$  is the workspeed.  $a_e$  is different and usually less than the set depth of cut  $a$  due to system deflections  $\delta$ , thermal expansion of the workpiece  $a_t$ , and wear of the grinding wheel  $a_{sw}$  during the pass of the grinding wheel over the workpiece. If the wear rate of the grinding wheel is significant the effective depth of cut can vary along the workpiece length. Volume removal rates can be used to evaluate process performance. Higher volume removal rates could give shorter manufacturing time but could have other impacts upon costs per part and part quality.

The effective depth of cut is calculated from

$$a_e = a - \delta - a_{sw} + a_t \quad (8)$$

Example of volume removal rate

$$100\text{mm} \times 0.01\text{mm} \times 8 \frac{\text{mm}}{\text{s}} = 8 \frac{\text{mm}^3}{\text{s}} \quad (9)$$

The volume removal rate of a process can be dependent upon the width of workpiece and be specific to that operation. A specific removal rate per unit of grinding contact width, allows comparisons to be made of different operations. Specific removal rate is given by

$$Q'_w = \frac{b_w \cdot a_e \cdot v_w}{b_w} \quad (10)$$

Eqn (10) can be simplified to

$$Q'_w = a_e \cdot v_w \quad (11)$$

Example

$$0.08 \text{ mm}^2/\text{s} = 0.01\text{mm} \times 8 \frac{\text{mm}}{\text{s}} \quad (12)$$

## **2.2 Contact lengths**

In this section the contact lengths and the importance of understanding contact length is discussed. Factors that can be affected by contact length are temperature in the grinding zone and heat flux.

Contact lengths occur within the contact area between the grinding wheel and the workpiece. Understanding the contact mechanics forms part of the understanding of how the material removal occurs and the workpiece conditions that remain afterwards. Contact lengths are formed due to the geometry of the workpiece and the grinding wheel, the relative motions between them and the forces that are generated. The elasticity of the workpiece, the grinding wheel and the dressing tool can affect the grinding action and the surface condition of the workpiece. Real contact area between the grinding wheel and the workpiece is smaller than the apparent contact area. The real contact area between the workpiece and the grinding wheel is the sum of the individual contact areas of the grains. As real contact area increases so do the grinding forces. Increase in grinding forces can be due to wear of the grits on the wheel.

Marinescu et al. (2012) make the analogy that the grinding process can be compared to a micro-milling process. This analogy allows the kinematics to be studied, and provides the size, dimensions of the chips, and contact lengths of the grits to be understood and gives the first stage of understanding of the process. A milling process usually has a cutter with cutting edges at known intervals. This is not the case with grinding, the grits in the abrasive wheel are spaced randomly. This can cause variation in the behaviour of individual grains. However, when the whole wheel surface is considered the average behaviour allows the micro-milling analogy to be applied. The distance between grits around the periphery of the grinding wheel is considered to be constant. By choosing to not include the variation in spacing of grits around the grinding wheel periphery, the derived formulas do not take into account the variation in contact lengths, chip thickness, chip width, contact time of the grits and the surface roughness produced. If the spacing between grits  $L$  is taken to be an average for the wheel surface condition, the results of calculations that use  $L$  must also be taken to be an average result.

### **2.2.1 Surface grinding geometric contact length**

Marinescu et al. (2012) states that contact length is significant in affecting the energy and forces in the contact zone as well as the wear rate of the grinding wheel.

For surface grinding when the grinding wheel diameter ( $d_s$ ) is much larger than the depth of cut ( $a_e$ ), a close approximation for the geometric contact length ( $l_g$ ) between the grinding wheel and workpiece is given by equation (13).

$$l_g = \sqrt{a_e \cdot d_s} \quad (13)$$

Example

$$2.236\text{mm} = \sqrt{0.01\text{mm} \times 500\text{mm}} \quad (14)$$

This equation is based on the geometric contact length being very close to the chord length. This is a reasonable assumption given that the diameter of the wheel is typically much greater than the contact arc. The above equation does not take into account any deformation of the workpiece or grinding wheel contact. Using a chord length also makes the assumption that the contact path of the grit is circular. This is not true due to the feed of the grinding wheel. However, if the wheel speed is much higher than the workpiece the path is very near circular.

The geometric contact length is shown in Figure 2-3.

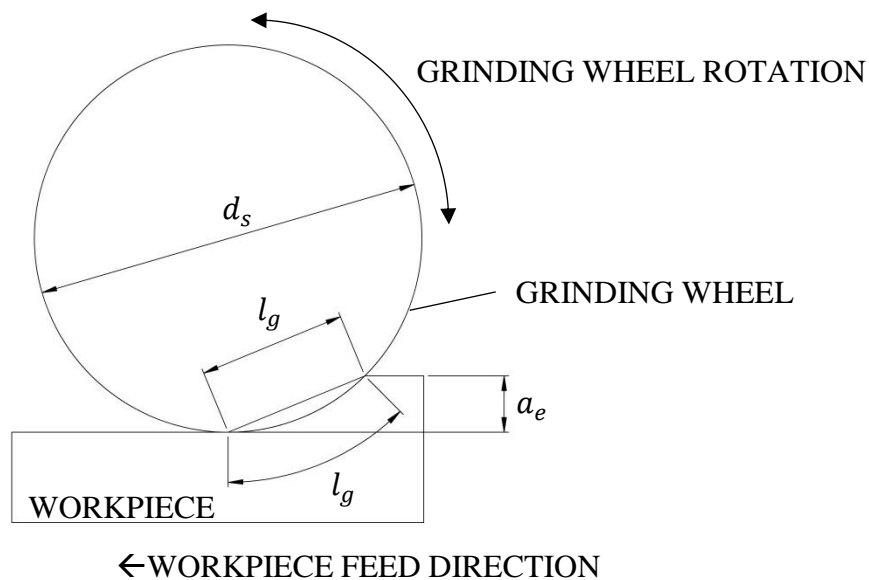


Figure 2-3 Straight surface grinding geometric contact length.

### 2.2.2 Surface grinding kinematic contact length

Increasing work speed also increases the contact length due to the feed distance per grit  $s$ . Due to the relative movement of the grit and the workpiece this is called the kinematic contact length  $l_k$  and is shown in Figure 2-4. The kinematic contact length is given by Eqn (15)

$$l_k = \left(1 \pm \frac{v_w}{v_s}\right) \cdot \left(l_g + \frac{s}{2}\right) \quad (15)$$

$v_s$  is the speed of the wheel. The contact length is slightly increased for up grinding (using + sign) a slightly decreased for down grinding (using – sign). Malkin and Changsheng (2008) stated that for most practical speed ratios of  $\frac{v_w}{v_s}$  the difference between up grinding and down grinding is extremely small. Also the contribution of  $\frac{s}{2}$  can be small and can be ignored for typical grinding speeds. This allows (15) to be simplified to

$$l_k = (1) \cdot (l_g) = l_g = \sqrt{a_e \cdot d_s} \quad (16)$$

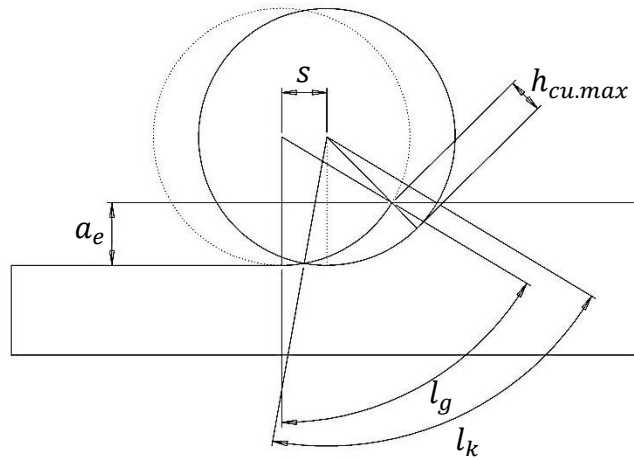


Figure 2-4 Surface grinding geometric and kinematic contact lengths.

### 2.2.3 Surface grinding chip thickness and aspect ratio

Figure 2-5 shows the maximum uncut chip  $h_{cu,max}$  which is given by

$$h_{cu.max} = s \cdot \sin(\theta_s - \theta'_s) \approx s \cdot \theta_s \quad (17)$$

Where  $\theta_s$  is angle of the geometric contact length and  $\theta'_s$  is the angle of contact length for maximum chip thickness for a cutting edge feed distance  $s$ .

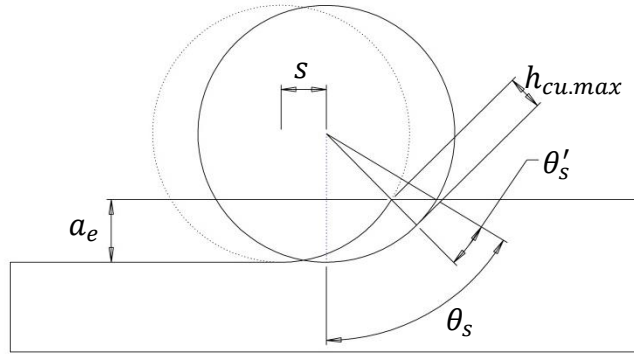


Figure 2-5 Maximum uncut chip thickness in surface grinding.

Marinescu et al. (2012) expanded this equation and showed that after removing some small values that had negligible effect it can be simplified to.

$$h_{cu.max} = 2s \sqrt{\frac{a_e}{d_s}} = 2L \frac{v_w}{v_s} \sqrt{\frac{a_e}{d_s}} \quad (18)$$

Therefore, the penetration of the grain cutting edge in to the workpiece is a function of the feed distance per cutting edge and the angle of contact. Changing these parameters affects the stress to the abrasive grain. An increase in chip thickness can increase wheel wear by causing bond fractures resulting in abrasive grains falling out.

The aspect ratio of the uncut chip thickness is given by

$$r_{cu} = \frac{l_g}{h_{cu.max}} = \frac{d_s}{2s} = \frac{v_s d_s}{2v_w L} \quad (19)$$

$L$  is the spacing between cutting edges in the cutting direction. The spacing between cutting edges on a grinding wheel has variation that is ignored, and an average value is usually used for calculations.

## 2.2.4 Surface form grinding contact length

Figure 2-6 illustrates surface grinding a form in a workpiece.

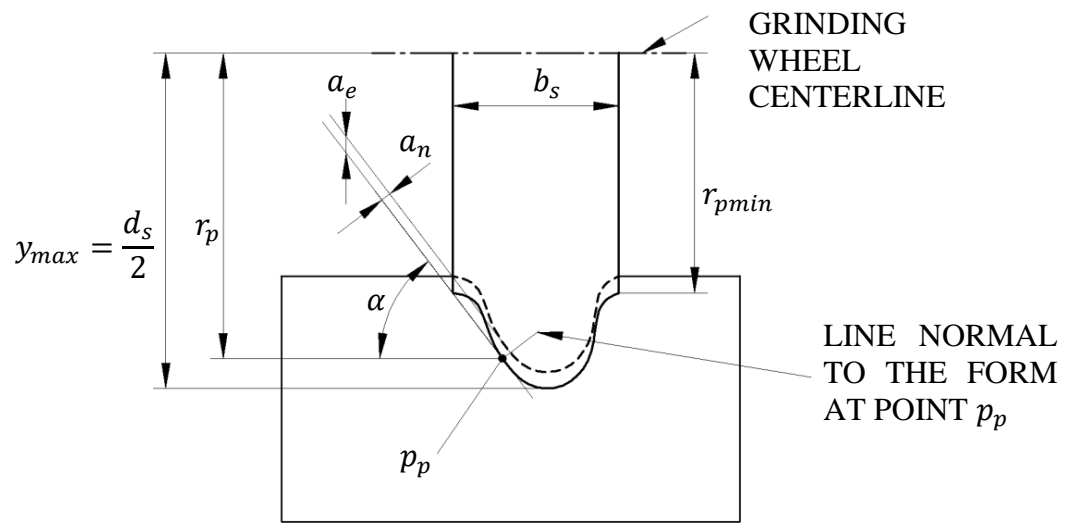
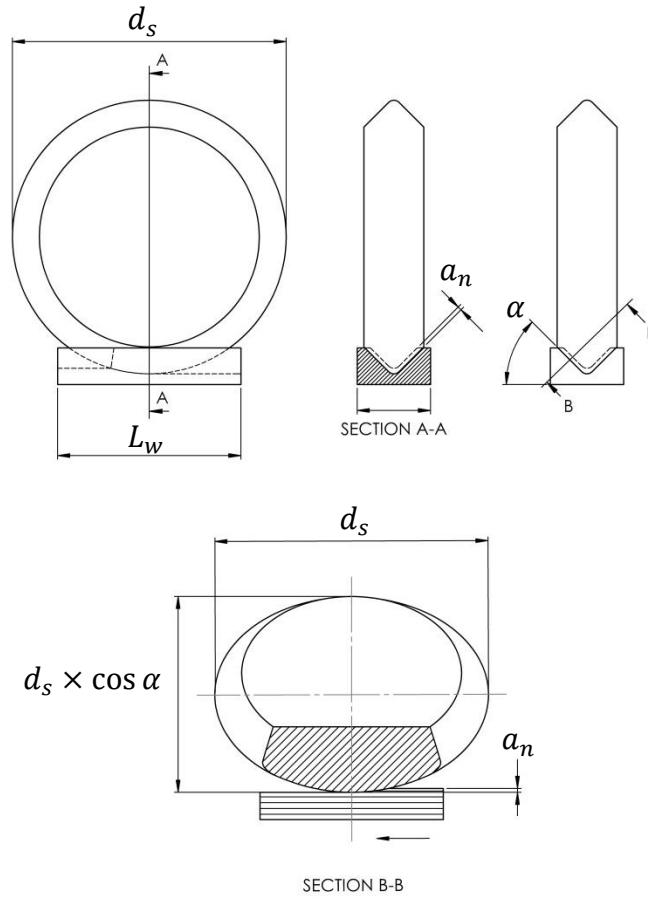


Figure 2-6 Surface form grinding.

In Figure 2-7 the projected sectional view is similar to Figure 2-3 with the exception that the wheel is elliptical in shape. The effective diameter of the grinding wheel at the contact point can be found by calculating the radius of curvature of the ellipse at the contact point.

Form grinding can cause variations if the depth of cut and the surface speed at a given point on the form. The effective diameter used for calculating the contact length will be different around the form as diameter  $d_s$  is not constant across the width of the form.



**Figure 2-7 Straight surface form grinding. Section B-B shows a section and projected view showing the process to be similar to straight surface grinding.**

The effective diameter for the point of interest on the form is given by (Malkin and Changsheng, 2008)

$$d_e = \frac{d_s}{\cos \alpha} \quad (20)$$

For points on the form where  $\alpha \neq 0$  the depth of cut normal to the point on the form  $a_n$  will be less than the effective depth of cut due to angle  $\alpha$ . The depth of cut normal to the surface is given by

$$a_n = a_e \cos \alpha \quad (21)$$

where

$$a_e = a - \delta - a_{sw} + a_t \quad (22)$$

$a_e$  is different and usually less than the set depth of cut  $a$  due to system deflections  $\delta$ , thermal expansion of the workpiece  $a_t$ , and wear of the grinding wheel  $a_{sw}$  during the pass of the grinding wheel over the workpiece. The angle of the point on the profile may need to be used to adjust the values for  $\delta$ ,  $a_t$  and  $a_{sw}$  depending on how the values have been measured or defined.

$$l_g = \sqrt{a_n \cdot d_e} \quad (23)$$

Substituting Eqn (20) and (21) in to (23) gives

$$l_g = \sqrt{a_e \cos \alpha \times \frac{d_s}{\cos \alpha}} \quad (24)$$

Eqn (24) can be simplified to

$$l_g = \sqrt{a_e \cdot d_s} \quad (25)$$

The angle of the point on the form can be ignored and the same formula used for straight surface grinding can be used for contact length. As  $d_s$  changes across the form the contact length will also change.

The surface speed of the grinding wheel can vary across the depth of the form due to the change in radius from the centre of rotation. If the form on the grinding wheel is defined in x and y coordinates from the centreline of the grinding wheel the surface speed at any point  $p_p$  on the form can be calculated from.

$$v_s = 2 \cdot r_p \cdot \pi \cdot n_s \quad (26)$$

$r_p$  is the distance from the grinding wheel centreline to point  $p_p$  on the form of the wheel,  $n_s$  is the rotational speed of the grinding wheel. The change in  $v_s$  across the form can affect the dimensions of the chips created.

Example of variation in geometric contact length across a form for a depth of cut of 0.01mm

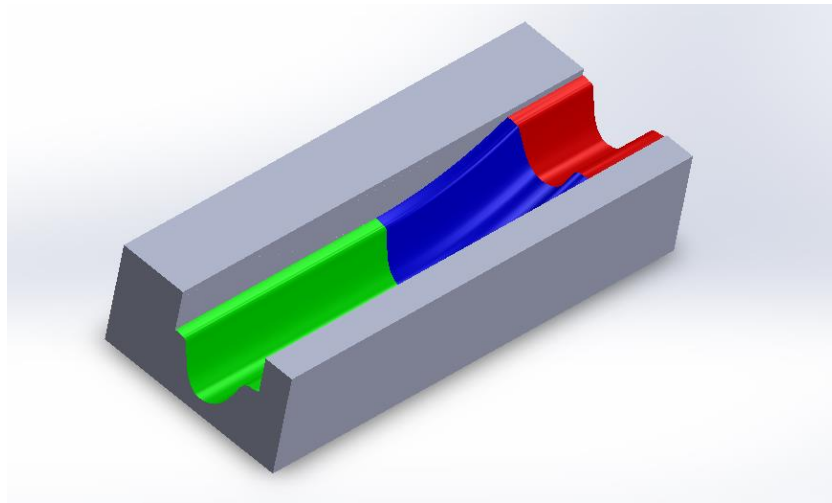
If  $r_{max} = 250mm$  then  $d_s = 500mm$  at the point on the form

$$l_g = \sqrt{0.01mm \times 500mm} = 2.24mm \quad (27)$$

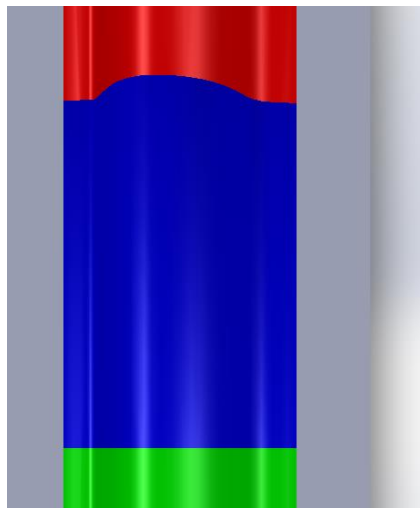
And if  $r_{min} = 190mm$  then  $d_s = 380mm$  at the point on the form

$$l_g = \sqrt{0.01mm \times 380mm} = 1.95mm \quad (28)$$

Figure 2-8 shows the apparent contact area between the grinding wheel and the workpiece in blue for a surface form grinding operation. In Figure 2-8 a) it can be seen that the points of the profile ground by the overall diameter of the grinding wheel extend further along the part and therefore have a longer contact length.



a)



b)

Figure 2-8 a) and b) are an example of a form ground slot. a) shows the full length of the slot and b) shows the apparent contact area viewed from directly above. The green area is the nascent surface created by the grinding wheel, the blue area is the apparent area of contact between the grinding wheel and the workpiece and the red area is existing surface that will be removed as the grinding wheel advances through the workpiece.

### 2.2.5 Helical form grinding contact length

Helical form grinding has similarities to cylindrical form grinding in that the curvature of the workpiece and the grinding wheel must be taken into account. Helical form grinding

requires that the curvature of the helix should also be taken into account as this will affect the effective diameter of the workpiece.

Makin states that the radius of curvature of a helical workpiece is given by (Sheth and Malkin, 1990).

$$\text{Radius of curvature of a helical workpiece} = \frac{(1 + y_2'^2)^{3/2}}{|y_2''|} \quad (29)$$

where

$$y_2' = \frac{\sin \alpha (q \cos \alpha - x_2 \sin \alpha)}{(m^2 - (q \cos \alpha - x_2 \sin \alpha)^2)^{1/2}} \quad (30)$$

$$y_2'' = \frac{-n^2 \sin^2 \alpha}{(n^2 - (q \cos \alpha - x_2 \sin \alpha)^2)^{3/2}} \quad (31)$$

$n$  is the radius of a spiral that passes through the point of interest

$$n^2 = x^2 + y^2 \quad (32)$$

Where  $x$  and  $y$  are coordinates of the workpiece profile in the transverse plane.  $\alpha$  is the angle of the grinding wheel to the workpiece axis.

The relative coordinate systems of the tool and the workpiece are shown in Figure 2-9.

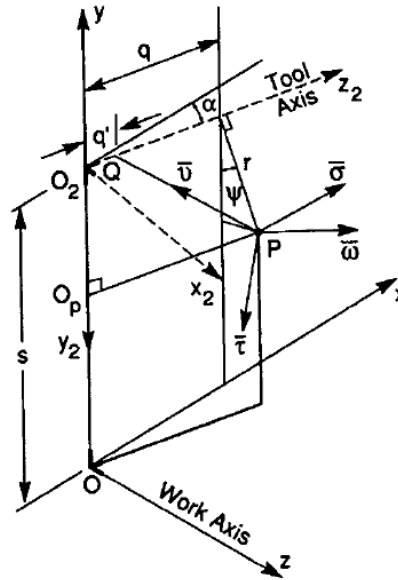


Figure 2-9 Coordinate frame for the tool and workpiece (Sheth and Malkin, 1990).

## 2.3 Contact mechanics

Contact mechanics need to be considered for the grinding wheel and workpiece contact as both have elastic properties. The bonds that hold the abrasive grits together are elastic and deflect when the grinding forces are applied. The workpiece surface can be deflected during the grinding process and stresses due to the grinding action can remain in the surface of the workpiece after grinding (Marinescu et al., 2012). The elastic deflections can affect dressing and grain wear.

### 2.3.1 Contact length

Contact length is an important parameter for understanding the contact mechanics. It has been shown that geometric contact length is not equal to the true contact length (Zhou and van Lutterwelt, 1992). The length of contact can affect the wear of the abrasive grain, the number of grains in contact, the time that the grain is in contact with the workpiece and cutting forces. The increased cutting length is due to the deflections of the workpiece and/or the grinding wheel. The contact length can be affected by the grinding forces, depth of cut and the roughness of the grinding wheel.

### 2.3.2 Contact length due to deflections

If a grinding wheel is pressed into a surface the contact length can be approximated with

$$l_f = 2\sqrt{\delta \cdot d_e} \quad (33)$$

$l_f$  is the contact length due to normal force,  $\delta$  is the distance that the wheel is presses into the surface and  $d_e$  is the effective diameter of the grinding wheel.

### 2.3.3 Contact length due to depth of cut

When the workpiece and the grinding wheel are considered to be ridged the contact length can be taken to be

$$l_g = \sqrt{a_e \cdot d_e} \quad (34)$$

and as shown in Figure 2-3.

### 2.3.4 Contact length due to deflections and DoC

Marinescu et al. (2012) discusses an approximate and an accurate method of calculating contact length for the combination of deflections and DoC. This section describes the accurate method. Figure 2-10 shows the effective diameters that need to be considered when dealing with deflections and DoC.

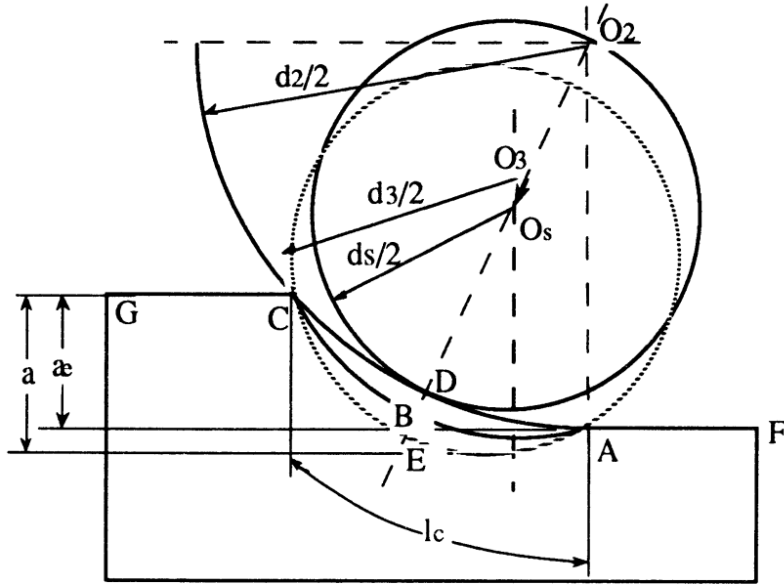


Figure 2-10 Contact arc due to depth of cut and deflections (Rowe et al., 1993). Where  $d_3$  is the contact curve during loading,  $d_2$  is undeformed diameter of the contact curve, and  $d_s$  is the undeformed wheel diameter.

If a wheel of effective diameter  $d_e$  is pressed against a workpiece diameter of  $d_{cu}$  (unloaded cut diameter) the effective diameter of both curvatures can be found by the sum of the two curvatures. As the curvatures are conformal they are subtracted from one another.  $d_{ef}$  is the effective diameter when cutting.

$$\frac{1}{d_{ef}} = \frac{1}{d_e} - \frac{1}{d_{cu}} \quad (35)$$

As stated before the geometric contact length without forces and deflections is given by

$$l_g = \sqrt{a_e \cdot d_e} \quad (36)$$

The contact length with grinding forces and deflections is given by

$$l_c = \sqrt{a_e \cdot d_{cu}} \quad (37)$$

The contact length is also equal to the contact length due to deflections of the effective diameter when cutting.

$$l_c = 2\sqrt{\delta \cdot d_{ef}} \quad (38)$$

Rearranging and substituting these formulas

$$\frac{4\delta}{l_c^2} = \frac{a_e}{l_g^2} - \frac{a_e}{l_c^2} \quad (39)$$

$$l_c^2 = l_g^2 + \frac{4\delta}{a_e} l_g^2 \quad (40)$$

From  $l_f = 2\sqrt{\delta \cdot d_e}$  and  $l_g = \sqrt{a_e \cdot d_e}$  this give

$$\frac{4\delta}{a_e} = \frac{l_f^2}{l_g^2} \quad (41)$$

Where  $l_f$  is the contact length due to normal force as described in section 2.3.2.

Substituting eqn (41) in to eqn (39) allow it to be simplified to

$$l_c^2 = l_g^2 + l_f^2 \quad (42)$$

### 2.3.5 Contact area

Contact area between the grinding wheel and the workpiece can be found from the contact length and width of the workpiece being ground. This can be referred to as the apparent area of contact. The true area of contact is the sum of the individual grain contacts. When the grains are sharp the area of contact is a lot less than the apparent area. As grains wear the real contact area increases, as this happens so do the forces. Although the real contact area can increase a lot with wheel wear the apparent area will not increase in the same proportion. Therefore, as the grinding forces increase due to grain wear the contact pressure increases. The rise in forces can give rise to greater deflections of the bonds between the grits of the grinding wheel. This can cause additional grits to start to contact with the

workpiece further increasing the real contact area. How a grinding wheel has been dressed can affect the real contact area due to the roughness of the grinding wheel.

Figure 2-11 shows the apparent contact area between the grinding wheel and the workpiece. The green area is the nascent surface created by the grinding wheel, the blue area is the apparent area of contact between the grinding wheel and the workpiece and the red area is existing surface that will be removed as the grinding wheel advances through the workpiece.

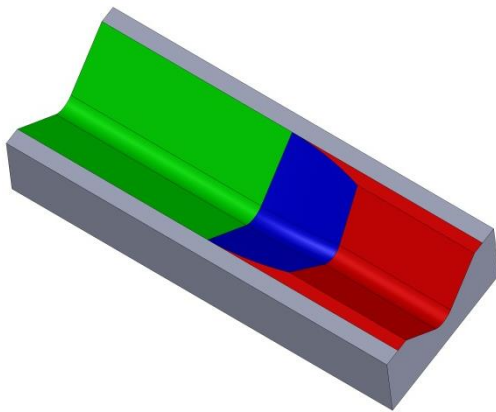


Figure 2-11 Example of apparent contact area for a surface form grinding workpiece.

## 2.4 Helical form grinding

In surface grinding with a cylindrical wheel of fixed width the depth of cut normal to the ground surface is constant across the wheel width. In form grinding the depth of cut normal to the ground surface can vary around the form. The industrial supporter of this study has an interest in helical compressor rotor profiles. The following section describes the geometry, production and quality problems that are experienced when producing helical compressor rotor profiles.

Helical components can have the form defined in a number ways. Usually the form is defined in either the transverse, normal or axial plane. The transverse plane is a plane perpendicular to the rotor axis. The normal plane is a plane created normal to the surface of the helical form at the pitch point. The normal and transverse planes are shown in Figure 2-12. The transverse plane is in the X-Y plane, the axial plane can be in either the X-Z or the Y-Z plane.

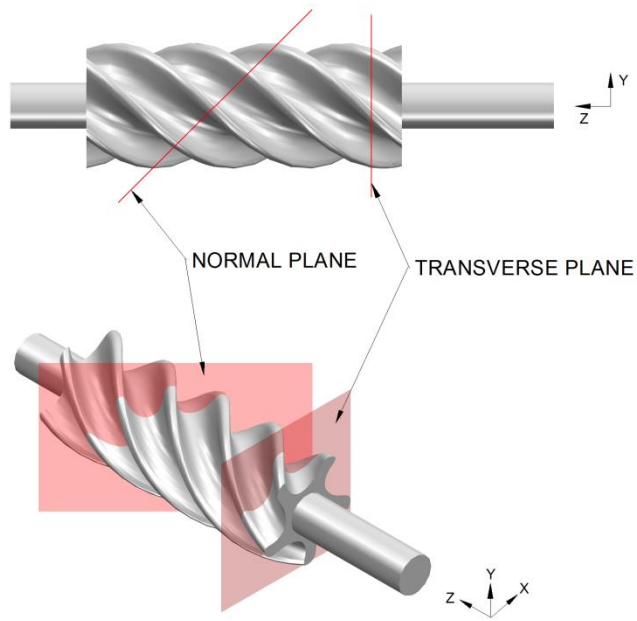


Figure 2-12 Principle axes, transverse and normal planes. The normal plane is perpendicular to two points on the profile at the pitch diameter.

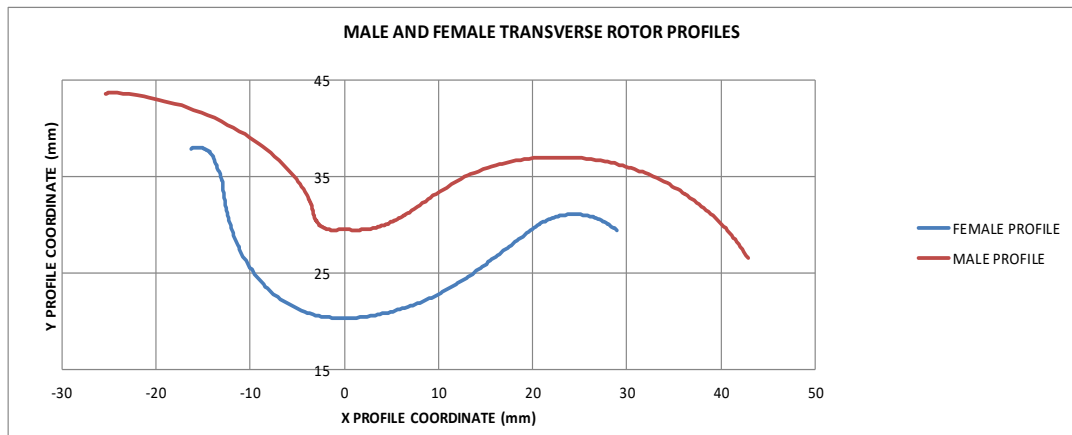


Figure 2-13 Male and female helical compressor rotor transverse profiles.

In the production environment compressor rotor profiles are split into regions. The point on the form with smallest radius to the workpiece centreline is referred to as the root radius or if the distance is doubled the root diameter. The majority of helical compressor rotor profiles are asymmetrical as shown in Figure 2-13. The asymmetrical form is split into two

general areas, the shorter steeper part of the profile (those appearing to the left of the x profile coordinate central axis in Figure 2-13) are referred to as ‘flat’ sides and conversely those to the right as ‘round’ sides. In some situations, the outside diameter is also ground when the form is ground, this area of the form is usually referred to as the overall diameter or OD for short. In the situations where the profiles are symmetrical the form is split again into two, but they are simply referred to as the left and right sides. However, it is important for both asymmetrical and symmetrical profiles to have a clear definition of which direction or end of the workpiece the profile is being viewed from to avoid misunderstanding.

The achieved DoC can be defined as the amount of material removed normal to the surface of the form/profile. The achieved DoC may differ from the programmed DoC due to deflection and thermal effects. The depth of cut is applied by moving the grinding wheel and workpiece centrelines closer together reducing the root radius and is referred to as a radial depth of cut. Figure 2-14 shows the variation in DoC normal to the surface around a female rotor profile for a radial depth of cut of 10 microns.

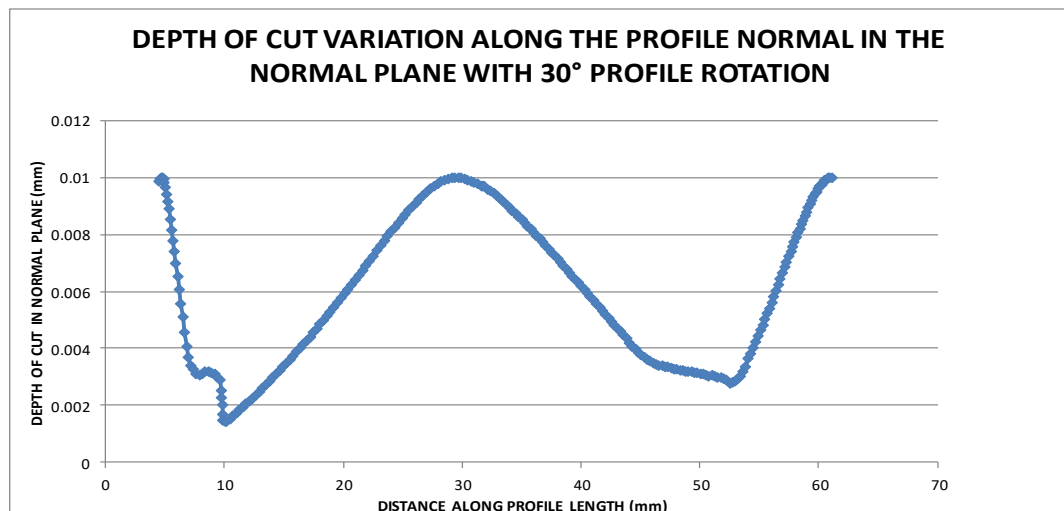


Figure 2-14 Depth of cut variation around a female profile.

The ratio between the maximum and minimum depths of cut is approximately 10:1 on this profile. The shape of this graph is defined by the shape of the rotor profile and does not change with different depths of cut. The variation in the depth of cut in turn causes the contact mechanics to change around the profile and therefore the grinding conditions.

Helical form grinding processes share similarities to both surface grinding and cylindrical grinding. The helix angle of the component affects how similar the process is to each of these processes. One of the main differences that helical form grinding differs to other grinding processes is the contact geometry between the wheel and workpiece. When grinding a helical part, the contact line between the workpiece and the grinding wheel is distributed over a larger amount of the circumference of the grinding wheel. If the helix angle of the workpiece is  $0^\circ$  the cutting geometries are the same as surface grinding. Increasing the helix angle to  $90^\circ$  creates an annular groove around the part and would create the same cutting conditions as form grinding an annular groove on a cylindrical grinder. Helical form grinding is more similar to cylindrical grinding due to the opposing curvatures of the grinding wheel and workpiece.

Around the helical form the contact conditions change:

- The radius of curvature of the wheel and the workpiece change, causing the contact length to change.
- The material removal rate is different around the form due to differences in helical feedrate. For example, the feedrate could be 1000mm/min at the pitch circle of the workpiece, 1025mm/min at the outside diameter of the form and 800mm/min at the root of the form.
- The pumping capacity of the wheel changes around the form. As the wheel diameter changes around the form the number of pores around the circumference of the wheel changes with the diameter. At smaller wheel diameters the number of pores is less this results in a low flow rate of grinding fluid through the grinding zone.

Figure 2-15 shows the feedrate variation around a profile for helical grinding and compares it to other grinding processes. Grinding a profile with the same radii on a cylindrical grinder gives much larger feedrate variation around the profile. However, offsetting the same profile radially and therefore increasing the radii of each point on the profile it is possible to achieve similar feedrate variation around the profile to that in helical grinding on a cylindrical grinder. Grinding the same profile using surface grinding gives the same feedrate around the profile. Figure 2-16 shows the variation in the geometric contact length when grinding a form in surface grinding.

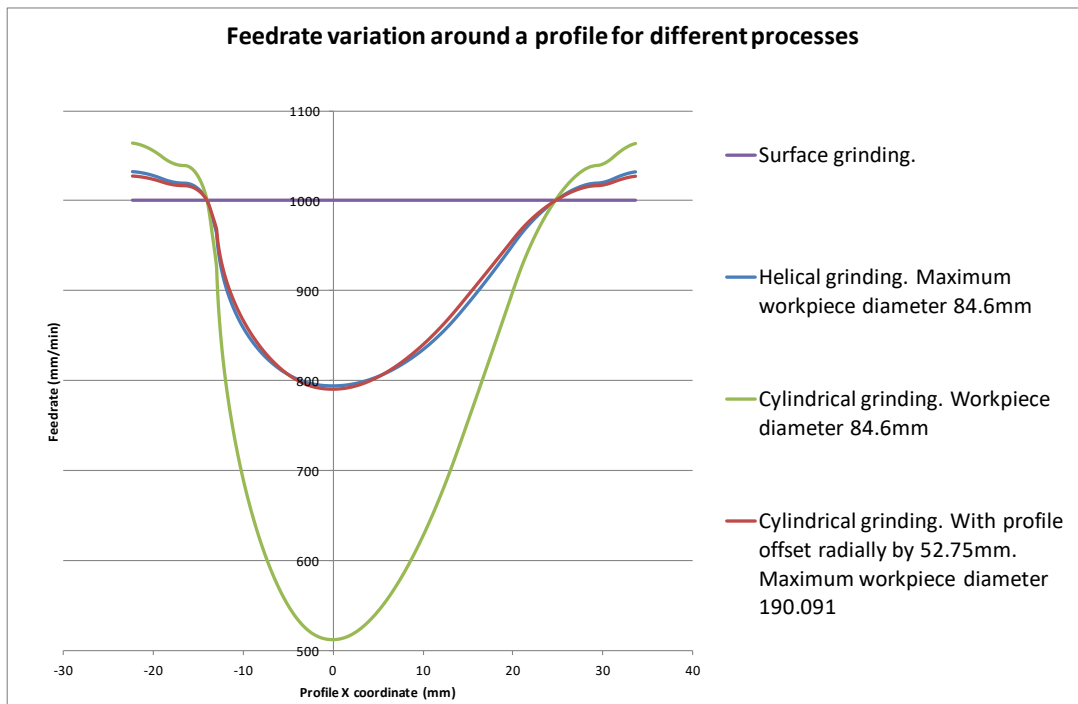


Figure 2-15 Variation of feedrate around a profile for different grinding processes.

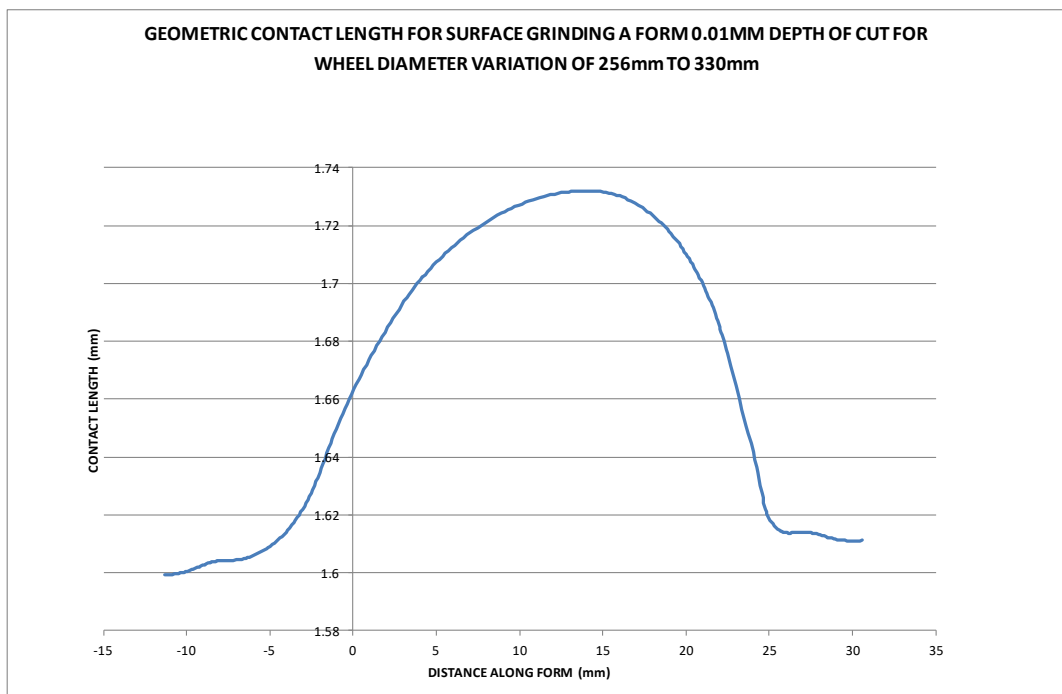


Figure 2-16 Variation of geometric contact length for surface grinding a form.

Figure 2-17 and shows the change in the helical length of the component with a change in diameter of the form.

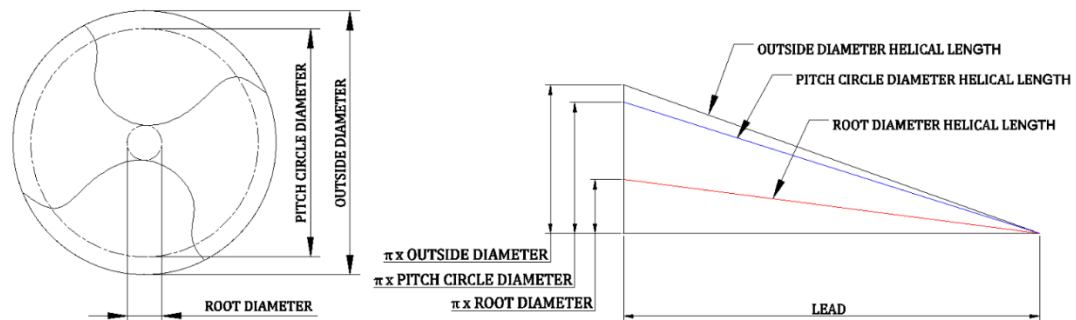


Figure 2-17 Change in helical length with diameter.

Grinding processes can have problems such as wheel wear, thermal damage, surface roughness, chatter, wheel loading and workpiece geometry errors. In the case of compressor rotor manufacture the main problems are wheel wear, geometric errors and thermal damage.

Compressor rotor profiles can be symmetrical or asymmetrical, in either case the edge angle that the helical profile make with the end face of the rotor changes around the profile. Small acute edge angles create small volumes of material adjacent to the grinding contact zone on entry and exit of the grinding wheel. These volumes can heat up rapidly due to not having the volume to dissipate the heat from the grinding action in to. This geometry can cause grinding damage at these small edge angles as shown in Figure 2-18.

Burn on end face where the edge angles are small.

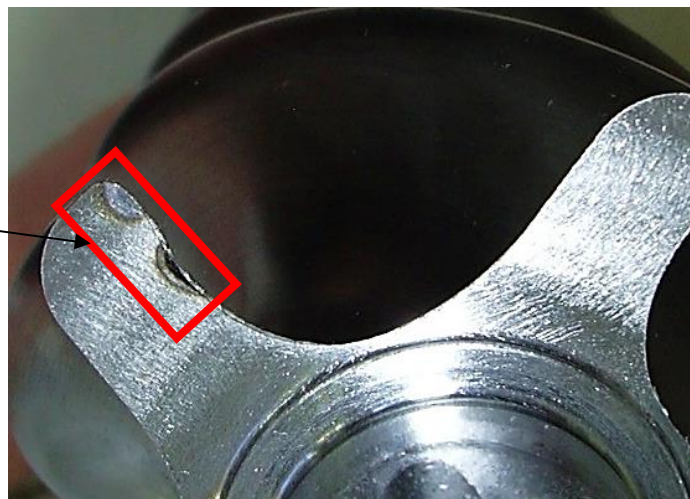


Figure 2-18 Burn on the end face of a compressor rotor where the edge angles are small.

In the case of an asymmetric workpiece profile the contact between the workpiece and the grinding wheel will usually be asymmetric. Depending upon which side of the workpiece body the grinding wheel enters either the flat or the round side of the helical flute will start

to be ground first. Only one side of the profile will start to be ground, as the wheel moves further into engagement with the part more of that side of the profile will start to be ground, until the grinding wheel contact reaches the root of the profile at which point the first side of the profile will be fully in contact with the grinding wheel, the other side of the profile will then start to be progressively ground. The progressive increase in the engagement of the grinding wheel with the part is thought to produce variation of grinding forces and factors such as coolant application. These variations are thought to affect the lead results of helical parts, sometimes referred to as push off.

The lead of a helical component is the axial advance of the helix along its axis for one complete turn (360°). Lead can be calculated from the pitch circle diameter and the helix angle. Figure 2-19 shows the relationship between rotor geometry and lead. Eqn (43) also expresses the relationship where  $d$  is the pitch diameter,  $L_e$  is the lead and  $\theta$  is the helix angle.

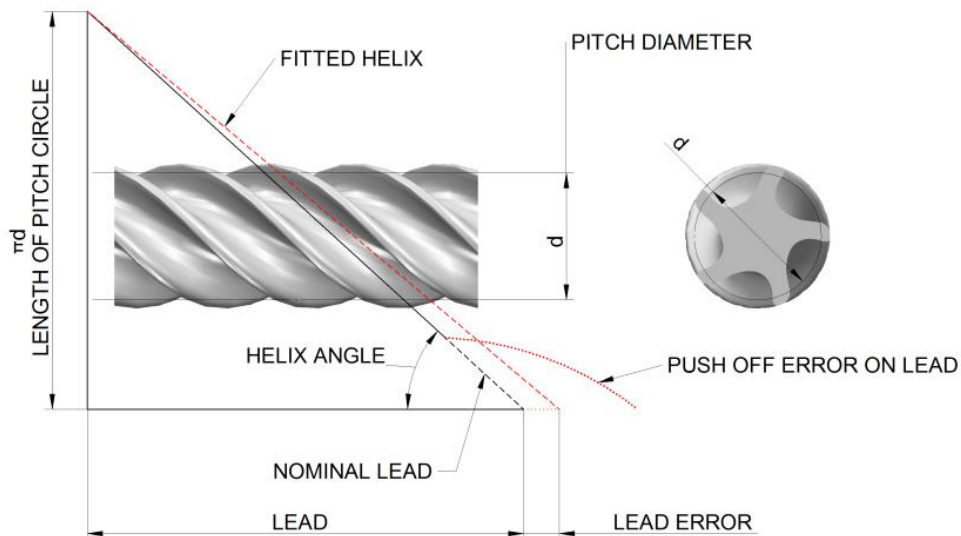
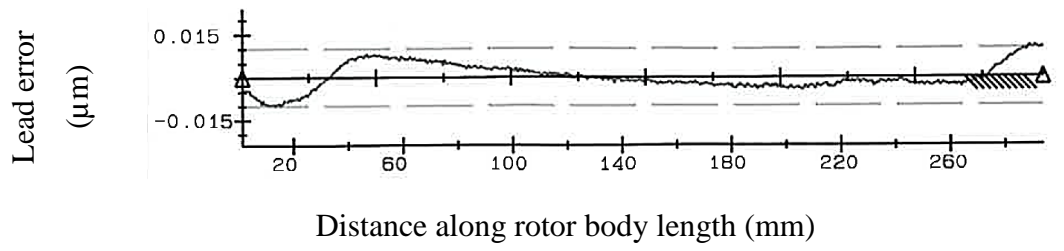


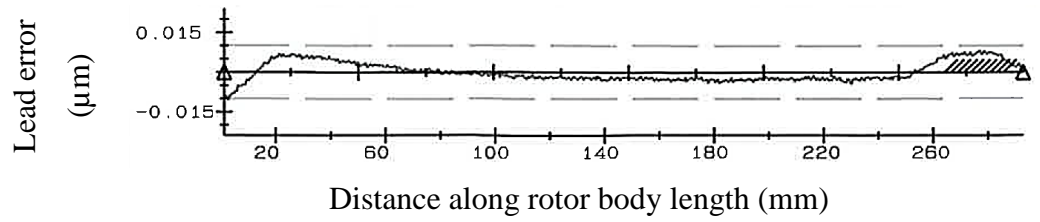
Figure 2-19 Relationship of rotor geometry to lead, and the result of a push off error on a fitted lead result.

$$\tan \theta = \frac{\pi d}{L_e} \quad (43)$$

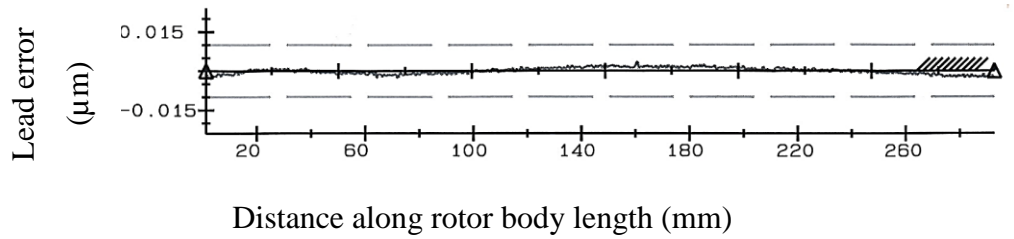
Figure 2-20 shows the lead results with push off effects for the round side of the profile (a), flat side of the profile (b) and a lead error that has minimal push off errors (c). One of the main quality measures for helical form components is the lead. Quality measures for lead include precision, variation between forms and straightness/form error. Push off errors affect both the form results and the precision of the lead. The lead result is calculated by fitting a straight line to the form of the result. Figure 2-19 shows the nominal lead, a push off error and how a fitted lead projects to create a lead error result. The push off errors in Figure 2-20 (a) and (b) are present for 20-40 mm from each end of the lead results. The push off errors in the lead, in combination with other compressor component manufacturing inconsistencies can cause operation inefficiency and operation noise. The contact between the male and female rotor are affected by the push off errors, this causes the seal line between the male and female rotors to be affected and causes losses in pressure.



a) Round side errors



b) Flat side errors



c) Good lead example will minimal push off errors.

Figure 2-20 Examples of lead errors.

### **3 Introduction to grinding/process fluids**

Grinding process fluids are sometimes referred to as coolants, though cooling is not its only function. A further important function of a grinding fluid is to lubricate the contact between the abrasive grit, bond and the workpiece to reduce the friction created and adhesive wear between them. The grinding fluid also provides a flushing action to remove chips and debris from the grinding zone and machine structure. It can also be used to thermally stabilise machine structures and protect the workpiece and machine from corrosion. The fluid helps reduce temperature rises due to wheel-work interaction by conduction and convection processes. The heat removed by the grinding fluid can help reduce the thermal distortions, as well as having a large influence on the process efficiency and part quality. Grinding fluids can improve tool life, surface finish and reduce forces. If the grinding process involves dressing of the abrasive to keep it conditioned for the grinding process the application of the grinding fluid can make the dressing process more efficient.

A grinding fluid can remove a significant amount of heat created by a grinding process, (Jin and Stephenson, 2003), and can be more than 90% in processes such as creep feed grinding. In conventional processes the remainder of the heat generated by the grinding process is transferred to the grinding wheel, air, workpiece and the chips. The amount of heat that is absorbed by each element of the process can depend upon the grinding conditions selected. High efficiency deep grinding (HEDG) uses large depths of cut and high workspeeds that give very high material removal rates (Marinescu et al., 2012) and only 5-10% of the grinding heat is removed by the fluid (Jin and Stephenson, 2003), but the fluid application is still important to ensure good lubrication so that the specific grinding energy can be kept low.

Howes et al. (1987) proved the effect of film boiling in shallow cut grinding which occurs when the surface temperature in the contact area exceeds the boiling temperature of the fluid. When the temperature in the contact area exceeds the boiling point the partitioning of heat changes to values close to that observed for dry grinding (Howes et al., 1987). Howes (1990) draws conclusions from previous research that film boiling is a critical limitation of the stock removal in grinding. Howes (1990) concluded that when film boiling occurs in creep feed grinding a sudden overheating of the workpiece occurs, and that the boiling temperatures of water based fluids and oil fluids is 130°C and 300°C respectively. When film boiling occurs, the fluid turns from a liquid to a vapour state in two steps. The

first step that the grinding fluid makes is nucleate boiling, the second step is that the fluid enters a vapour state. In the nucleate boiling state the transfer of heat from the workpiece to the fluid rises. As the temperatures in the grinding zone rises the nucleate boiling changes to film boiling that forms a vapour film. The vapour film is created between the workpiece and the fluid and acts as an insulator that suppresses heat transfer from the workpiece to the fluid. Guo and Malkin (1994) refer to the amount of heat flux that creates film boiling temperatures as the critical burn-out limit. They also state that for exceeding the critical limit for burn-out is catastrophic for creep feed grinding but not for shallow cut grinding. Rowe and Jin (2001) states that after the burnout point convection is severely reduced.

In shallow cut grinding the contact area and time are small and therefore little opportunity for convective heat transfer to the grinding fluid. The main effect of grinding fluid in shallow cut grinding is reducing temperatures by reducing frictional forces and wheel dulling (Marinescu et al., 2012). Oil based grinding fluids provide better lubrication and tend to lower the specific grinding energy of the process (Marinescu et al., 2007). The lubricity of the grinding fluid reduces the frictional forces the heat generated and helps to achieve greater wheel life (Brinksmeier et al., 1999). Malkin (2008, p213) concluded that “More effective cooling requires delivery of more and/or cooler grinding fluid to the grinding zone.”

In surface and thread grinding the grinding fluid application conditions can change at the ends of the workpiece. The nip created between the workpiece and the grinding wheel can aid the direction and application of the grinding fluid to the grinding contact zone. In form or slot grinding a pre-existing form or slot ahead of the grinding wheel path helps to guide grinding fluid to the nip between the grinding wheel and workpiece, and helps reduce flow around the sides of the wheel. However, during surface and thread grinding operations the nip between the wheel and workpiece changes as the grinding wheel nears the end of the workpiece closest to the nozzle. The grinding fluid can be deflected down the face of the workpiece starving the grinding zone of grinding fluid. Starvation of the grinding fluid can result in thermal damage and geometrical errors in the workpiece due to the lack of lubrication, convection and conduction cooling that it provides. The lack of lubrication and cooling can cause the workpiece material to expand increasing the effective depth of cuts and removing more material.

When grinding helical forms, the contact between the wheel and the workpiece changes as the wheel nears the edges of the workpiece. The contact decreases from full form contact

across the full wheel width to contact one side of the wheel width and eventually to no contact as the wheel exits the workpiece. As the amount of contact between the workpiece and the grinding wheel is changing the forces between them are also changing. Changing the forces causes changes in the deflections of the grinding system causing workpiece geometry errors. The change in the contact creates a change in the channel geometry between the wheel and the workpiece. As the wheel exists the workpiece and the contact changes to one side of the wheel a gap between the non-contact side of the wheel and the workpiece is created and becomes larger as the wheel exits further. The gap created allows another exit path for coolant. The opposite effect happens when the grinding wheel enters the workpiece, the gap between the non-contact side of the wheel is large as the wheel starts to grind and becomes smaller as the wheel enters full engagement with the part. The additional exit path changes the conditions of the coolant application due to the channel not providing the same fluid guidance. The gap may also allow changes in hydrodynamic pressure conditions between the workpiece and the grinding wheel causing the changes in deflections of the grinding system resulting in geometrical workpiece errors.

### **3.1 Types of grinding fluids**

Most grinding applications apply the grinding fluid in a steady flow liquid form, less commonly sprays, mist, gases or solid lubricants are used. Legislations involving health and safety and the environment have created an interest in these less common applications of grinding fluids and solids, due to increased costs of meeting the requirements of the legislation. Grinding fluids can be classified according to the base fluid, typically neat oils and water based fluids. Standards such as DIN 51385 classify coolants as water-immiscible, water-miscible and water composite fluids.

Steady flow streams are used in the majority of helical form grinding applications due to it providing the best combination of lubrication, contact area cooling, bulk cooling, flushing performance, and corrosion protection for that grinding application. Therefore, this study will be constrained to grinding fluids applied in steady flow streams.

Water-immiscible coolants are not mixed with water. Water-miscible coolants are emulsifying or emulsifiable and need to be combined with water before use. Water-composite cooling fluids are made up of water and water-miscible coolants in a premixed form. Water-composite coolants are further subdivided in DIN 51385 to categories of Oil-

in-water emulsions, Water-in-oil emulsions and cooling lubricant solutions. Table 3-1 summaries the advantages and disadvantages of the different types of grinding fluid.

Table 3-1 Grinding fluid characteristics (1= worst, 4 =best) (Webster, 1995).

	Synthetics	Semi-synthetics	Soluble Oil	Neat oil
Heat removal	4	3	2	1
Lubricity	1	2	3	4
Maintenance	3	2	1	4
Filterability	4	3	2	1
Environmental	4	3	2	1
Cost	4	3	2	1
Wheel life	1	2	3	4
G-Ratios	2.5-7.5	2.5-6.5	4-12	60-120

### 3.2 Grinding fluid lubrication

It is known that one of the most important functions of the grinding fluid is the lubrication of the grinding action (Brinksmeier et al., 1999, Marinescu et al., 2012). Lubrication helps to minimise the friction between the interacting faces of the workpiece and the grinding wheel grit and bond. Grinding forces, surface roughness and tool wear are reduced due to the application of lubricant while grinding (Brinksmeier et al., 1999). In shallow cut grinding the main effect of the grinding fluid is the lubrication of the process within the contact area (Marinescu et al., 2012).

### 3.3 Grinding fluid application

The grinding fluid is added to the grinding process via a nozzle that positions and directs the coolant at part of the machining process. To avoid temperature changes during the process the grinding fluid is usually supplied continuously. The nozzles used for the application of coolant can be described in a number of ways, how the fluid is focused (such as spray, jet, through tool or flood) and the nozzle geometry (such as needle, shoe, squashed

pipe, rectangular, round). Much research has been done on the application of coolant to grinding. The research has covered areas concerning the nozzle design, coolant type, flowrate and pressure, coolant application aids such as air scrapers and workpiece extensions/coolant guides, research reported in these areas is Webster et al. (2002), Howes (1990), Mandal et al. (2012), Gviniashvili (2003), Howes et al. (1987), Wu (2009), Jackson (2008), Baines-Jones (2010), Morgan et al. (2008), Massam (2008), Catai et al. (2006).

A boundary layer of air around the grinding wheel can create an air barrier that has been shown to stop coolant from entering the grinding contact zone Wu (2009), and was clearly shown by Ebbrell et al. (2000) as shown in Figure 3-1. The air barrier is a layer of low pressure high velocity air around the periphery of the grinding wheel that prevents the coolant reaching the grinding wheel surface. The depth of the air barrier is affected by the roughness of the wheel and the permeability of the grinding wheel. The air barrier can be more of a problem with high porosity wheels, Rowe (2009) explains that the wheel acts like a pump drawing air in from the sides and exiting tangentially from the periphery to create the air barrier. Marinescu et al. (2012) states that masking / side sealing the sides of the wheel can reduce the air barrier. The air in the boundary layer does not pass through the grinding contact zone causing it to pass down the sides of the grinding wheel or reverse direction at the nip created between the grinding wheel and the workpiece. The kinetic energy of flood coolant is not enough to penetrate the air barrier. For medium to high wheel speeds the grinding fluid needs to be applied in such a way that overcomes the air barrier. Fluid is best applied tangentially to the grinding wheel surface directed at or just before the nip between the grinding wheel and the workpiece. The air barrier can be less of a problem if the coolant jet velocity matches the wheel surface speed.



Figure 3-1 Air barrier holding back the coolant (Ebbrell et al., 2000).

### 3.3.1 Useful flow

Jackson (2008) investigated useful flow through the grinding contact zone and defined useful flow in three sections.

1. The convenient flow is the amount of fluid that physically passes through the grinding contact region due to the topography of the contact only and can depend upon conditions such as wheel speed, porosity and width.
2. The useful flow includes convenient flow and additional fluid flow through the contact caused by other conditions such fluid pressure allowing more flow through the wheel.
3. The optimal useful flow is the minimum amount of grinding fluid that gives the best process efficiency workpiece quality and minimum waste beyond which no additional benefit is gained.

The optimal useful flow that a process requires can depend upon process requirements such as size holding and material removal rate. A truly optimised process may require that the optimal flow is changed throughout the process. A process that has both roughing and finishing passes may require that the roughing DoC needs more flow than finishing DoC

for optimal flow. Also machining process that have different wheel types or specifications can require different optimal flows.

### **3.3.2 Coherent jet**

A jet of fluid begins to disperse and entrain air as the distance from the nozzle exit increases. Adding air to the contact zone reduces the effectiveness of the grinding fluid, therefore the nozzle exit is placed as close to the nip as is possible. However, this is not always practical in the case of large thread grinding operations, where the nozzle has to be placed at greater distances from the nip due to interference problems with the workpiece or machine structure. As the nozzles are placed further away from the nip the exit area is usually increased to ensure that the flow that reached the nip has not dispersed due to turbulence in the jet. Using jets that are designed to produce a jet that has coherent flow for greater distances from the nozzle exit allows the nozzles to be positioned in a more practical position that gives less interference problems.

### **3.3.3 Auxiliary nozzles**

A wheel scrubber nozzle can be used to improve a grinding processes by using a high pressure jet of grinding fluid directed at the surface of the grinding wheel. The purpose of a wheel scrubber is to remove chips and loose wheel grits from the surface of the grinding wheel. The pressures required to perform this can be in the region of 40-100 bar.

### **3.3.4 Coolant applications aids**

An air scraper can be used to help remove most of the air barrier from the wheel. An air scraper is typically a plate that is placed close to the wheel surface with a gap in the region of 30 $\mu$ m between them. An alternative to an air scraper plate is to use a high pressure jet of fluid. Mandal et al. (2012) also found that a pneumatic barrier could be used to reduce the air pressure of the air barrier by 53%. The application of a fluid to reduce the air barrier has the advantage of not needing to be adjusted as frequently as a plate air scraper. Using an air scraper removes or reduces the air barrier and if placed correctly (Wu, 2009) reduces the need for high pressure grinding fluid jet.

## **4 Introduction to conditioning of grinding wheels**

Conditioning a grinding wheels involves the preparation and maintenance of the grinding wheel surface for material removal. Conditioning can be split into three operations:

1. Trueing to achieve a good form around the entire periphery of the grinding wheel, ensuring that it is concentric with the axis of rotation.
2. Cleaning the wheel to remove areas that have become loaded or clogged with the workpiece material. Loading can occur at the grain contact point or in the pores of the grinding wheel.
3. Dressing to create or maintain an efficient cutting action.

When using vitrified grinding wheels often the same process is used for all three operations and the term dressing is used for all these operations. Superabrasive wheels are usually conditioned in one operation and then touch dressed with small dressing passes typically only a few microns in a separate operation.

The grinding process performance can be altered by controlled changes to the dressing parameters. Changing the dressing parameters alters the topography of the grinding wheel and the distribution of grits which affect the grinding efficiency, grinding forces, wheel wear and workpiece surface quality (Malkin and Changsheng, 2008, Marinescu et al., 2007)

It is possible to achieve self-dressing conditions that involves the abrasive grains fracturing when they become dull. The friable abrasive grains are required to micro or macro fracture at the cutting edge to expose a new cutting edge and help maintain the process efficiency. A self-dressing process can be desirable as it can reduce or eliminate a separate dressing process that may add to the machining cycle time. However, the wear rate of the grinding wheel for a self-dressing process needs to be such that the workpiece geometry and surface finish requirements are maintained without the need for frequent separate conditioning operations to maintain acceptable workpiece limits. When self-dressing is not achieved the abrasive grits wear to create flats, this is referred to as glazing. Glazing can be seen on a stationary grinding wheel as the wear flat on the abrasive grit reflects light. The wear flat on the abrasive grits reduces the cutting efficiency and increases the grinding forces.

## **4.1 Dressing**

The process of dressing affects the sharpness of the grinding wheel and how open the wheels micro-topography is. Dressing is performed to create the required topography on the grinding wheel surface, the topography required depends upon the workpiece and process requirements. Dressing is an important step as the topography of the grinding wheel influences:

- grinding forces
- temperatures created during grinding
- surface roughness created on the workpiece
- The maximum material removal rate
- The process efficiency

## **4.2 Conditioning methods**

Conventional or traditional conditioning methods involve a tool that is passed over or pressed against the periphery of the grinding wheel and remains in contact with the wheel during the dressing process. Several different dressing methods exist they can be split in to fixed point and rotary. Hand conditioning methods exist, however, they can be considered as less controllable and repeatable for the type of form grinding considered in this study. Unconventional dressing methods do not involve contact between the grinding wheel and the dressing tool, giving lower forces and wear.

## **4.3 The main conventional dressing methods**

### **4.3.1 Rotary dressing**

Rotary dressing tools have a number of diamonds around the periphery of the disc which is driven by a powered spindle drive that gives control of the disc speed. The number of diamonds on the disc gives the dresser longer life than the stationary dressers. Rotary dressing methods can be split in to form and profile dressing.

#### 4.3.1.1 Profile dressers

The width of a profile dresser covers the full width of the grinding wheel and has geometry that contains the negative shape that is required on the grinding wheel. The profile dresser is moved radially into the grinding wheel at a controlled rate. Profile dressers use a large volume of diamond and are therefore expensive, do not give much flexibility and allow quick dressing times. The high cost and limited flexibility results in profile dressers mainly being used for large volume work. The variables that affect the wheel topography created by the form dressing process are radial feed  $f_{rd}$ , speed ratio  $q_d$ , and the number of rollout revolutions. Due to profile dressers covering the full width of the wheel they can be used for continuous dressing, allowing the wheel to be kept in a sharp condition.

#### 4.3.1.2 Form dressers

Form dressing creates the wheel geometry by controlled movements of the dressing tool in an axial and radially directions. Form dressing can allow control of the profile on the wheel. Grinding helical profiles can require the shape to change on the grinding wheel as the wheel diameter reduces. The magnitude of the profile change depends upon the change in wheel diameter and the size and shape of the profile being ground. For example, a screw compressor rotor can require the grinding wheel profile to change by 0.2mm in places as the wheel diameter changes from 500mm to 350mm. Changes of this magnitude cannot be accommodated with the profile dressing methods and therefore machines made for this application use the form dressing method.

The variables that affect the wheel topography created by the form dressing process are the depth of dress  $a_d$ , speed ratio  $q_d$ , dressing lead  $f_d$  and overlap ratio  $U_d$ . Both the grinding wheel and the dressing disk rotate during the dressing process. Changing the relative speeds and directions of the two allows control of the conditioning of the grinding wheel. The relative speeds of the grinding wheel and the rotary dressing tool is called the speed ratio  $q_d$  also known as crush ratio and is calculated using equation (44).  $v_{sd}$  is the speed of the dresser and  $v_s$  is the speed of the grinding wheel.

$$q_d = \frac{v_{sd}}{v_s} \quad (44)$$

Synchronous dressing also known as uni-directional dressing that has a positive speed ratio and asynchronous dressing also known as counter directional dressing that has a negative speed ratio. The relative direction between the dresser and the grinding wheel influences the forces between them and the surface finish that is produced on the workpiece. The higher forces created during synchronous create higher dresser wear (Marinescu et al., 2007).

Crush dressing is also possible with form dressers. Due to the point contact in form dressing some of the disadvantages of crush dressing with profile dressers are avoided. As a point contact occurs at a single diameter the relative velocities can be maintained by changing either the grinding wheel speed or the dresser disc speed. Also, the point contact is a small area and the forces are much smaller.

Matching the velocity of the grind wheel and the dressing disc for crush dressing reduces wear of the dressing tool (Derkx et al., 2008). Derkx et al. (2008) designed and tested a form dressing system that controls the speed of the disc by using the principle of natural synchronisation between the form disc and the grinding wheel. The tests investigated different dressing depths and the effect that it has on the wear rate of the form dresser and grinding wheel. Increasing the dressing depth showed an increase in the wear of the grinding wheel and reduced grinding forces.

#### 4.3.2 Traverse dressing

Traverse conditioning is the process of passing the diamond over the periphery of the grinding wheel in a controlled feed motion. The dressing lead  $f_d$  is the distance moved across the wheel per revolution of the grinding wheel and can be calculated using equation (45). Where  $v_{fd}$  is the dressing traverse feedrate,  $v_s$  is the grinding wheel velocity and  $d_s$  is the initial diameter of the grinding wheel. Changing the dressing depth and the dressing lead affects the surface finish that is produced on the workpiece.

$$f_d = \frac{\pi \cdot d_s \cdot v_{fd}}{v_s} \quad (45)$$

$U_d$  is the overlap ratio and indicates how often a point on the grinding wheel is passed by the effective width of the dresser.  $U_d$  is calculated by equation (46).

$$U_d = \frac{b_d}{f_d} \quad (46)$$

$U_d$  is the overlap ratio,  $b_d$  is the effective contact width of the dresser on the grinding wheel. The effective contact width of the dresser is calculated by equation (47)

$$b_d = 2\sqrt{(r^2 - (r - a_d)^2)} \quad (47)$$

$b_d$  is the effective contact width of the dresser on the grinding wheel,  $r$  is the tip radius of the dresser and  $a_d$  is the depth of dress.

### 4.3.3 Fixed dressing

Fixed dressers typically used are single and multiset diamonds. Single point dressers are usually made of one diamond held a metal matrix and steel shank holder with approximately one third of the diamond protruding out of the matrix. Accurate radii can be produced on the diamond so that they can be used for dressing forms on to wheels. They are mainly used on conventional abrasives.

### 4.3.4 Continuous dressing

Continuous dressing is the process of dressing the wheel while grinding. Dressing during grinding can help the wheel to remain sharp throughout a grinding operation. This can allow more consistent quality to be achieved throughout the grinding pass and can help maintain the form accuracy. As the wheel condition is maintained during grinding, the process can be run at optimum conditions throughout the grinding pass, rather than reduced conditions selected in anticipation of the wheel condition changing during the grinding pass. It has the added advantage that it can help the overall process efficiency as the non-productive

dressing is done simultaneously during the grinding pass and therefore reduces the cycle time of the process.

#### **4.4 Tool materials**

The dressing tool surface that is in contact with the grinding wheel contains a hard material. Natural Diamond (ND) and Synthetic Diamonds (SD) are used to form the dressing tool edges. The natural diamonds are classed as not suitable for use in jewellery as they are not a perfect purity, form or colour. Several different synthetic diamond types are used for constructing dressers, the type used can depend upon the dresser type and application. Typical synthetic diamond types are Chemical Vapour Deposition (CVD) logs, Polycrystalline Diamond (PCD), Monocrystalline Diamond (MCD) and synthetic (SD) grits. Synthetic diamonds can offer some advantages over natural diamond (ND) such as MCD logs that have uniform section, hardness and structure throughout the crystal, which help to give more predictable performance.

## **5 Preliminary grinding trials**

### **5.1 Introduction**

Due to machine system deflections and temperature effects the amount of material removed during grinding can be different to the set depth of cut (DoC). The DoC achieved is usually less than the set DoC. It is important to know the true DoC for the calculation of process performance characteristics such as contact temperature and process efficiency.

### **5.2 Aim**

1. To investigate the relationship between applied and true DoC.

### **5.3 Objectives**

1. To modify system compliance by varying applied DoC and machining parameters. Two workpieces will be ground without grinding fluid to the same height. A DoC applied, and one pass of the workpiece made. The difference in height between the two workpieces will then be measured using a dial test indicator (DTI), magnetic base and ground parallels. Repeated for two further larger depths of cut.
2. To explore the effect on DoC of other factors such as coolant. Apply coolant to the grinding wheel and repeat the grinding passes at the same applied depths of cut and measure the results in the same way.

### **5.4 Theory**

The main elements of a grinding machine system are, the workpiece, the abrasive tool, the kinematics of the abrasive, the machine, the environment and the grinding fluid.

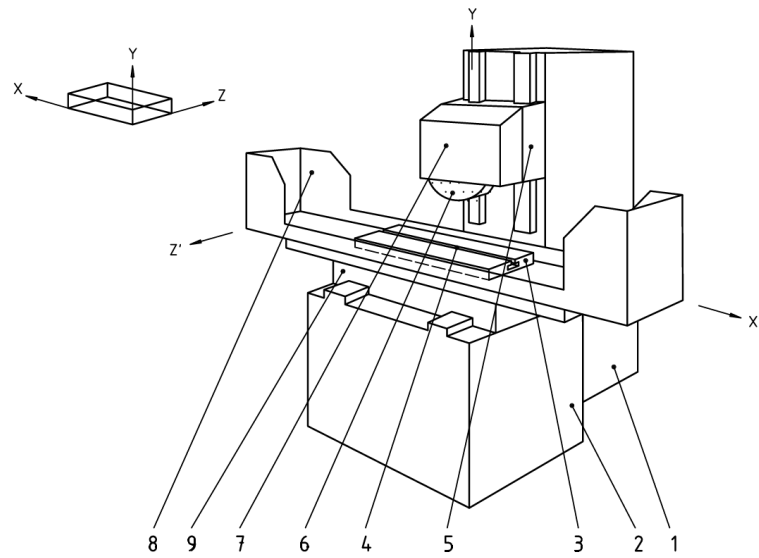
The applied DoC can be affected by the stiffness of: the workpiece geometry / material, the workpiece fixture, the abrasive tool and the machine tool. The machine tool is required to give good static and dynamic constraint to the abrasive tool and workpiece by resisting the forces from the process. The machine should also allow accurate setting of the applied DoC and have thermal stability as well as resisting vibrations.

The design of the machine tool structure can influence the stiffness and constraint provided to the abrasive tool and workpiece. A surface grinder with a cantilever design was used for these experiments. An example of the cantilever design type surface grinding machine design used in this experiment is shown in Figure 5-1. This type of machine design has

several drawbacks. The force between the workpiece and the grinding wheel pushes the grinding wheel up which transmits the force on to the wheelhead.

The wheelhead weight can affect the column deflections if the design does not have a counterbalance weight to act against the weight of the wheelhead hanging off the front of the column. The column deflection can increase as the wheelhead moves up the infeed axis (y axis) away from the support at the base of the column. The grinding forces act against the weight of the wheelhead and change the deflections in the column.

If the grinding forces are sufficient to overcome the weight of the wheelhead the wheelhead can be moved through any backlash within the system which would allow further separation of the wheel from the workpiece. If the force is great enough to move the wheelhead through any backlash in the infeed axis the forces will be transferred to the column causing it bend away from the grinding contact zone thereby reducing the contact between the grinding wheel and the workpiece. The amount of column deflection for a given grinding force depends upon the position of the wheelhead along the infeed axis. The higher the workpiece surface being ground and the larger the wheel diameter the further the wheelhead will be from the column base and the greater the deflections due to the force acting at a greater distance from the base of the column. Machine deflections and backlash can be controlled better with a closed loop control system with a scale arrangement. However, such control systems are only able to use the information provided by the machine scale to make corrections for deflections, and as it is not possible to place the scale exactly where the grinding action takes place. Deflections and Abbé errors can still exist due to the system stiffness between the scale and the point of grinding action.



	English
1	Column
2	Bed
3	Table
4	Reference T-slot
5	Wheelhead
6	Grinding wheel
7	Wheel guard
8	Splash guard
9	Saddle

Figure 5-1 Schematic of surface grinding machine with horizontal wheel spindle and reciprocating table, adapted from BSO (2014).

A diagram of the elements that make up the stiffness of the machine is shown in Figure 5-2. The ground in the diagram represents the machine bed and is assumed to have no significant stiffness that needs to be considered.

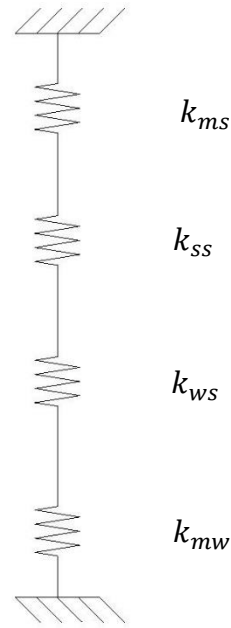


Figure 5-2 Diagram of grinding system stiffness.

The machine stiffness can be determined from

$$\frac{1}{k_m} = \frac{1}{k_{ms}} + \frac{1}{k_{mw}} \quad (48)$$

Where  $k_{ms}$  is the machine stiffness of the wheelhead and column supporting the centre of the grinding wheel,  $k_{mw}$  is the machine stiffness of the table and fixture supporting the workpiece.

The stiffness of the grinding wheel and workpiece contact  $k_a$  can be determined from

$$\frac{1}{k_a} = \frac{1}{k_{ws}} + \frac{1}{k_{ss}} \quad (49)$$

Where  $k_{ss}$  is the stiffness of the grinding wheel structure from the grinding contact point to the centre of the grinding wheel, and  $k_{ws}$  is the stiffness of the workpiece.

The overall stiffness  $k_e$  is determined from

$$\frac{1}{k_e} = \frac{1}{k_m} + \frac{1}{k_a} \quad (50)$$

### 5.4.1 Grinding Fluids

Grinding fluids have two main roles of providing cooling and lubrication. For the type of grinding used for these experiments the main benefit to the process is likely to be lubrication. Cooling is also important as heat can enter the workpiece and grinding wheel causing them to grow and increase the DoC. The lubrication provided by the grinding fluid reduces friction and grit dulling which reduces grinding forces and temperatures.

## 5.5 Apparatus

The apparatus used for the experiments was:

Machine:

Abwood 5025 surface grinding machine shown in Figure 5-3 the specification of the machine is given in Table 5-1.

Table 5-1 Abwood 5025 surface grinder specification

<b>Parameter</b>	<b>Value</b>
Spindle motor power	2.2 kW continuous power 8 kW instantaneous power
Spindle speed	Variable up to 6000 rpm
Longitudinal travel via worktable	530 mm
Cross traverse of head via headstock	260 mm – Handwheel dial resolution 20 $\mu$ m
Vertical traverse of head via head stock	350 mm – Handwheel dial resolution 2 $\mu$ m
Maximum wheel size	254 mm x 25 mm
Other information	Cantilever wheelhead, mechanical magnetic chuck



Figure 5-3 Abwood 5025 surface grinder.

Grinding fluid:

Water based grinding fluid using Castrol Hysol XF semi-synthetic soluble oil at a concentration of 5% by volume. Flood application flowrate and pressure not measured.

Grinding wheel:

Make and type: Tyrolit Viper Ultra VU33A602HH10VB1

Diameter: 215mm (approximate)

Width: 20mm

Maximum speed: 63m/s 5460RPM

Direction: Up-grinding

Workpiece:

Material: EN9

Length: 60mm

Width: 16mm

Distance between workpieces: 36mm

Height of workpiece from magnetic table surface: Approximately 50mm

Measurement:

Magnetic base with a DTI mounted on a ground parallel shown in Figure 5-4. DTI type Verdict finger clock 0.001”



Figure 5-4 Magnetic base and finger dial test indicator mounted on a ground parallel.

Dresser:

Single point diamond in holder attached to magnetic base when dressing is required shown in Figure 5-5.



Figure 5-5 Single point dresser in holder.

## 5.6 Method

1. The grinding machine was setup with the workpieces and the wheel dressed.
2. The grinding wheel was set at 500RPM and run for 30 minutes to allow temperatures to stabilise before any grinding passes were taken.
3. The grinding spindle speed was set to 1400RPM which produced a surface speed of 15.7m/s at the surface of the grinding wheel.
4. A permanent marker pen was used to draw a wave on the surface of the workpieces. The waves covered the full width and length of the top surface on both workpieces. The grinding wheel was brought into contact with the workpiece and a depth of cut was applied.
5. The workpiece was passed under the wheel without coolant using the manual traverse handwheel, repeat passes in both directions were done until little or no sparks were seen this took approximately 10 passes.
6. The wheel was then moved to the other workpiece and passed under the grinding wheel followed by repeat passes until little or no sparks were seen this took approximately 10 passes.
7. The surface of the workpieces was visually inspected to see if all the marker pen had been removed.
8. Steps 4-7 were repeated for more depths of cut until all the workpiece surface had been ground and spark-out passes performed.
9. The grinding wheel was aligned with the workpiece nearest the front of the machine.
10. A 10 $\mu$ m DoC was applied.
11. The workpiece was passed under the grinding wheel using the powered traverse feed of 7m/min.
12. The table was moved clear of the grinding wheel and the surfaces of the workpieces and the parallels were wiped clean.
13. The DTI and parallel were placed on the two parallels on the magnetic work table. The DTI finger was first placed on the workpiece that had not been ground during the last pass to take a reading. The DTI was then slid along the parallels to move the finger to the workpiece surface that had just been ground and a second reading observed. Repeat observations were made between the two workpieces the difference between the two workpiece DTI readings was the recorded DoC result.

14. The grinding wheel was moved back to align the wheel with the back workpiece that was not ground during the last pass. The table was moved under the grinding wheel by hand.
15. The workpiece was passed under the wheel without coolant using the manual traverse handwheel, repeat passes in both directions were done until little or no sparks were seen.
16. The wheel was then moved to the other workpiece and passed under the grinding wheel followed by repeat passes until little or no sparks were seen.
17. Steps 10-16 were repeated but for a 20 $\mu$ m DoC.
18. Steps 10-13 were repeated but for a 30 $\mu$ m DoC.
19. Spark-out passes were performed by manually passing the workpiece under the wheel and the difference between the two workpieces was observed and the result recorded.
20. The grinding wheel was moved back to align the wheel with the back workpiece that was not ground during the last pass. The table was moved under the grinding wheel by hand.
21. The workpiece was passed under the wheel without coolant using the manual traverse handwheel, repeat passes in both directions were done until little or no sparks were seen.
22. The point dresser was attached the magnetic table by releasing the magnetic force and then reapplying the magnetic force once the table had been cleaned and the single pint diamond had been positioned.
23. Coolant was applied to the grinding wheel.
24. The single point diamond dresser was used to dress the wheel using four 5 $\mu$ m dressing passes then a 2 $\mu$ m dressing pass. Powered feed was used to move the diamond across the wheel for all passes
25. A permanent marker pen was used to draw a wave on the surface of the workpieces. The waves covered the full width and length of the top surface on both workpieces. The grinding wheel was brought into contact with the workpiece and a depth of cut was applied.
26. The workpiece was passed under the wheel with coolant using the manual traverse handwheel, repeat passes in both directions were done until little or no sparks were seen this took approximately 10 passes.

27. The wheel was then moved to the other workpiece and passed under the grinding wheel followed by repeat passes until little or no sparks were seen this took approximately 10 passes.
28. A 10 $\mu$ m DoC was applied.
29. The workpiece was passed under the grinding wheel using the powered traverse feed of 7m/min with coolant applied to the grinding wheel.
30. The table was moved clear of the grinding wheel and the surfaces of the workpieces and the parallels were wiped clean.
31. The DTI and parallel were placed on the two parallels on the magnetic work table. The DTI finger was first placed on the workpiece that had not been ground during the last pass to take a reading. The DTI was then slid along the parallels to move the finger to the workpiece surface that had just been ground and a second reading observed. Repeat observations were made between the two workpieces the difference between the two workpiece DTI readings was the recorded DoC result.
32. The grinding wheel was move back to align the wheel with the back workpiece that was not ground during the last pass. The table was moved under the grinding wheel by hand.
33. The workpiece was passed under the wheel with coolant using the manual traverse handwheel, repeat passes in both directions were done until little or no sparks were seen.
34. The wheel was then moved to the other workpiece and passed under the grinding wheel followed by repeat passes were done until little or no sparks were seen.
35. Steps 28-34 were repeated but for a 20 $\mu$ m DoC.
36. Steps 28-31 were repeated but for a 30 $\mu$ m DoC.
37. Spark-out passes were performed by manually passing the workpiece under the wheel and the difference between the two workpieces was observed and the result recorded.

## 5.7 Results and calculations

Table 5-2 Depth of cut trial result no grinding fluid

<b>NO GRINDING FLUID</b>				
MEASUREMENT No	SET DoC (µm)	AVERAGE MEASURED AMOUNT OF MATERIAL REMOVED (µm)	CORRECTED AMOUNT OF MATERIAL REMOVED (µm)	% OF SET DoC FOR THE CORRECTED AMOUNT
1	10	5	3.60	36.0
2	20	12	8.63	43.2
3	30	15	10.79	36.0
4	30	21	15.11	50.4

Table 5-3 Depth of cut trial results with grinding fluid

<b>WITH GRINDING FLUID</b>				
MEASUREMENT No	SET DoC (µm)	MEASURED AMOUNT OF MATERIAL REMOVED (µm)	CORRECTED AMOUNT OF MATERIAL REMOVED (µm)	% OF SET DoC FOR THE CORRECTED AMOUNT
1	10	6	4.32	43.2
2	20	14	10.07	50.4
3	30	25	17.98	59.9
4	30	28	20.14	67.1

Measurement number 4 in both Table 5-2 and Table 5-3 are the measured amount of material removed after sparking out the 30µm set DoC.

The corrected DoC was calculated by multiplying the measured DoC by the cosine of the angle between the workpiece surface and the finger of the DTI. This is discussed in more detail in the discussion of results section.

Figure 5-6 and Figure 5-7 show the results graphed for the different applied DoC, without fluid and with fluid.

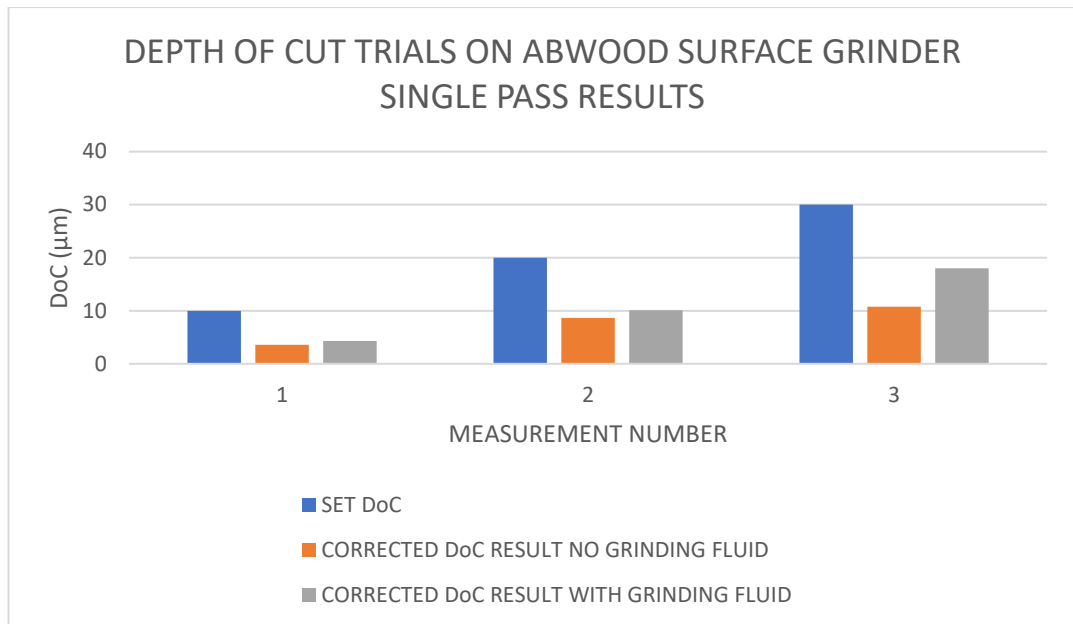


Figure 5-6 DoC trial results using the corrected measurement values.

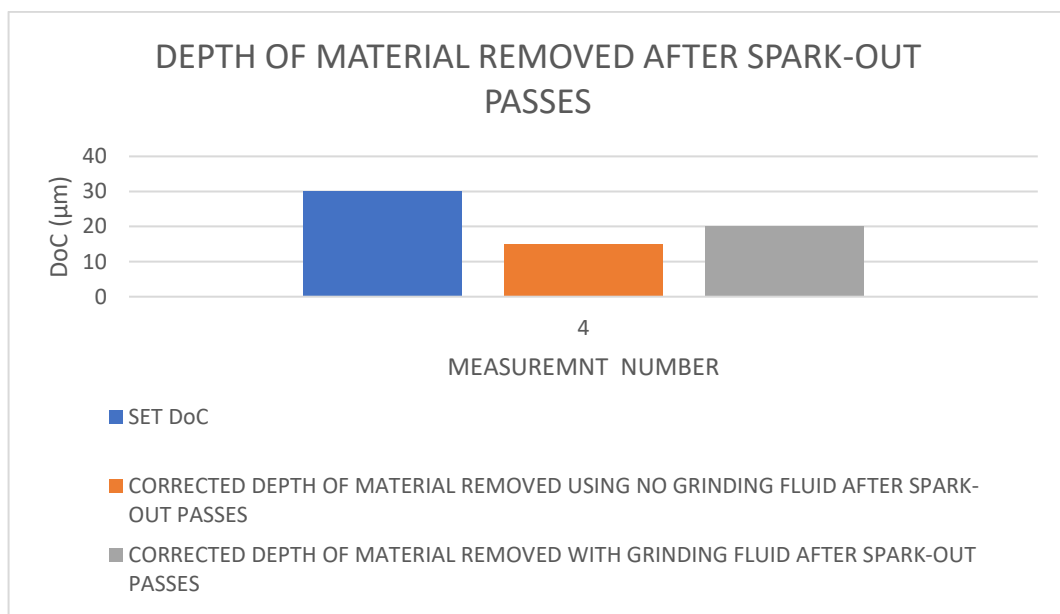


Figure 5-7 Depth of material removed for measurement number 4 after spark-out passes.

## 5.8 Discussion of results

Due to the angle that the clock was presented to the workpiece the measured depth of cut has an error. From Figure 5-8 it is estimated that the angle of the dial test indicator stylus to the workpiece surface is approximately  $44^\circ$ . It is generally regarded as bad practice to

use a dial test indicator in this way. The stylus should be as close as possible to parallel to the workpiece surface so as not to introduce a cosine error in the readings. A cosine error can increase the reading seen on the dial test indicator. However, the increased reading can be an advantage when using a DTI that has a resolution that makes it difficult to observe the deviations that need to be measured. If the angle is known a correction factor can be used to remove the error. To correct for the error the readings taken from the dial test indicator should be multiplied by a correction factor of  $\cos(44) = 0.72$ .

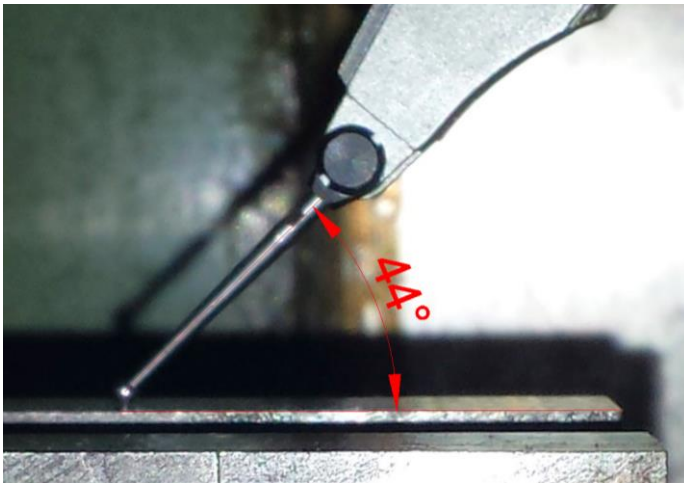


Figure 5-8 Finger dial test indicator angle to workpiece surface.

The aim was to demonstrate that the true DoC is less than the set DoC and that factors other than stiffness affect the true DoC, both these aims were achieved. All the grinding passes resulted in a true DoC less than the set DoC. For the passes performed without grinding fluid the true depths of cut achieved were 36%, 43% and 36% for the set depths of cut of 10 $\mu$ m, 20 $\mu$ m and 30 $\mu$ m respectively. The result for the 30 $\mu$ m DoC is lower than expected, which may be due to wheel dulling and the normal grinding forces increasing resulting in greater deflections, it is also possible that some wheel wear may have occurred. As no forces or power measurements were taken it is not possible to confirm these theories directly. After allowing several spark-out passes after the 30 $\mu$ m DoC pass the amount of material removed was 50% of the set depth of cut. The spark-out passes should have involved lower forces and therefore have smaller deflections allowing further material to be removed.

For the passes performed with grinding fluid the true depths of cut achieved were 43.2%, 50.4% and 59.9% for the set depths of cut of 10 $\mu$ m, 20 $\mu$ m and 30 $\mu$ m respectively. The addition of grinding fluid allowed a larger percentage of the set DoC to be achieved. The added lubrication provided by the fluid reduces the friction which in turn reduces the forces which should reduce the deflections of the machining setup. After allowing several spark-out passes the after the 30 $\mu$ m DoC pass the amount of material removed was 67.1% of the set depth of cut.

## **5.9 Conclusions**

The grinding system behaviour clearly shows the necessity to measure the true DoC as the set DoC cannot be used for calculations due to the difference between them varying so much and behaviour depending on several factors that can affect the result. Further tests should include more cuts at the same settings to confirm any variation that may be present in the achieved DoC and to confirm if wheel dulling is occurring. The measurement equipment should have a better resolution that suits the response magnitude that is trying to be measured.

## 6 System and equipment design

The main elements of the system design were:

1. Abwood 5025 grinding machine
2. Kistler Force dynamometer
3. Workpiece holding fixture
4. Grinding fluid nozzle
5. LVDT metrology station
6. LVDT guides
7. DAQ system

Figure 6-1 show the Abwood surface grinder used to create the relative motions between the grinding wheel and workpiece. The Kistler force dynamometer is used to measure the grinding forces acting on the workpiece. The force dynamometer is attached to the Abwood grinder by a magnetic chuck. The workpiece holding fixture is attached to the Kistler force dynamometer using bolts, and securely holds the workpiece during the grinding pass. The grinding nozzle is positioned to apply grinding fluid to the nip created between the workpiece and the grinding wheel so that it can enter the grinding zone. The LVDT metrology station is attached to the Abwood column casting. The Metrology station is used to measure points on the workpiece surface and datum surface points. The LVDT guides are used to preload LVDT probes and provide a smooth transition of the LVDT probe onto the workpiece surface during a measurement. The LVDT guides can also be used as grinding fluid guides aiding grinding fluid application at the ends of the workpiece. The DAQ system is used to record measurements during a grinding pass. The measurements recorded by the DAQ system are 6 LVDT probe deflections, the Abwood X axis linear scale position, the grinding fluid pressure and the three orthogonal axis forces of the Kistler force dynamometer.

Figure 6-2 shows the grinding machine arrangement with the metrology station. A force dynamometer is used to measure the normal, tangential and axial grinding forces during a grinding pass. The metrology station allows the workpiece to be measured immediately after the surface has been cleaned up and sparked out and then after a grinding pass has

been taken to remove material from the workpiece. The two measurements can be then be compared to find the true depth of cut taken on the workpiece.



Figure 6-1 Abwood 5025 surface grinder.

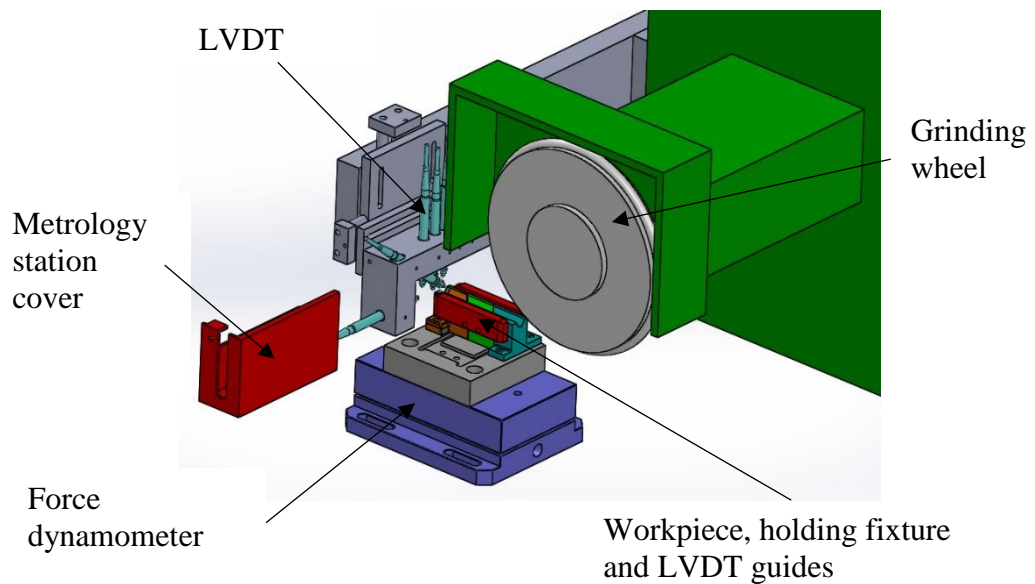


Figure 6-2 Grinding machine arrangement with metrology station.

## **6.1 Fixture design**

A work holding fixture assembly and a metrology station has been designed to suit the available grinding machine. The contact conditions in helical form grinding were analysed to establish a workpiece design that replicates some of the conditions of helical form grinding. The workpiece has been designed to incorporate a form that closely resembles the forms in helical screw compressor rotors using simplified geometry. The test workpiece also closely matches the varying entry and exit conditions found in helical form grinding of screw compressor rotors. The fixture design has included the ability to include coolant guides. Coolant guides effectively extend the workpiece and could possibly help balance the grinding forces or create more consistent coolant application during the entry and exit regions of the part. With the inclusion of the force dynamometer in the equipment arrangement it will be possible to measure and quantify any effects that they have. An engineering drawing of the fixture design is provided in Appendix P .

## **6.2 Nozzle design**

The selected grinding machine was fitted with a low-pressure flood lock line type coolant nozzle that would not allow the recommended coolant application methods found in literature (Baines-Jones, 2010, Jackson, 2008). The forms in helical grinding can be varied and benefit could be found in reducing the cost of the manufacture of complex nozzles that are needed to meet the recommended application methods and be efficient. 3D printing is an emerging technology that could aid the manufacture of the complex shapes needed for the internals of a grinding fluid nozzle. A nozzle was designed, and 3D printed using an FDM printing process. Some post printing work was required for the nozzle. The threads needed some filing to remove some excess plastic. The exit face for the nozzle holes was milled flat and the holes drilled square to the face making sure the hole edges remained sharp. The 3D printed nozzle was tested, the design and results are presented in a later section. Following the tests a future design was created that integrated an adjustable air scraper in the design (Figure 6-3 and Figure 6-4). The aim of the air scraper was to reduce the effects of the air boundary layer on the grinding fluid application, reduce the need for high pressures and therefore achieve more laminar flow between the nozzle outlet and the grinding nip. Appendix R shows a drawing of the coolant nozzle with overall dimensions.

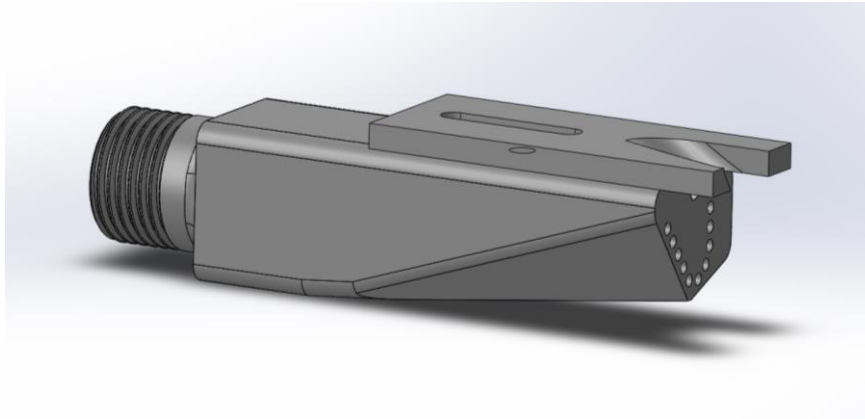


Figure 6-3 Coolant nozzle with integrated adjustable air scraper.

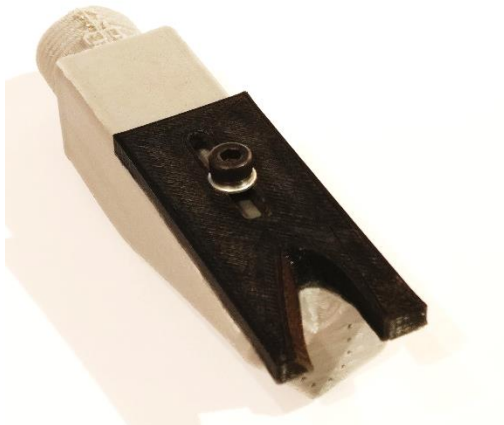


Figure 6-4 3D printed version of the grinding fluid nozzle with adjustable air scraper.

### 6.3 Grinding wheel form capture

It has been necessary to design a method of capturing grinding wheel form so that the ratio of workpiece volume removed to the wheel volume removed (known as G-ratio) can be calculated. The methods used by other researchers have involved using a razor blade and measuring the step created on a surface roughness machine. The university does not have a means of measuring the depth of form being investigated in this research, so it was necessary to design a method that could be measured by the research sponsor Holroyd using a CMM. A CMM could have difficulty measuring a razor blade due to its small thickness. A 3mm thick graphite sheet was selected to use for the method due to it being easy to machine and therefore little impact on the result and the thickness should be easy to measure on a CMM. The graphite sheet has two edges that can be used, one edge will be used to capture the wheel form before any grinding of the workpiece the other edge will be used to

capture the grinding wheel form after the workpiece has been ground. The grinding wheel is required to be plunged in to the graphite sheet ensuring that the two unused cylindrical surfaces of the grinding wheel form are captured so that they can be used as reference surfaces for the CMM to create a coordinate system from. Figure 6-5 shows the graphite sheet holder holding a black 3D printed representation of the grinding wheel form. Appendix S shows an engineering drawing of the graphite sheet holder and Appendix T a drawing of the graphite sheet holder clamp plate.

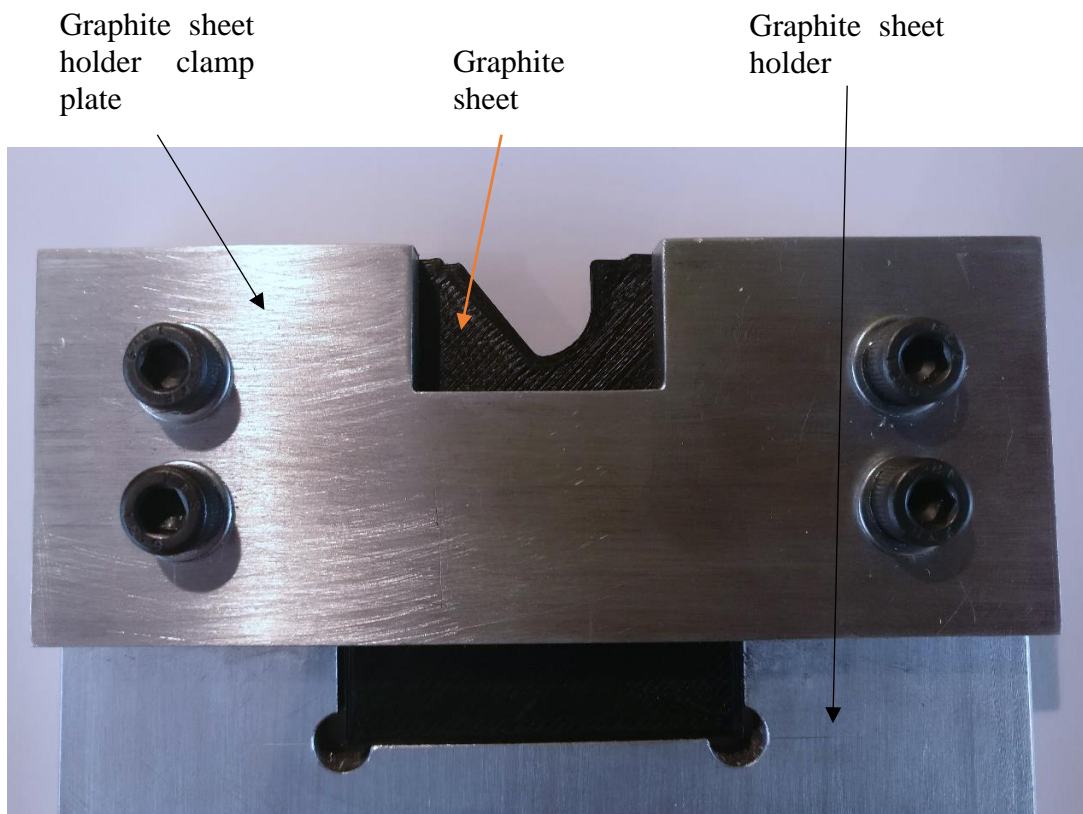


Figure 6-5 Holder for graphite sheet used to capture grinding wheel form. Shown with 3D printed example of what the grinding wheel form would look like.

#### 6.4 Workpiece design

The workpiece has been designed to have a similar form to those found in helical screw compressor rotors. Figure 6-7 shows a comparison between the form in the designed workpiece and a typical male and female form found in helical screw compressor rotors. It was not possible to design one form that closely matches both the male and female

compressor forms. Therefore, a compromise was made by including some features of both forms using simple geometry to create an asymmetric form. The male compressor form is drawn in a green line, the female form is shown in a red line and the compromise workpiece form in black. Manufactures of helical screw compressor rotors refer to one side of the form as the round side and the other the flat side. The workpiece form is constructed using a straight line to represent the flat side of the compressor forms and closely matches the angle of the male flat side. A radius was used to represent the round side of the compressor form and closely matches the round side of the female round side. Where the straight line and the radius on the workpiece form meet a small radius has been used to replicate the radius found on the male profile. This radius on the male profile is a common area that screw compressor manufacturers observe wheel wear and is therefore an area of interest and needed to be included in the design.

The ends of the workpiece were designed with angled ends which gives the workpiece an overall a parallelogram shape. The angle of the end faces was chosen to be  $45^\circ$  as this is a typical helix angle found in screw compressor rotors and represents the angle that the helical form breaks through in to the end face of the rotor body. Figure 6-6 shows a large pair of screw compressor rotors, the helical forms of each flute break through to the end faces at a similar angle. If one of the helical flutes were to be unwrapped in to a straight line it would produce a parallelogram shape. However, the distance between the angled faces would be much longer than the designed workpiece. The workpiece length was designed to ensure that the grinding wheel would have full engagement with the workpiece to allow grinding forces to reach equilibrium and give an engagement time long enough to capture the grinding forces. Having a longer workpiece would increase the grinding time and amount of data that needed to be recorded and processed, Figure 6-8 shows a drawing of the designed workpiece. Figure 6-9 shows the workpiece mounted on the workpiece fixture and Kistler force dynamometer. The workpiece is bolted to the workpiece fixture using two M6 bolts inserted from the bottom of the workpiece fixture. Figure 6-10 show the workpiece with two LVDT datum guides that are attached to the workpiece using four M4 bolts. Figure 6-11 shows the same items as Figure 6-10 with the addition of LVDT and grinding fluid guides used to extend the workpiece helping to guide grinding fluid onto the workpiece and providing a smooth transition of the LVDT probes onto the workpiece during measurements. Figure 6-2 shows the relative position of the workpiece and holding

fixture relative to the grinding wheel. Appendix Q shows an engineering drawing of the workpiece design. The workpiece was made from unhardened C1141 material.

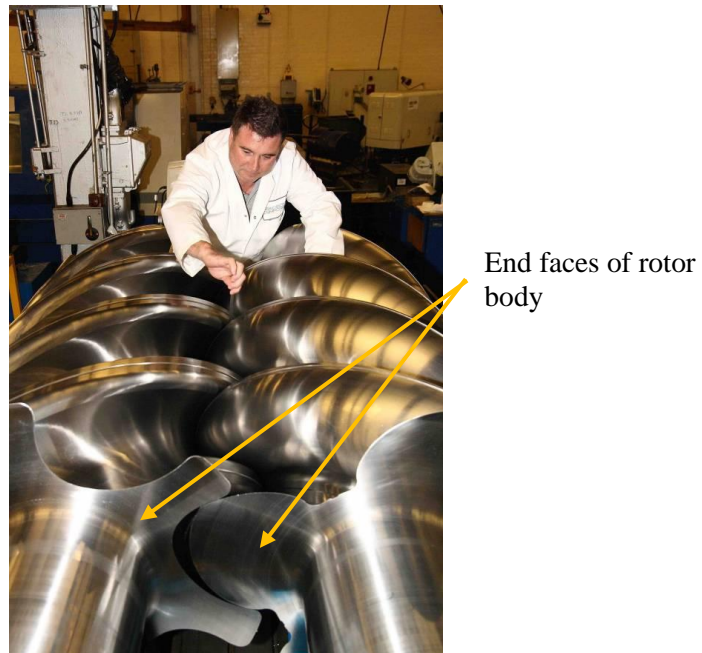


Figure 6-6 A large pair of screw compressor rotors.

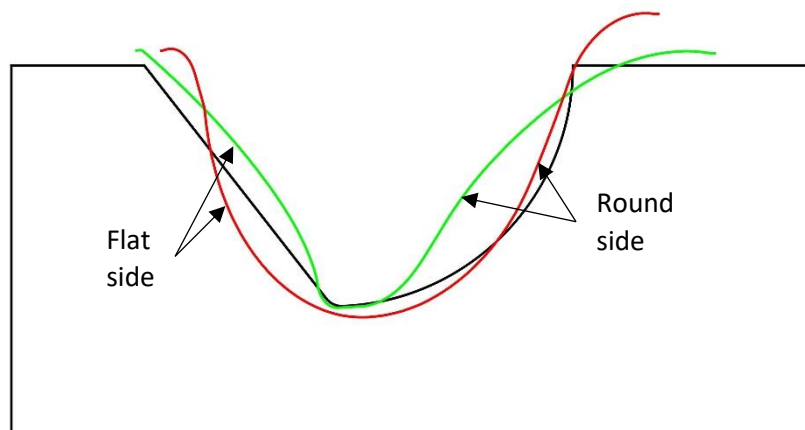


Figure 6-7 Comparison of form in workpiece with typical male and female profiles found in helical screw compressor rotors. Male form in green, female form in red and the workpiece form in black.

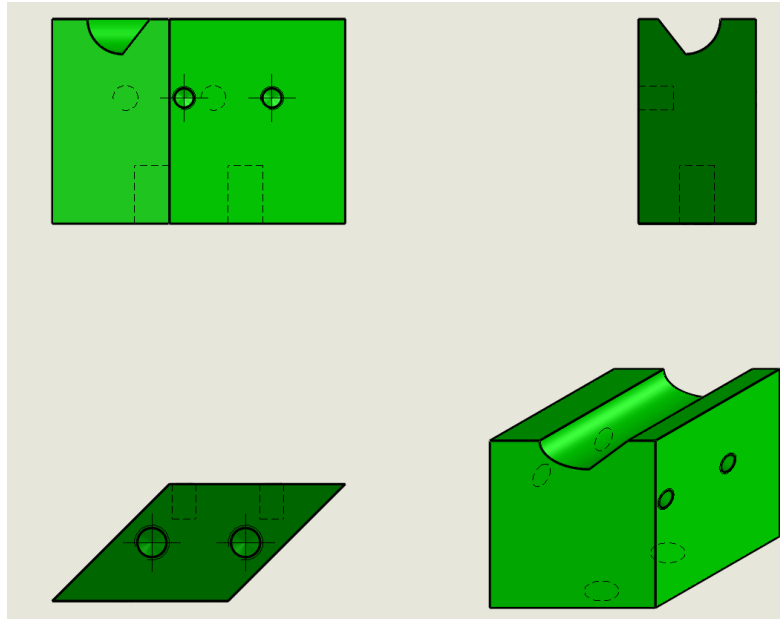


Figure 6-8 Parallelogram workpiece design with angled ends and asymmetric form.

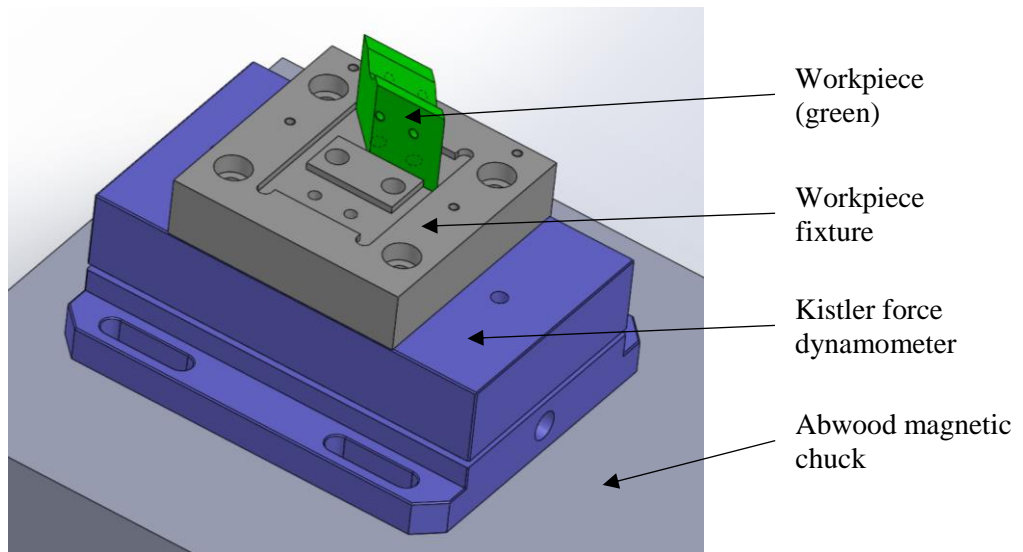


Figure 6-9 workpiece and workpiece fixture located on the Kistler force dynamometer.

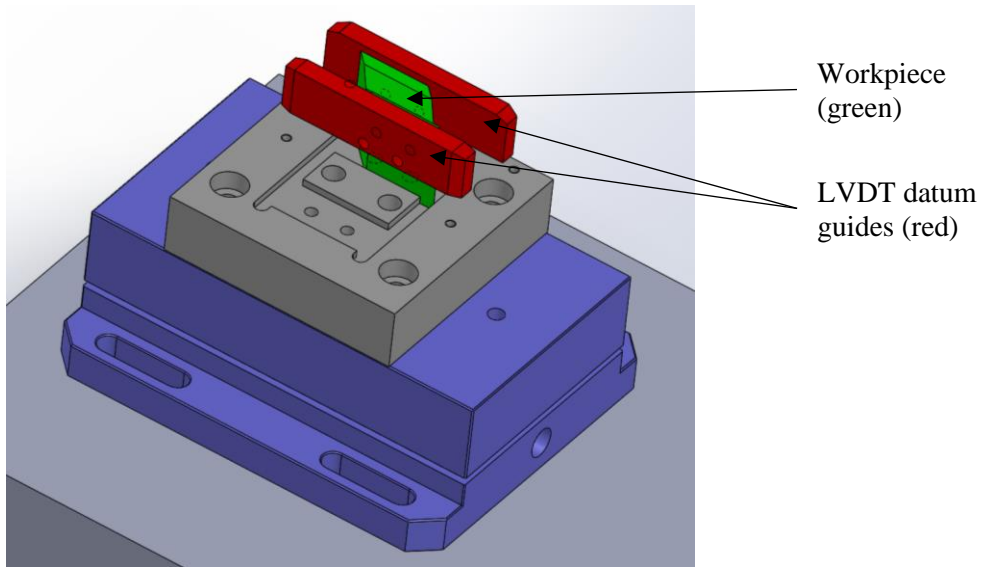


Figure 6-10 workpiece with LVDT datum guides.

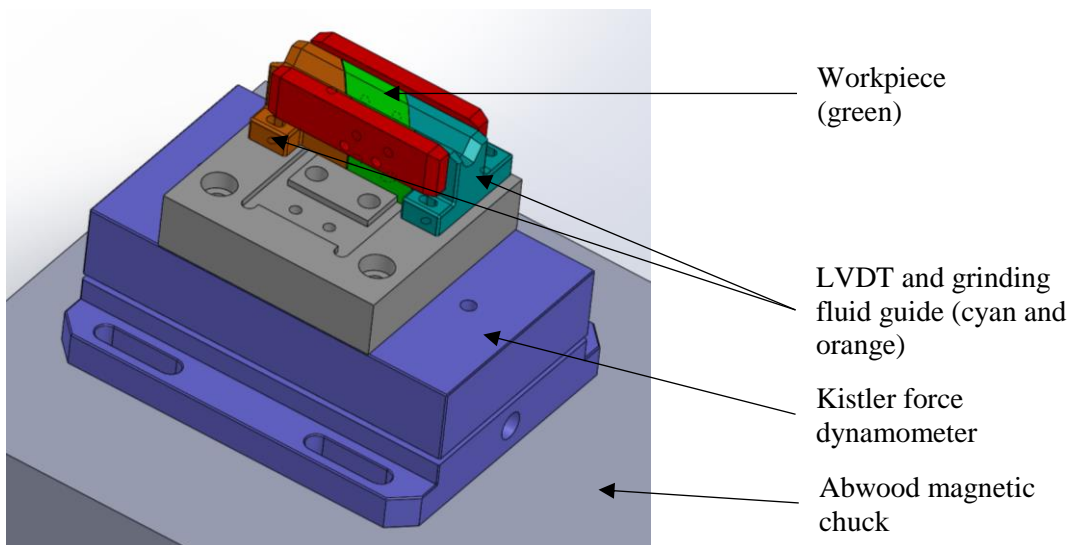


Figure 6-11 workpiece with LVDT datum guides and LVDT and grinding fluid guides. The LVDT and grinding fluid guides are shown in cyan and orange colours.

## 6.5 Abwood series 5020 surface grinding machine

Initial grinding trials were carried out on the Abwood series 5020 grinding machine due to its availability and capacity to take the existing tooling. The Abwood machine is capable

of conventional wheel speeds and has automatic traverse cycles. However, accurate control of the traverse speed was problematic due to the hydraulic control technology used. An AC servo motor allows variable spindle speed control up to 6000 rpm. Table 6-1 shows the Abwood 5020 grinding machine specification.

A Goodwin DRO (Digital readout) was added to the machine so that the traverse position and speed could be recorded. The quadrature signals from the traverse X axis were broken out and captured on a DAQ system.

Table 6-1 Abwood series 5020 surface grinding machine specification.

Parameter	Value
Spindle motor power	2.2 kW continuous power 8 kW instantaneous power
Spindle speed	Variable up to 6000 rpm
Longitudinal travel via worktable	530 mm - Scale Resolution 5 $\mu$ m
Cross traverse of head via headstock	260 mm – Scale resolution 5 $\mu$ m
Vertical traverse of head via head stock	350 mm - Scale resolution 5 $\mu$ m
Maximum wheel size	254 mm x 25 mm
Other information	Cantilever headstock, mechanical magnetic chuck

## 6.6 On machine DoC measurement

The DoC taken during a grinding pass needs to be known accurately so that the specific grinding energy can be calculated. LVDT probes are accurate and reasonably robust enough to deal with the grinding environment. LVDT sensors have three wire coils within a tube, a primary coil in the middle and two secondary coils, one each side. Alternating current drives the primary coil that causes a voltage to be induced in the secondary coils. A ferromagnetic core is mounted along the axis of the probe and is connected to or displaced by the object that is to be measured. As the ferromagnetic core moves through the coils the voltage in each of the secondary coils changes. When the ferromagnetic core is in the middle of the two secondary coils the voltage produced by each coil should be equal cancelling each other out. The ferromagnetic core moves away from the central position each coil produces a different voltage. It is the voltage difference between the two coils that

is used to measure the displacement of the ferromagnetic core. A picture of a TESA GT21 LVDT probe is shown in Figure 6-12.

LVDT probes were selected due to:

1. Good repeatability of  $0.01\mu\text{m}$ .
2. A measuring range of  $\pm 1\text{mm}$ .
3. A small diameter of 8mm allowed for a compact arrangement of the probes.
4. International protection marking of IP 65 and nitrile seals. The IP 65 rating should protect from dust and low-pressure jets. The nitrile seals are resistant to oils found in grinding fluids.
5. Good linearity of  $3.2\mu\text{m}$  over 1mm.



Figure 6-12 GT21 LVDT probe.

The LVDT probes were connected to a TESA R2M-1 rack that had two TESA M4P-2 modules installed (Figure 6-13). The TESA M4P-2 cards had the gains set to 5 resulting in an output range of  $\pm 6.25\text{V}$ .



Figure 6-13 TESA R2M-1 rack with two M4P-2 modules installed and power supply underneath.

A close-up view of the metrology station with LVDT probes in contact with the workpiece and the datum faces is shown in Figure 6-14.

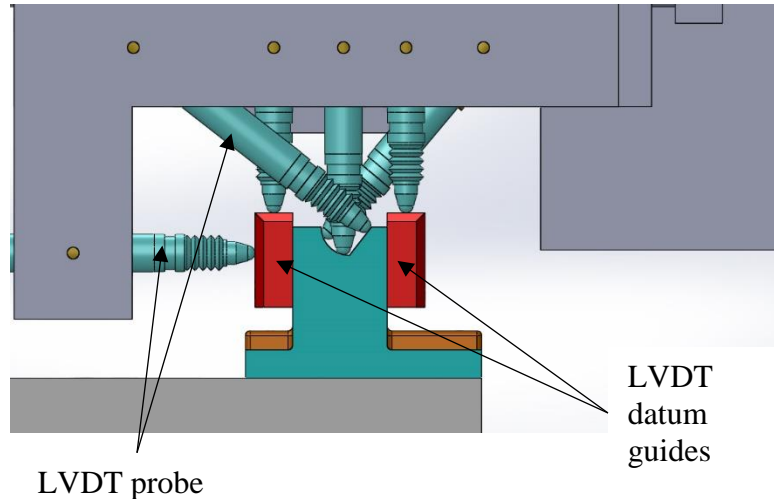


Figure 6-14 LVDT probe arrangement on workpiece.

## 6.7 Grinding fluid system

Figure 6-15 show the grinding fluid system used to supply for the Abwood Grinder. The system is a standalone unit that can be moved around to other machines. The system is equipped with a pump that is larger than the standard pump fitted to the Abwood grinder and capable of greater pressures than the standard Abwood system. The pump can deliver 55 PSI at a flowrate of 32 L/minute. The system is also fitted with an inline flow meter and a pressure gauge with analogue output. The holding tank holds around 200L of fluid and has two openings that allow easy access for cleaning when the fluids are to be changed. No internal baffles are present in the tanks so the filtering of the fluid returning to the tank is needed. Fluid entering the Abwood machine will drain in to the standard fluid delivery and filtering system on the Abwood. The standard fluid delivery system will be used to return the fluid back to the stand along system once the fluid has been filtered. The system is fitted with two valves that can be used to control how much of the flow is returned to the tank and how much goes to the nozzle. This also provides a means to control the pressure in the pipe that supplies the nozzle. If a certain pressure and flow is required, the nozzle exit area will need to be adjusted to give the required flowrate.

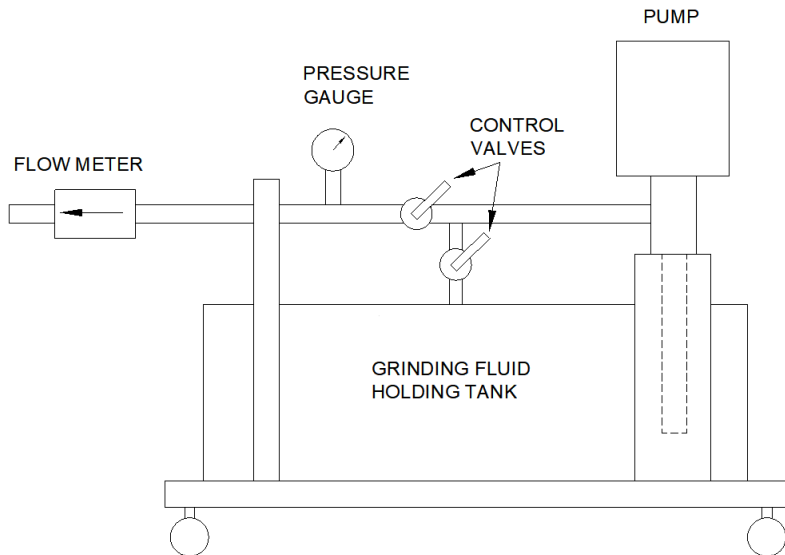


Figure 6-15 Grinding fluid delivery system.

### 6.7.1 Pressure gauge

The pressure gauge fitted to the grinding fluid supply system is an Omega PG-5000 1000PSI pressure gauge with 0-5V output. Figure 6-16 and Figure 6-17 show the pressure gauge fitted to the system.



Figure 6-16 Omega PG-5000 1000PSI pressure gauge with 0-5V output.



Figure 6-17 Model number spec and pinout details for pressure gauge.

### 6.7.2 Flow meter

The flow meter fitted to the system is an Omega FTG792-L that measures pulses from a rotating turbine. The turbine is calibrated for water. If an oil is used in the system, it would require recalibration due to the different fluid density. The specification of the flow meter is given in Table 6-2, and Figure 6-18 shows the front flow meter display. The LCD display on the meter allows the flow reading to be read when flow is running.



Figure 6-18 Omega Flow meter.

Table 6-2 FTB792 specification.

Linear Flow Range	7.6-75.7 Litres per minute
Maximum Flow	113.6 Litres per minute
Frequency Range in Linear Flow Range	37-370 Hz
Connections NPT Female Inlet/Outlet Size	3/4 in.
Wrench Size:	33mm
Weight Kilograms	1.1 kg

## **6.8 Form replication**

### **6.8.1 Introduction**

Workpiece form measurements will be required at points throughout the grinding trials to see if the form has changed due to wheel wear for example. Although on machine form measurement is possible for some machines, it usually requires CNC control systems to control the measurement process or special static measuring systems can be used however these can be expensive. Budget restricted the procurement of static form measuring devices with a high enough accuracy and the available machine does not have CNC control system. Therefore, an alternative approach was required. It would be possible to remove the workpiece from the grinding machine and measure externally on, for example, a CMM and then return the workpiece to the machine. The accuracy of returning the workpiece to the machine in the same place may cause additional setup time before grinding could resume and therefore extend the testing time.

The university facilities did not have suitable form measuring equipment to take the required measurements of the workpiece form. Holroyd have available a Leitz PMM (Precision Measuring Machine) a high accuracy CMM capable of measuring the workpiece forms. Holroyd is not located close to the university and a round drive trip would take approximately 2.5 hours not including any measurement time. Therefore, removing the workpiece from the grinding machine and taking it for measurement at Holroyd was not an economic method.

Therefore, in situ replication of the workpiece form on the grinding machine, and measurement of the replicate on an external measurement machine appeared to be the only practical solution available. In situ replication of the workpiece form on the grinding machine involves creating a cast of the workpiece. The replica casting can be measured on an external measuring device. The replica materials such as silicone polymers, resins and metals can be used. An advantage of using a replicate is that the replicate can also duplicate the surface finish of the workpiece, that can also be measured on an external measuring device. Replicate techniques have several disadvantages that also need to be considered. The curing or setting of the replicate material can generate heat as part of the chemical reaction. If molten metal is used it is usually heated to a temperature greater than the workpiece material. This heat can be transferred to the workpiece altering its size. Also, the replicate material can shrink once set. As the replication is performed in situ it may not be possible to perform any other tests while the replicate material is curing. Another consideration is that the replicate gives an indirect measurement of the workpiece and as such it can be expected to introduce some variance into the measurement process.

Taking a moulding or casting of the workpiece would allow the workpiece to remain in the machine preserving its location accuracy. Moulding or replication kits are relatively inexpensive when compared to some of the on-machine measurement equipment available. A mould can be taken of the workpiece and would take approximately 20 minutes to perform. Once the moulding has been removed the grinding trials can resume and the mouldings can be taken to Holroyd and measured once the grinding trials have finished.

It was necessary to find a moulding material that would not deform when subjected to the pressures of a CMM stylus as this could affect the accuracy of the measurement. H Roberts & Sons were contacted after finding Plastiform MD-3P RT001 product on their website ((H Roberts & Sons (DI) Limited, 2016)) that offered a hardness of 100 Shore A.

H Roberts & Sons offered to conduct some trials and send the samples back for consideration. Table 6-3 shows a summary of the different products tested. The following sections contain pictures of the samples received, any observations and tests conducted.

Name	Flexibility	Hardness	Moulds can be measured using	Feature replication	Claimed accuracy	Curing time	Working time	Removal constraint
Plastiform B.A.D CA-005 Fluid	Semi-flexible	50 Shore A	Optical methods & low pressure measuring instruments	Profile/form	Better than 1µm	8 mins	1 min	Can tolerate 10%
Plastiform D.A.V CA-001 Fluid	Very Flexible	20 Shore A	Optical methods only	Profile/form and surface roughness	Better than 1µm	8 mins	1 min	Can tolerate 30%
Plastiform LK-AD MT-003 Malleable Putty	Semi-flexible	70 Shore A	Optical methods only	Profile/form	1µm	4 mins	1 min	Can tolerate 5%
Plastiform MD-3P RT-001 Fluid	Rigid	100 Shore A	Optical methods & contact measuring instruments	Profile/form and surface roughness	Better than 1µm	10 mins	1 mins	Can tolerate 0%
Plastiform PE-AD CA-006 Fluid	Semi-flexible	65 Shore A	Optical methods & low pressure measuring instruments	Profile/form and surface roughness	Better than 1µm	6 mins	1 min	Can tolerate 5%
Plastiform PF-AD MT-005 Putty	Semi-Rigid	80 Shore A	Optical methods	Profile/form	10µm	45 mins	6 mins	Can tolerate 0%
Plastiform S.O.F.T CA-008 Pasty	Flexible	35 Shore A	Optical methods	Profile/form and surface roughness	Better than 1µm	8 mins	1 min	Can tolerate 20%
Plastiform R.G.X CA-009 Pasty	Semi-Rigid	80 Shore A	Optical methods	Profile/form and surface roughness	Better than 1µm	6 mins	1 mins	Can tolerate 0%

Table 6-3 Summary of Plastiform product characteristics.

### 6.8.2 Plastiform MD-3P RT-001

The cured impression is rigid with a hardness of 100 Shore A and would not deform with the pressures of a CMM stylus. The product is capable of capturing form and surface roughness. As the final cured impression is rigid it will not tolerate any removal constraint. Figure 6-19 shows a sample moulding using Plastiform MD-3P RT-001.

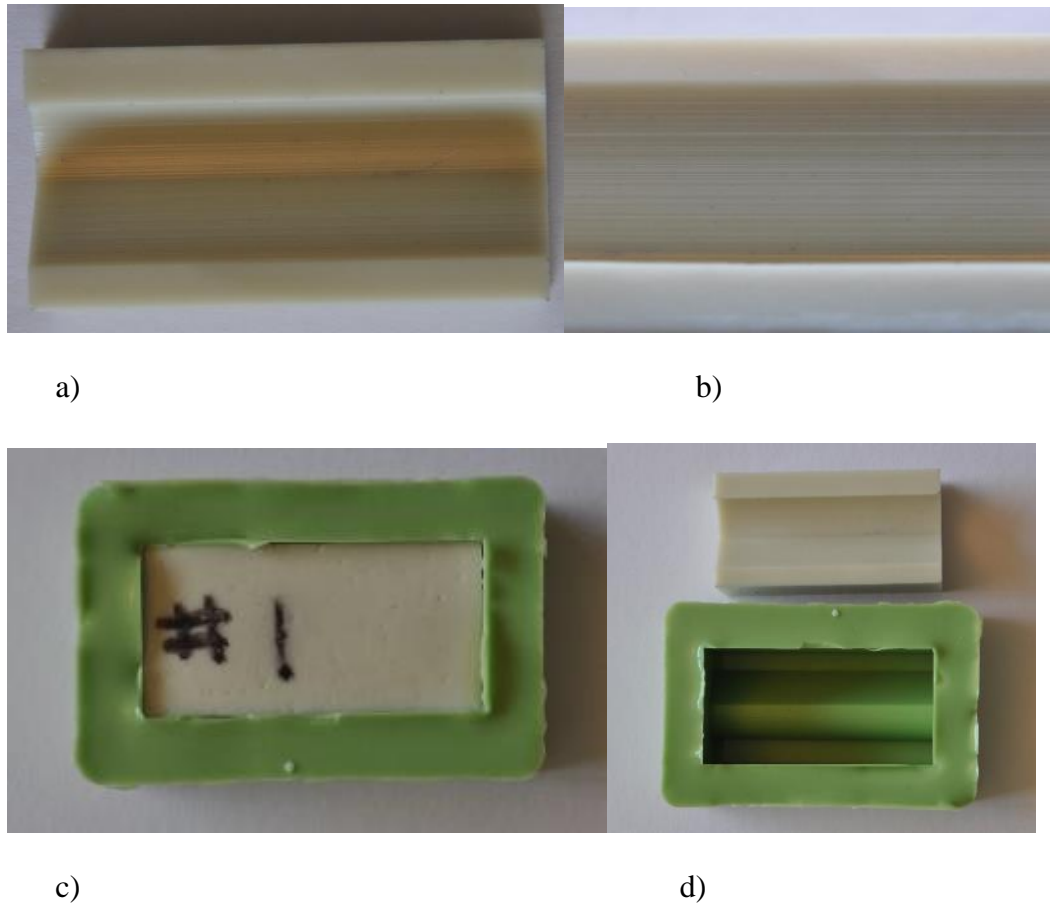


Figure 6-19 Sample moulding using Plastiform MD-3P RT-001. a) view of positive moulding of workpiece. b) view of the surface roughness replicated by moulding. c) Positive moulding inside the moulding using Plastiform D.A.V CA-001. d) The positive and negative moulds separated.

The MD-3P was also used directly on the workpiece. Due to concerns about the mould being hard to release from the workpiece a release agent was used (Plastiform reference: Turnout spray AC-020). Figure 6-20 shows the result of the moulding that used the AC-020. The moulding is unusable as the AC-020 mixed with the MD-3P and caused holes in

the surface of the mould. It is possible that too much AC-020 was used and that using less may give a better result.

Figure 6-21 shows the moulding done directly on the workpiece without using any AC-020. The moulding has no holes and the surface looks good apart from two visible defects. The moulding shows two small areas that look like part of the mould may have broken off when it was released from the workpiece. Figure 6-22 shows the damaged areas. There is still a significant area of the moulding that is unaffected and can be used for measurement.

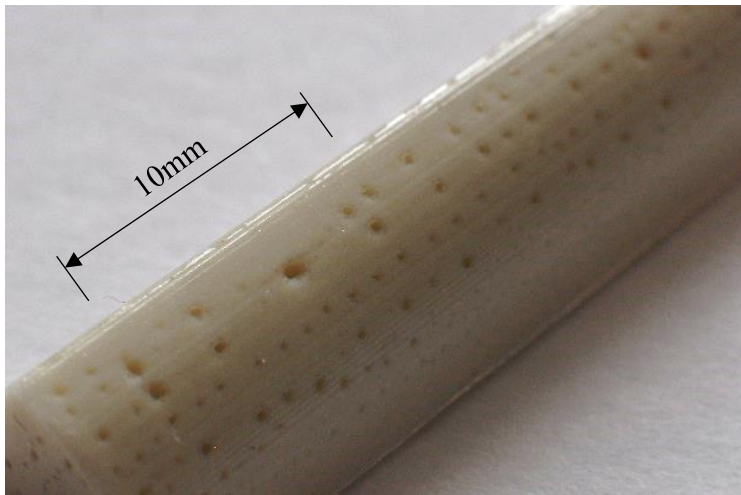


Figure 6-20 MD-3P mould used with AC-020.

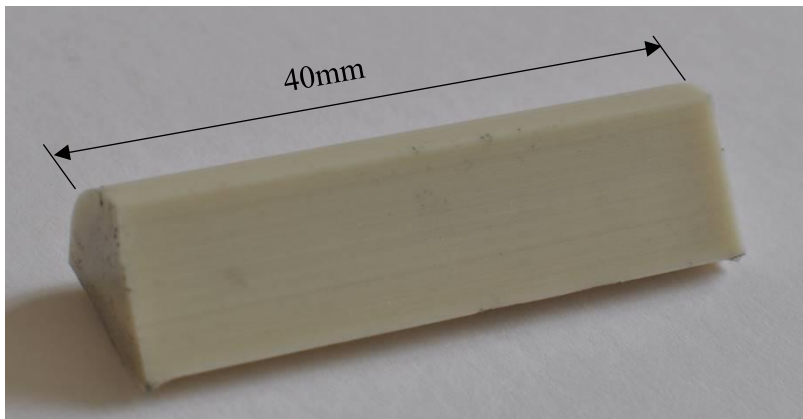


Figure 6-21 MD-3P moulding applied directly to workpiece without AC-020.



Figure 6-22 Damage seen to moulding at the radius between the flat and round sides of the profile.

Surface roughness measurements were taken of the flat side of workpiece from which the moulds were taken and the MD-3P moulds to compare the surface roughness captured by the mould of the workpiece. A Taylor Hobson Surtronic 3P was used to for the measurements, the arrangement used for the measurements is shown in Figure 6-24. Each item was measured 6 times at 3 places along its length (one at each end and one in the middle). The average of the 6 readings were calculated for each position. The results of the surface roughness measurements are shown in Table 6-4 and in Figure 6-23. Both mouldings differed from the workpiece slightly with the largest difference of  $-0.026 \text{ Ra } (\mu\text{m})$  for the MD-3P direct moulding. Looking at the average of all three positions for each item the MD-3P direct moulding is closest to the average of the workpiece. Compared to the workpiece average the average for the MD-3P direct mould is  $-0.07 \text{ Ra } (\mu\text{m})$ , this is 1.2% of the workpiece average reading. The mouldings appear to have captured the surface roughness well.

Table 6-4 Surface roughness measurement results for workpiece and MD-3P mouldings.

	Workpiece (Ra)	MD-3P mould created using D.A.V (Ra)	MD-3P direct moulding (Ra)
Position 1 (average of 6 measurements)	5.59	5.61	5.76
Position 2 (average of 6 measurements)	5.82	5.66	5.56
Position 3 (average of 6 measurements)	5.85	5.51	5.72
Average	5.75	5.59	5.68

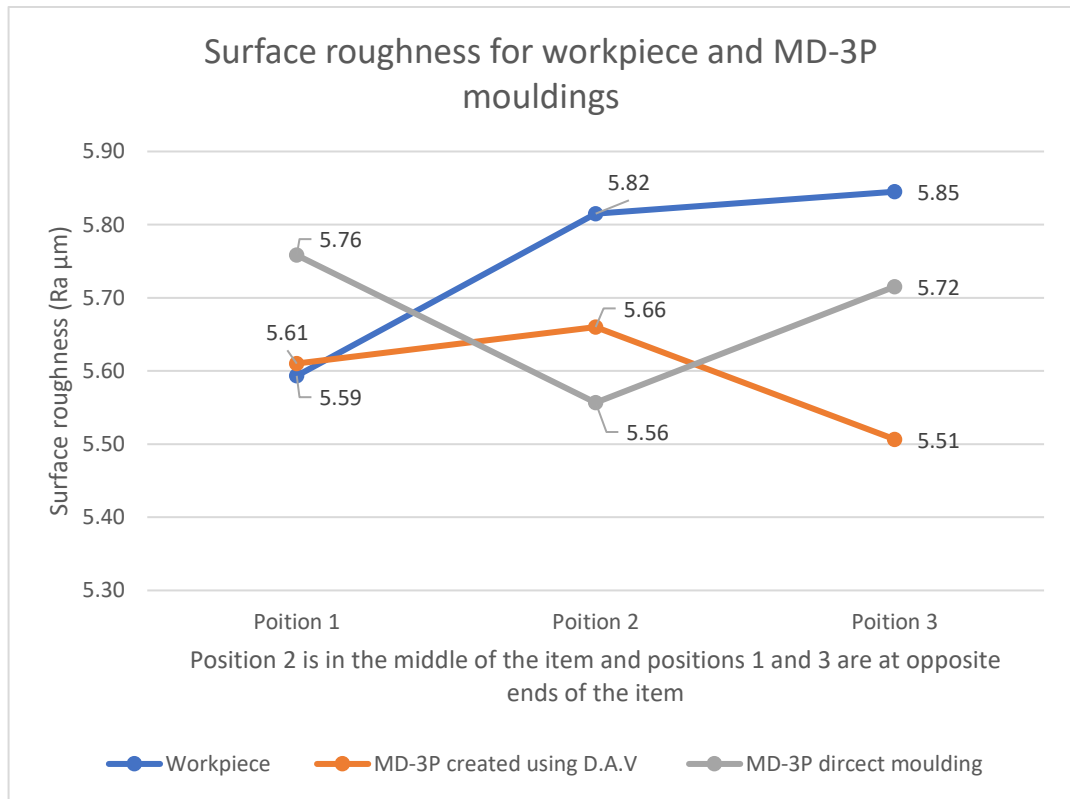


Figure 6-23 Graph of surface finish measurements on MD-3P mouldings.

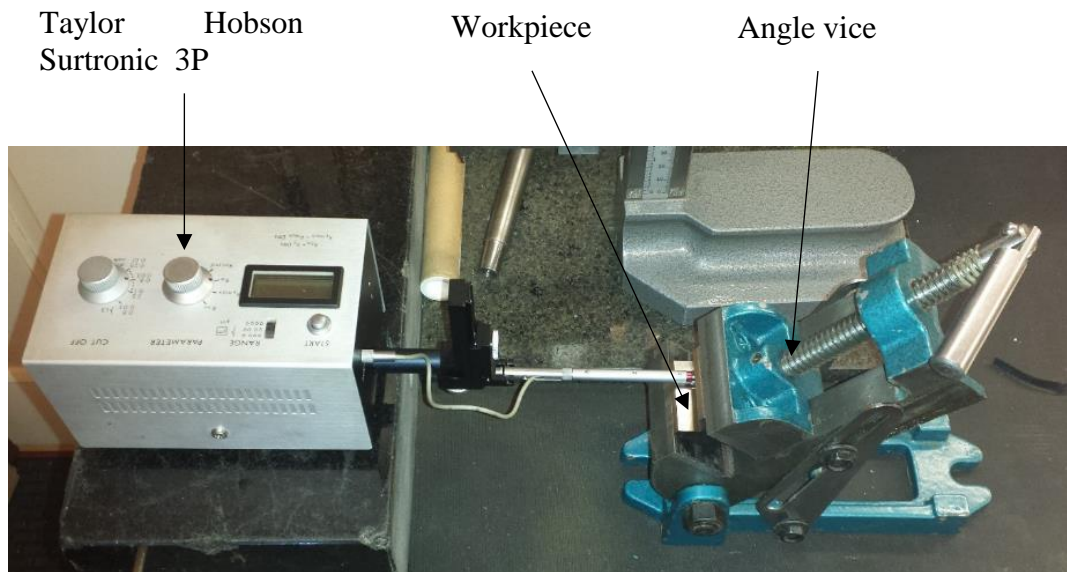


Figure 6-24 Arrangement used to measure surface roughness of the workpiece and moulds. The angle vice was adjusted so that the flat side surface of the form was parallel to the movement of the Surtronic stylus.

Appendix A contains the discussion of the other Plastiform products tested.

### 6.8.3 Best product for the application

Of the products tested only Plastiform MD-3P RT-001 would appear to meet the needs of the test requirements. It is accurate, hard enough to withstand the pressures of the CMM, and can capture the profile/form and the surface roughness. However, careful observation is needed to see if the moulding has any small damage after removal and to ensure that any form/profile measurement avoid these areas.

## 6.9 Data acquisition systems

A National Instrument NI6250 card was installed in a Windows 7 personal computer and a VI created in LabVIEW 2011 to capture 10 analogue inputs and a counter. 6 of the analogue inputs were used to capture the LVDT readings from the TESA R2M-1 rack that had two TESA M4P-2 modules installed. Another of the analogue inputs was used to capture the grinding fluid pressure gauge output. 3 more analogue inputs were used to capture the three orthogonal forces from a force dynamometer.

Figure 6-25 show the system diagram used for capturing the force readings from the dynamometer. The counter input was used to capture the traverse linear encoder position.

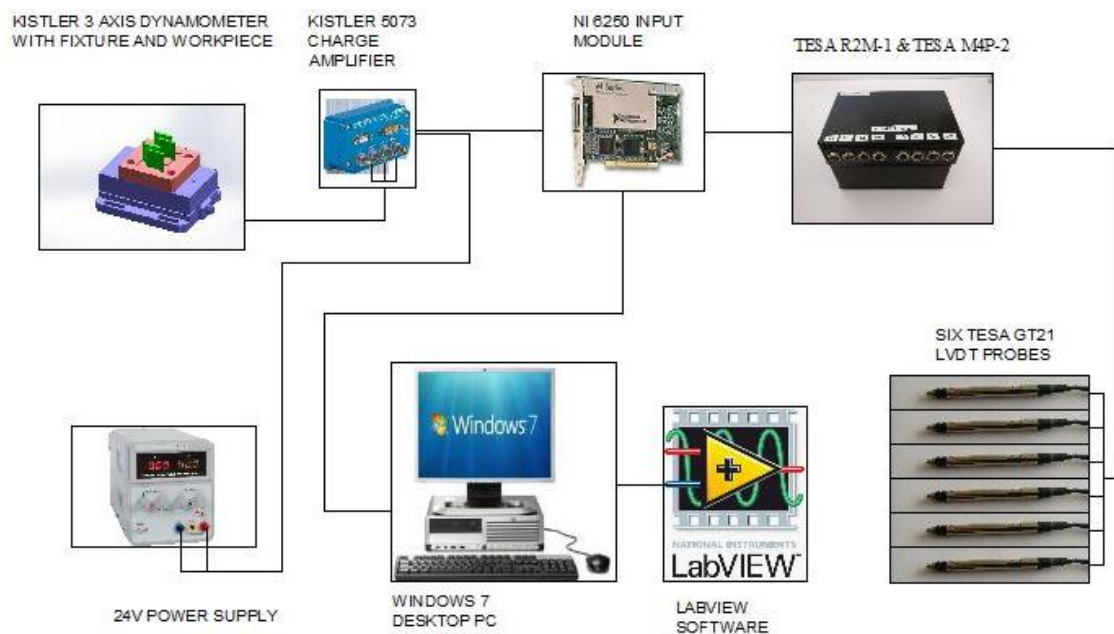


Figure 6-25 NI6250 data acquisition system diagram used to capture dynamometer readings.

## **6.10 Virtual instrument design**

A LabVIEW virtual instruments (VI) was created to capture the grinding forces from the force dynamometer during a grinding pass, pressure gauge output and to capture the machine encoder position and the LVDT readings when the metrology station is used. Figure 6-26 shows the LabVIEW VI design that was modified from an existing design available on the LabVIEW forum (Eric.S, 2017). Figure 6-27 shows the front panel for the design that the user will see when taking measurements.

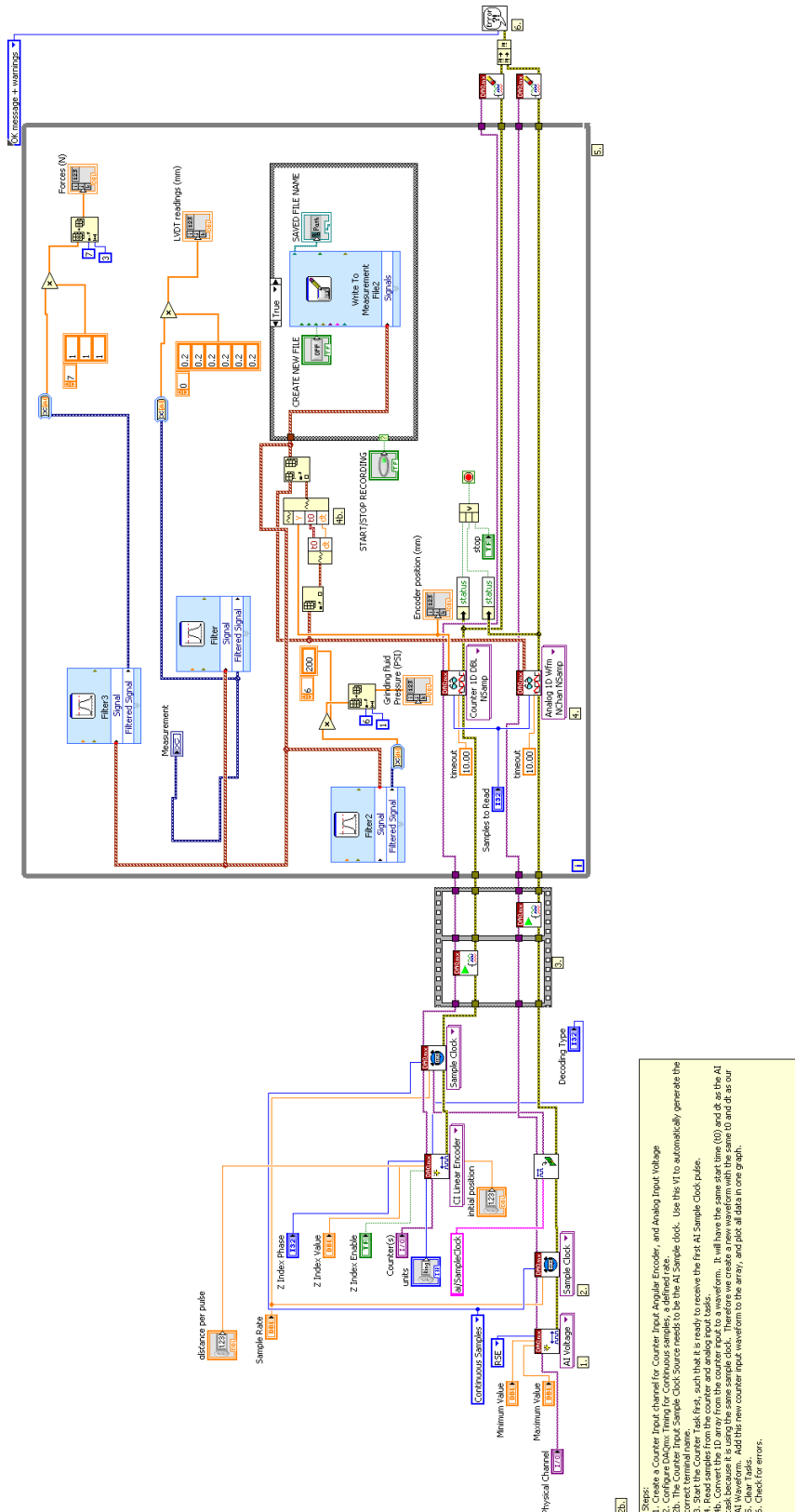


Figure 6-26 LabVIEW Virtual instrument for simultaneous encoder and 10 analogue input data capture.

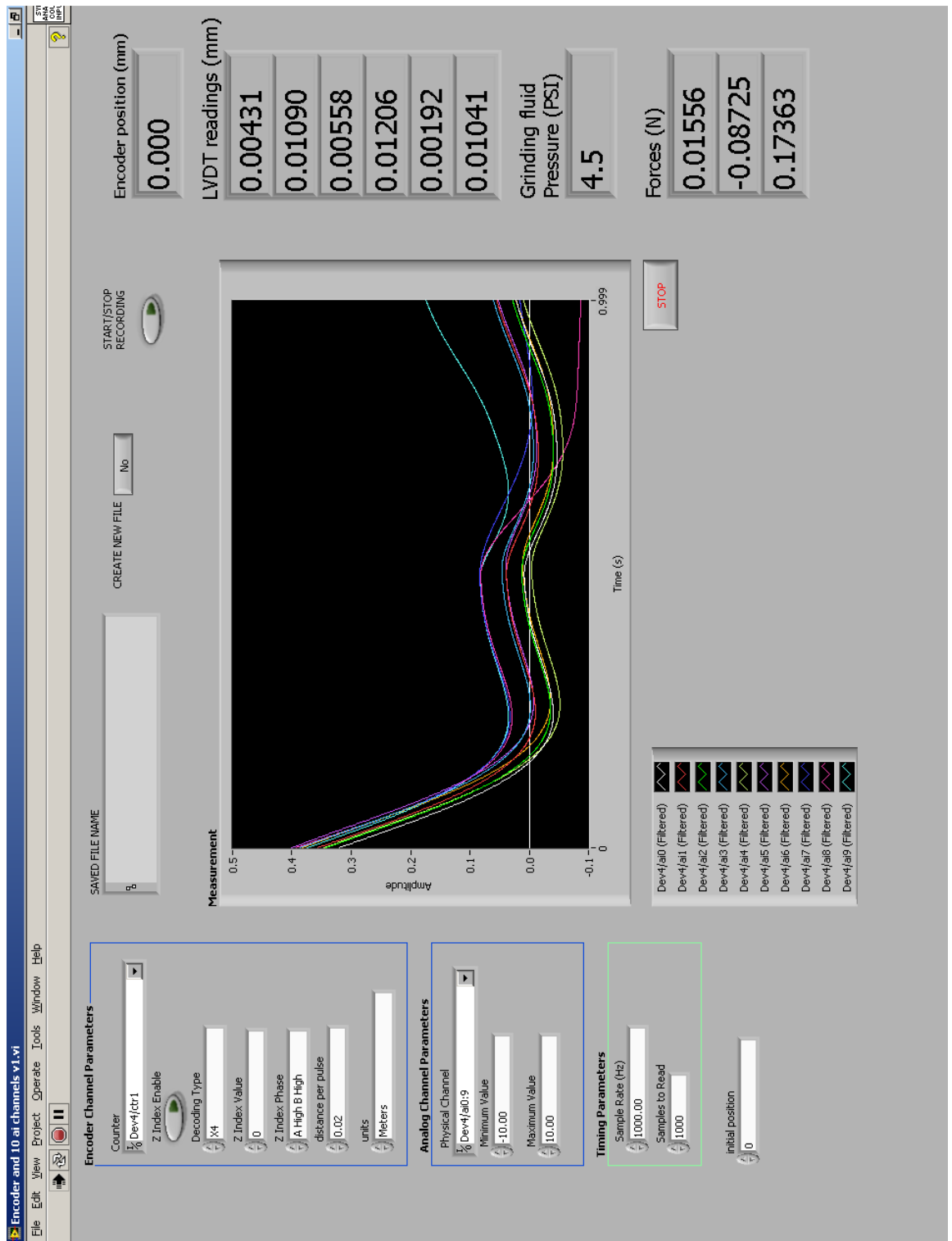


Figure 6-27 Front panel of LabVIEW Virtual instrument for simultaneous encoder and 10 analogue input data capture.

## **7 System calibration**

A number of the measurement systems used in the system required validation by calibration. The system elements that were calibrated were the force dynamometer, flowmeter, pressure gauge and LVDT gauges. The following section details the calibration methods and result for these elements of the system.

### **7.1 Tesatronic LVDT gauge equipment initial testing**

#### **7.1.1 Introduction**

The use of an LVDT was considered for the use of measuring DoC on the grinding machine with the aim of making the tests more efficient by not having to remove the workpiece from the machine to take workpiece measurements. Several LVDT probes would be needed for the metrology station on the machine. Before purchasing the gauges and the necessary data capture apparatus an assessment of the single LVDT gauge of the same type was assessed for its repeatability and accuracy to see if it was suitable for the application. The tests aimed to assess

1. If the gauge is repeatable.
2. If the gauge is accurate when compared to several reference value objects that covered the typical size range that the gauge was expected to work within.
3. If the gauge has the same accuracy across all the reference values.

Figure 7-1 shows the axis configuration of a surface grinder. These axis designations are used to refer to the axes tested.

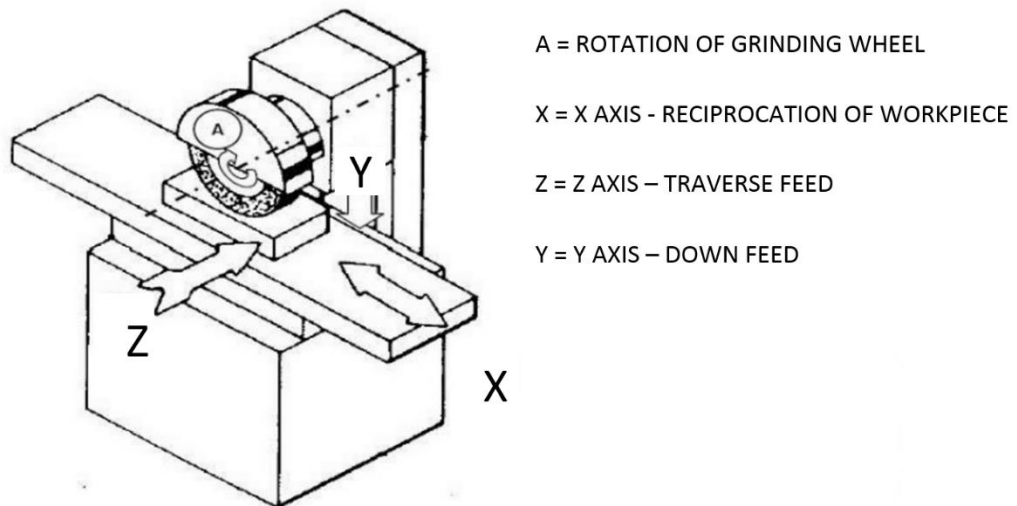


Figure 7-1 Axis configuration of surface grinder, adapted from Singh (2015).

### 7.1.2 Tests conducted on granite surface plate

1. Repeatability by moving the LVDT between two gauge blocks
2. Accuracy test using gauge blocks.

#### 7.1.2.1 Repeatability test

##### 7.1.2.1.1 Aim

To assess the variation in the gauge readings when a reference artefact is measured several times.

The apparatus, equipment setup, method, results and discussion of results in Appendix B.

##### 7.1.2.1.2 Conclusion

The results show that for this specific setup the gauge repeatability is well within the recommended limits. As the result is good the testing could proceed to include an accuracy test.

### **7.1.2.2 Accuracy test (linearity and bias) using gauge blocks**

#### **7.1.2.2.1 Aim**

To assess the accuracy of the LVDT gauge readings compared against reference artefacts, to see if the readings are bias in a particular direction and assess if the bias amount is varying over the range of readings.

The apparatus, equipment setup, method, results and discussion of results in Appendix C.

#### **7.1.2.2.2 Conclusion**

The measurements system for this setup has a small positive bias and the gauge does not have a linearity problem. The testing could progress to testing the gauge on the grinding machine to test if the grinding machine introduces any variance or introduces any accuracy errors.

## **7.2 Tesatronic LVDT tests conducted on Abwood 5025 surface grinder**

The LVDT tests conducted on the Abwood grinder were:

1. Basic linearity test using movement of Z the axis
2. Repeatability test between two points on the same surface moving the Z axis.
3. Repeatability between two surfaces moving the Z axis
4. Repeatability test between two points on the same surface moving the X axis.
5. Repeatability between two surfaces moving the X axis
6. Repeatability test between two points on the same surface moving the Z axis using two LVDT probes.
7. Repeatability between two surfaces moving the Z axis using two LVDT probes.

### **7.2.1 Basic linearity test using movement of the Z axis**

#### **7.2.1.1 Aim**

A basic linearity test was performed to compare the gauge reading with the machine DRO. It was intended as a basic quick check to observe any large errors. A more meaningful linearity test would involve a linearity and bias test using known reference artefacts.

The apparatus, equipment setup, method, results and discussion of results in Appendix D.

#### **7.2.1.2 Conclusion**

The linearity is good after scaling the two readings to remove the DRO error.

### **7.2.2 Repeatability test between two points on the same surface by moving the Z axis**

#### **7.2.2.1 Aim**

To assess variation in the LVDT gauge readings after moving the machine Z axis and keeping the gauge on the same surface.

The apparatus, equipment setup, method, results and discussion of results in Appendix E.

#### **7.2.2.2 Conclusion**

The results show that this specific setup fails to meet the gauge repeatability requirements due to drift in the results. As the error trend appears to be a steady slope it would be worthwhile repeating the test after a warm up period.

### **7.2.3 Repeatability test between two surfaces by moving the Z axis**

#### **7.2.3.1 Aim**

The intended use of the probe will involve the probes moving on and off the surfaces of the workpiece. Moving off the workpiece will allow all the preload to be released from the LVDT probe. This test aims to see if the action of moving the probe on to and off the edge of the workpiece (resulting in addition and removal of the gauge preload) causes any variation.

The apparatus, equipment setup, method, results and discussion of results in Appendix F.

#### **7.2.3.2 Conclusion**

The results show that for this specific setup fails to meet the gauge repeatability requirements due to the drift seen in the results. As the error trend appears to be a steady slope it would be worthwhile repeating the test after a warm up period.

#### **7.2.4 Repeatability test between two points on the same surface by moving the X axis.**

##### **7.2.4.1 Aim**

To assess if the variation in the gauge readings after moving the machine X axis.

The apparatus, equipment setup, method, results and discussion of results in Appendix G.

##### **7.2.4.2 Conclusion**

The results show that this specific setup meets the gauge repeatability requirements with acceptable variation and the X axis is not introducing any drift.

#### **7.2.5 Repeatability test between two surfaces by moving the X axis.**

##### **7.2.5.1 Aim**

The intended use of the probe will involve the probes moving on and off the surfaces of the workpiece. Moving off the workpiece will allow all the preload to be released from the LVDT probe. This test aims to see if the addition and removal of the preload by the action of moving the probe on to and off the edge of the workpiece causes any variation.

The apparatus, equipment setup, method, results and discussion of results in Appendix H.

##### **7.2.5.2 Conclusion**

The results show that this specific setup meets the gauge repeatability requirements the variation is acceptable.

#### **7.2.6 Repeatability test between two points on the same surface moving the Z axis using two LVDT probes**

##### **7.2.6.1 Aim**

As the previous repeatability test was conducted using a single LVDT probe, the results for the Z axis showed drift that was thought to be thermal drift of either the measuring

equipment or the machine structure. The test aims to observe if the same behaviour is seen after the measuring equipment has had a long warmup period. A second LVDT is used to take measurements to observe if it also registers a drift and to simulate the use of a datum surface. The purpose of measuring a datum surface is to record any machine structure drift and then subtract that from the readings of any other LVDT readings. If the test results show drift, then the result from the second LVDT probe for the datum surface will be subtracted from the other LVDT measurement to find the difference.

The apparatus, equipment setup, method, results and discussion of results in Appendix I.

#### **7.2.6.2 Conclusion**

As the results still show drift for the individual LVDT results and that the test equipment was switched on 2.5 hours before the start of the test it would indicate that the drift is unlikely to be due to the warmup of the measuring equipment. When the change in the datum surface LVDT reading is subtracted from the other LVDT reading the results show that the system has good repeatability and should be capable.

#### **7.2.7 Repeatability between two surfaces moving the Z axis using two LVDT probes.**

The intended use of the probe will involve the probes moving on and off the surfaces of the workpiece. Moving off the workpiece will allow all the preload to be released from the LVDT probe. This test aims to see if the addition and removal of the preload and the action of moving the probe on to and off the edge of the workpiece causes any variation. A previous repeatability test was conducted using a single LVDT probe, the results for the z axis showed drift that was thought to be thermal drift of either the measuring equipment or the machine structure. The test aims to observe if the same behaviour is seen after the measuring equipment has had a long warmup period. A second LVDT is used to take measurements to observe if it also registers a drift and to simulate the use of a datum surface. The purpose of measuring a datum surface is to record any drift and then subtract that from the readings of any other LVDT readings. If the test results show drift, then the result from the probe for the datum surface will be subtracted from the other LVDT measurement to find the difference.

The apparatus, equipment setup, method, results and discussion of results in Appendix J.

### **7.2.7.1 Conclusion**

As the results still show drift for the individual LVDT results and that the test equipment was switched on 3 hours before the start of the test it would indicate that the drift is unlikely to be due to the warmup of the measuring equipment. When the change in the datum surface LVDT reading is subtracted from the other LVDT reading the results show that the system has good repeatability and should be capable. This test is the closest representation of how the gauges would be used in the end application and the results show the system should be capable. Following the results of these tests it was concluded that the purchase of the full probe system could be made.

### **7.3 Dynamometer calibration**

#### **7.3.1 Aim**

Calibrate the response of the force dynamometer in the 3 axes to understand the response of the system.

#### **7.3.2 Objective**

Use known masses and a pulley to apply forces to the dynamometer in the three directions.

The equipment, method, results and discussion of results in Appendix K.

### **7.4 Conclusion**

The force dynamometer and DAQ system are capable of capturing the force inputs in a linear way, and appears to be sensitive enough for the expected force levels.

## **7.5 Flowmeter calibration tests**

### **7.5.1 Aim**

The flowmeter had not been used for several months and it had been reported that the readings could not be relied on. The flowmeter has few moving parts and little that could go wrong with it, after removing the flowmeter to check the turbine movement the meter was reinstalled after not finding fault with the moving parts or electronics apart from depleted batteries. The readings needed to be tested to check that they are correct and to understand any errors that the meter has.

### **7.5.2 Objective**

To capture flow that has passed through the flow meter over a timed period and then measure the mass of that fluid. The measured mass and the time were then used to calculate the actual flowrate.

The equipment, method, results and discussion of results in Appendix L.

## **7.6 Conclusion**

The flowmeter gave accurate readings with errors of less than 8% and is acceptable for the planned tests. However, the calibration test should be repeated if a grinding fluid with significantly different density is used in the grinding fluid delivery system.

## **7.7 Omega pressure gauge calibration tests**

### **7.7.1 Aim**

It had been reported by a previous user that the pressure gauge was giving strange readings above 14PSI. Faults were found with the wiring; the wiring was redone to correct the faults. The gauge reading, and output needed to be tested to check that the readings and output were correct.

### **7.7.2 Objective**

To pressurise the gauge using two different pressure sources and reference gauges over a range to see if the readings are linear and observe the difference to the other reference gauges.

The equipment, method, results and discussion of results is Appendix M.

## **7.8 Conclusion**

The pressure reading on the Omega pressure gauge appeared to be good to the two reference sources used. The reading is linear with no sign of significant curvature. The output from the Omega pressure gauge also tracks the gauge reading with only minor errors.

## **8 Grinding fluid nozzle trials**

### **8.1 Introduction**

A grinding fluid nozzle was needed to apply fluid to the grinding wheel when it was being dressed and when the workpiece was being ground. A simple round nozzle could have been used however, the diameter of the nozzle would have to be large to cover the full profile. 3D printing technology has enabled complex shapes to be created quickly when compared to traditional manufacturing techniques. Fused Deposition Modelling (FDM) can be used to shape plastics such as Acrylonitrile Butadiene Styrene (ABS), Polylactic acid (PLA). The main problem in using FDM technology to make grinding fluid nozzles is that the surface finish can be rough. The rough surface could cause drag and turbulence in the grinding fluid flow. It is also hard to form sharp edges using the FDM process. A grinding fluid nozzle was designed to suit the workpiece and grinding wheel form.

The grinding fluid nozzle was manufactured in two stages, first the nozzle was printed using the FDM method using ABS material with smaller pilot holes for the nozzle exit. The 3D printed nozzle was then finished using traditional manufacturing techniques of milling and drilling. The nozzle was mounted on a milling machine and the front exit face was milled square to the body and then holes were drilled perpendicular to the milled face. The milled face and the drilled holes allowed a sharp edge to be formed where the fluid exits the nozzle this helps to reduce nozzle losses and turbulence. Drilling the holes gave good size control for the nozzle exit area and removed the rough surface finish in the pilot holes.

It was necessary to test the nozzle on its own while not grinding as it was not clear in the nozzle could withstand the fluid pressures. If the nozzle were to break apart during grinding it could be dangerous as any loose parts could travel into the grinding nip and cause damage to the grinding wheel and fixturing.

### **8.2 Aim**

1. To investigate the level of nozzle jet dispersion at different nozzle pressures and flowrates.
2. To see if the nozzle could withstand the fluid pressure without breaking.

### **8.3 Objectives**

1. Mount the grinding fluid nozzle on a machine that allows easy viewing of the jet dispersion.
2. Visually observe the nozzle for jet breakup and for nozzle body breakup or delamination of the printed layers.

### **8.4 Theory**

Grinding fluid nozzles are required to apply fluid to the grinding nip at a velocity that matched the grinding wheel speed to overcome the air barrier at the surface of the wheel. If the air barrier can be removed with an air scrapper then the nozzle velocity does not need to match the wheel speed as fluid does not need momentum to get through the air barrier.

The apparatus, method, results and discussion are in Appendix N.

### **8.5 Conclusions**

The nozzle body withstood a pressure of 55PSI without breaking apart. The apparatus limited the testing, the maximum pressures and flows of the grinding fluid supply system were not reached. At the higher flowrates the grinding fluid could not drain back to the tank fast enough without flooding out of the machine. Run 2 showed more jet dispersion at the higher flowrate and pressure. If a grinding wheel is to be tested at several surface speeds several nozzles could be needed to achieve jet speed that matches wheel surface speed. Having a well placed air scraper could remove the need for matching wheel speed and therefore the number of nozzles and adjustments required when performing grinding trials. The area of the nozzle could stay fixed and the nozzle supply pressure kept low to avoid jet dispersion.

## **9 Cost model**

A preliminary cost model has been developed to include specific requirements for form grinding process. Using the cost model could allow the users to investigate the range of machining parameters that meet quality requirements and understand the impact on the cost per part. The cost model has been developed in MS Excel, Figure 9-1 shows the input screen for the cost model and Figure 9-2 shows the calculations page of the cost model.

The purpose of the cost model is to help the comparison between different technologies by considering the total process costs. The types of technologies that the cost model could be useful for are comparing abrasive types used in grinding wheels such as aluminium oxide, CBN or the new precision shaped abrasive used within 3M™ Cubitron™ II Vitrified wheels. Other uses could be comparison of different grinding fluids such as synthetic oils and mineral oils, and different diamond types. Some of the inputs to the model do require estimations or empirical tests to find the values.

### **9.1 Additional considerations for form dressing**

Typically, helical form grinding machines that grind large forms such as those found in screw compressor rotors use one or two form dressing disks or rolls to dress the form onto the grinding wheel. The Holroyd TG and Zenith machines use two form disks, the distance between the disks can be adjusted to accommodate different widths of wheel. The cost model by Ebbrell (2003) does not account for the setup costs. The setup costs include abrasive removed to true and dress the wheel ready for use and its associated time costs. Form dressing configurations as used on the Holroyd TG and Zenith machines can have errors that result in the dresser path being incorrect, resulting in an incorrect form being dressed on to the wheel. The wheel is then used to grind the workpiece, followed by the workpiece being measured and calculations performed to create a modified dresser path that will remove the dresser path errors. The errors in the dresser configuration consist of:

1. The geometry of the dresser form disk. The tip radius of a used dresser disk may be worn and no longer a true radius. The machine can be told the radius of the dresser disk. However, the operator cannot input any finer detail for the geometry

of the tip radius that would inform the machine of the wear flat on the radius. Therefore, the machine generates the dresser paths on the assumption that the tip radius is a true radius.

2. The position of the form dresser disks on Holroyd TG and Zenith machines are set using a setting fixture. The dresser disks are touched on the sides and the diameter of a setting ring. Once a light touch is achieved between the dresser disk and the setting fixture the machine uses the dresser axis positions and the geometry information entered for the dresser disks to calculate offset for the position of the dresser disk. Variation between operators can be as much as 20 $\mu$ m. Positional errors of this magnitude can result in the part being out of tolerance and the wheel must be redressed. These positional errors have the greatest impact upon forms that have near vertical sides on the wheel profile. The error may have caused the form on the wheel to be dresser to one side putting it out of position, they could cause the wheel to be narrow or wide or one side of the profile could be at a different radial position to the other side. If the sides of the profile are near vertical larger amounts of abrasive need to be removed from the wheel to correct the error. This not only uses more abrasive but also takes more time and also adds additional wear to the form dresser disks.
3. The dresser axis positional accuracy, repeatability, squareness between axes and thermal errors can contribute to the errors that are dressed onto the wheel for the first dress when setting up.

The additional cost associated with these errors can impact on the cost per part. The batch size or number of parts produced before the machine is set up for a different workpiece type can have a large effect on the cost per part. It would be useful to understand the influence of batch size on the cost per part when choosing a different technology. For example, for screw compressor rotors a batch size could be in the order of 30 to 60 workpieces between machine setups, would it be economical to use vitrified CBN wheels for such batch sizes when each time the machine is setup 0.1mm of abrasive is used to compensate for setup errors?

<b>PROCESS TYPE : SURFACE FORM GRINDING</b>				
<b>INFORMATION AREA</b>	<b>FACTOR</b>	<b>DESCRIPTION</b>	<b>VALUE</b>	<b>UNITS</b>
<b>TOOLING</b>	$d_{s\ max}$	MAXIMUM WHEEL DIAMETER	500	mm
	$d_{s\ min}$	MINIMUM WHEEL DIAMETER	260	mm
	$b_s$	WHEEL WIDTH	40	mm
		GRIT DIAMETER	0.181	mm
		WHEEL POROSITY	50	%
		WHEEL PORE DEPTH (Rui Cai Ch5)	1	mm
		RADIAL THICKNESS OF USABLE WHEEL		
	$r_{su}$	ABRASIVE	100	mm
		GRINDING WHEEL TYPE	ALUMINIUM OXIDE	▼
		DRESSER TYPE	PROFILE ROLLER	▼
	DRESSER MATERIAL	PCD	▼	
<b>WORKPIECE</b>	$L_w$	LENGTH	100	mm
	$b_w$	WIDTH	35	mm
		HARDNESS	28	HRC
	$f_d$	FORM DEPTH	50	mm
<b>COSTS</b>	$c_l$	LABOUR RATE	100	£/hour
	$c_s$	WHEEL COST	450	£
	$c_f$	GRINDING FLUID COSTS	1.75	£/L
	$c_{fd}$	DISPOSAL COST OF GRINDING FLUID	0.5	£/L
	$c_e$	ELECTRICITY COST	0.1	£/kWh
	$C_{mc}$	COST OF MACHINE	850000	£
	$C_{mmc}$	MACHINE MAINTENANCE COST	3500	£/YEAR
	$C_{sd}$	GRINDING WHEEL DISPOSAL COST	10	£
	$l_s$	SHIFTS	3.00	N/A
	$l_h$	WORKING HRS./WEEK	37	HRS/WEEK
$l_w$	WORK WKS/YR	46	WKS/YEAR	
<b>MACHINING PARAMETERS</b>	$v_s$	WHEEL SPEED	35	m/s
	$v_w$	WORKPIECE FEEDRATE?	1750	mm/min
	$a$	DEPTH OF CUT	0.1	mm
<b>DRESSING PARAMETERS</b>	$a_d$	DRESSING DEPTH	0.05	mm
	$n_g$	NUMBER OF GRINDING PASSES BEFORE DRESSING	10	N/A
	$n_d$	NUMBER OF DRESSING PASSES	1	N/A
	$N_d$	NUMBER OF PARTS PER DRESS	0.33	N/A
	$r_s$	RADIAL WHEEL WEAR PER DRESS	0.003	mm
	$t_s$	CYCLE TIME PER PART EXCLUDING DRESSING TIME (FLOOR TO FLOOR)	15.5	minutes
	$n_{ds}$	NUMBER OF DRESSES REQUIRED WHEN SETTING UP	20	N/A
	$a_{ds}$	DRESSING DEPTH USED FOR SETUP	0.05	mm
	$N_{ws}$	BATCH SIZE PRODUCED BETWEEN SETUPS	400	N/A
	$b_p$	DRESSING PROFILE LENGTH	50	mm
	$u_d$	DRESSER OVERLAP RATIO	2	N/A
	$r$	DRESSER RAD	0.5	mm
	<b>MACHINE</b>	$\gamma_t$	LIFE TIME OF MACHINE/PAYBACK PERIOD	3
$m_l$		MACHINE LOADING	70.00%	%
$m_r$		MACHINE POWER RATING	40	kW
<b>GRINDING FLUID</b>		GRINDING FLUID DELIVERY SYSTEM POWER RATING	15	kW
	$n_f$	GRINDING FLUID TANK SIZE	6000	L
	$\gamma_f$	LIFETIME OF GRINDING FLUID	750	HOURS
		AMOUNT OF FLUID LOST FOR EACH PART	0.02	L

Figure 9-1 Cost model inputs tab.

<b>Calculations</b>				
<b>FACTOR</b>	<b>EQUATION</b>	<b>DESCRIPTION</b>	<b>RESULT</b>	<b>UNITS</b>
$C_t$	$C_t = C_l + C_m + C_s + C_f$	TOTAL VARIABLE COST PER PART	41.34	£/part
$C_e$	$C_e = C_m + C_s + C_f$	TOTAL VARIABLE COST PER PART EXCLUDING LABOUR AND OVERHEAD	14.63	£/part
$C_l$	$C_l = c_l \div N_l$	LABOUR COST PER PART INCLUDING OVERHEAD CONTRIBUTION	26.71	£/part
$C_m$	$C_m = (C_{mc} + (C_{mmc} \times y_t)) \div N_{mc}$	MACHINE COST PER PART	8.75	£/part
$C_s$	$C_s = (c_s + c_{sd}) \div N_w$	WHEEL COST PER PART	1.071839827	£/part
$C_f$	$C_f = ((c_f + c_{fd}) \times n_f \div y_f) \div N_l$	GRINDING FLUID COST PER PART	4.8086	£/part
$Q_w$	$Q_w = b_w \times v_w \times a$	WORKPIECE VOLUMETRIC REMOVAL RATE	6125	mm <sup>3</sup> /min
$V_{wt}$	$V_{wt} = b_w \times a \times L_w \times n_g$	VOLUME OF WORKPIECE REMOVED	3500	mm <sup>3</sup>
$V_w$	$V_w = b_w \times a \times L_w$	VOLUME OF WORKPIECE REMOVED PER PASS	350	mm <sup>3</sup>
$V_{st}$	$V_{st} = b_s \times a_d \times \pi \times d_{smax} \times n_d$	VOLUME OF WHEEL REMOVED	3141.5927	mm <sup>3</sup>
$V_s$	$V_s = b_s \times a_d \times \pi \times d_{smax}$	VOLUME OF WHEEL REMOVED PER DRESSING PASS	3141.5927	mm <sup>3</sup>
$G$	$G = V_{wt} \div V_{st}$	G-RATIO (Grinding ratio)	1.1141	N/A
$C_{sd}$	$C_{sd} = c_s \div (r_{su} \div a_d)$	COST OF ABRASIVE REMOVED PER DRESSING PASS	0.225	£
$b$	$b = c_s \div \left( \left( \pi \times \left( \frac{d_{smax}}{2} \right)^2 \right) - \left( \pi \times \left( \left( \frac{d_{smax}}{2} \right) - r_{su} \right)^2 \right) \right) \times b_s$	COST OF GRINDING WHEEL PER UNIT VOLUME OF USABLE ABRASIVE	4.95638E-05	£/mm <sup>3</sup>
$N_w$	$N_w = N_d \times (r_{suf} \div (r_s + (a_d \times n_d) + (r_{ssp} \times N_d)))$	NUMBER OF PARTS PRODUCED PER WHEEL	429.168602	N/A
$r_{suf}$	$r_{suf} = ((d_{smax} - d_{smin}) \div 2) - f_d$	AMOUNT OF RADIAL USABLE ABRASIVE	70	mm
$N_l$	$N_l = 1 \div t_t$	NUMBER OF PARTS PER UNIT TIME	3.743311659	PARTS/HOUR
$t_t$	$t_t = t_s + (t_d \div N_d) + (t_{ds} \div N_{ws})$	CYCLE TIME PER PART INCLUDING DRESSING AND SETUP	0.267143132	hours
$r_{ss}$	$r_{ss} = n_{ds} \times a_{ds}$	RADIAL AMOUNT OF WHEEL USED FOR SETUP	1	mm
$C_{ss}$	$C_{ss} = r_{ss} \div (a_{ds} \times c_s)$	COST OF ABRASIVE USED FOR SETUP	4.5	£
$v_d$	$v_d = (b_d \div u_d) \times (v_s \div (\pi \times d_s))$	DRESSER FEEDRATE	4.856182193	mm/s
$t_d$	$t_d = b_p \times n_d \div v_d \div 60$	DRESSING TIME	0.171602568	minutes
$t_{ds}$	$t_{ds} = b_p \times n_{ds} \div v_d \div 60$	SETUP DRESSING TIME	3.432051353	minutes
$b_d$	$b_d = 2 \times \sqrt{(r^2 - (r - a_d)^2)}$	EFFECTIVE WIDTH OF DRESSING TOOL	0.435889894	mm
$r_{ssp}$	$r_{ssp} = n_{ds} \times a_{ds} \div N_{ws}$	AMOUNT OF WHEEL RADIUS USED FOR SETUP PER PART	0.0025	mm
$N_B$	$N_B = N_w \div N_{ws}$	NUMBER OF BATCHES PER WHEEL	1.072921505	N/A
$C_{ft}$	$C_{ft} = c_f \times n_f$	COST TO FILL GRINDING FLUID TANK	10500	£
$N_{mc}$	$N_{mc} = y_t \times N_l$	THE NUMBER OF PARTS PRODUCED DURING MACHINE PAYBACK PERIOD	98374.2304	N/A
$C_{py}$	$C_{py} = m_l \times m_r \times c_e \times l_s \times l_h \times l_w$	COST OF POWER TO RUN GRINDING MACHINE FOR A	14296.8	£
$C_{pp}$	$C_{pp} = m_l \times m_r \times c_e \div N_l$	COST OF POWER TO RUN GRINDING MACHINE FOR ONE PART	0.748000769	£

Figure 9-2 Cost model calculation tab.

The cost model could be improved in several areas.

1. Grinding fluid lost per part. Evaporation losses. Mist losses from the machine due to hot air rising. Grinding fluid is lost on the workpiece surface when the part is removed from the machine.
2. Dresser wear rates could be added along with the cost of a new dressers, cost of a relap and number of relaps.

The preliminary cost model was presented as a paper at ICMR 2017 (Hart et al., 2017). A copy of the paper is included in Appendix O.

## 10 Conclusions

The problems presented by helical form grinding were investigated to understand how they can be included in a pseudo-helical grinding process on a smaller more commonly available machine.

Test grinds using the machine assigned to the research project have been completed and assessed showing a need to measure and true depth of cut.

A workpiece has been designed to closely replicate the entry and exit contact conditions and form that are found in the grinding of helical screw compressor rotors.

The workpiece fixturing design allows the varying axial, normal and tangential grinding forces to be investigated during the entry and exit regions of the workpiece, as well as the resultant forces produced by the asymmetric form when the grinding wheel is in full engagement.

LVDTs were chosen to measure the true depth of cut following repeatability, linearity and bias testing that showed that LVDTs were capable for the DoC magnitudes that the grinding machine was capable of. The new work holding fixture and metrology station has been designed and manufactured.

Replication materials used to measure workpiece form and surface roughness have been researched, a selection made and purchased. An on machine method of capturing grinding wheel form before and after a test has been designed and created.

A LabVIEW virtual instrument have been designed, for capturing grinding force readings from a force dynamometer, to capture encoder scale position, the metrology station values and grinding fluid pressure.

A preliminary cost model has been created to include features relevant to the helical form grinding processes to aid in the assessment of grinding wheel and grinding fluids costs. The model can be used to establish the cost per part for a given set of machining parameters. The model has further potential to include other variables relevant for helical form grinding and production strategies such as batch size variation.

## 11 Further work

Further work will include the setting and testing the virtual instruments. Accuracy and repeatability testing of: the metrology station, the replication material casting process, CMM measurements of the replicates and the surface roughness measurements of the replicates. Preliminary grinding trials with the new workpiece holding fixture and measurement devices to commission its functionality and make any adjustments that may be necessary.

Tests to be conducted:

1. Grinding tests to evaluate water based grinding fluid and oil grinding fluid.
2. Grinding tests to evaluate two grinding wheels with two different abrasive technologies.
3. Grinding tests to observe the effect of using grinding fluid guides on grinding forces.
4. Grinding tests to observe the effect of using high and low pressure coolant on grinding forces and specific grinding energy.

The grinding tests will involve conducting a Taguchi test to identify the main effects of the responses of the process. Once the main effects are identified a larger response surface methodology (RSM) test will be designed using the factors that have been shown to affect the process. The results of response surface methodology (RSM) test will be used to generate a model of the measured responses. Model reduction will be performed by using analysis of variance (ANOVA) methods on the model factors and the outcome used to assess and remove terms that are not significant. Confirmation test grinds will be conducted within ranges of the original test limits to test model accuracy. The confirmed models can then be utilised within a software optimisation tool that will allow users to explore the multiple response behaviour and choose the process factor levels to give the optimum response.

The analysis of results will provide new insight into the efficacy of the designed system. Based on this knowledge refinements may be introduced to deliver a final robust industrialised version.

The optimisation tool will be validated with a selected industry application in the context of the confirmation studies.

Further refinement to the proposed economic model will be introduced based on information gained from the industry sponsor as it becomes available.

Analytic models of the process will be validated and explored.

## References

- BAGHERIAN AZHIRI, R., TEIMOURI, R., GHASEMI BABOLY, M. & LESEMAN, Z. (2014). Application of Taguchi, ANFIS and grey relational analysis for studying, modeling and optimization of wire EDM process while using gaseous media. *The International Journal of Advanced Manufacturing Technology*, 71, 279-295.
- BAINES-JONES, V. A. L. J. M. U. (2010). *Nozzle Design for Improved Useful Fluid Flow in Grinding*, Liverpool John Moores University.
- BRINKSMEIER, E., HEINZEL, C. & WITTMANN, M. (1999). Friction, Cooling and Lubrication in Grinding. *CIRP Annals - Manufacturing Technology*, 48, 581-598.
- BSO (2014). BS ISO 1986-1:2014 Test conditions for surface grinding machines with horizontal grinding wheel spindle and reciprocating table. Testing of the accuracy Machines with table length of up to 1 600 mm. London: BSI British Standards.
- CATAI, R. E., BIANCHI, E. C., ZILIO, F. M., VALARELLI, I. D. D., ALVES, M. C. D. S., SILVA, L. R. & AGUIAR, P. R. D. (2006). Global analysis of aerodynamics deflectors efficiency in the grinding process. *J. Braz. Soc. Mech. Sci. & Eng. Journal of the Brazilian Society of Mechanical Sciences and Engineering*, 28, 140-145.
- CHOMSAMUTR, K. & JONGPRASITHPORN, S. (2012). Optimization Parameters of tool life Model Using the Taguchi Approach and Response Surface Methodology. *International Journal of Computer Science*, 9, 120-125.
- DERKX, J. M., HOOGSTRATE, A. M., SAURWALT, J. J. & KARPUSCHEWSKI, B. (2008). Form crush dressing of diamond grinding wheels. *CIRP Annals - Manufacturing Technology*, 57, 349-352.
- DHAVLIKAR, M. N., KULKARNI, M. S. & MARIAPPAN, V. (2003). Combined Taguchi and dual response method for optimization of a centerless grinding operation. *Journal of Materials Processing Technology*, 132, 90-94.

- DOJA, B. (2012). Analysis and Effect of Process Parameters on Surface Roughness and Tool Flank Wear in Facing Operation. *International Journal of Engineering Research and Technology*. ESRSA Publications.
- EBBRELL, S. (2003). *Process requirements for precision grinding*, Liverpool, Liverpool John Moores University.
- EBBRELL, S., WOOLLEY, N. H., TRIDIMAS, Y. D., ALLANSON, D. R. & ROWE, W. B. (2000). The effects of cutting fluid application methods on the grinding process. *International Journal of Machine Tools and Manufacture*, 40, 209-223.
- ERIC.S. (2017). *Synchronize Encoder Counter Input and Analog Input with DAQmx* [Online]. Available at: <https://forums.ni.com/t5/Example-Programs/Synchronize-Encoder-Counter-Input-and-Analog-Input-with-DAQmx/ta-p/3498784> [Accessed 24 April 2017].
- GUO, C. & MALKIN, S. (1994). Analytical and Experimental Investigation of Burnout in Creep-Feed Grinding. *CIRP Annals - Manufacturing Technology*, 43, 283-286.
- GVINIASHVILI, V. L. J. M. U. (2003). *Fluid application system optimisation for high speed grinding*, Liverpool, Liverpool John Moores University.
- H ROBERTS & SONS (DI) LIMITED. (2016). *Plastiform RI-001 MD-3P Rigid Set Resin, Powder & Hardener To Make 500ml Dries Like Resin - H Roberts* [Online]. Available at: <http://www.hroberts-di.com/metrology-equipment-/plastiform-precision-moulding/rigid-compounds/plastiform-ri-001-md-3p-rigid-set-resin-powder-hardener-to-make-500ml-dries-like-resin/> [Accessed 24 August 2016].
- HART, P. W., MORGAN, M. N. & THE INTERNATIONAL CONFERENCE ON MANUFACTURING RESEARCH, I. (2017). Economic analysis of the helical form grinding process. *Adv. Transdiscipl. Eng. Advances in Transdisciplinary Engineering*, 6, 573-578.
- HOWES, T. (1990). Assessment of the Cooling and Lubricative Properties of Grinding Fluids. *CIRP Annals - Manufacturing Technology*, 39, 313-316.

- HOWES, T. D., NEAILEY, K., HARRISON, A. J. & MCKEOWN, P. A. (1987). Fluid Film Boiling in Shallow Cut Grinding. *CIRP Annals - Manufacturing Technology*, 36, 223-226.
- JACKSON, A. L. J. M. U. (2008). *An investigation of useful fluid flow in grinding*, Liverpool, Liverpool John Moores University.
- JAMAL, M., PEAVOY, D. & MORGAN, M. N. (2017). A digital process optimization, process design and process informatics system for high-energy abrasive mass finishing. *Int J Adv Manuf Technol International Journal of Advanced Manufacturing Technology*, 1-17.
- JIN, T. & STEPHENSON, D. J. (2003). Investigation of the heat partitioning in high efficiency deep grinding. *International Journal of Machine Tools and Manufacture*, 43, 1129-1134.
- KILICKAP, E. (2010). Optimization of cutting parameters on delamination based on Taguchi method during drilling of GFRP composite. *Expert Systems with Applications*, 37, 6116-6122.
- MALKIN, S. (1989). *Grinding technology : theory and applications of machining with abrasives*, Chichester; New York, E. Horwood ; Halsted Press.
- MALKIN, S. & CHANGSHENG, G. (2008). *Grinding technology : theory and application of machining with abrasives*, New York, Industrial Press.
- MANDAL, B., SINGH, R., DAS, S. & BANERJEE, S. (2012). Development of a Grinding Fluid Delivery Technique and Its Performance Evaluation. *Materials & Manufacturing Processes*, 27, 436-442.
- MARINESCU, I. D., HITCHINER, M., UHLMANN, E., ROWE, W. B. & INASAKI, I. (2007). *Handbook of machining with grinding wheels*, Boca Raton, FL, CRC / Taylor & Francis Group, LLC ;.
- MARINESCU, I. D., ROWE, W. B., INASAKI, I. & DIMITROV, B. (2012). *Tribology of abrasive machining processes*, Norwich, NY, William Andrew Pub.
- MASSAM, M. C. U. (2008). *Thermal characteristics of grinding fluids*. Cranfield University.
- MORGAN, M. N., CAI, R., GUIDOTTI, A., ALLANSON, D. R., MORUZZI, J. L. & ROWE, W. (2007). Design and implementation of an intelligent grinding assistant system. *International Journal of Abrasive Technology*, 1, 106-135.

- MORGAN, M. N., JACKSON, A. R., WU, H., BAINES-JONES, V., BATAKO, A. & ROWE, W. B. (2008). Optimisation of fluid application in grinding. *CIRP Annals - Manufacturing Technology*, 57, 363-366.
- ROWE, W. B. (2009). *Principles of modern grinding technology*, Oxford; Burlington, MA, William Andrew.
- ROWE, W. B., HONGSHENG, Q. I., MORGAN, M. N. & HUANWEN, Z. (1993). The Real Contact Length in Grinding Based on Depth of Cut and Contact Deflections. 187-193.
- ROWE, W. B. & JIN, T. (2001). Temperatures in High Efficiency Deep Grinding (HEDG). *CIRP Annals - Manufacturing Technology*, 50, 205-208.
- SHETH, D. S. & MALKIN, S. (1990). CAD/CAM for Geometry and Process Analysis of Helical Groove Machining. *CIRP Annals - Manufacturing Technology*, 39, 129-132.
- SINGH, M. (2015). *Grinding and Grinding Machine* [Online]. Available at: <https://www.slideshare.net/ManishSingh414/grinding-52112102> [Accessed 8 December 2018].
- STOSIC, N. (2006). A geometric approach to calculating tool wear in screw rotor machining. *International Journal of Machine Tools and Manufacture*, 46, 1961-1965.
- WEBSTER, J., BRINKSMEIER, E., HEINZEL, C., WITTMANN, M. & THOENS, K. (2002). Assessment of Grinding Fluid Effectiveness in Continuous-Dress Creep Feed Grinding. *CIRP Annals - Manufacturing Technology*, 51, 235-240.
- WEBSTER, J. A. (Year) Published. Selection of Coolant Type and Application Technique in Grinding. Supergrind 1995 -Grinding and Polishing with Superabrasives., November 2-3 1995 Connecticut, USA. p.205 - 220.
- WU, H. L. J. M. U. (2009). *Investigation of Fluid Flow in Grinding using LDA Techniques and CFD Simulation*, Liverpool John Moores University.
- YAMADA, T., LEE, H. S., MIURA, K. & MORGAN, M. (2012). Calculation of effective ground depth of cut by means of grinding process model. *Key Eng Mat Key Engineering Materials*, 496, 7-12.

YAMADA, T., LEE, H. S., MIURA, K., MORGAN, M. & THE INTERNATIONAL SYMPOSIUM ON ADVANCES IN ABRASIVE TECHNOLOGY, I. (2011). Calculation of the contact stiffness of grinding wheel. *Adv. Mater. Res. Advanced Materials Research*, 325, 54-59.

ZHOU, Z. X. & VAN LUTTERWELT, C. A. (1992). The Real Contact Length between Grinding Wheel and Workpiece A New Concept and a New Measuring Method. *CIRP CIRP Annals - Manufacturing Technology*, 41, 387-391.

## Appendix A - Discussion of other Plastiform products tested

### A.1 Plastiform B.A.D CA-005

The cured impression is semi flexible with a hardness of 50 Shore A and would likely deform with the pressures of a CMM stylus. Figure A-1 shows a sample moulding of Plastiform B.A.D CA-005.



Figure A-1 Sample moulding using Plastiform B.A.D CA-005

### A.2 Plastiform D.A.V CA-001

The cured impression is flexible with a hardness of 20 Shore A and would likely deform with the pressures of a CMM stylus. This product was used to make an impression on all but one sides of the workpiece. This impression was then later used to make a positive impression effectively making a replicate of the workpiece. Figure A-2 shows a sample moulding using Plastiform D.A.V CA-001



Figure A-2 Sample moulding using Plastiform D.A.V CA-001

### A.3 Plastiform LK-AD MT-003

The cured impression is semi flexible with a hardness of 70 Shore A and would likely deform with the pressures of a CMM stylus. Slices have been cut through the mould to demonstrate that the form could be more easily measured on some optical measuring devices. Figure A-3 shows a sample moulding using Plastiform LK-AD MT-003

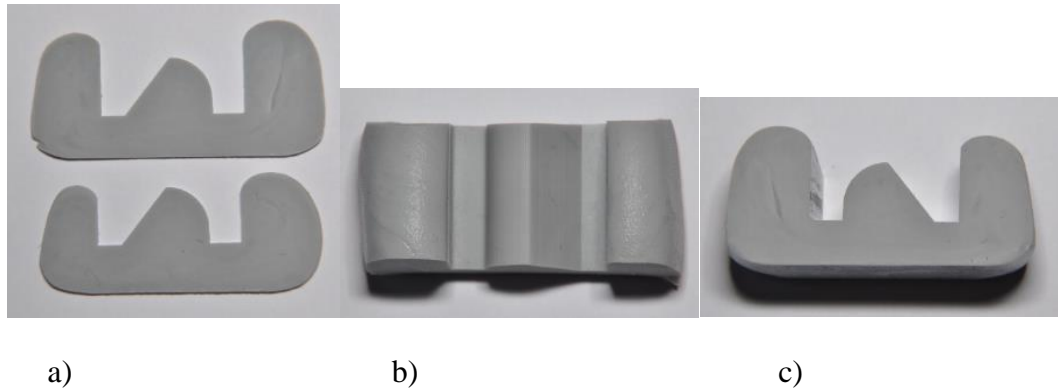


Figure A-3 Sample moulding using Plastiform LK-AD MT-003. a) Thin sections cut from the impression for a clear view of the form. b) Top view of impression from which the sections were cut. c) End view of impression from which the sections were cut.

### A.4 Plastiform PE-AD CA-006

The cured impression is semi flexible with a hardness of 65 Shore A and would likely deform with the pressures of a CMM stylus. Figure A-4 shows a sample moulding using Plastiform PE-AD CA-006.



Figure A-4 Sample moulding using Plastiform PE-AD CA-006

### A.5 Plastiform PF-AD MT-005

The cured impression is semi-rigid with a hardness of 80 Shore A and would likely deform with the pressures of a CMM stylus. The accuracy is not suitable and the curing time is long. Figure A-5 shows a sample moulding using Plastiform PF-AD MT-005

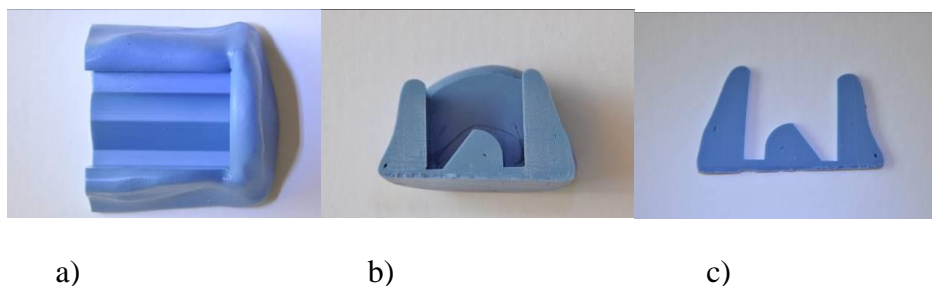


Figure A-5 Sample moulding using Plastiform PF-AD MT-005. a) Top view of impression from which the section were cut. b) End view of impression. c) Thin section cut from the impression for a clear view of the form.

### A.6 Plastiform R.G.X CA-009

The cured impression is semi-rigid with a hardness of 80 Shore A and would likely deform with the pressures of a CMM stylus. The main purpose of this product is for indirect surface roughness measurement however, it can also be used for profile/form measurement. Figure A-6 shows a sample moulding using Plastiform R.G.X CA-009.

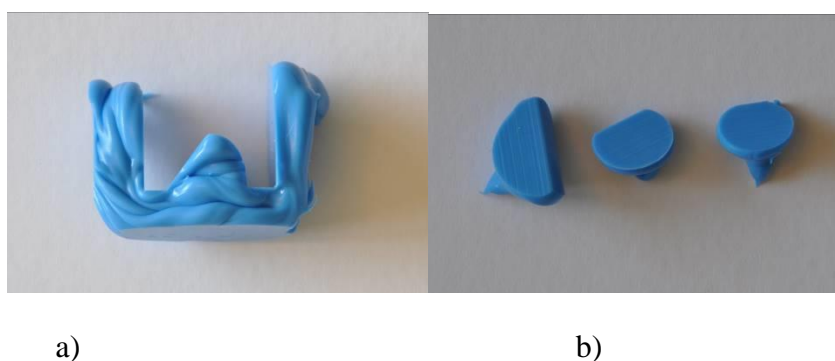


Figure A-6 Sample moulding using Plastiform R.G.X CA-009. a) End view of impression. b) small drop applications that can be used when only the surface roughness needs to be measured.

### A.7 Plastiform S.O.F.T CA-008

The cured impression is flexible with a hardness of 35 Shore A and would likely deform with the pressures of a CMM stylus. Figure A-7 shows a sample moulding using Plastiform S.O.F.T CA-008.

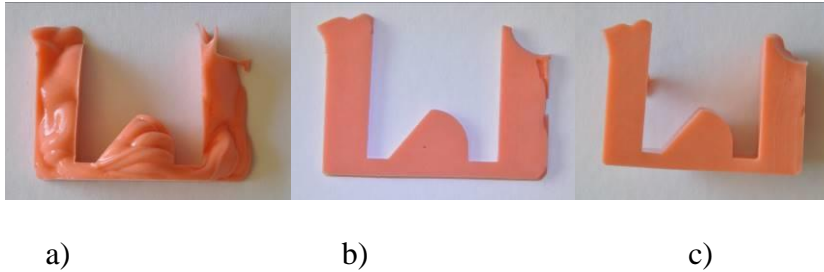


Figure A-7 Sample moulding using Plastiform S.O.F.T CA-008. a) End view of impression. b) Thin section cut from the impression for a clear view of the form. c) End view of impression.

## Appendix B - Supplementary information for LVDT repeatability test

### B.1 Apparatus

1. Granite surface plate.
2. Adjustable magnetic base.
3. Tesatronic LVDT (GT21 axial probe) and analogue meter (Tesatronic TTA 20 probe display unit).
4. Tool makers vice.
5. Mitutoyo ceramic gauge blocks ranging from 1.001mm to 1.030mm.

### B.2 Equipment Setup

The tool makers vice was used to provide a heavy weight that the magnetic base could be attached to. The LVDT probe was attached to the end of the magnetic base and positioned so that the probe axis was perpendicular to the surface of the granite surface plate. Gauge blocks were positioned between the surface of the granite and the spherical end on the LVDT probe. The equipment setup is shown in Figure B-1. The analogue meter was set to a scale of  $\pm 3\mu\text{m}$ .

### B.3 Method –Repeatability test

1. The surface of the granite plate was cleaned with a cloth.
2. A 1.030mm gauge block was cleaned and placed between the granite surface plate and the LVDT probe tip.
3. The magnetic base was adjusted to roughly zero the reading on the analogue meter. The fine adjustment was used to set the needle of the analogue meter to read zero.
4. A 1.020mm gauge block was cleaned and used to push out the 1.030mm gauge block from under the LVDT probe tip until it was under the probe tip. The 1.030mm gauge block was then used to push the 1.020mm gauge block out from under the LVDT probe tip until it was back under the LVDT probe tip.
5. The analogue meter reading was read and recorded.
6. Steps 4 and 5 were repeated 20 times.
7. The results were entered into Minitab 17 statistical software and a Type 1 gage study was performed.



Figure B-1 Equipment setup used for repeatability test

#### **B.4 Results**

The measurements results are shown in Table B-1, and the graph of the Minitab calculated results is shown in Figure B-2.

Table B-1 Table of results for repeatability test

RUN NUMBER	MEASUREMENT ( $\mu\text{m}$ )
1	0.1
2	-0.1
3	0.1
4	-0.1
5	0.0
6	0.1
7	0.2
8	0.1
9	-0.1
10	0.1
11	-0.1
12	0.1
13	0.1
14	-0.1
15	-0.1
16	0.1
17	0.1
18	0.2
19	0.1
20	0.1

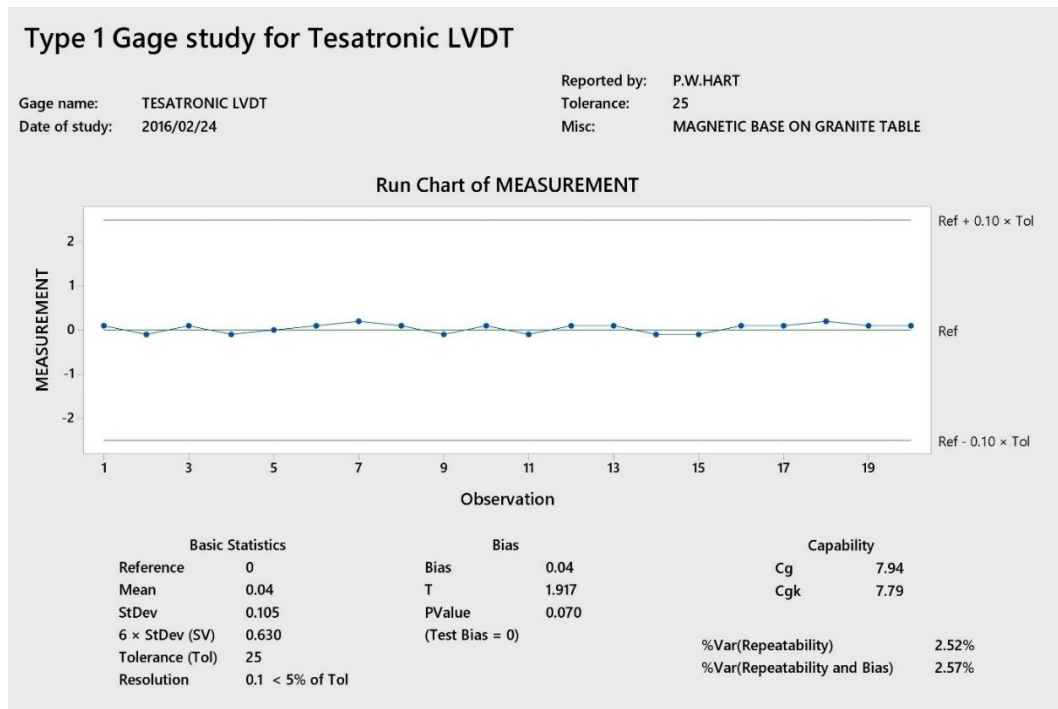


Figure B-2 Minitab 17 type 1 gage test results graph for the repeatability test

### B.5 Discussion of results

Figure B-2 shows the Minitab graph and calculated values for the type 1 gage test. The gauge was set to zero at the start of the test therefore the bias amount only indicates how far the mean of the readings is from the initial set point of zero. Minitab recommends that 25 measurements are taken for a good sample size. The sample size of 20 taken during the test should still give a reasonable representation of the variation. This test is to be used as an indication for the gauge in near ideal conditions, the test will have to be repeated for the end application of the gauge. The Cg value is calculated by comparing the measurement variation with the tolerance and Cgk compares both the measurement of the variation and the bias. The value of these terms should be 1.33 or higher to indicate that it is acceptable for the process that is being considered. Larger values indicate that variation in the measurement system is small compared to the tolerance. Minitab also recommends that the resolution of the measurement system is less than 5% of the tolerance. The finest scale was used for this repeatability test, which gave a resolution of 0.1µm. The range of this scale would not be adequate for the DOC measurements a larger range would be needed which would provide a resolution of 1µm. However, even at this larger resolution the gauge would still meet this requirement. The PValue is higher than the set confidence level and we can

therefore conclude that the bias is not significant. The %Var (Repeatability and %Var (Repeatability and Bias)) values are lower than the Minitab recommendation of 15% indicating that the variation and bias of the system is acceptable.

## Appendix C - Supplementary information for LVDT Accuracy test

### C.1 Apparatus

1. Granite surface plate.
2. Adjustable magnetic base.
3. Tesatronic LVDT (GT21 axial probe) and analogue meter (Tesatronic TTA 20 probe display unit).
4. Tool makers vice.
5. Mitutoyo ceramic gauge blocks ranging from 1.001mm to 1.030mm.

### C.2 Equipment Setup

The tool makers vice was used to provide a heavy weight that the magnetic base could be attached to. The LVDT probe was attached to the end of the magnetic base and positioned so that the probe axis was perpendicular to the surface of the granite surface plate. Gauge blocks were positioned between the surface of the granite and the spherical end on the LVDT probe. The equipment setup is shown in Figure C-1. The analogue meter was set to a scale of  $\pm 30\mu\text{m}$ .



Figure C-1 Equipment setup used for linearity and bias test

### C.3 Method –Repeatability test

1. The surface of the granite plate was cleaned with a cloth.

2. A 1.001mm gauge block was cleaned and placed between the granite surface plate and the LVDT probe tip.
3. The magnetic base was adjusted to roughly 1 $\mu$ m reading on the analogue meter. The fine adjustment was used to set the needle of the analogue meter to read +1 $\mu$ m.
4. A 1.002mm gauge block was cleaned and used to push out the 1.001mm gauge block from under the LVDT probe tip until it was under the probe tip.
5. The analogue meter reading was read and recorded.
6. Steps 4 and 5 were repeated with the gauge block size increasing by 1 $\mu$ m each time up to 1.010mm, then a 1.020mm and 1.030mm block was used.
7. Steps 4 to 6 were repeated another two times.
8. The results were entered into Minitab 17 statistical software and a Gage linearity and bias test was performed.

#### **C.4 Results**

The measurements results are shown in Table C-1, and the graph of the Minitab calculated results is shown in Figure C-2.

Table C-1 Table of results for linearity and bias test

REFERENCE	REFERENCE SIZE (μm)	MEASUREMENT (μm)
1	1	1.0
2	2	2.5
3	3	3.0
4	4	4.0
5	5	6.0
6	6	7.0
7	7	8.0
8	8	9.0
9	9	10.0
10	10	11.5
11	20	21.5
12	30	31.0
1	1	1.0
2	2	2.0
3	3	3.5
4	4	4.0
5	5	5.0
6	6	6.0
7	7	7.0
8	8	8.0
9	9	9.0
10	10	10.0
11	20	20.0
12	30	29.5
1	1	1.0
2	2	2.0
3	3	3.0
4	4	4.0
5	5	5.0
6	6	6.0
7	7	7.0
8	8	8.0
9	9	9.0
10	10	10.0
11	20	19.5
12	30	29.5

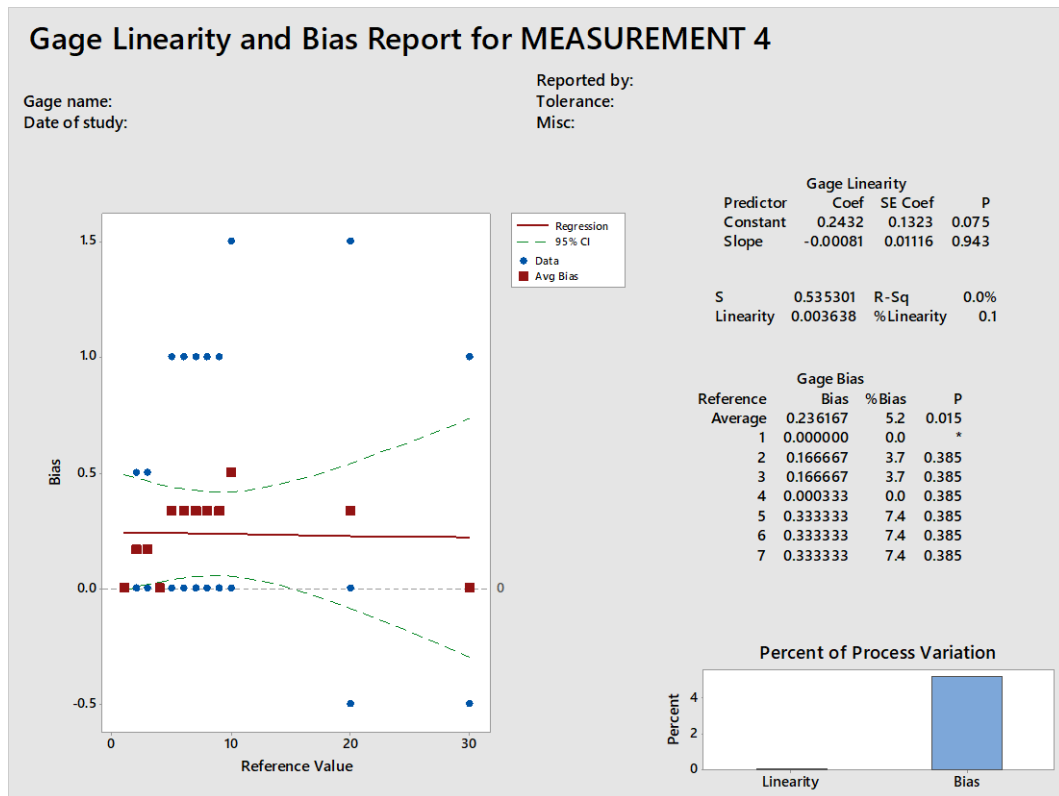


Figure C-2 Minitab 17 linearity and bias test results graph.

### C.5 Discussion of results

Figure C-2 shows the results from the linearity and bias test. The gauge was set to zero at the start of the test therefore the bias amount only indicates how far the mean of the readings is from the initial set point of zero. The majority of the data points are positive values, which has resulted in the average bias of the results being  $+0.236\mu\text{m}$ . The linearity is good through the sizes ranges and is not a problem. The linearity is used to evaluate how the average bias changes through the operating range.

## Appendix D - Supplementary information for linearity test using Z axis

### D.1 Apparatus

1. Abwood 5025 surface grinder.
2. Adjustable magnetic base.
3. Tesatronic LVDT (GT21 axial probe) and analogue meter (Tesatronic TTA 20 probe display unit).
4. Ground vee block.

### D.2 Equipment Setup

The LVDT probe was attached to the end of the magnetic base and positioned so that the probe axis was parallel to the Z axis and was perpendicular to the surface of a vee block that was held magnetically to the work table. The magnetic base was attached to the side of the wheel guard. The analogue meter was set to a scale of  $\pm 100\mu\text{m}$ .

### D.3 Method – basic linearity test

1. The surface of the vee block was cleaned with a cloth.
2. The Z axis of the grinding machine was adjusted to roughly zero the reading on the analogue meter. The fine adjustment on the analogue meter was used to set the needle to read zero. The machine DRO was set to zero.
3. The machine Z axis dial was moved  $10\mu\text{m}$ .
4. The analogue meter and DRO readings were read and recorded.
5. Steps 3 and 4 were repeated 9 more times until the machine dial had been moved  $100\mu\text{m}$ .

### D.4 Results

The measurements results are shown in Table D-1, and the linearity graph of results is shown in Figure D-1.

Table D-1 Table of results for basic linearity test

MACHINE DIAL ( $\mu\text{m}$ )	LVDT MEASUREMENT ( $\mu\text{m}$ )	DRO READING ( $\mu\text{m}$ )
2	0	+5
10	-10	+45
20	-20	+95
30	-30	+150
40	-40	+200
50	-50	+245
60	-62	+300
70	-72	+350
80	-82	+400
90	-92	+445
100	-100	+500

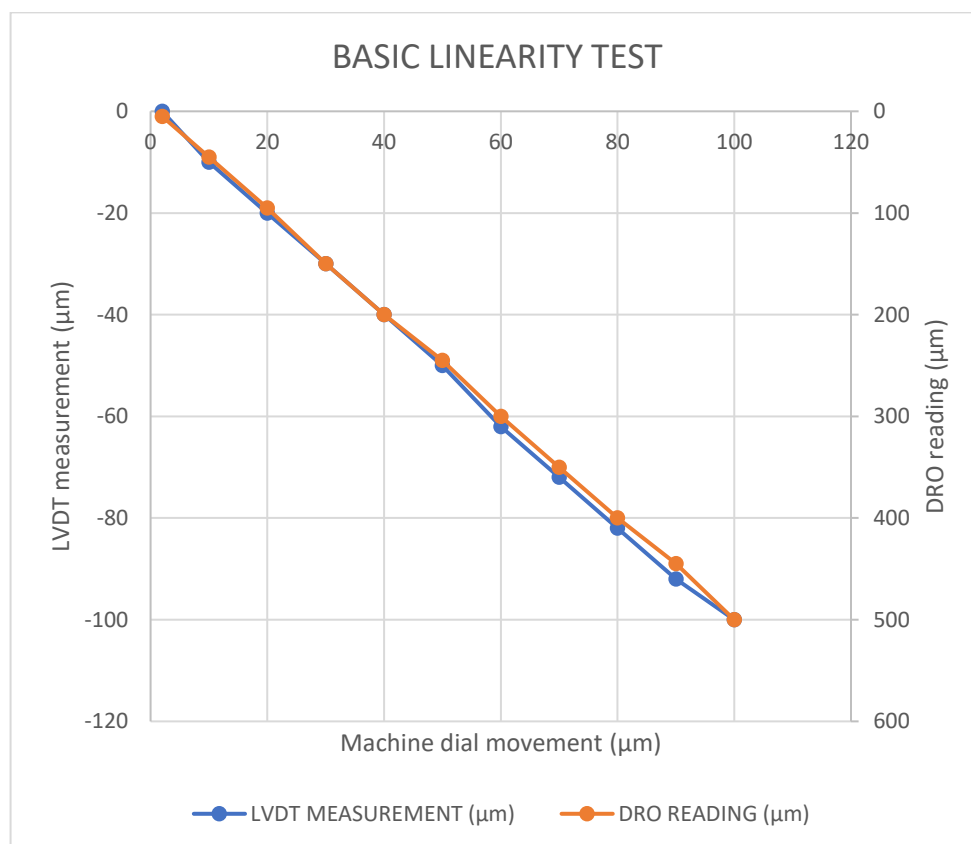


Figure D-1 Graph of results for basic linearity test

### **D.5 Discussion of results**

The results are reasonably linear. However, a major difference is that the DRO reading is 5 times greater than both the machine dial setting and the LVDT meter reading. This was caused by an incorrect setting in the DRO for the resolution of the scale that was fitted to the machine.

## **Appendix E - Supplementary information for 2 position repeatability test on the same surface by moving the Z axis**

### **E.1 Apparatus**

1. Abwood 5025 surface grinder.
2. Adjustable magnetic base.
3. Tesatronic LVDT (GT21 axial probe) and analogue meter (Tesatronic TTA 20 probe display unit).
4. Ground vee blocks.

### **E.2 Equipment Setup**

The LVDT probe was attached to the end of the magnetic base and positioned so that the probe axis was parallel to the Y axis of the machine and perpendicular to the top surface of a vee block that was held magnetically to the work table. The magnetic base was attached to the side of the wheel guard. The analogue meter was set to a scale of  $\pm 3\mu\text{m}$ . The equipment setup is shown in Figure E-1.

### **E.3 Method – Repeatability test**

1. The surface of the vee block was cleaned with a cloth.
2. The LVDT was positioned on the top surface of one of the vee blocks.
3. The DRO was zeroed for the Z axis.
4. The Y axis of the grinding machine was adjusted to roughly zero the reading on the analogue meter. The fine adjustment on the analogue meter was used to set the needle to read zero.
5. The machine Z axis was moved 5mm, then moved back to zero.
6. The analogue meter was zeroed again.
7. The machine Z axis was moved 5mm, then moved back to zero.
8. The analogue meter reading was read and recorded.
9. Steps 7 and 8 were repeated 24 more times to obtain a total of 25 repeat measurements.

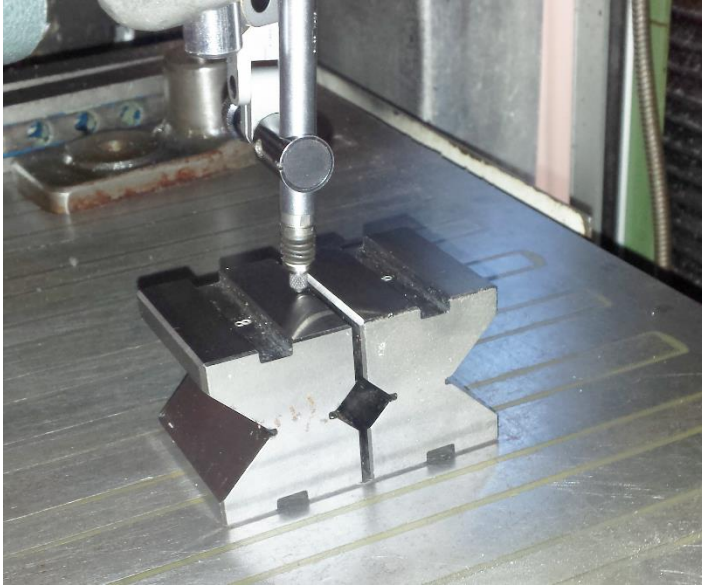


Figure E-1 Equipment setup used for repeatability test

#### **E.4 Results**

The measurements results are shown in Table E-1, and the graph showing the Minitab calculated results is shown in Figure E-2.

Table E-1 Table of results for repeatability test

RUN NUMBER	LVDT READING/ MEASUREMENT ( $\mu\text{m}$ )
1	-0.40
2	-0.60
3	-0.60
4	-0.70
5	-0.90
6	-1.10
7	-1.20
8	-1.25
9	-1.50
10	-1.60
11	-1.75
12	-1.90
13	-2.00
14	-2.20
15	-2.20
16	-2.35
17	-2.10
18	-2.50
19	-2.70
20	-2.75
21	-2.75
22	-3.00
23	-3.00
24	-2.90
25	-2.90

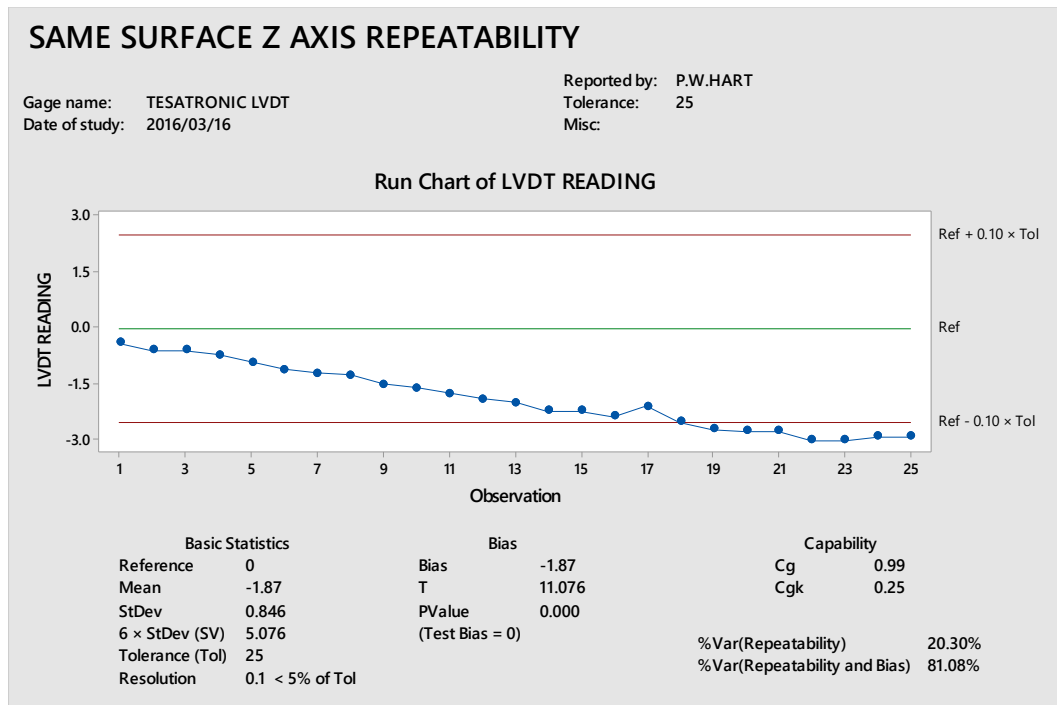


Figure E-2 Minitab 17 type 1 gage test results graph for the repeatability test on the same surface with movement of the Z axis

### E.5 Discussion of results

Figure E-2 shows the Minitab graph and calculated values for the type 1 gage test. The gauge was set to zero at the start of the test therefore the bias amount only indicates how far the mean of the readings is from the initial set point of zero. The Cg and Cgk values are below the recommended value of 1.33. This indicates that the measurement system has variation in it that is large compared to the process tolerance. The PValue is lower than the set confidence level and we can therefore conclude that the bias is significant. The %Var (Repeatability) and %Var (Repeatability and Bias) values are higher than the Minitab recommendation of 15% indicating that the variation and bias of the system is not acceptable. The results show a steady slope until the last 4 readings. The test took 25 minutes to conduct the measurement and it is possible that the equipment could have been warming up or the machine structure warming or cooling causing changes in the machine structure. It would be worthwhile repeating the test after a warmup period for both the machine and the equipment to see if this trend repeats.

## Appendix F - Supplementary information for repeatability test between two surfaces by moving the Z axis

### F.1 Apparatus

1. Abwood 5025 surface grinder.
2. Adjustable magnetic base.
3. Tesatronic LVDT (GT21 axial probe) and analogue meter (Tesatronic TTA 20 probe display unit).
4. Ground vee blocks.

### F.2 Equipment Setup

The LVDT probe was attached to the end of the magnetic base and positioned so that the probe axis was parallel to the Y axis of the machine and perpendicular to the top surface of a vee block that was held magnetically to the work table. A second vee block was positioned with a gap that allowed the LVDT probe to fully extend and release any preload. The magnetic base was attached to the side of the wheel guard. The analogue meter was set to a scale of  $\pm 10\mu\text{m}$ . The equipment setup is shown in Figure F-1.

### F.3 Method –Repeatability test

1. The surface of the vee block was cleaned with a cloth.
2. The LVDT was positioned on the top surface of one of the vee blocks.
3. The DRO was zeroed for the Z axis.
4. The Y axis of the grinding machine was adjusted to roughly zero the reading on the analogue meter. The fine adjustment on the analogue meter was used to set the needle to read zero.
5. The machine Z axis was moved 8mm so that the LVDT probe moved across the gap and on to the top surface of the other vee block.
6. The analogue meter was zeroed again.
7. The Z axis was moved back to zero.
8. The machine Z axis was moved 8mm so that the LVDT probe moved across the gap and on to the top surface of the other vee block.
9. The analogue meter reading was read and recorded.

10. The Z axis was moved back to zero.
11. The analogue meter reading was read and recorded.
12. Steps 8 and 11 were repeated 24 more times to obtain a total of 25 repeat measurements.

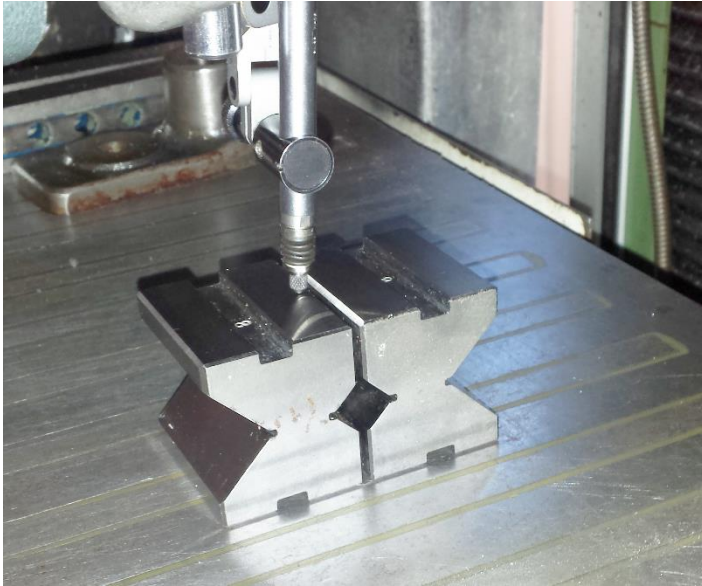


Figure F-1 Equipment setup used for repeatability test

#### **F.4 Results**

The measurements results are shown in Table F-1, and the graph showing the Minitab calculated results is shown in Figure F-2.

Table F-1 Table of results for repeatability test

RUN NUMBER	PART 1 MEASUREMENT (μm)	PART 2 MEASUREMENT (μm)
1	-3.25	0.00
2	-3.50	-0.40
3	-3.75	0.00
4	-4.00	-0.25
5	-4.00	-0.50
6	-5.00	-0.60
7	-5.00	-1.30
8	-5.50	-1.50
9	-5.50	-1.60
10	-5.50	-1.80
11	-5.50	-1.80
12	-5.80	-2.20
13	-6.00	-2.30
14	-6.00	-2.50
15	-6.20	-2.80
16	-6.30	-3.00
17	-6.30	-3.00
18	-6.50	-3.50
19	-6.50	-3.60
20	-7.00	-4.00
21	-6.80	-4.00
22	-7.20	-4.00
23	-7.00	-4.30
24	-7.50	-4.50
25	-7.60	-4.50

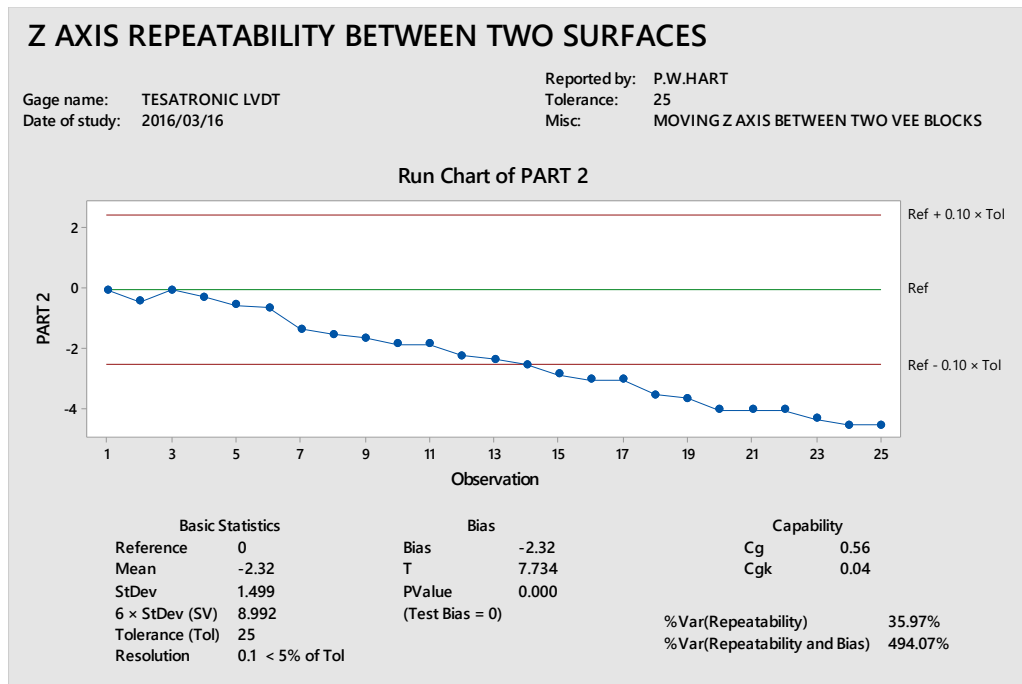


Figure F-2 Minitab 17 type 1 gage test results graph for the repeatability test between two surfaces with movement of the Z axis

### F.5 Discussion of results

Figure F-2 shows the Minitab graph and calculated values for the type 1 gage test. The gauge was set to zero at the start of the test therefore the bias amount only indicates how far the mean of the readings is from the initial set point of zero. The Cg and Cgk values are below the recommended value of 1.33. This indicates that the measurement system has variation in it that is large compared to the process tolerance. The PValue is lower than the set confidence level and we can therefore conclude that the bias is significant. The %Var (Repeatability) and %Var (Repeatability and Bias) values are higher than the Minitab recommendation of 15% indicating that the variation and bias of the system is not acceptable. The results show a steady slope, this could be caused by thermal drift of the measuring device or the grinding machine. The test took 25 minutes to conduct the measurement equipment could have been warming up or the machine structure warming or cooling causing changes in the machine structure. It would be worthwhile repeating the test after a warmup period for both the machine and the equipment to see if this trend repeats. The results are a little worse than the previous test that involved keeping the probe on the same surface. It may be that moving the probe on and off the surface of the vee block causes the magnetic base to move.

## **Appendix G - Supplementary information for repeatability test between two points on the same surface by moving the X axis**

### **G.1 Apparatus**

1. Abwood 5025 surface grinder.
2. Adjustable magnetic base.
3. Tesatronic LVDT (GT21 axial probe) and analogue meter (Tesatronic TTA 20 probe display unit).
4. Ground vee blocks.

### **G.2 Equipment Setup**

The LVDT probe was attached to the end of the magnetic base and positioned so that the probe axis was parallel to the Y axis of the machine and perpendicular to the top surface of a vee block that was held magnetically to the work table. The magnetic base was attached to the side of the wheel guard. The analogue meter was set to a scale of  $\pm 10\mu\text{m}$ . The equipment setup is shown in Figure G-1.

### **G.3 Method – Repeatability test**

1. The surface of the vee block was cleaned with a cloth.
2. The LVDT was positioned on the top surface of one of the vee blocks.
3. The DRO was zeroed for the X axis.
4. The Y axis of the grinding machine was adjusted to roughly zero the reading on the analogue meter. The fine adjustment on the analogue meter was used to set the needle to read zero.
5. The machine X axis was moved 10mm, then moved back to zero.
6. The analogue meter was zeroed again.
7. The machine X axis was moved 10mm, then moved back to zero.
8. The analogue meter reading was read and recorded.
9. Steps 7 and 8 were repeated 24 more times to obtain a total of 25 repeat measurements.

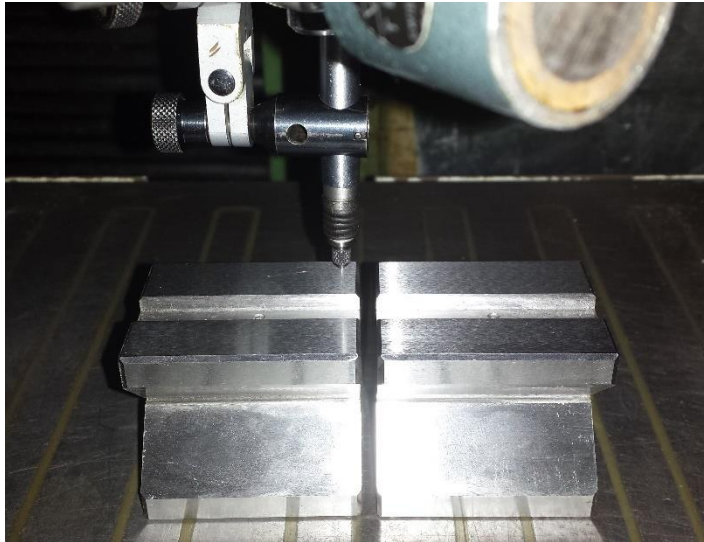


Figure G-1 Equipment setup used for repeatability test

#### **G.4 Results**

The measurements results are shown in Table G-1, and the graph showing the Minitab calculated results is shown in Figure G-2.

Table G-1 Table of results for repeatability test

RUN NUMBER	LVDT READING/ MEASUREMENT ( $\mu\text{m}$ )
1	0.0
2	0.2
3	0.0
4	-0.1
5	-0.1
6	0.0
7	0.0
8	-0.1
9	-0.2
10	0.0
11	-0.1
12	-0.1
13	0.2
14	0.2
15	-0.4
16	-0.4
17	0.0
18	-0.3
19	-0.3
20	-0.5
21	-0.5
22	-0.1
23	0.1
24	-0.5
25	-0.3

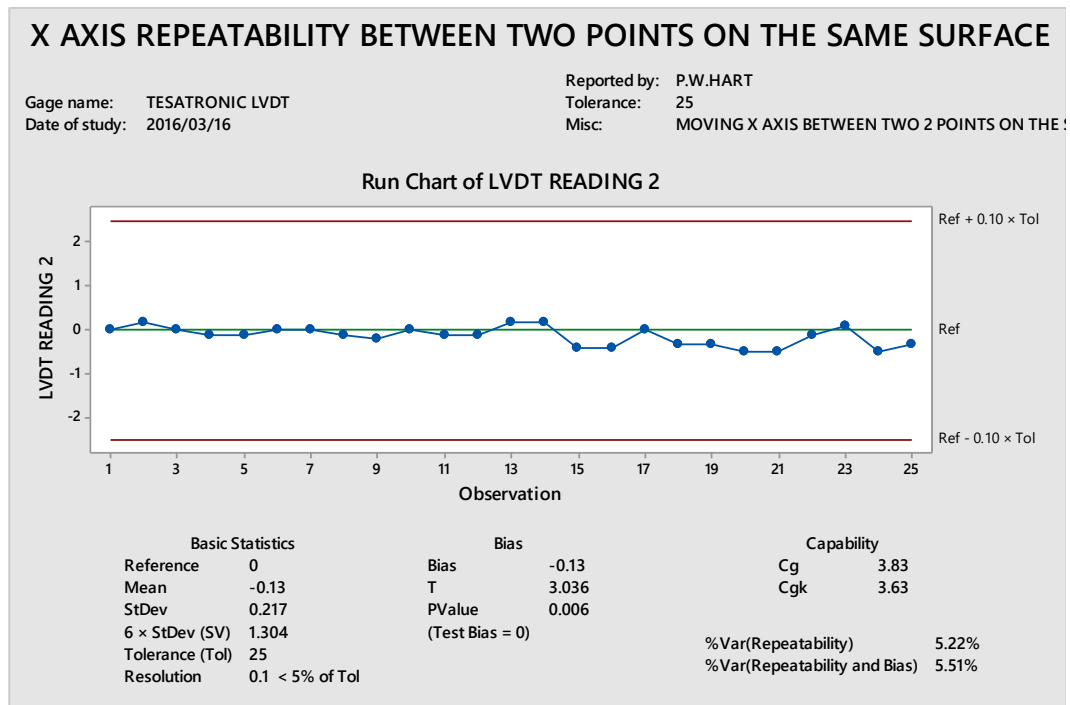


Figure G-2 Minitab 17 type 1 gage test results graph for the repeatability test on the same surface with movement of the X axis

### G.5 Discussion of results

Figure G-2 shows the Minitab graph and calculated values for the type 1 gage test. The gauge was set to zero at the start of the test therefore the bias amount only indicates how far the mean of the readings is from the initial set point of zero. The Cg and Cgk values are above the recommended value of 1.33. This indicates that the measurement system has variation in it that is acceptable when compared to the process tolerance. The PValue is lower than the set confidence level and we can therefore conclude that the bias is significant. The % Var (Repeatability) and % Var (Repeatability and Bias) values are lower than the Minitab recommendation of 15% indicating that the variation and bias of the system is acceptable. This test did not show a significant steady slop as was observed in the Z axis test. This could be that the thermal drift of the measuring equipment or the machine structure has stopped. It could also indicate that the drift in results for the Z axis test is caused by the movement of the Z axis its self.

## **Appendix H - Supplementary information for repeatability test between two surfaces by moving the X axis**

### **H.1 Apparatus**

1. Abwood 5025 surface grinder.
2. Adjustable magnetic base.
3. Tesatronic LVDT (GT21 axial probe) and analogue meter (Tesatronic TTA 20 probe display unit).
4. Ground vee blocks.

### **H.2 Equipment Setup**

The LVDT probe was attached to the end of the magnetic base and positioned so that the probe axis was parallel to the Y axis of the machine and perpendicular to the top surface of a vee block that was held magnetically to the work table. A second vee block was positioned with a gap that allowed the LVDT probe to fully extend and release any preload. The magnetic base was attached to the side of the wheel guard. The analogue meter was set to a scale of  $\pm 10\mu\text{m}$ . The equipment setup is shown in Figure H-1.

### **H.3 Method – Repeatability test**

1. The surface of the vee block was cleaned with a cloth.
2. The LVDT was positioned on the top surface of one of the vee blocks.
3. The DRO was zeroed for the X axis.
4. The Y axis of the grinding machine was adjusted to roughly zero the reading on the analogue meter. The fine adjustment on the analogue meter was used to set the needle to read zero.
5. The machine X axis was moved 30mm so that the LVDT probe moved across the gap and on to the top surface of the other vee block.
6. The analogue meter was zeroed again.
7. The X axis was moved back to zero.
8. The machine X axis was moved 30mm so that the LVDT probe moved across the gap and on to the top surface of the other vee block.
9. The analogue meter reading was read and recorded.

10. The X axis was moved back to zero.
11. The analogue meter reading was read and recorded.
12. Steps 8 and 11 were repeated 24 more times to obtain a total of 25 repeat measurements.

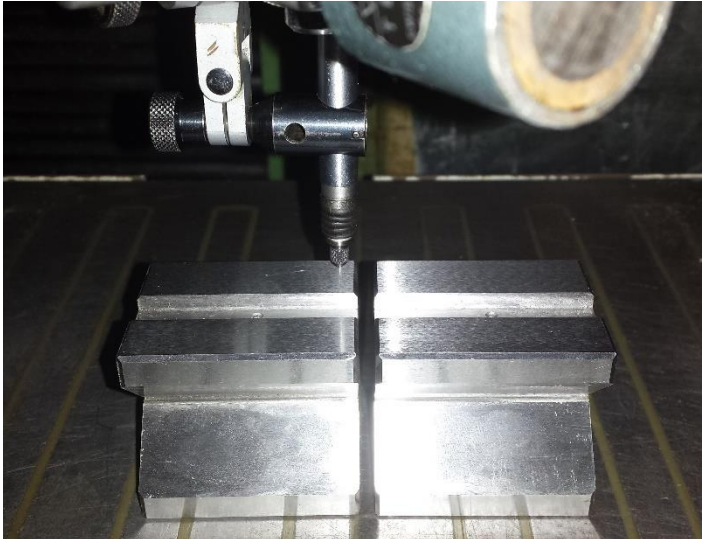


Figure H-1 Equipment setup used for repeatability test

#### **H.4 Results**

The measurements results are shown in Table H-1, and the graph showing the Minitab calculated results is shown in Figure H-2.

Table H-1 Table of results for repeatability test

RUN NUMBER	PART 1 MEASUREMENT (μm)	PART 2 MEASUREMENT (μm)
1	0.0	-4.3
2	0.0	-5.0
3	0.1	-4.7
4	-0.5	-4.5
5	-0.2	-2.8
6	-0.3	-4.8
7	-0.4	-5.0
8	-0.6	-5.0
9	-0.3	-4.5
10	-0.4	-5.0
11	-0.5	-5.0
12	-0.6	-5.2
13	-0.5	-5.5
14	-0.2	-5.5
15	-0.6	-5.5
16	-0.3	-5.5
17	0.0	-5.5
18	-0.6	-5.5
19	-0.4	-5.8
20	-0.5	-5.8
21	-0.4	-5.6
22	-0.5	-6.0
23	-0.6	-5.5
24	-0.5	-5.6
25	-0.6	-6.0

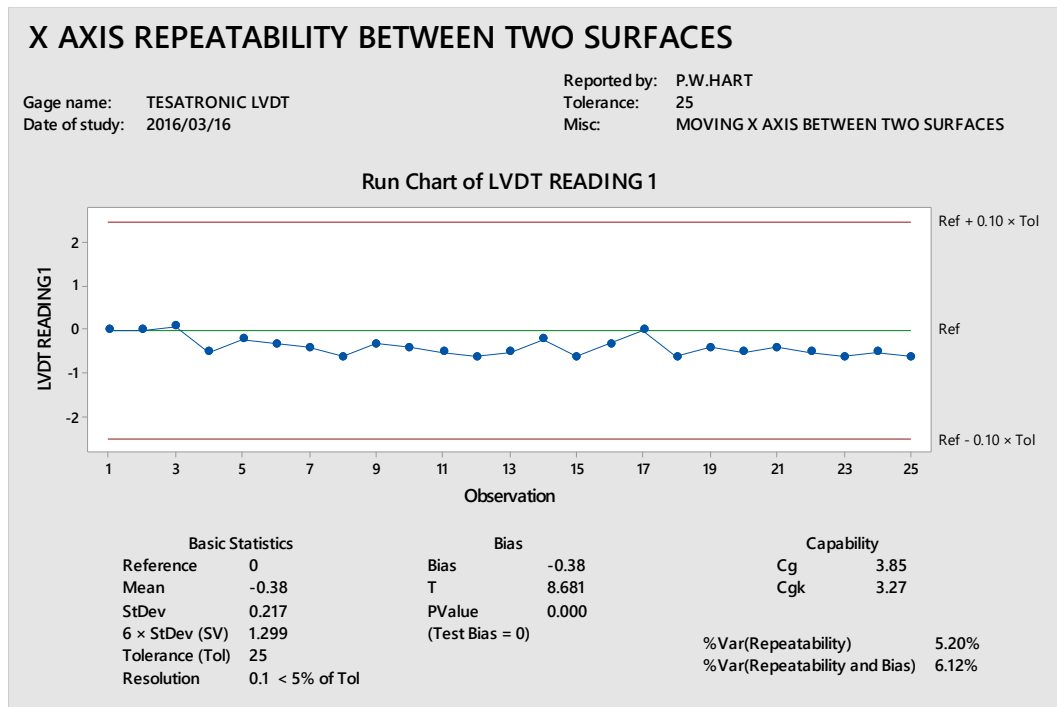


Figure H-2 Minitab 17 type 1 gage test results graph for the repeatability test between two surfaces with movement of the X axis

### H.5 Discussion of results

Figure H-2 shows the Minitab graph and calculated values for the type 1 gage test. The gauge was set to zero at the start of the test therefore the bias amount only indicates how far the mean of the readings is from the initial set point of zero. The Cg and Cgk values are above the recommended value of 1.33. This indicates that the measurement system has variation in it that is small compared to the process tolerance. The PValue is lower than the set confidence level and we can therefore conclude that the bias is significant. The %Var (Repeatability) and %Var (Repeatability and Bias) values are lower than the Minitab recommendation of 15% indicating that the variation and bias of the system is acceptable.

**Appendix I - Supplementary information for repeatability test  
between two points on the same surface moving the Z axis  
using two LVDT probes**

**I.1 Apparatus**

1. Abwood 5025 surface grinder.
2. Adjustable magnetic base.
3. Two Tesatronic LVDTs (GT21 axial probe) and analogue meter (Tesatronic TTA 20 probe display unit).
4. Ground vee blocks.

**I.2 Equipment Setup**

The two LVDT probes were attached to the end of the magnetic base and positioned so that the probe axes were parallel to the Y axis of the machine and perpendicular to the top surface of a vee block that was held magnetically to the work table. The magnetic base was attached to the side of the wheel guard. The analogue meter was set to a scale of  $\pm 10\mu\text{m}$ . The equipment setup is shown in Figure I-1. The analogue meter was turned on 2.5 hours before the test started.

**I.3 Method**

1. The surface of the vee block was cleaned with a cloth.
2. The two LVDTs were positioned on the top surface of the vee block.
3. The DRO was zeroed for the Z axis.
4. The Y axis of the grinding machine was adjusted to roughly zero the reading on the analogue meter. The fine adjustment on the analogue meter was used to set the needle to read zero.
5. The machine Z axis was moved 5mm using the handwheel dial, then moved back to zero.
6. The analogue meter was zeroed again.
7. The analogue meter reading was read and recorded.
8. The machine Z axis was moved 5mm using the handwheel dial.
9. The analogue meter reading was read and recorded.

10. The machine Z axis was moved back to zero using the handwheel dial.
11. Steps 7 and 10 were repeated 24 more times to obtain a total of 25 repeat measurements.

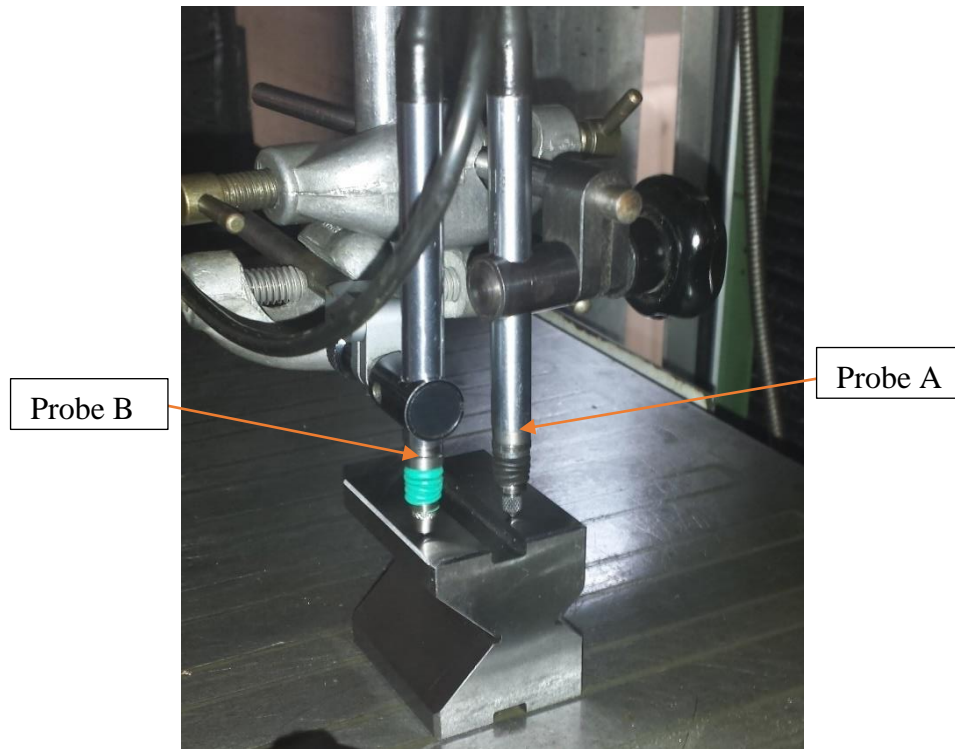


Figure I-1 Equipment setup used for repeatability test

#### **I.4 Results**

The measurements results are shown in Table I-1, and graphs showing the Minitab calculated results is shown in Figure I-2 to Figure I-7.

Table I-1 Table of results for repeatability test

RUN NUMBER	PROBE A POSITION 1 (μm)	PROBE B POSITION 1 (μm)	PROBE A POSITION 2 (μm)	PROBE B POSITION 2 (μm)
1	0	0	5	4
2	-0.5	-0.3	4.75	3.75
3	-0.5	-0.5	4.5	3.5
4	-1	-0.8	4.4	3.4
5	-1	-0.8	4.1	3.2
6	-1	-0.9	4	3
7	-1.2	-1	4	3
8	-1.5	-1.4	3.8	2.8
9	-1.5	-1.3	3.7	2.7
10	-1.5	-1.3	3.7	2.5
11	-1.6	-1.5	3.6	2.5
12	-1.7	-1.5	3.5	2.4
13	-1.8	-1.6	3.5	2.4
14	-1.9	-1.7	3.3	2.2
15	-2	-1.8	3.3	2.2
16	-2	-1.8	3.2	2.1
17	-2	-1.9	3.2	2
18	-2	-2	3.1	2
19	-2.1	-2.1	3	1.9
20	-2.2	-2.2	3	1.8
21	-2.2	-2.2	2.9	1.8
22	-2.3	-2.3	2.8	1.7
23	-2.3	-2.2	2.8	1.6
24	-2.4	-2.3	2.7	1.5
25	-2.3	-2.3	2.6	1.5

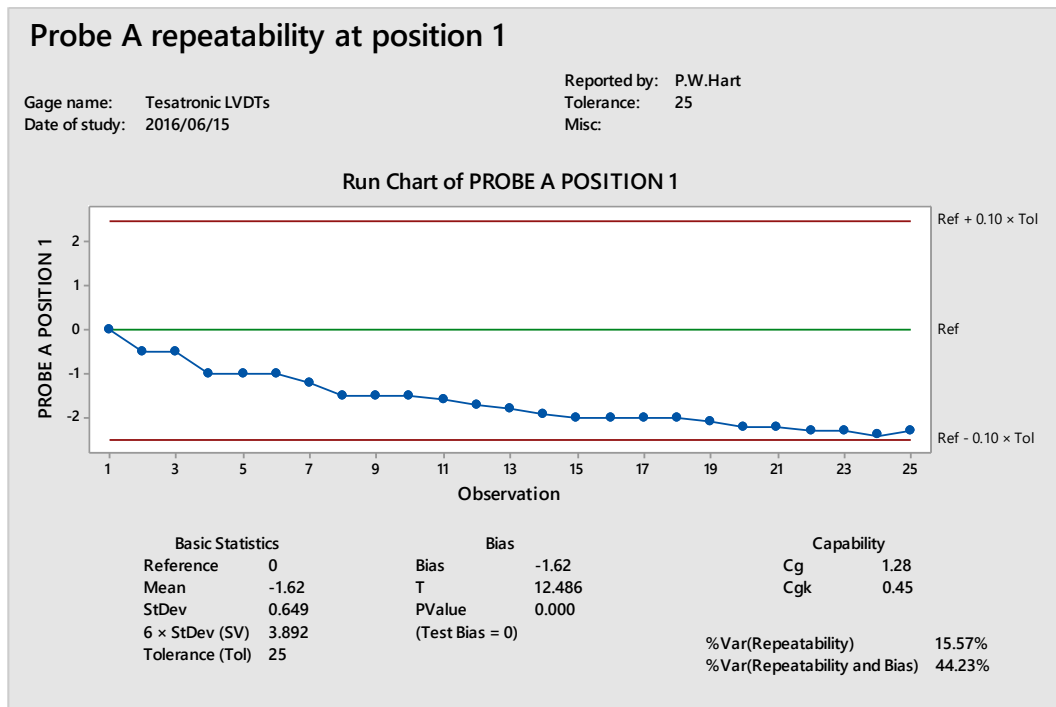


Figure I-2 Minitab 17 type 1 gage test results graph for Probe A repeatability position 1

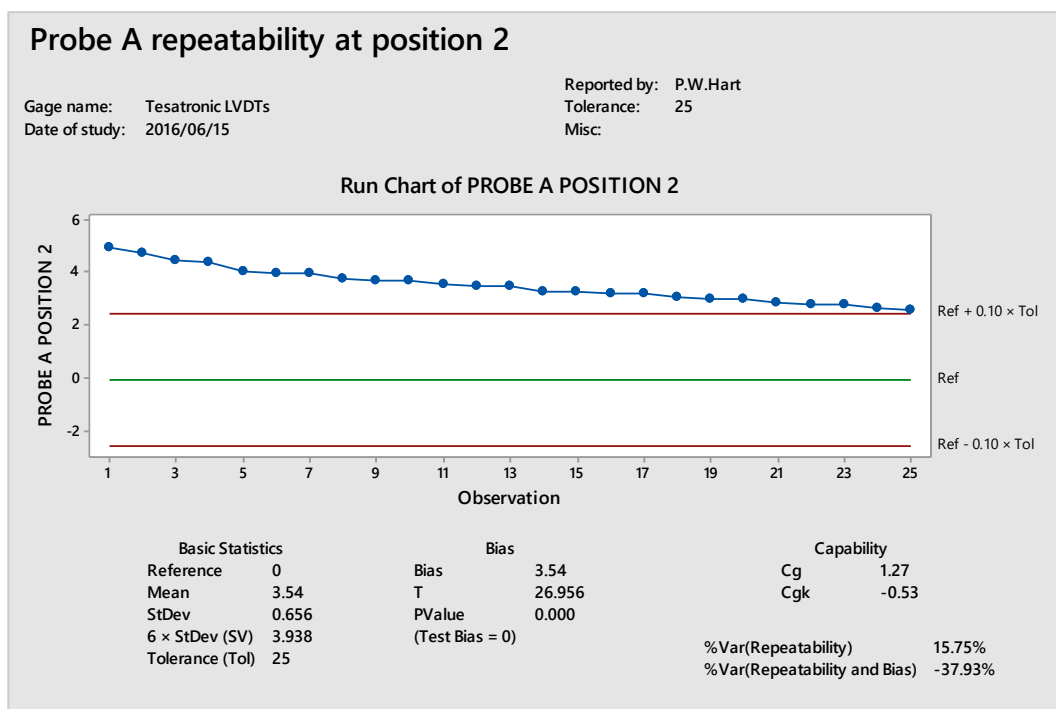


Figure I-3 Minitab 17 type 1 gage test results graph for Probe A repeatability position 2

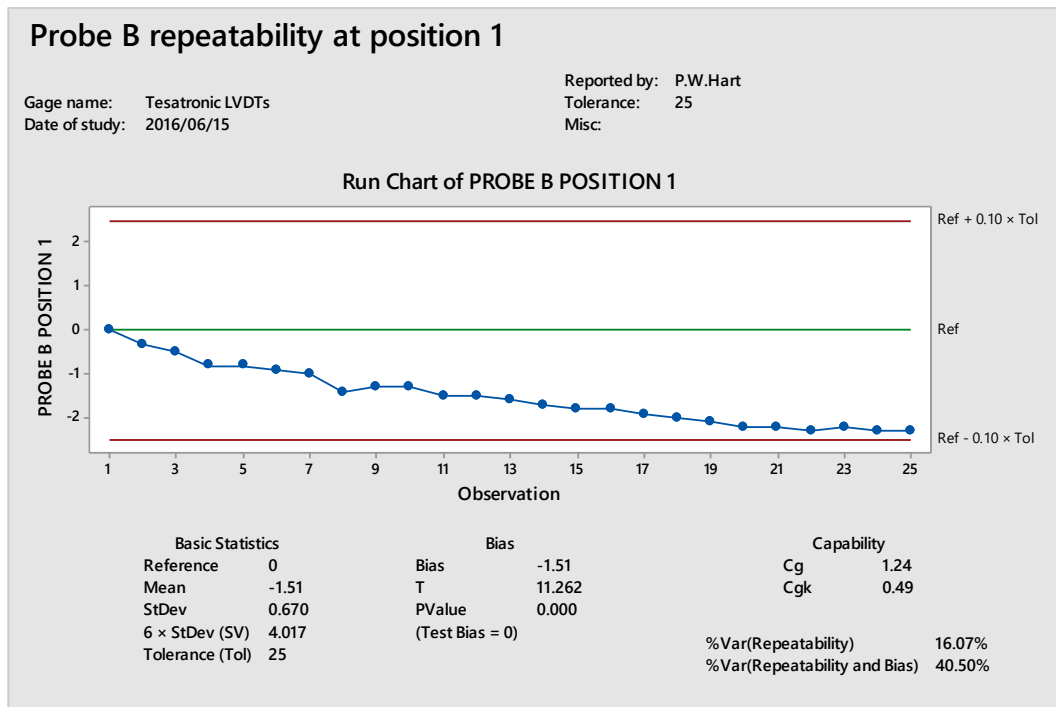


Figure I-4 Minitab 17 type 1 gage test results graph for Probe B repeatability position 1

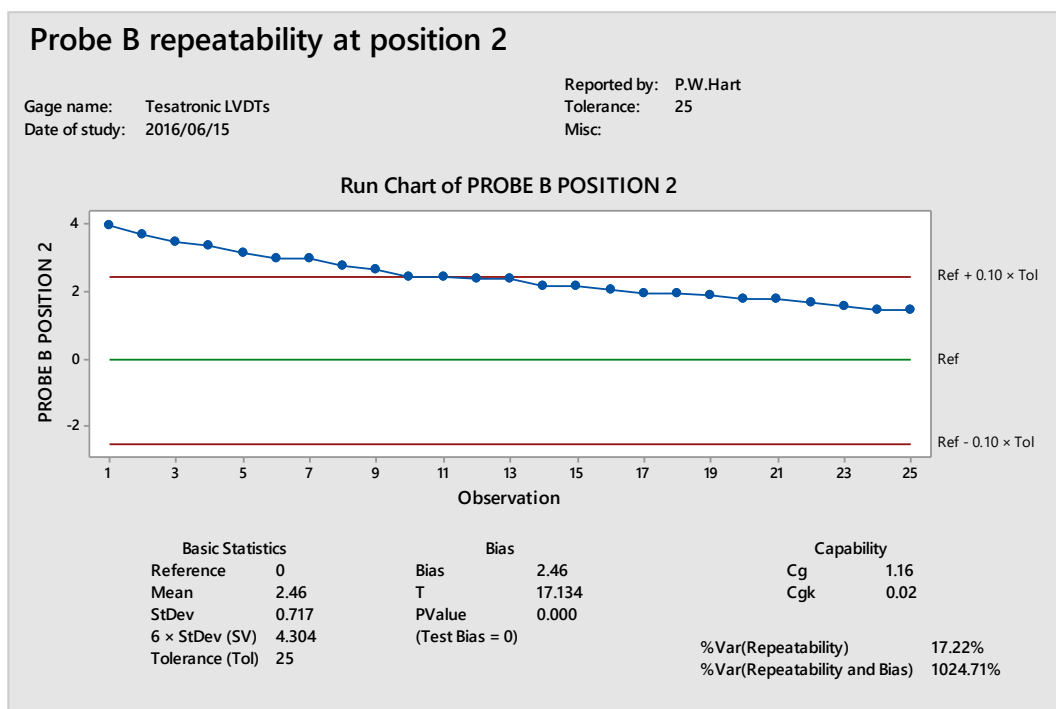


Figure I-5 Minitab 17 type 1 gage test results graph for Probe B repeatability position 2

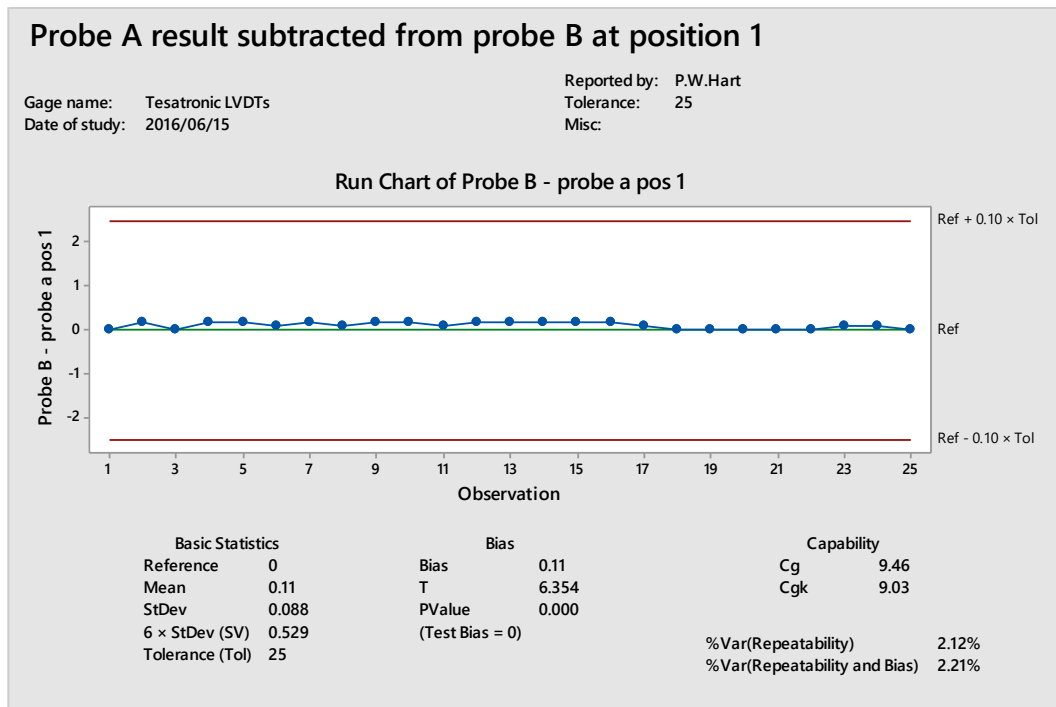


Figure I-6 Minitab 17 type 1 gage test results graph for repeatability by moving the Z axis, assessed by subtracting Probe A result from Probe B result at position 1

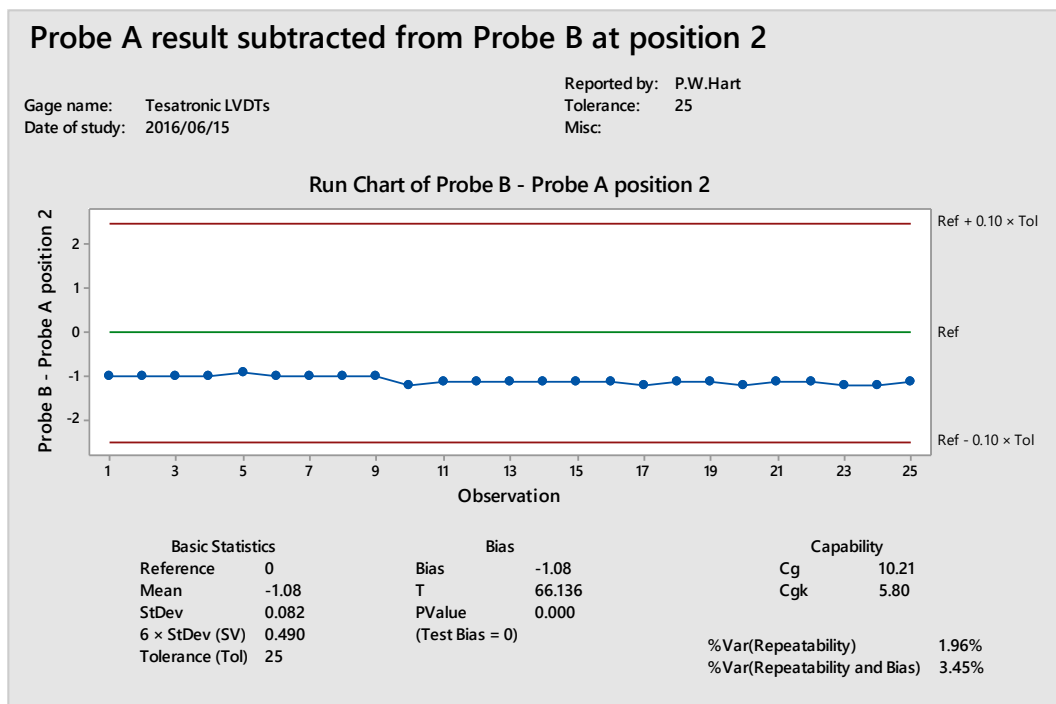


Figure I-7 Minitab 17 type 1 gage test results graph for repeatability by moving the Z axis, assessed by subtracting Probe A result from Probe B result at position 2

### **I.5 Discussion of results**

The results shown in Figure I-2, Figure I-3, Figure I-4 and Figure I-5 for the individual probes in both positions all show drift in the results. Each of these results on their own fail to meet the recommended requirements.

Figure I-6 shows the Minitab graph and calculated values for the type 1 gage test after the results recorded from probe A has been subtracted from that for probe B at position 1. The gauge was set to zero at the start of the test therefore the bias amount only indicates how far the mean of the readings is from the initial set point of zero at position 1. Position 2 has a small bias as the surface of the vee block is not parallel to the Z axis movement. The Cg and Cgk values are above the recommended value of 1.33. This indicates that the measurement system has small variation in it compared to the process tolerance. The PValue is lower than the set confidence level and we can therefore conclude that the bias is significant. The %Var (Repeatability) and %Var (Repeatability and Bias) values are significantly lower than the Minitab recommendation of 15% indicating that the variation and bias of the system is acceptable. The steady slope observed in the individual probes has been removed.

A similar result is seen in Figure I-7 for position 2.

## Appendix J - Supplementary information for repeatability between two surfaces moving the Z axis using two LVDT probes

### J.1 Apparatus

1. Abwood 5025 surface grinder.
2. Adjustable magnetic base.
3. Two Tesatronic LVDT (GT21 axial probe) connected to an analogue meter (Tesatronic TTA 20 probe display unit).
4. Ground vee blocks.

### J.2 Equipment Setup

The LVDT probe was attached to the end of the magnetic base and positioned so that the probe axis was parallel to the Y axis of the machine and perpendicular to the top surface of a vee block that was held magnetically to the work table. A second vee block was positioned with a gap that allowed the LVDT probe to fully extend and release any preload. The magnetic base was attached to the side of the wheel guard. The analogue meter was set to a scale of  $\pm 10\mu\text{m}$ . The equipment setup is shown in Figure J-1. The analogue meter was turned on 3 hours before the test started.

### J.3 Method

1. The surface of the vee block was cleaned with a cloth.
2. The LVDT was positioned on the top surface of one of the vee blocks.
3. The DRO was zeroed for the Z axis.
4. The Y axis of the grinding machine was adjusted to roughly zero the reading on the analogue meter. The fine adjustment on the analogue meter was used to set the needle to read zero.
5. The machine Z axis was moved 12mm so that the LVDT probe moved across the gap and on to the top surface of the other vee block.
6. The Z axis was moved back to zero.
7. The machine Z axis was moved 12mm so that the LVDT probe moved across the gap and on to the top surface of the other vee block.
8. The analogue meter reading was read and recorded.

9. The Z axis was moved back to zero.
10. The analogue meter reading was read and recorded.
11. Steps 7 to 10 were repeated 24 more times to obtain a total of 25 repeat measurements.

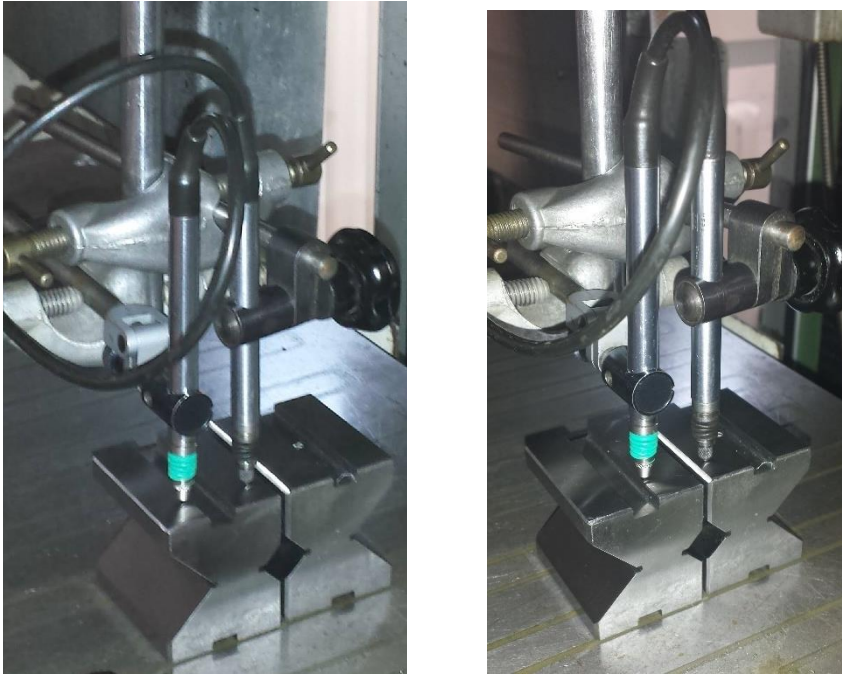


Figure J-1 Equipment setup used for repeatability test. Position 1 left picture and position 2 right picture.

#### **J.4 Results**

The measurements results are shown in Table J-1, and the graph showing the Minitab calculated results is shown in Figure J-2 to Figure J-7.

Table J-1 Table of results for repeatability test

RUN NUMBER	PROBE A POSITION 1 (μm)	PROBE B POSITION 1 (μm)	PROBE A POSITION 2 (μm)	PROBE B POSITION 2 (μm)
1	-1.5	-1.4	5.1	-2.5
2	-1.8	-1.8	4.2	-3.3
3	-2.5	-2.5	3.5	-4
4	-2.8	-2.9	3	-4.4
5	-3	-3	3	-4.4
6	-2.8	-2.8	2.6	-4.8
7	-3	-3	2.5	-5
8	-3	-3	2.3	-5.2
9	-3.5	-3.5	2.4	-5.2
10	-3.3	-3.4	2.3	-5.3
11	-3.6	-3.6	2.3	-5.3
12	-4	-4	2.1	-5.5
13	-3.9	-3.9	2	-5.5
14	-4	-4	1.8	-5.7
15	-4.1	-4.1	1.6	-5.9
16	-4.3	-4.3	1.6	-5.9
17	-4.1	-4.1	1.5	-6
18	-4.1	-4	1.6	-5.9
19	-4	-3.9	1.6	-5.9
20	-4.1	-4	1.6	-5.9
21	-4.4	-4.2	1.5	-6
22	-4	-4.3	1.5	-6
23	-4.5	-4.1	1.8	-5.5
24	-4.3	-4	1.8	-5.6
25	-4.1	-3.9	1.8	-5.6

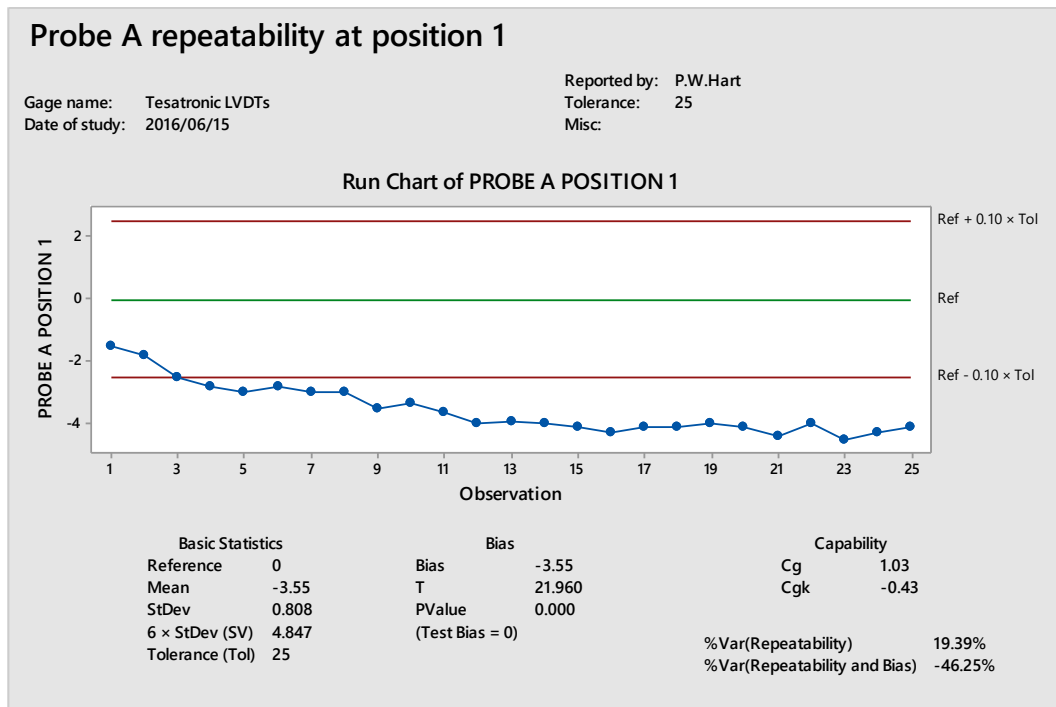


Figure J-2 Minitab 17 type 1 gage test results graph for Probe A repeatability position 1

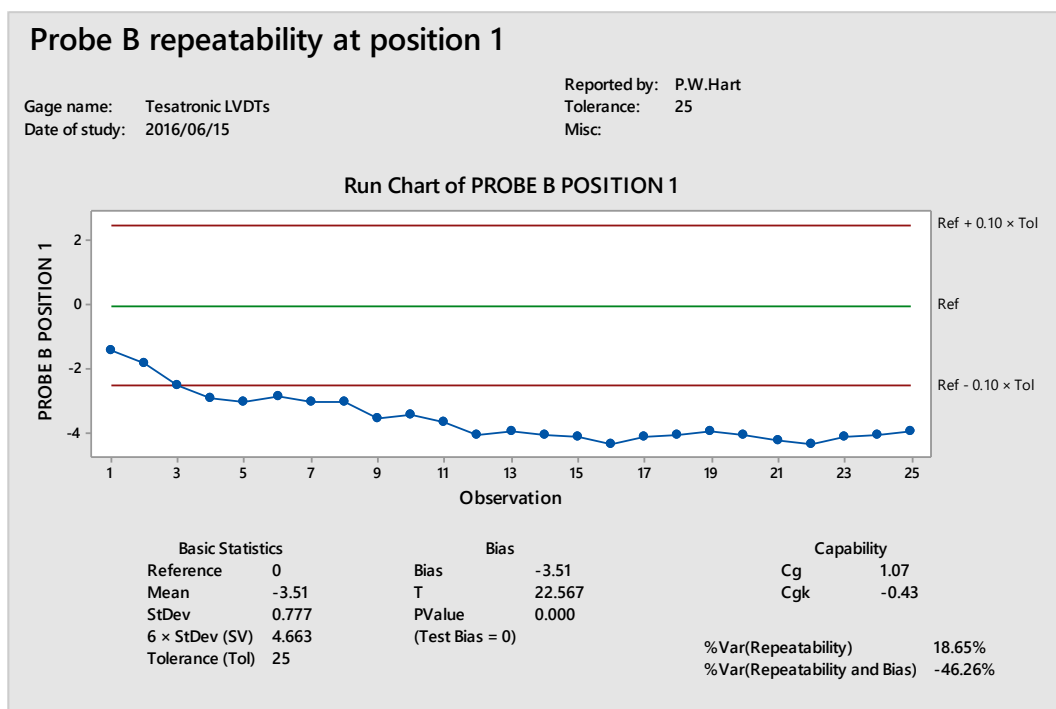


Figure J-3 Minitab 17 type 1 gage test results graph for Probe B repeatability position 1

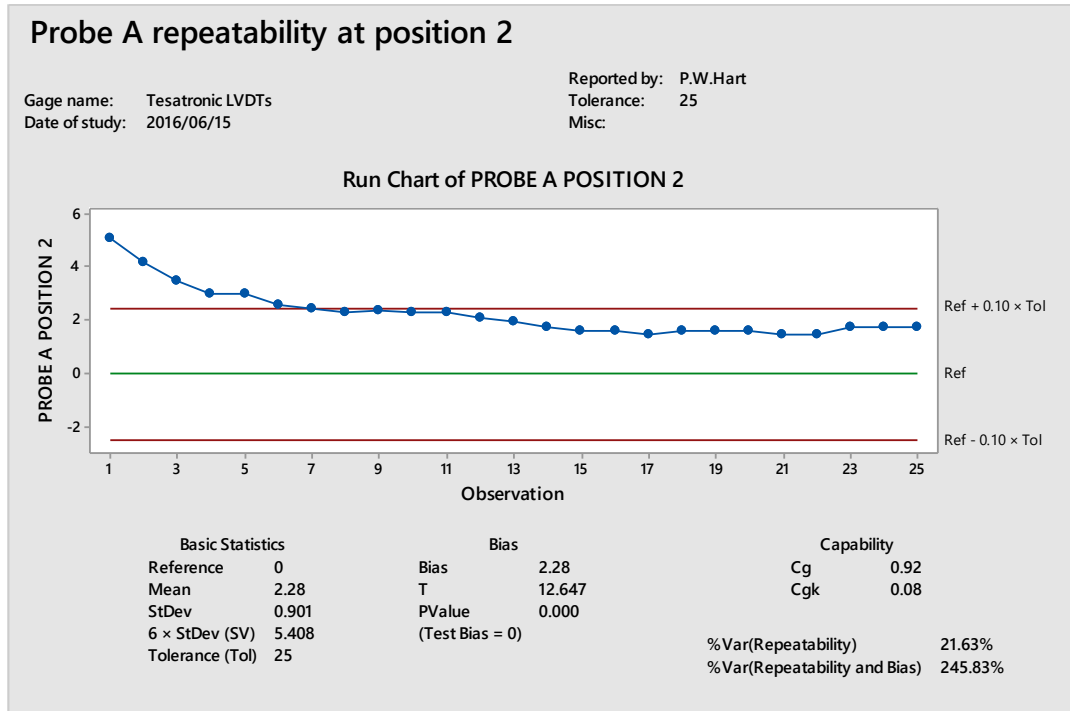


Figure J-4 Minitab 17 type 1 gage test results graph for Probe A repeatability position 2

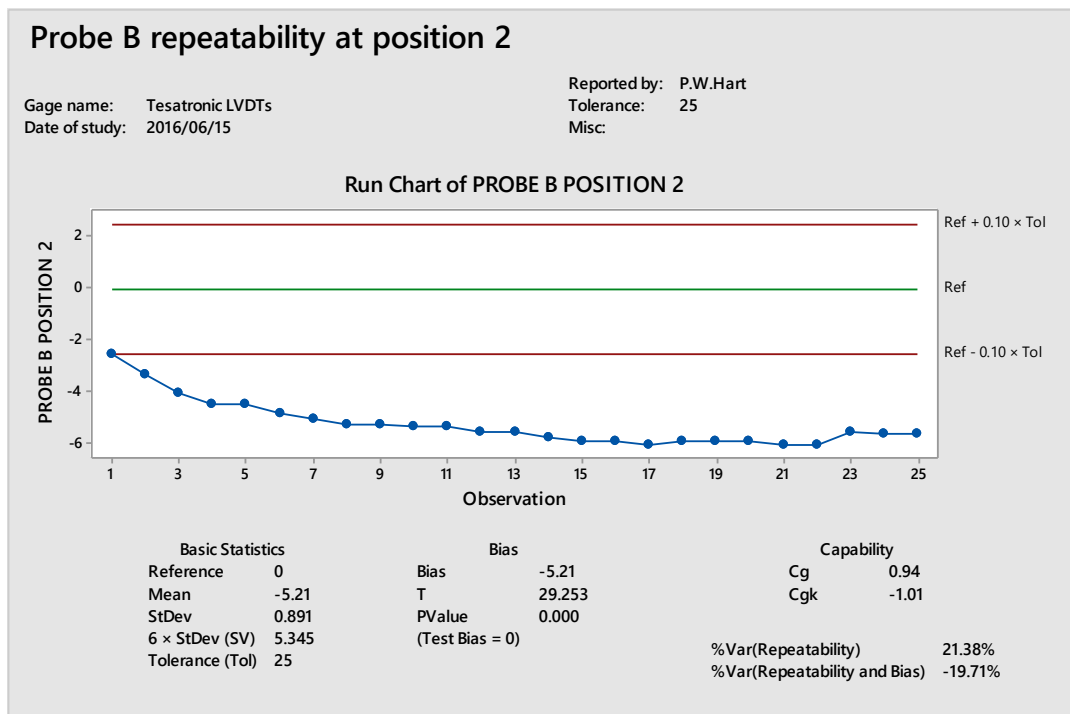


Figure J-5 Minitab 17 type 1 gage test results graph for Probe B repeatability position 2

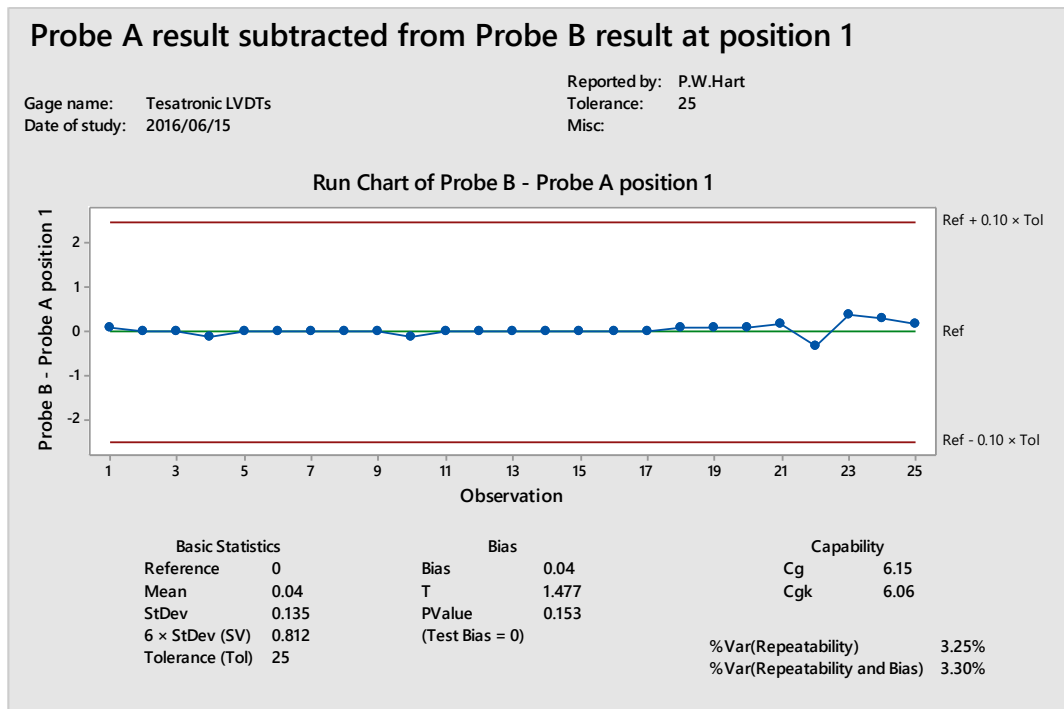


Figure J-6 Minitab 17 type 1 gage test results graph for repeatability by moving the Z axis between two surfaces assessed by subtracting Probe A result from Probe B result at position 1

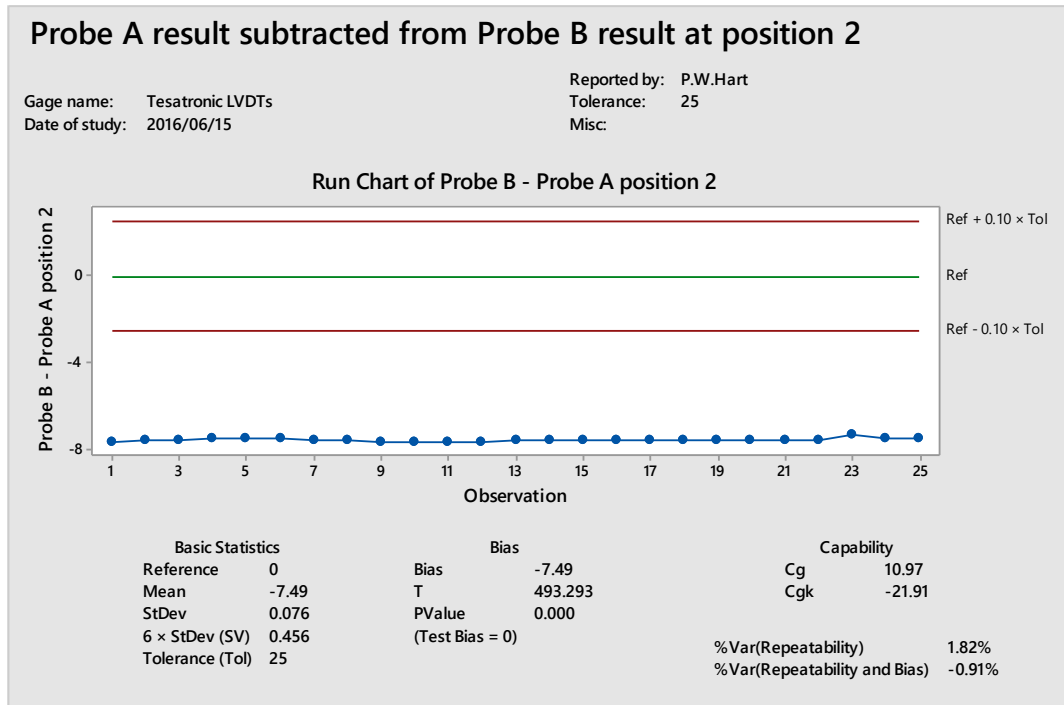


Figure J-7 Minitab 17 type 1 gage test results graph for repeatability by moving the Z axis between two surfaces assessed by subtracting Probe A result from Probe B result at position 2

### **J.5 Discussion of results**

The results shown in Figure J-2, Figure J-3, Figure J-4 and Figure J-5 for the individual probes in both positions all show drift in the results. Each of these results on their own fail to meet the recommended requirements.

Figure J-6 shows the Minitab graph and calculated values for the type 1 gage test after the results recorded from probe A has been subtracted from that for probe B at position 1. The gauge was set to zero at the start of the test therefore the bias amount only indicates how far the mean of the readings is from the initial set point of zero. The Cg and Cgk values are above the recommended value of 1.33. This indicates that the measurement system has small variation in it compared to the process tolerance. The PValue is higher than the set confidence level and we can therefore conclude that the bias is not significant. The %Var (Repeatability) and %Var (Repeatability and Bias) values are significantly lower than the Minitab recommendation of 15% indicating that the variation and bias of the system is acceptable. The steady slope observed in the individual probes has been removed.

A similar result is seen in Figure J-7 for position 2, however the results show significant bias due to the reading not being zeroed at that position at the start of the test.

## Appendix K - Supplementary information for dynamometer calibration

### K.1 Equipment

1. Kistler dynamometer 9257A.
2. Kistler Charge amplifier 5073
3. 24v power supply
4. PC with Labview 2014 and NI PCI 6250 DAQ card
5. Bench mounted pulley
6. 1 Kg and 0.5Kg known masses
7. Nylon rope load rating 18.1 KG.

The equipment used for the dynamometer calibration is shown in Figure K-1. Figure K-2, Figure K-3 and Figure K-4 show the orientation of the dynamometer on the grinding machine table and the position of the nylon rope on the test piece for the calibration of the X axis.

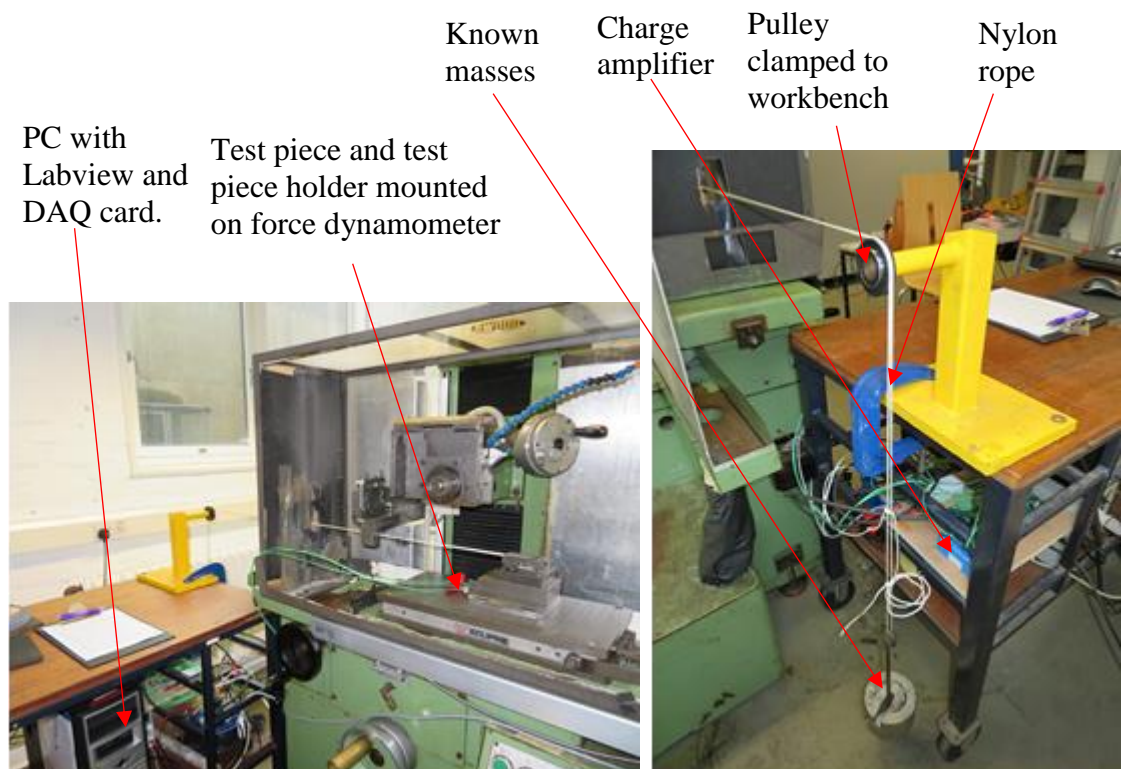


Figure K-1 Equipment arrangement used for dynamometer calibration

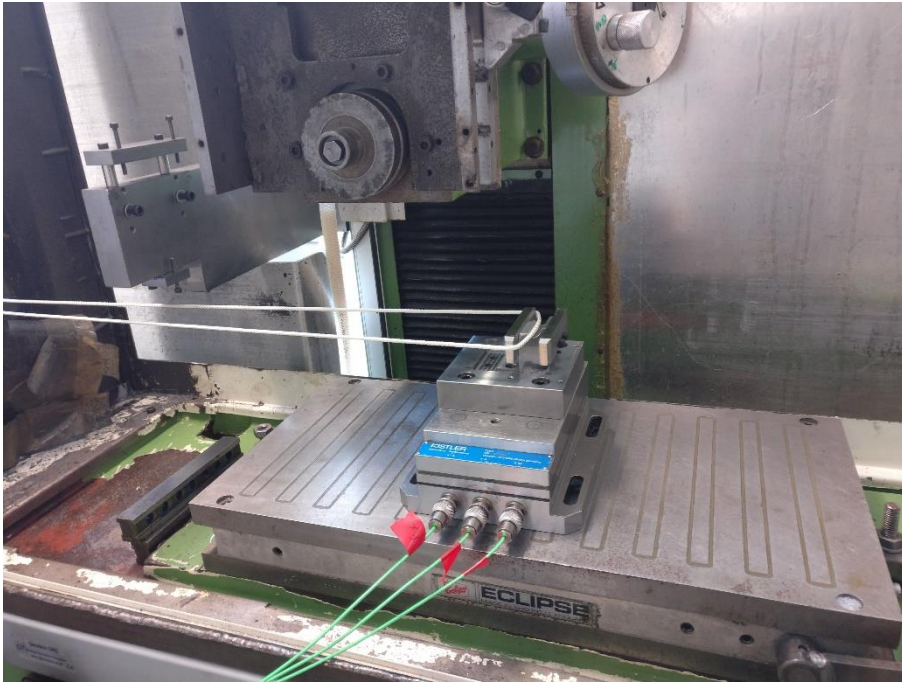


Figure K-2 X axis positive direction loading

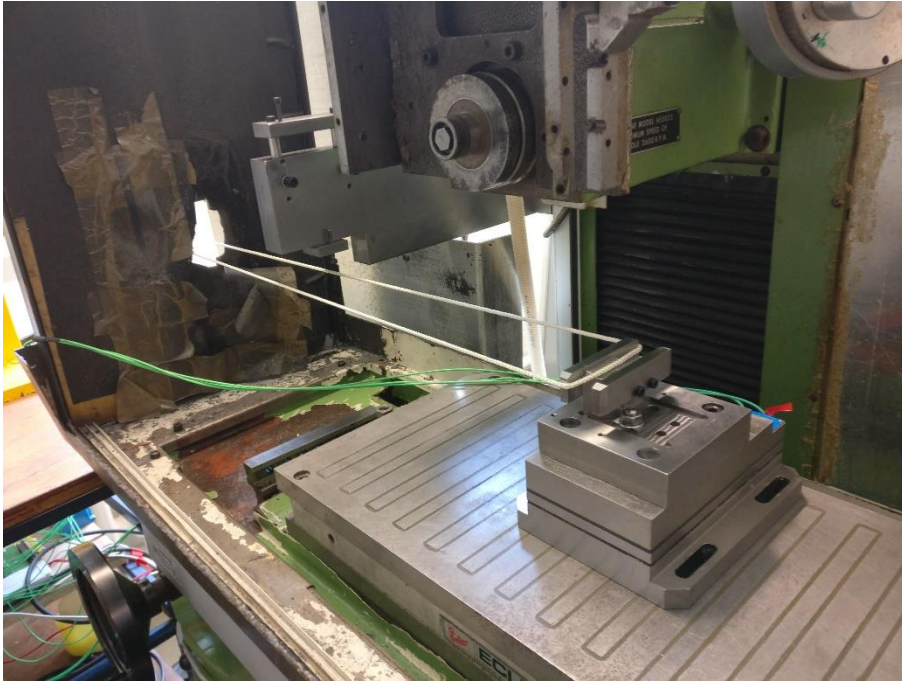


Figure K-3 X axis negative direction loading

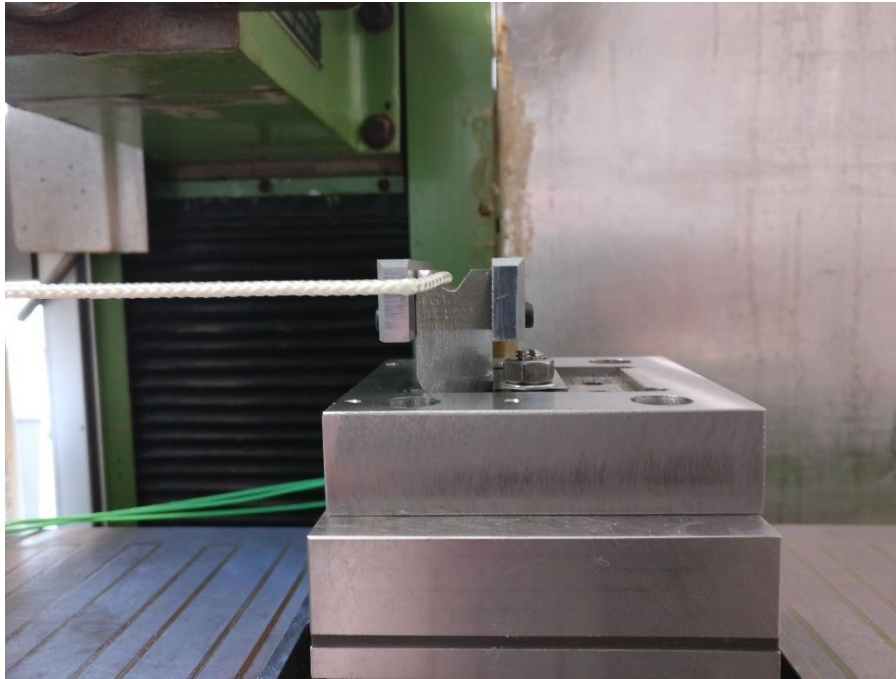


Figure K-4 X axis negative direction loading rope position on test piece.

The nylon rope was attached to the workpiece at a height above the dynamometer where the grinding forces between the grinding wheel and test piece would be present.

## **K.2 Method**

### **K.2.1 X axis calibration**

1. The rope was attached to the workpiece at the same height from the dynamometer mounting surface that the grinding forces between the test piece and the grinding wheel would act.
2. The rope was fed through the side of the machine enclosure and over the bench mounted pulley. Care was taken to ensure that the rope did not touch the sides of the hole on the enclosure.
3. The charge amplifier was turned on and the DAQ set to record data to file at 1KHz.
4. The reading was allowed to settle for 10 seconds and then the readings on the Labview VI was recorded.
5. A 0.5Kg mass was added to the end of the rope.
6. The reading was allowed to settle for 10 seconds and then the readings on the Labview VI was recorded.
7. Steps 5 and 6 were repeated until a total of 10Kg was reached.
8. A 0.5Kg mass was removed from the end of the rope.

9. The reading was allowed to settle for 10 seconds and then the readings on the Labview VI was recorded.
10. Steps 8 and 9 were repeated until all masses had been removed.
11. The DAQ system was set to stop recording.
12. The Dynamometer was turned 180° so that the force from the masses acted in the opposite direction.
13. Steps 1 and 11 were repeated.

### **K.2.2 Y axis calibration**

1. The rope was attached to the workpiece at the same height from the dynamometer mounting surface that the grinding forces between the test piece and the grinding wheel would act.
2. The rope was fed through the side of the machine enclosure and over the bench mounted pulley. Care was taken to ensure that the rope did not touch the sides of the hole on the enclosure.
3. The charge amplifier was turned on and the DAQ set to record data to file at 1KHz.
4. The reading was allowed to settle for 10 seconds and then the readings on the Labview VI was recorded.
5. A 0.5Kg mass was added to the end of the rope.
6. The reading was allowed to settle for 10 seconds and then the readings on the Labview VI was recorded.
7. Steps 5 and 6 were repeated until a total of 10Kg was reached.
8. A 0.5Kg mass was removed from the end of the rope.
9. The reading was allowed to settle for 10 seconds and then the readings on the Labview VI was recorded.
10. Steps 8 and 9 were repeated until all masses had been removed.
11. The DAQ system was set to stop recording.

### **K.2.3 Z axis calibration**

1. The charge amplifier was turned on and the DAQ set to record data to file at 1KHz.
2. The reading was allowed to settle for 10 seconds and then the readings on the Labview VI was recorded.
3. A 0.5Kg mass was added on top of the test piece.
4. The reading was allowed to settle for 10 seconds and then the readings on the Labview VI was recorded.

5. Steps 3 and 4 were repeated until a total of 10Kg was reached.
6. A 0.5Kg mass was removed from the top of the test piece.
7. The reading was allowed to settle for 10 seconds and then the readings on the Labview VI was recorded.
8. Steps 6 and 7 were repeated until all masses had been removed.
9. The DAQ system was set to stop recording.

### **K.3 Results**

Table K-1, Table K-2, Table K-3 and Table K-4 show the recorded results from the test. Figure K-7, Figure K-8, Figure K-9 and Figure K-10 graphs of the recorded results.

Table K-1 readings recorded for X axis negative direction.

Mass (kg)	Force (N)	Voltage (mV)	Mass (kg)	Force (N)	Voltage (mV)
0	0	7.8	9.5	93.15225	-176.4
0.5	4.90275	-3.3	9	88.2495	-166.2
1	9.8055	-12.6	8.5	83.34675	-158.8
1.5	14.70825	-21.8	8	78.444	-148.8
2	19.611	-31.2	7.5	73.54125	-141
2.5	24.51375	-40.6	7	68.6385	-128.4
3	29.4165	-50.3	6.5	63.73575	-121.4
3.5	34.31925	-59.6	6	58.833	-112
4	39.222	-69	5.5	53.93025	-103.4
4.5	44.12475	-78.3	5	49.0275	-93.2
5	49.0275	-88	4.5	44.12475	-84.4
5.5	53.93025	-98	4	39.222	-73.6
6	58.833	-107	3.5	34.31925	-64.5
6.5	63.73575	-116.5	3	29.4165	-54.6
7	68.6385	-126.3	2.5	24.51375	-45.3
7.5	73.54125	-136.2	2	19.611	-35.4
8	78.444	-146.2	1.5	14.70825	-26.2
8.5	83.34675	-155.4	1	9.8055	-16.1
9	88.2495	-164.6	0.5	4.90275	-6.7
9.5	93.15225	-174.8	0	0	7.2
10	98.055	-184.1			

Table K-2 reading recorded for X axis positive direction.

Mass (kg)	Force (N)	Voltage (mV)	Mass (kg)	Force (N)	Voltage (mV)
0	0	-3.2	9.5	93.15225	176.6
0.5	4.90275	7.9	9	88.2495	166.9
1	9.8055	17	8.5	83.34675	159.2
1.5	14.70825	25.8	8	78.444	150.3
2	19.611	35.2	7.5	73.54125	142.1
2.5	24.51375	44.5	7	68.6385	130.7
3	29.4165	53.9	6.5	63.73575	123
3.5	34.31925	62.9	6	58.833	113.6
4	39.222	72.1	5.5	53.93025	105.1
4.5	44.12475	81.8	5	49.0275	94.9
5	49.0275	91.2	4.5	44.12475	86.5
5.5	53.93025	100.4	4	39.222	75.4
6	58.833	109.8	3.5	34.31925	67.2
6.5	63.73575	118.9	3	29.4165	56.9
7	68.6385	128.2	2.5	24.51375	48.3
7.5	73.54125	138.2	2	19.611	38.6
8	78.444	147.5	1.5	14.70825	29.2
8.5	83.34675	156.7	1	9.8055	19.1
9	88.2495	165.9	0.5	4.90275	9.8
9.5	93.15225	175.8	0	0	-3.9
10	98.055	185.3			

Table K-3 readings recorded for Y axis

Mass (kg)	Force (N)	Voltage (mV)	Mass (kg)	Force (N)	Voltage (mV)
0	0	0.8	9.5	93.15225	179.5
0.5	4.90275	11.8	9	88.2495	168.8
1	9.8055	20.8	8.5	83.34675	160.9
1.5	14.70825	29.8	8	78.444	151.4
2	19.611	39.1	7.5	73.54125	142.5
2.5	24.51375	48.5	7	68.6385	130.5
3	29.4165	57.7	6.5	63.73575	122.8
3.5	34.31925	67.3	6	58.833	112.7
4	39.222	76.5	5.5	53.93025	104.1
4.5	44.12475	85.6	5	49.0275	93.5
5	49.0275	95.1	4.5	44.12475	84.4
5.5	53.93025	104.2	4	39.222	74.5
6	58.833	113.5	3.5	34.31925	65.1
6.5	63.73575	123.2	3	29.4165	54.5
7	68.6385	132.4	2.5	24.51375	45.3
7.5	73.54125	141.5	2	19.611	34.8
8	78.444	150.7	1.5	14.70825	25.5
8.5	83.34675	159.4	1	9.8055	14.5
9	88.2495	168.5	0.5	4.90275	5.8
9.5	93.15225	178.5	0	0	-8
10	98.055	188.1			

Table K-4 readings recorded for Z axis

Mass (kg)	Force (N)	Voltage (mV)	Mass (kg)	Force (N)	Voltage (mV)
0	0	6.1	9.5	93.15225	98.8
0.5	4.90275	11.1	9	88.2495	94
1	9.8055	16	8.5	83.34675	88.9
1.5	14.70825	20.7	8	78.444	84.1
2	19.611	25.7	7.5	73.54125	79.5
2.5	24.51375	30.6	7	68.6385	74.6
3	29.4165	35.1	6.5	63.73575	69.5
3.5	34.31925	40.3	6	58.833	64.8
4	39.222	45.2	5.5	53.93025	60.1
4.5	44.12475	50	5	49.0275	55.4
5	49.0275	54.9	4.5	44.12475	50.3
5.5	53.93025	59.9	4	39.222	45.7
6	58.833	64.5	3.5	34.31925	40.7
6.5	63.73575	69.3	3	29.4165	35.8
7	68.6385	74.3	2.5	24.51375	31.1
7.5	73.54125	79.4	2	19.611	26.4
8	78.444	84.1	1.5	14.70825	21.7
8.5	83.34675	89	1	9.8055	17
9	88.2495	94	0.5	4.90275	12.2
9.5	93.15225	98.8	0	0	7.5
10	98.055	103.5			

#### K.4 Filtering of results

Following the calibration test the data recorded from the DAQ system was loaded into MATLAB the signals showed noise that made it difficult to make a reading. Figure K-5 shows an example of the recorded data loaded in MATLAB. The FILTFILT Zero-phase forward and reverse digital IIR filtering command was used to filter the results. Using this command did not shift the results to the right as would normally be seen when filters are applied. This is important as then force measurements are taken during a grinding pass the scale positions will also be recorded. Establishing a filtering method that does not affect

the position of the forces allows a better comparison between different grinding passes. Figure K-6 shows and enlarges section of Figure K-5 , the orange line is the filtered result. Reading for the filtered result were compared with the values recorded from the VI during the test and the differences were negligible.

The filter used was a Butterworth 2<sup>nd</sup> order, lowpass with a half power frequency of 5.

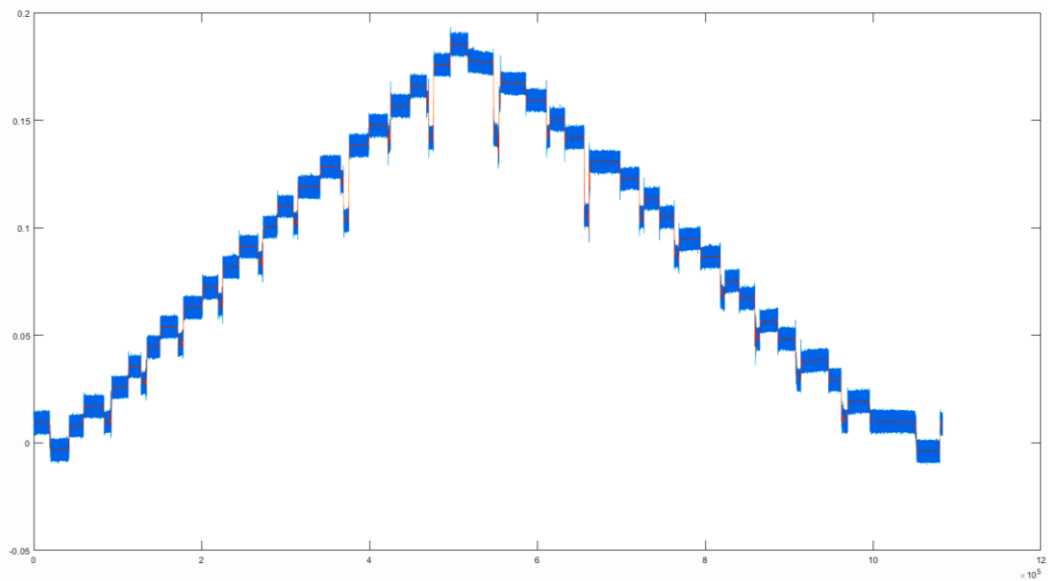


Figure K-5 Graph of X axis +ve calibration results loaded into MATLAB

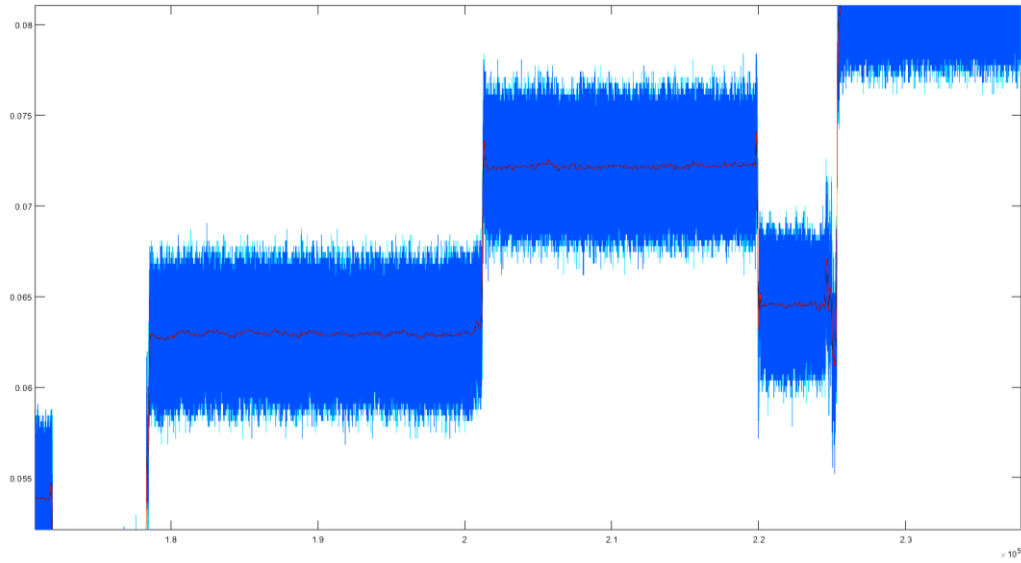


Figure K-6 Enlarged section of X axis +ve calibration results loaded into MATLAB with the the recorded result in blue and the filtered result line result in orange.

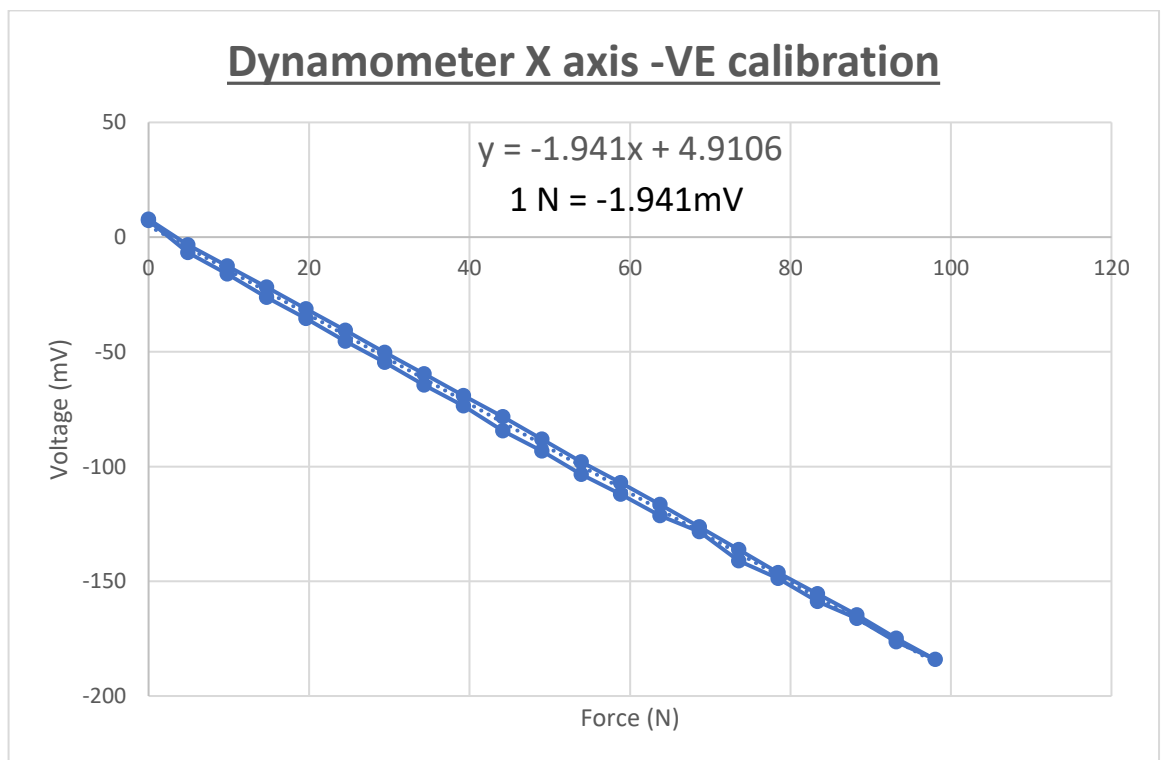


Figure K-7 graph of X axis calibration in negative direction.

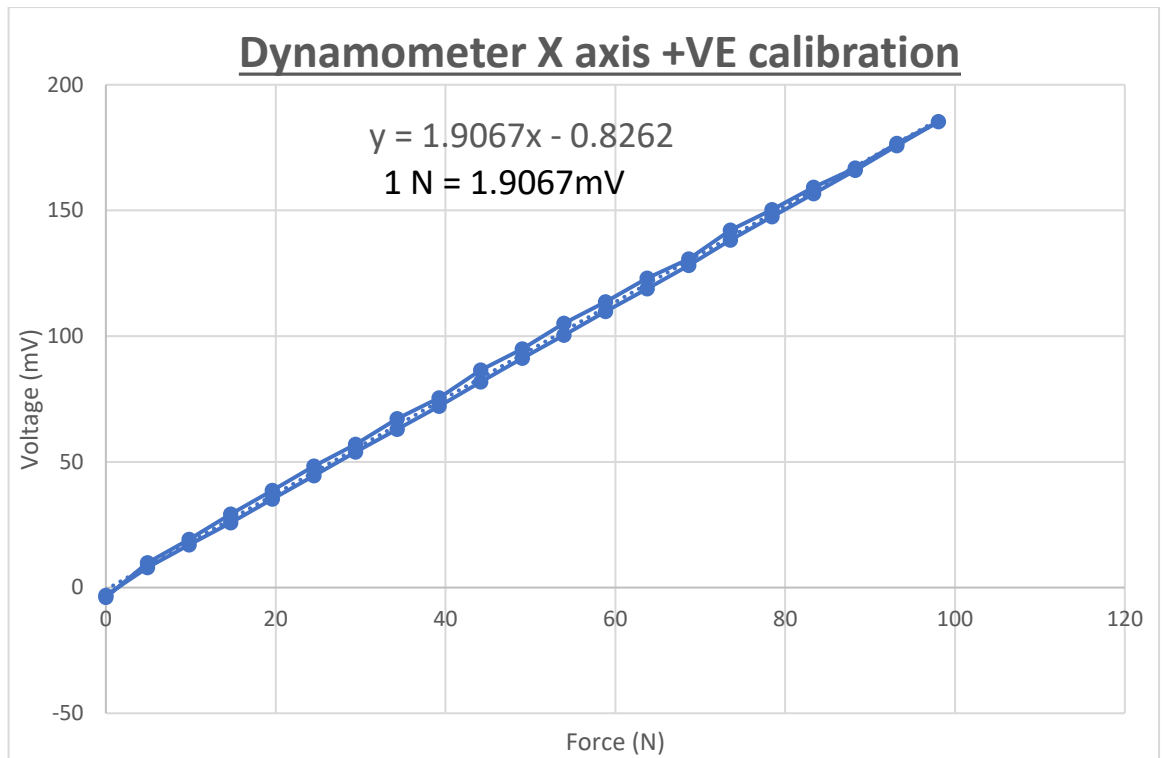


Figure K-8 graph of X axis calibration in positive direction.

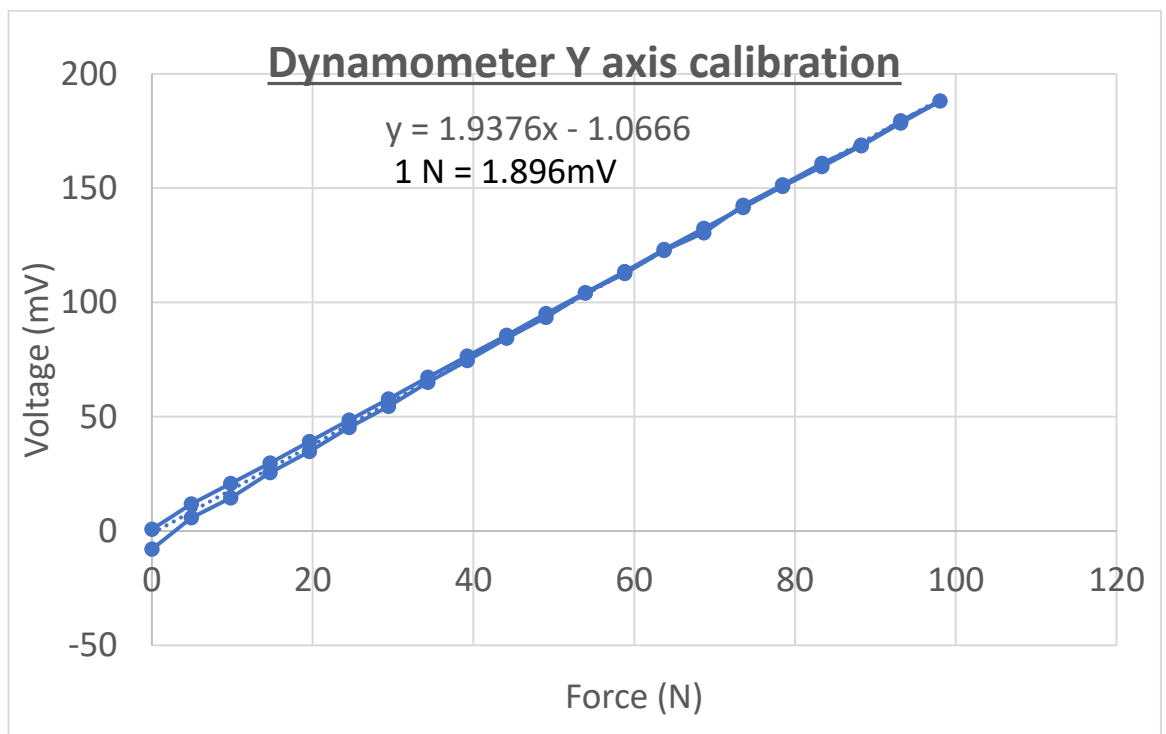


Figure K-9 graph of Y axis calibration.

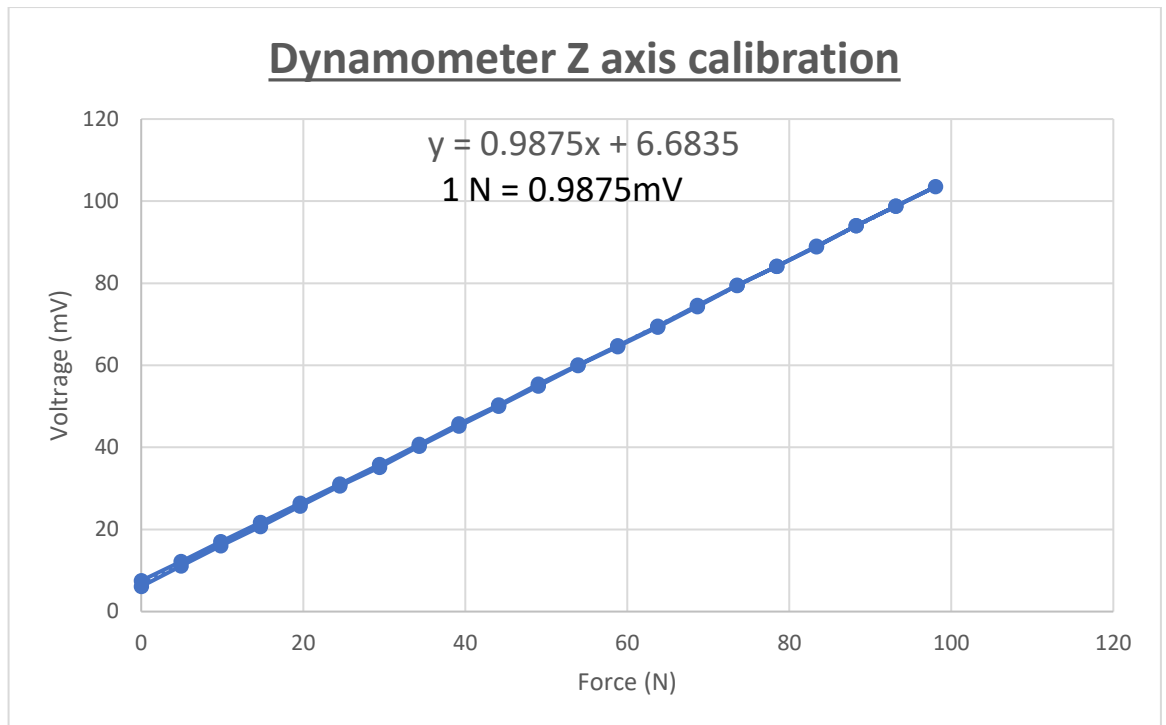


Figure K-10 graph of Z axis calibration.

### K.5 Discussion of results

All the axes appear to be linear in their response to the forces. The Z axis response was not expected to pass through zero as the dynamometer has the weight of the fixture on it. The Z axis also shows little difference between the increase and decrease of the loading. The Y axis passes very close to zero but shows a greater decrease in voltage between the penultimate and last readings. The Y axis results appear to show a greater amount of separation for the last quarter of the test. This could be due to drift in the charge amplifier. Each calibration test took approximately 25 minutes to conduct. Dynamometer readings can drift if measurements are taken over a long period of time. Both X axis directions are linear and with little separation between the increasing and decreasing of the load. The initial readings with zero load at the start and the end of the test are similar indicating no drift in these cases. However, it is interesting to observe that the no load voltage is different between the positive and negative directions. This should not cause a problem during test grinds providing that the force measurements are taken as a relative reading from when the grinding wheel is known not to be in contact with the test workpiece. It is not understood why the Z axis has an output response that is approximately half that of the other two axes. It is possible to configure the charge amplifier to different scale ranges and it is possible

that the Z axis could have been set to a different scale range. The necessary cable and software were not available to confirm this. It was considered not to be a problem as long as the response for that axis is known then measurements can be taken.

## Appendix L - Supplementary information on flow meter calibration

### L.1 Equipment

1. The flow meter used was an Omega FTG792-L that measures pulses from a rotating turbine. Figure L-1 show the omega flowmeter.



Figure L-1 Omega flowmeter.

Table L-1 shows the FTB792 specification.

Table L-1 FTB792 specification

Linear Flow Range	7.6-75.7 Litres per minute
Maximum Flow	113.6 Litres per minute
Frequency Range in Linear Flow Range	37-370 Hz
Connections NPT Female Inlet/Outlet Size	3/4 in.
Wrench Size:	33mm
Weight Kilograms	1.1 kg

2. Stopwatch.
3. Buckets.
4. Grinding fluid supply system filled with water based grinding fluid (Castrol Hysol XF) 5% concentration. Figure L-2 shows the grinding fluid delivery system.
5. Known masses 0.495kg, 0.502Kg, 2kg x 2.
6. Digital kitchen weighing scales 0-5kg.

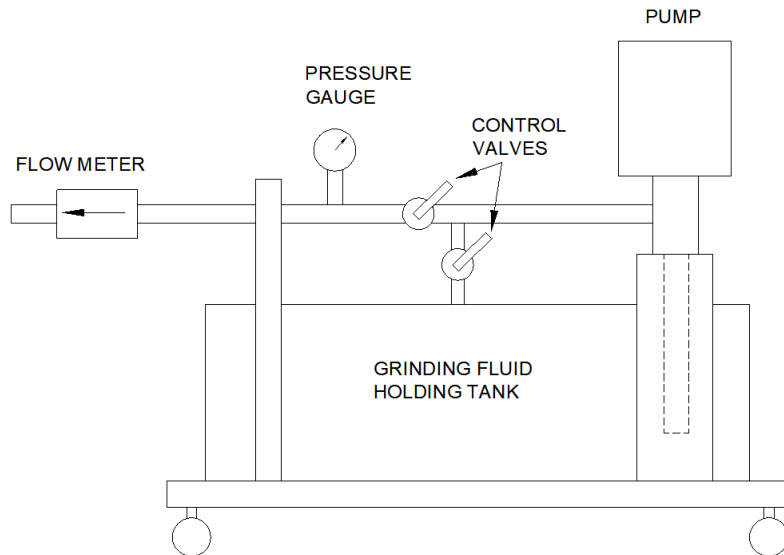


Figure L-2 Grinding fluid delivery system

The kitchen weighing scales had a maximum limit of 5kg, the empty bucket used had a mass of 0.608kg. Therefore, a target mass of 3kg was set for each measurement so that the captured fluid would still be in the range of the weighing scales.

## L.2 Methods

### L.2.1 Kitchen weighing scale calibration.

1. The kitchen scales were turned on and set to zero.
2. A known mass was added to the scales and the scale reading recorded.
3. Other masses were added to the scale to cover a range up to 4.5KG and the scale readings recorded.
4. All masses were removed to check that the scale reading returned to zero at the end of the test.

### L.2.2 Flowmeter calibration

1. The grinding fluid supply system was set so that outlet of the rubber supply hose downstream of the flowmeter returned flow to the back to the holding tank.
2. The grinding fluid delivery system was started.

3. The control valves were adjusted so that the reading on the flowmeter was within a few tenths of a 5L/min target value. Flow was allowed to run for 15 seconds without adjustment to check for a stable reading.
4. The outlet end of the rubber supply hose was quickly transferred from the holding tank to the empty bucket and simultaneously the stopwatch started.
5. Flow was allowed to enter the bucket for a theoretical time that should allow 3KG to be collected in the bucket. The theoretical time for the target flowrates are shown in Table L-2.
6. After the time had elapsed the outlet end of the rubber supply hose was returned to the holding tank and simultaneously the stopwatch was stopped.
7. The grinding fluid supply system was turned off.
8. The flowmeter reading and stopwatch reading were recorded.
9. The bucket containing the captured fluid was weighed. The kitchen scales were small in comparison to the diameter of the bucket. It was not possible to clearly read the display on the scales when the bucket was on the scales. To take a reading from the scales the following method was used:
  - a. Turn on the scales and set to zero.
  - b. Place bucket containing fluid on the scales.
  - c. Zero scales using zero button.
  - d. Remove bucket.
  - e. The scales display a negative reading, indicating the amount of mass that has been removed. The negative sign was ignored when recording the reading.
10. Steps 2 to 9 were repeated for the other target flowrates and times listed in Table L-2.

Table L-2 target flowrates and times required to capture 3kg of fluid at target flowrate.

Target Flowrate (L/min)	Time to capture 3 kg (s)
5	36
10	18
15	12
20	9
25	7.2
30	6

### L.3 Results

Table L-3 shows the result of the kitchen scales calibration test the largest error is 1.01%. Figure L-3 shows a graph of the calibration result. Figure L-4 shows a graph of the flow meter calibration result and Table L-4 shows the recorded reading and the calculated flow results.

Table L-3 kitchen weighing scales results.

Known mass (kg)	Weighing scale result (kg)	Weighing scale error (%)
0.502	0.505	0.60
0.495	0.5	1.01
0.997	1.005	0.80
2	2.015	0.75
2.495	2.512	0.68
2.997	3.025	0.93
4.495	4.507	0.27
0	0	0.00

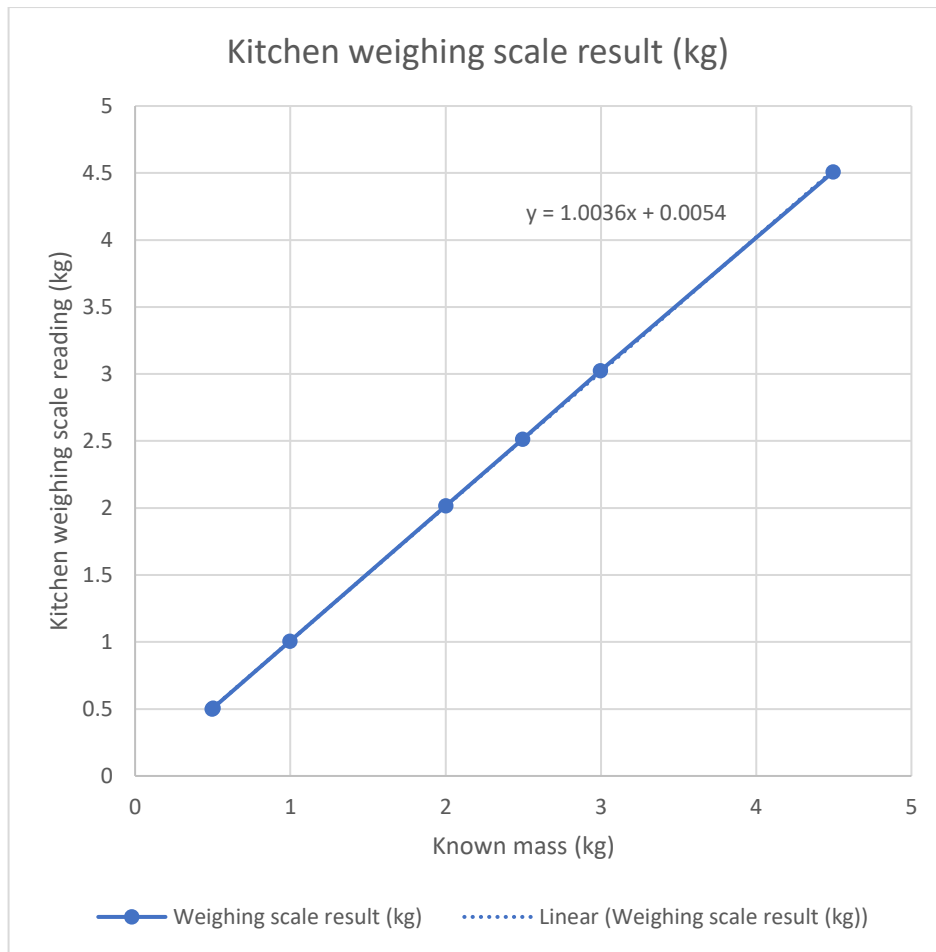


Figure L-3 Kitchen weighing scale calibration result.

Table L-4 Flowmeter calibration results.

Flowmeter reading (L/min)	Measurement time (s)	Weighing scale reading with bucket (kg)	Captured fluid mass (kg)	Calculated flowrate (L/min)	Flowmeter error (%)
5.4	30.45	3.566	2.958	5.83	-7.35
9.8	18.9	3.958	3.35	10.63	-7.85
15	12.59	3.84	3.232	15.40	-2.61
19.9	9.62	3.726	3.118	19.45	2.33
24.9	8.2	4.046	3.438	25.16	-1.02

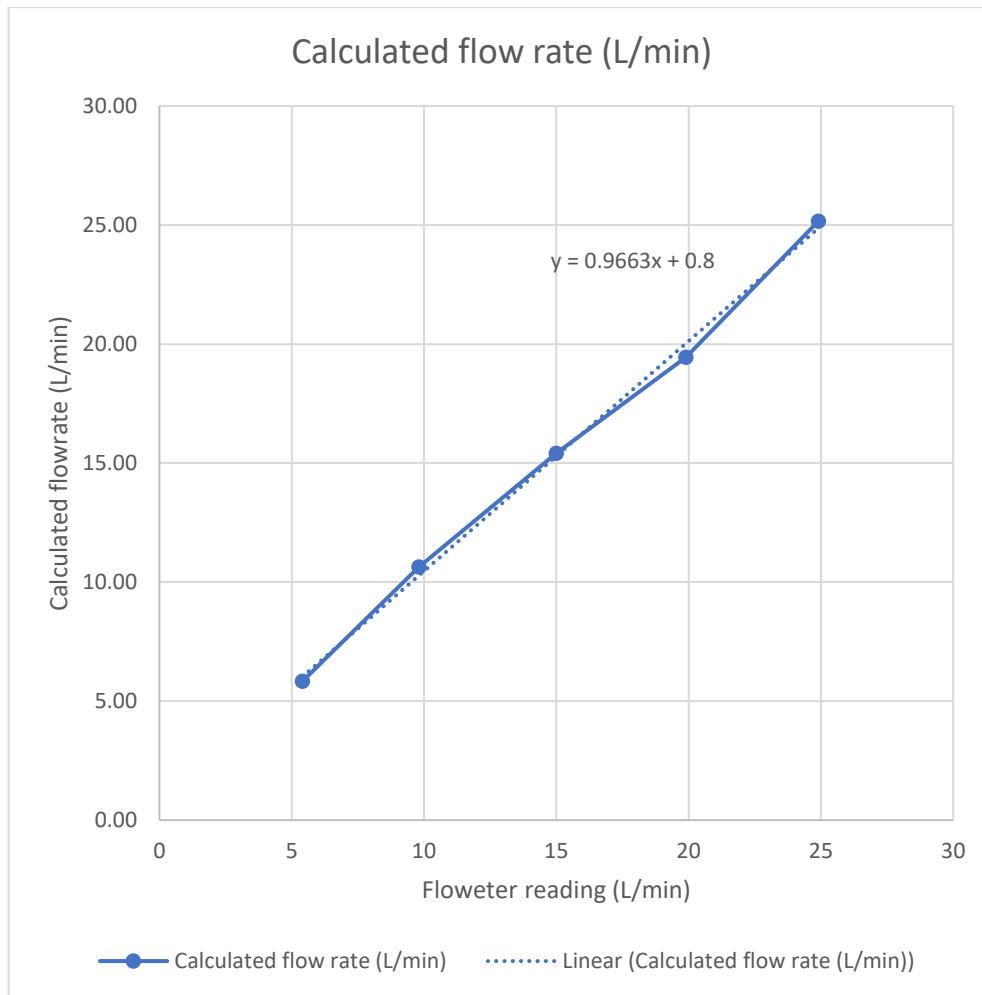


Figure L-4 flowmeter reading and calculated flowrate readings.

#### L.4 Discussion of results

Figure L-3 shows a graph with a good linear relationship between the known masses and the scale readings. The kitchen weighing scales have an error range of +0.27% to +1.01% across the range tested. The errors are acceptable and will have a negligible effect on the calibration results of the flowmeter.

Table L-4 show the measurement results for the flowmeter calibration test. Figure L-4 shows a reasonably linear relationship between the flowmeter readings and the calculated flowrate. The flowmeter under reads and has an error range of -1.02% to -7.85% over the measurement range used. The error gets smaller as the flowrate increases. At flowrates of 15L/min and above the error is 2.6% or less. All errors are less than 8% of the actual flowrate. A relation of 1L of water is equal to 1kg of water has been used for the

calculations. The grinding fluid used is water based with 5% of soluble oil (Castrol Hysol XF). The oil will be a slightly lower density, which has not been accounted for. The oil would give an error in the region of 0.005kg/L or 0.5%, which is considered negligible. If a different grinding fluid is used with a significantly different density the calibration procedure should be repeated to check the meter reading for that fluid. The last target flowrate was not tested as significant spray and splashing was created during the previous target flowrate, and it was considered too messy to test at the last target flowrate.

It is possible that the reports of the flowmeter giving incorrect readings are due to either something temporarily blocking or jamming the turbine. Or possibly due to low battery power as the batteries needed to be replaced to get the electronics in the meter to work.

## Appendix M - Supplementary information for Omega pressure gauge calibration test

### M.1 Equipment

1. Omega pressure gauge model number PG-5000-1000-PSI-G-H1-L3-E1-N1-B1, range 1000PSI, Output range 0-5 VDC.
2. Fluke 175 true RMS multimeter (calibrated).
3. Farnell 0-30V power supply.
4. Manual hydraulic hand pump with 1000PSI analogue gauge.
5. Workzone pneumatic pressure regulator with 180PSI analogue gauge.
6. Workzone 25L portable air compressor.

The equipment used for the hydraulic test is shown in Figure M-1. Figure M-2 shows the pneumatic air regulator used for the pneumatic test and Figure M-3 show the mounting of the Omega pressure gauge in the air gun.

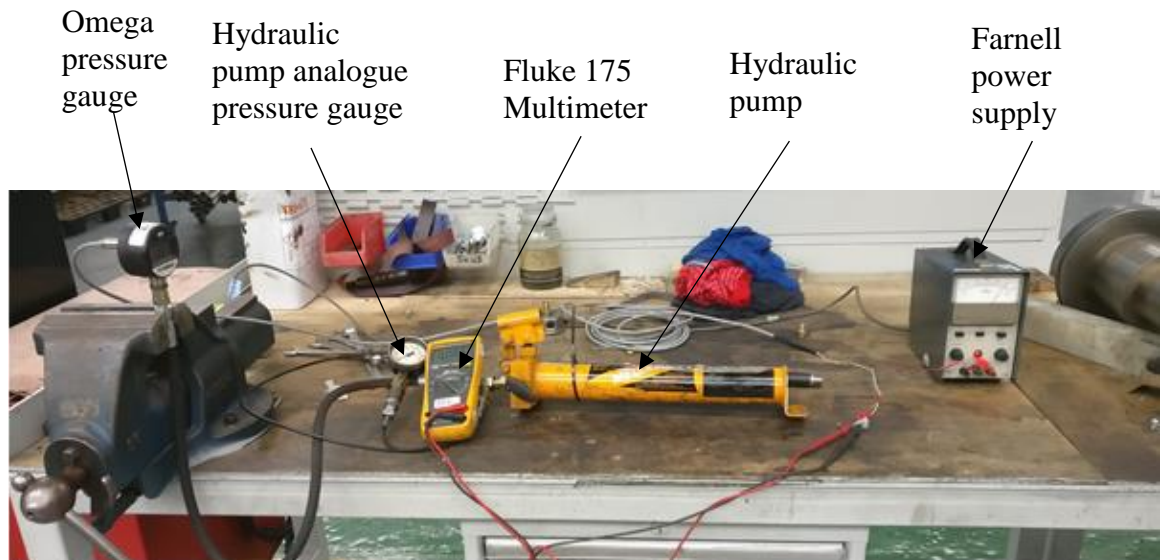


Figure M-1 Equipment arrangement used for hydraulic test



Figure M-2 Workzone pneumatic pressure regulator used for pneumatic test.



Figure M-3 Omega pressure gauge held in air gun.

## **M.2 Methods**

### **M.2.1 Hydraulic test**

1. The Omega pressure gauge input was attached to the pipe from the output of the hydraulic hand pump.
2. The Omega pressure gauge was connected to the Farnell power supply that was set to give 24V.
3. The signal wires from the output were connected to the probes of the Fluke multimeter that was set to measure direct current voltage that was auto ranging.

4. With no hydraulic pressure the Omega pressure gauge was set to read zero by adjusting the trimming potentiometer.
5. The Omega pressure gauge reading, the Omega pressure gauge voltage output and the pressure gauge reading on the manual hydraulic pump were recorded.
6. The hydraulic hand pump was used to raise the pressure by 50 PSI.
7. The Omega pressure gauge reading, the Omega pressure gauge voltage output and the pressure gauge reading on the manual hydraulic pump were recorded.
8. Steps 6 and 7 were repeated up to a pressure of 950PSI.
9. The pressure relief knob on the manual pump was used to lower the pressure in the system by 50 PSI.
10. The Omega pressure gauge reading, the Omega pressure gauge voltage output and the pressure gauge reading on the manual hydraulic pump were recorded.
11. Steps 9 and 10 were repeated down to a pressure of 0PSI.

#### **M.2.2 Pneumatic test**

1. The Omega pressure gauge input was attached to the nozzle of an air gun at the end of a pipe that was attached to the air regulator that was attached to the output from the air compressor.
2. The Omega pressure gauge was connected to the Farnell power supply that was set to give 24V.
3. The signal wires from the output were connected to the probes of the Fluke multimeter that was set to measure direct current voltage that was auto ranging.
4. The compressor tank was pressurised to the maximum that it could reach (106PSI), the regulator was set to give this maximum output.
5. The Omega pressure gauge reading, the Omega pressure gauge voltage output and the pressure gauge reading on the pneumatic pressure regulator were recorded.
6. The pressure was reduced using the regulator by 5 PSI
7. The Omega pressure gauge reading, the Omega pressure gauge voltage output and the pressure gauge reading on the pneumatic pressure regulator were recorded.
8. Steps 6 and 7 were repeated down to a pressure of 0PSI.
9. The pressure regulator was used to raise the pressure in the system by 10 PSI.
10. The Omega pressure gauge reading, the Omega pressure gauge voltage output and the pressure gauge reading on the pneumatic pressure regulator were recorded.

11. Steps 9 and 10 were repeated up to a pressure of 100PSI.

### **M.3 Result**

Table M-1 shows the recorded values for the hydraulic test, and Figure M-4 show a graph of the Omega pressure gauge readings and the gauge voltage output. Figure M-5 shows a graph of the pneumatic pressure test for the Omega gauge readings and the gauge voltage output. Table M-2 shows the recorded results for the pneumatic test.

Table M-1 reading recorded for hydraulic test.

Pressure gauge (PSI)	Omega Pressure Gauge (PSI)	Omega Pressure Gauge Output (V)
0	0	0
55	58	0.289
95	101	0.506
150	152	0.764
222	220	1.109
285	285	1.438
310	311	1.565
370	373	1.876
420	427	2.143
495	504	2.534
570	576	2.891
655	653	3.284
700	705	3.542
800	805	4.054
875	878	4.413
950	955	4.8
890	894	4.5
695	697	3.521
530	533	2.694
475	473	2.396
355	353	1.787
280	278	1.408
205	200	1.017
100	99	0.503
40	49	0.254
0	0	0.001

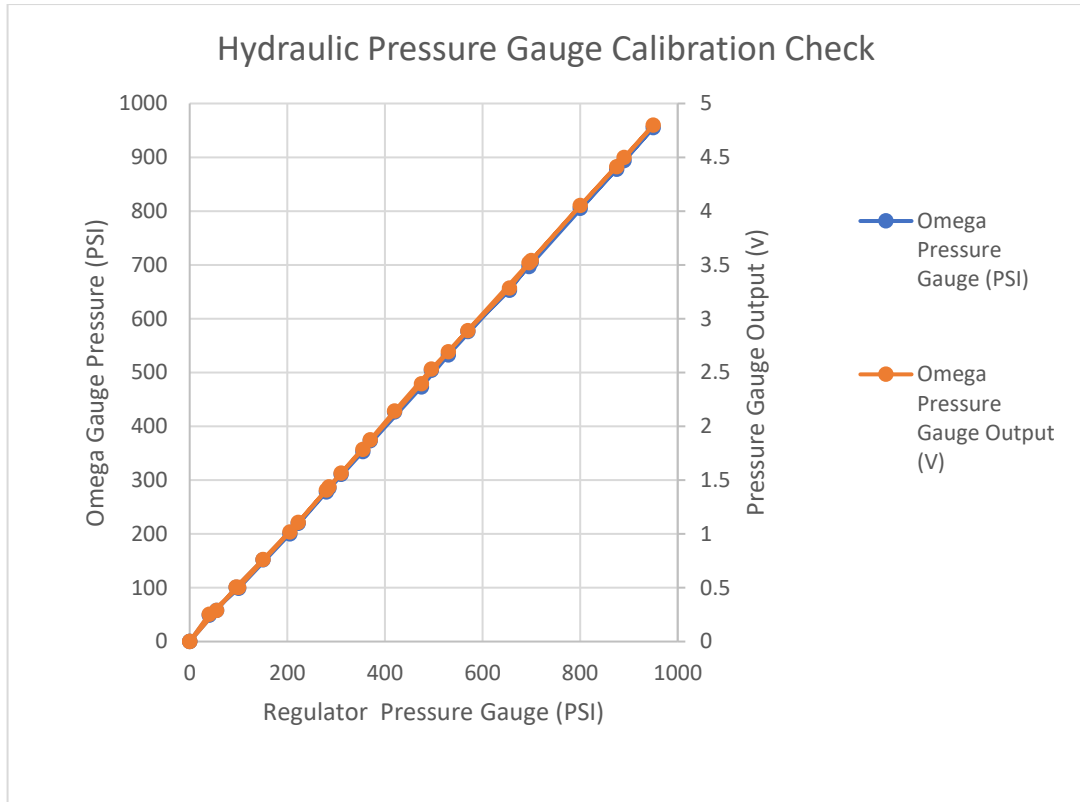


Figure M-4 graph of reference gauge against Omega pressure reading and output voltage.

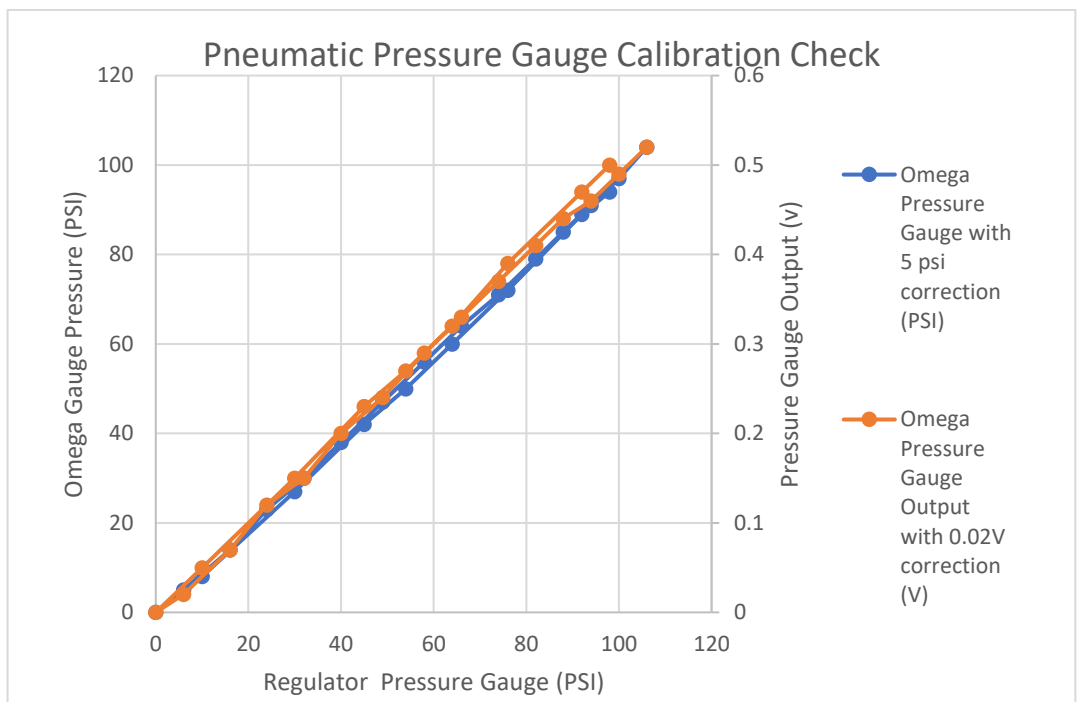


Figure M-5 graph of reference gauge pressure against the Omega pressure gauge reading and the Omega output voltage.

Table M-2 Recorded results from the pneumatic tests.

Regulator Pressure (PSI)	Omega Pressure Gauge with 5 PSI correction (PSI)	Omega Pressure Gauge (PSI)	Omega Pressure Gauge Output with 0.02V correction (V)	Omega Pressure Gauge Output (V)
106	104	109	0.52	0.54
100	97	102	0.49	0.51
94	91	96	0.46	0.48
88	85	90	0.44	0.46
82	79	84	0.41	0.43
74	71	76	0.37	0.39
66	64	69	0.33	0.35
58	56	61	0.29	0.31
49	47	52	0.24	0.26
40	38	43	0.2	0.22
32	30	35	0.15	0.17
24	23	28	0.12	0.14
16	14	19	0.07	0.09
6	5	10	0.02	0.04
0	0	5	0	0.02
10	8	13	0.05	0.07
30	27	32	0.15	0.17
45	42	47	0.23	0.25
54	50	55	0.27	0.29
64	60	65	0.32	0.34
76	72	77	0.39	0.41
92	89	94	0.47	0.49
98	94	99	0.5	0.52

#### M.4 Discussion of results

The method was difficult to follow for both the hydraulic and pneumatic test when the pressure adjustments were made. It proved difficult to make exact adjustments. Although the recorded points are not evenly spread, the distribution of points should have picked up any curvature to the readings. The pneumatic test was over a smaller pressure range but did

allow finer resolution of readings. Both the pneumatic and hydraulic results are linear and for both rising and falling pressures. Also, the voltage output tracks the pressures with good correlation.

At the start of the pneumatic test the Omega pressure gauge was not set to zero using the trim potentiometer. This caused the Omega pressure gauge to give a residual reading of 5PSI when no pressure was applied. The 5 PSI reading also caused the output voltage to be incorrect by 0.02V. The results were corrected for this error after the test.

## Appendix N - Supplementary information for grinding fluid nozzle tests

### N.1 Apparatus

#### N.1.1 Grinding fluid:

Water based grinding fluid using Castrol Hysol XF semi-synthetic soluble oil at a concentration of 5% by volume.

#### N.1.2 Grinding fluid nozzle:

Material: ABS

Printer settings: 100% density, printer nozzle temperature 255°C, heated bed temperature 110°C, printer nozzle diameter 0.4mm, layer thickness 0.2mm.

Design name: Coolant nozzle 5 - holes

Size: 10 2mm diameter holes, total exit area 31.415mm<sup>2</sup>

Connection: External ½ BSPP thread.

When the nozzle was designed it was necessary to keep in mind the method of manufacture so that suitable quality could be achieved. Overhanging features needed to be avoided if possible. However, if overhanging features cannot be avoided such as the internal chamber in the nozzle the angle or the rate of change between layers should be minimised so that the next layer that is printed has some support from the previous layer. The length of the exit holes needed to be limited to the length that was possible to drill using a set of number drills. For a 2mm hole diameter the ratio of hole length to hole diameter is approximately 20:1. Number drills have small enough increments between the sizes that the total exit area could be controlled reasonably accurately to suit flow requirements.

Figure N-1, Figure N-2 and Figure N-3 show the solid model and sectional views of the nozzle and the internal chambers.

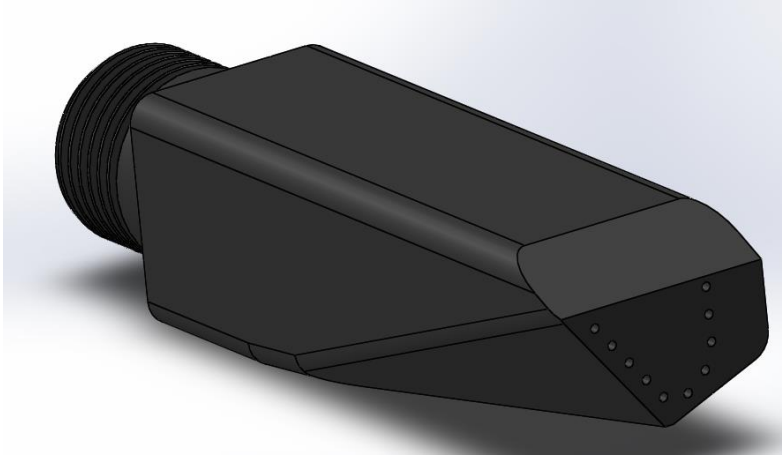


Figure N-1 coolant nozzle 5 - holes solid model view.

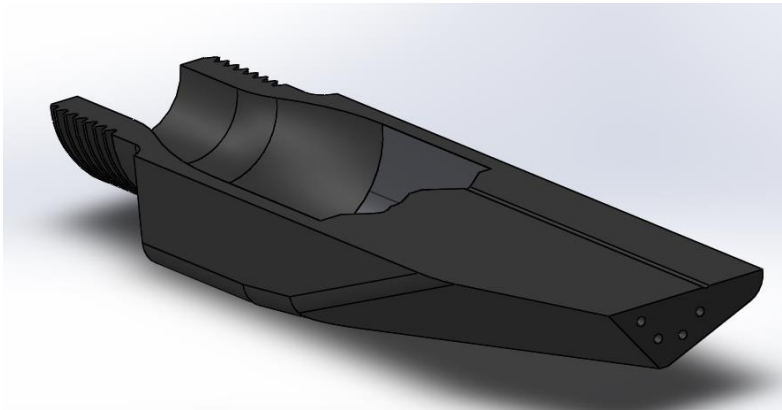


Figure N-2 Sectional view of coolant nozzle 5 - holes design showing the length of the exist holes.

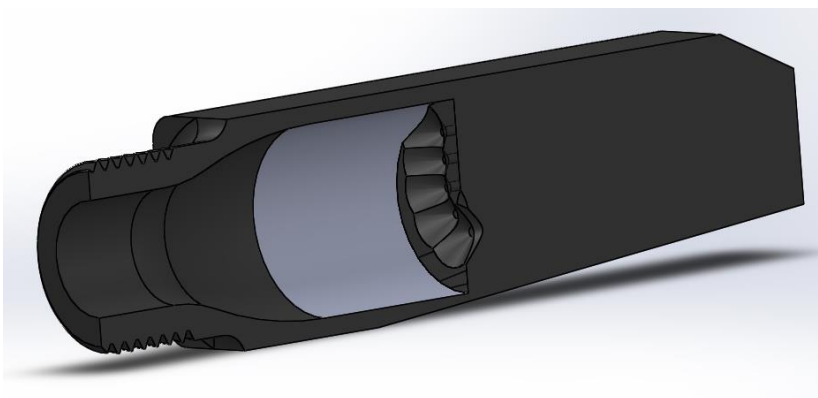


Figure N-3 sectional view of coolant nozzle 5 - holes showing the lead in chamfers at the entry of the exit holes.

### N.1.3 Grinding fluid system

Figure N-4 shows a diagram of the fluid delivery system used.

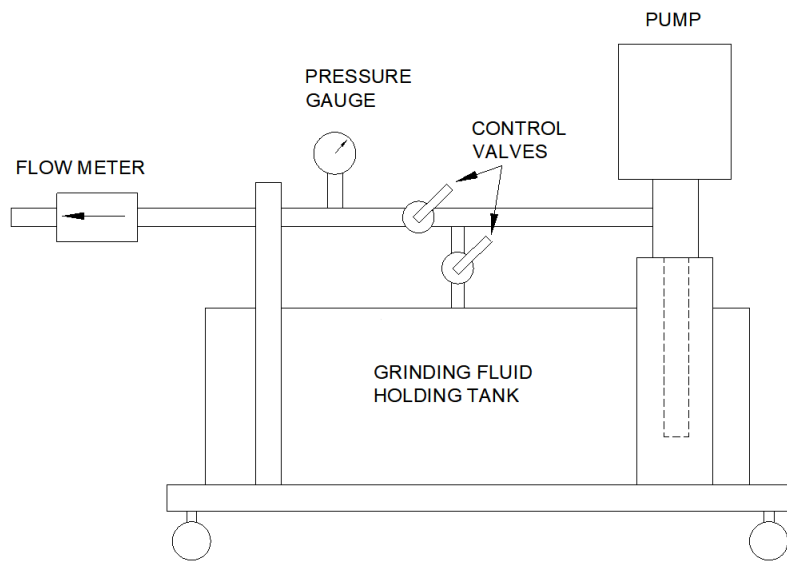


Figure N-4 Grinding fluid delivery system

### N.1.4 Pressure gauge

The pressure gauge installed on the grinding fluid system is shown in Figure N-5 and Figure N-6.



Figure N-5 Omega PG-5000 1000PSI pressure gauge with 0-5V output



Figure N-6 Model number spec and pinout details for pressure gauge

### N.1.5 Flow meter

The flow meter used on the grinding fluid system was an Omega FTG792-L that measures pulses from a rotating turbine

Table N-1 shows the FTB792 specification

Table N-1 FTB792 specification

Linear Flow Range	7.6-75.7 Litres per minute
Maximum Flow	113.6 Litres per minute
Frequency Range in Linear Flow Range	37-370 Hz
Connections NPT Inlet/Outlet Size	3/4 in.
Wrench Size:	33mm
Weight Kilograms	1.1 kg

### N.1.6 Jakobson grinder

A Jakobson surface grinder that had been specially adapted for coolant nozzle trials with an enclosure was used for the trials and is shown in Figure N-7.



Figure N-7 Jakobson surface grinder.

### **N.2 Method**

1. The nozzle was attached to the supply pipe inside the enclosure.
2. The valves on the grinding fluid supply system were set to divert all flow back to tank.
3. The valves were adjusted to allow a low pressure of 11 PSI.
4. A picture of the flow from the exit of the nozzle was taken.
5. Observations of the nozzle body was made to make note of any leaks.
6. The valves were altered to give a higher pressure of 55PSI.
7. A picture of the flow from the exit of the nozzle was taken.
8. Observations of the nozzle body was made to make note of any leaks.

### N.3 Results

Table N-2 Nozzle test log showing the pressures and flow rates.

Nozzle design: Coolant nozzle 5 (10x 2mm diameter holes)		
Hole size: 2mm diameter		
Equipment used: Castrol Hysol XF (5%?)		
Run	Pressure (PSI)	Flowrate (L/min)
1	11	13.9
2	55	32.1



Figure N-8 run 1 nozzle dispersion.

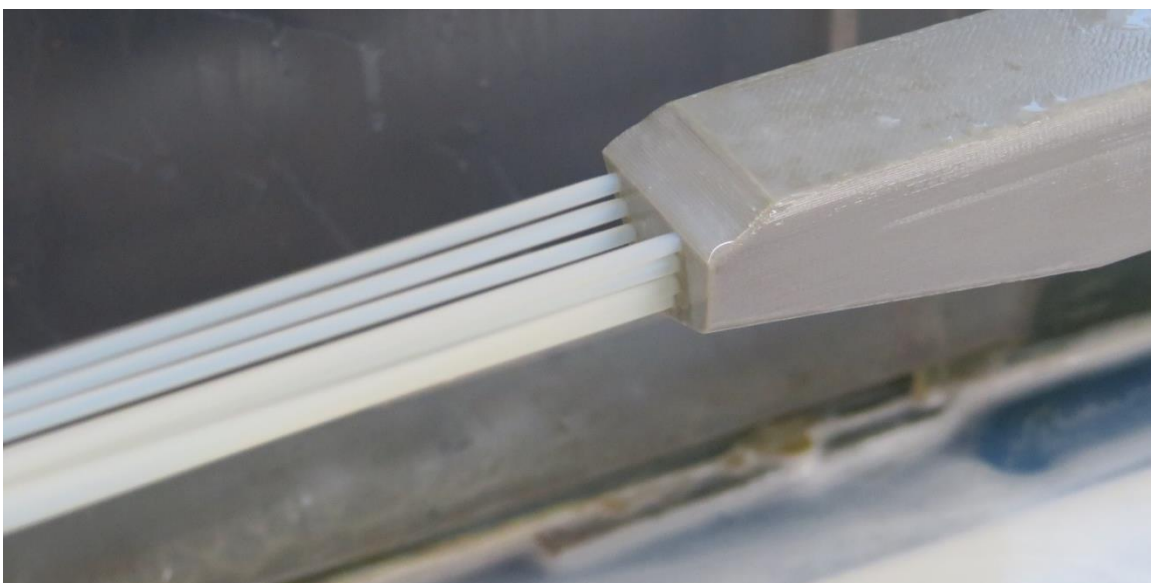


Figure N-9 run 1 nozzle dispersion.



Figure N-10 run 2 nozzle dispersion.

#### **N.4 Discussion of results**

The nozzle jet dispersion was small for run one. However, this is at a low pressure that would give a jet velocity that is much slower than a typical grinding wheel surface speed. The nozzle dispersion for run 2 is larger, it can be seen that the diameter of the jet becomes larger a few millimetres from the exit and the individual jets appear to merge further away from the exit. An approximate calculation based on the nozzle exit area and the recorded flowrate for run 2 gives a jet speed of 17 m/s. This could match a low grinding wheel surface speed; however, it is far from matching a typical aluminium oxide maximum surface speed of 50m/s. It was not possible to test at higher flow rates without flooding the grinding machine as it was unable to drain away the fluid fast enough. The nozzle did not show any signs of the print layers detaching from one another, and no unexpected jets from the body of the nozzle were observed when the nozzle was running under pressure.

# Economic Analysis of the Helical Form Grinding Process

P W HART<sup>a,1</sup> and M N MORGAN<sup>a</sup>

<sup>a</sup>*General Engineering Research Institute, Faculty of Technology and Environment, Liverpool John Moores University, Byrom Street, Liverpool L3 3AF, UK*

**Abstract.** There would be real benefit to industry should an efficient and economic appraisal methodology be established that can be carried out on a standard and commonly available grinding machine that would allow independent assessment of grinding process variables and technologies and provide industrial users with the data that they need for process improvements or design. One of the steps in assessing changes in grinding process variables or different technologies used in grinding is to evaluate the associated costs. New technologies can sometimes have a high purchase price that can be make it hard to convince manufacturers to test how they perform. Performing an economic analysis can show if the new technology or different process parameters can give an advantage despite higher purchase cost. Both quality of the workpiece and costs need to be considered when choosing the optimum operating conditions for a process. Typically, manufacturers would choose quality of the workpiece as the first requirement to be meet, followed by minimum cost. It may be possible to produce acceptable quality over a range of process parameters. Once the parameter ranges are known an economic analysis can be performed over the ranges to find the minimum cost. This paper breaks down the costs associated with helical form grinding processes. The cost areas covered are grinding wheel, grinding fluid, machine cost and labour. Form grinding of helical screw compressor rotors using dressable grinding wheels can have additional costs due to the dressing methods used to establish an accurate form on the grinding wheel.

**Keywords.** form, helical, grinding fluid, cost model, grinding wheel

## 1. Introduction

Grinding of helical workpieces, usually on expensive, high-accuracy machines, can often be the bottleneck of a manufacturing line and is usually one of the last operations. As a result, it can be hard for manufacturers to suspend production to conduct new product evaluations. Also, workpieces are often in a high value-added condition. Changing process settings can result in thermal damage, poor surface finish or geometric errors [1, 2], which could cause the workpiece to be scrapped. Large manufacturers may be able to invest in such research; however, smaller enterprises can find it hard to undertake appraisals on a regular basis as new production technologies come to market. There would be real benefit to industry should an economic appraisal methodology be established that can be carried out on a small, relatively inexpensive and non-specialist grinding machine, suitably instrumented, that would allow assessment of new products

---

<sup>1</sup>Corresponding author, General Engineering Research Institute, Faculty of Technology and Environment, Liverpool John Moores University, Byrom Street, Liverpool L3 3AF, UK; E-mail: P.W.Hart@2014.ljmu.ac.uk

and provide users with benchmark data that they need for process improvements or design. The measurement of experimental response data such as material removal rate, power, forces, geometric form errors and surface finish can be used to assess and model new product performance. In the case of helical forms it is important to consider how the process differs from more widely used processes such as cylindrical grinding, so that the experimental methodology can accommodate these differences in to a pseudo-helical process. One of the steps in assessing changes in grinding process variables or different technologies used in grinding is to evaluate the associated costs. New technologies can sometimes have a high purchase price that can be make it hard to convince manufacturers to test how they perform. Performing an economic analysis can show if the new technology or different process parameters can give an advantage despite higher purchase cost. Both quality of the workpiece and costs need to be considered when choosing the optimum operating conditions for a process. Typically, manufacturers would choose quality of the workpiece as the first requirement to be meet, followed by minimum cost. It may be possible to produce acceptable quality over a range of process parameters. Once the parameter ranges are known an economic analysis can be performed over the ranges to find the minimum cost.

## 2. Mathematical Model

The analytical model is based on an existing cost model [3]. Some realistic and well considered assumptions and exclusions were necessary to permit development of a global model whilst retaining detail. The value of the machine is assumed to be zero at the end of its life. A used grinding fluid has no value at the end of life. However, grinding oil could be used as a combustible fuel, steps would have to be taken to remove toxins before burning [4]. The dressing calculations assume the use of a single point or form dressing disk. The calculations do not allow for profile dressing rolls.

Exclusions from the model include:

1. Acceleration and deceleration of movements.
2. Movements to withdraw the grinding wheel from the workpiece or movements to a machine home or unload position. Usually at the end of the machining cycle the grinding wheel will move away from the workpiece, typically to give more room to load and unload the workpiece. This is usually a small amount of time.
3. Movements required to move the grinding wheel to a dressing position.
4. Rapid feedrates or return time. If each grinding or dressing pass is done unidirectionally then the machine will take time to return to the start position for the next pass.
5. Cycle time and dressing time are not calculated by the model based on wheel/profile length, number of cuts, feedrates etc. A single time is input, the time can be from empirical trials or calculated on a separate cycle time estimator.
6. The calculations for the volume removed from the workpiece are simplified. Helical length changes with radius form the workpiece centreline. For this model the helical length of the workpiece is taken at half the form depth. This typically gives a small percentage error for a screw compressor rotor.
7. No account of electricity costs for the grinding machine and fluid delivery.

8. Setup dressing time would also involve performing some dressing, grinding a part off-size and taking measurements of the workpiece, calculating some adjustments and then dressing the wheel further to remove the errors.

### 1.1. Parameters

The parameters used in the model are shown in Figure 1 and listed in Table 1.

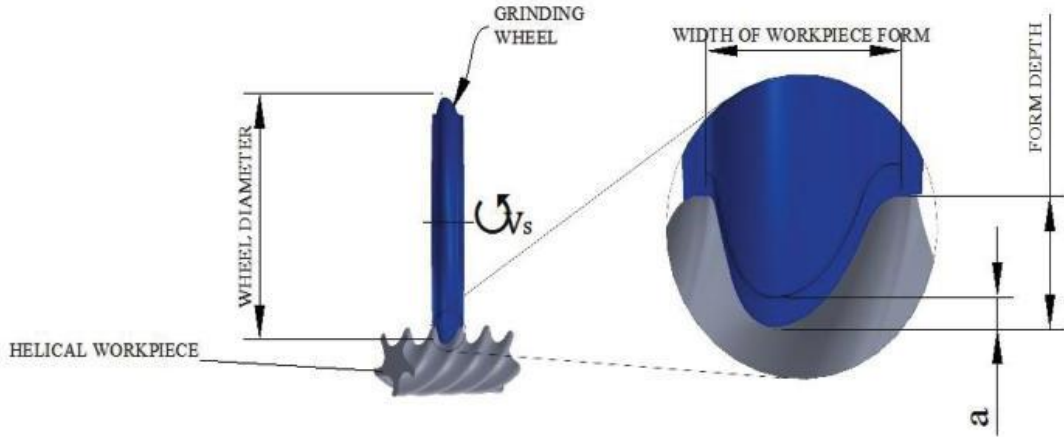


Figure 1 Model parameters

Table 1 Model input parameters notations

Parameter	Description	Parameter	Description
$a$	Depth of cut (mm)	$f_d$	Form depth (mm)
$a_d$	Dressing depth (mm)	$n_d$	Number of dressing passes
$a_{ds}$	Dressing depth used for setup (mm)	$N_d$	Number of parts per dress
$b_p$	Dressing profile length (mm)	$n_{ds}$	Number of dresses required when setting up
$b_w$	Width of workpiece form (mm)	$n_f$	Grinding fluid tank size (L)
$c_f$	Grinding fluid costs (£/L)	$N_{ws}$	Batch size produced between setups
$c_{fd}$	Disposal cost of grinding fluid (£/L)	$r$	Dresser radius (mm)
$c_l$	Labour rate (£/hour)	$r_s$	Radial wheel wear per dress (mm)
$C_{mc}$	Cost of grinding machine (£)	$t_s$	Cycle time per part excluding dressing time - floor to floor (minutes)
$C_{mmc}$	Machine maintenance cost (£/year)	$u_d$	Dresser overlap ratio
$c_s$	Wheel cost (£)	$v_s$	Wheel speed (m/s)
$c_{sd}$	Grinding wheel disposal cost (£)	$v_w$	Workpiece feedrate (mm/min)
$d_{smax}$	Maximum wheel diameter (mm)	$y_f$	Lifetime of grinding fluid (hours)
$d_{smin}$	Minimum wheel diameter (mm)	$y_t$	Life time of machine/payback period (years)

### 1.2. Model Calculations

Labour costs ( $C_l$ ) - The cost of the labour assignable to the production of one part.

$$C_l = c_l \div N_l \quad (1)$$

Machine costs ( $C_m$ ) - Cost of the grinding machine that can be assigned to the production of one part.

$$C_m = (C_{mc} + (C_{mmc} \times y_t)) \div N_{mc} \quad (2)$$

Grinding wheel costs ( $C_s$ ) - The cost of the grinding wheel that can be assigned to the production of one part.

$$C_s = (c_s + c_{sd}) \div N_w \quad (3)$$

Grinding fluid costs ( $C_f$ ) - The cost of the grinding fluid that can be assigned to the production of one part.

$$C_f = \left( (c_f + c_{fd}) \times \frac{n_f}{y_f} \right) \div N_l \quad (4)$$

Total costs excluding labour ( $C_e$ ) - The cost of the labour that can be assigned to the production of one part. Labour costs can contribute a large amount of the total cost.

$$C_e = C_m + C_s + C_f \quad (5)$$

Total costs ( $C_t$ ) - The total cost to produce one workpiece.

$$C_t = C_l + C_m + C_s + C_f \quad (6)$$

Workpiece volume removal rate ( $Q_w$ ) - The rate at which the material is removed from the workpiece.

$$Q_w = b_w \times v_w \times a \quad (7)$$

Number of parts produced per wheel ( $N_w$ ) - The total number of parts produced by the wheel during its life.

$$N_w = N_d \times \left( r_{suf} \div \left( r_s + (a_d \times n_d) + (r_{ssp} \times N_d) \right) \right) \quad (8)$$

Amount of radial usable abrasive ( $r_{suf}$ ) - The distance of abrasive in a radial direction that can be dressed off the wheel from new before it can no longer be used.

$$r_{suf} = ((d_{smax} - d_{smin}) \div 2) - f_d \quad (9)$$

Number of parts per unit of time ( $N_l$ ) - The rate at which parts are produced.

$$N_l = 1 \div t_t \quad (10)$$

Cycle time per part including dressing and setup ( $t_t$ ) - The total cycle time including an allowance for the time to setup the process and to dress the wheel.

$$t_t = t_s + (t_d \div N_d) + (t_{ds} \div N_{ws}) \quad (10)$$

Dresser feedrate ( $v_d$ ) - Feedrate that the diamond dresser passes over the wheel profile.

$$v_d = (b_d \div u_d) \times \left( v_s \div \left( \pi \times \left( \frac{d_{smax} + d_{smin}}{2} \right) \right) \right) \quad (11)$$

Dressing time ( $t_d$ ) - The time needed to dress the grinding wheel before the workpiece can be ground.

$$t_d = b_p \times n_d \div v_d \div 60 \quad (12)$$

Setup dressing time ( $t_{ds}$ ) - The time needed to dress the grinding wheel when setting up the process.

$$t_{ds} = b_p \times n_{ds} \div v_d \div 60 \quad (13)$$

Effective width of dressing tool ( $b_d$ ) - The effective width of the dressing tool used to calculate the dresser feedrate.

$$b_d = 2 \times \sqrt{(r^2 - (r - a_d)^2)} \quad (14)$$

Amount of wheel radius used for setup per part ( $r_{ssp}$ ) - The reduction in grinding wheel radius due to setup that can be assigned to the production of one workpiece.

$$r_{ssp} = n_{ds} \times a_{ds} \div N_{ws} \quad (15)$$

Number of parts produced during payback period ( $N_{mc}$ ) - The total number of parts produced during the lifetime of the machine.

$$N_{mc} = y_t \times N_l \quad (16)$$

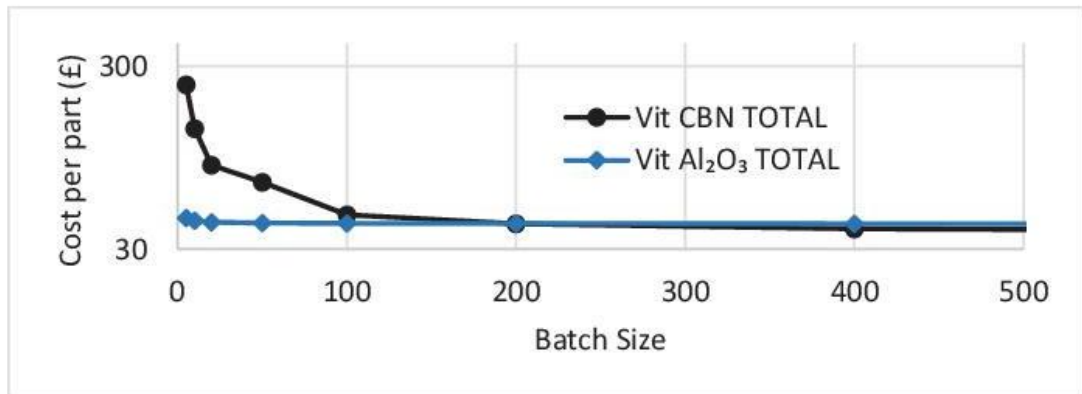


Figure 2 Effect of batch size on Vit CBN and Vit Al<sub>2</sub>O<sub>3</sub> total cost per part

### 3. Helical form grinding

For technologies such as vitrified cubic boron nitride (CBN) redress life can have a large effect on wheel cost per part. The amount of dressing needed for setup allows for an error of  $87\mu\text{m}$  on a  $5^\circ$  profile angle that can be typical of the steepest part on the grinding wheel profile for a compressor rotor. As mentioned above this error can be made up of dresser wear, dresser mounting errors such as runout, the dresser axes positioning errors, wheel mounting position error and machine thermal distortions of the dresser relative to the wheel and the wheel relative to the dresser. The in-cycle time for vitrified CBN is shorter than the  $\text{Al}_2\text{O}_3$  as the dressing time is a fraction of that for  $\text{Al}_2\text{O}_3$ . The vitrified CBN wheel is dressed and then multiple parts are ground before redressing the wheel, whereas the  $\text{Al}_2\text{O}_3$  wheel is dressing several times during the cycle. Figure 2 shows the effect of batch size on cost per part for the two different grinding wheel types, and Table 2 show the parameter values used to perform the analysis for the different wheel types.

**Table 2** Vitrified CBN and  $\text{Al}_2\text{O}_3$  parameter values for used for cost comparison

Parameter	Value Vitrified CBN	Value Vitrified $\text{Al}_2\text{O}_3$
Grinding wheel cost	£5000	£450
Number of parts per dress	25 or 500 passes	1/3 or 8 passes
Number of dresses per part	1/25	3
Dressing depth	$2\mu\text{m}$	$50\mu\text{m}$
Number of dresses on setup	200	20
Dressing depth when setting up	$5\mu\text{m}$	$50\mu\text{m}$
Maximum wheel diameter	400	500
Minimum wheel diameter	288	260
Radial wheel wear between dresses	$1\mu\text{m}$	$3\mu\text{m}$
Cycle time	14 minutes	15.5 minutes
Wheel speed	70m/s	35m/s

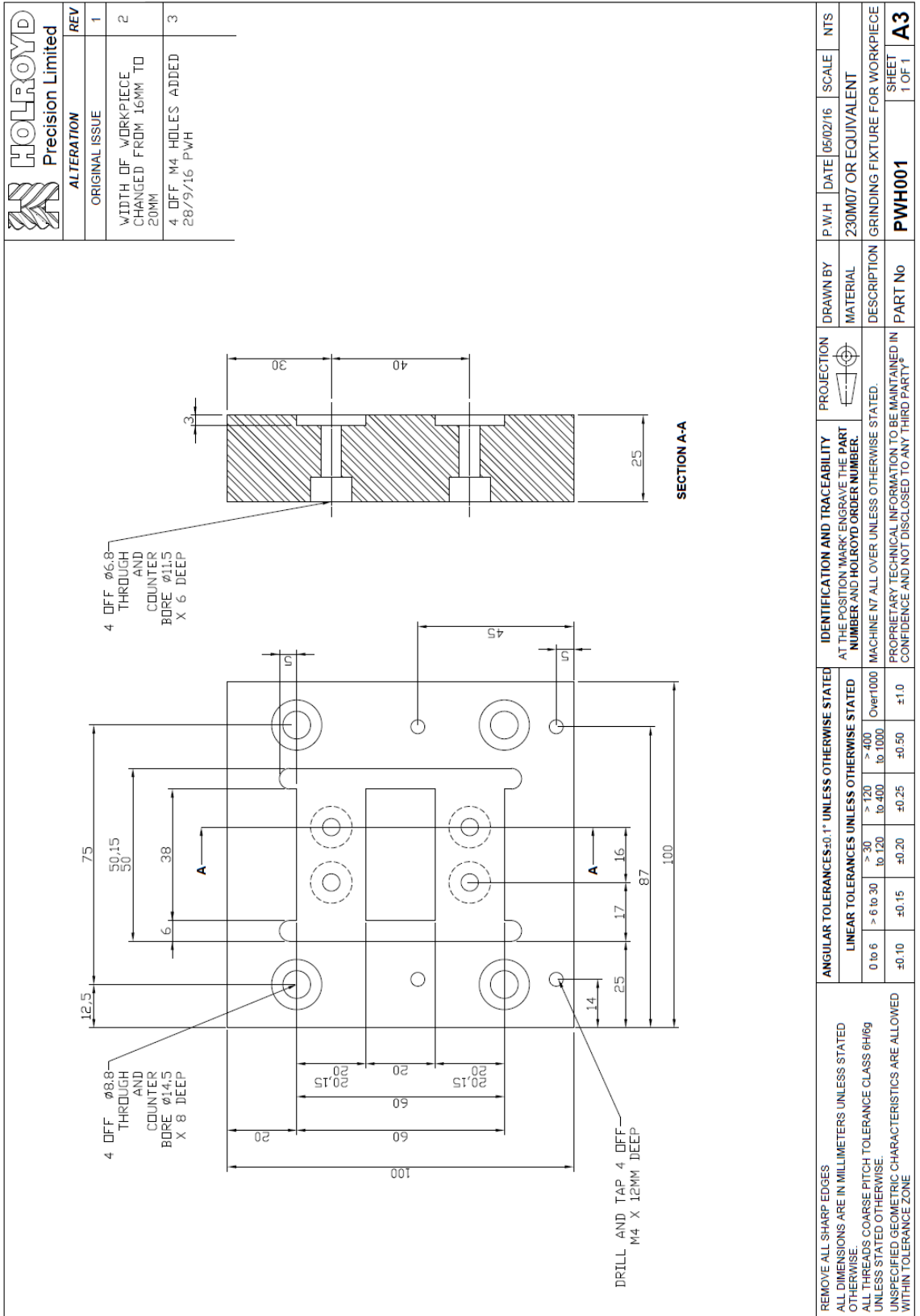
### 4. Conclusions

Performing an economic analysis can show the true cost of using a particular grinding technology, and help to understand how to use it to get the lowest cost per part. It can also help to understand the cost impact should it be necessary to use the technology to achieve another goal such as better quality or faster production. It would be useful to expand the model to include the electrical running costs for the grinding machine and the grinding fluid delivery system. Incorporating some of the exclusions listed could also help improve the accuracy of the results given by the analysis.

### References

- [1] S.G.C. Malkin, *Grinding technology : theory and application of machining with abrasives*. 2008, New York: Industrial Press.
- [2] W.B. Rowe, et al., *Tribology of abrasive machining processes*. 2nd Edition ed. 2012, Norwich, NY: William Andrew Pub.
- [3] S. Ebbrell, *Process requirements for precision grinding*. 2003, Liverpool: Liverpool John Moores University.
- [4] T.D. Howes, et al., *Environmental Aspects of Grinding Fluids*. CIRP Annals - Manufacturing Technology, 1991. 40(2): p. 623-630.

# Appendix P - Workpiece Fixture Design



ANGULAR TOLERANCES: ±0.1° UNLESS OTHERWISE STATED		IDENTIFICATION AND TRACEABILITY		DRAWN BY		P.W.H		DATE		SCALE		NTS	
REMOVE ALL SHARP EDGES ALL DIMENSIONS ARE IN MILLIMETERS UNLESS STATED OTHERWISE. ALL THREADS COARSE PITCH TOLERANCE CLASS 6H/6g UNLESS STATED OTHERWISE. UNSPECIFIED GEOMETRIC CHARACTERISTICS ARE ALLOWED WITHIN TOLERANCE ZONE		AT THE POSITION 'MARK' ENGRAVE THE PART NUMBER AND HOLROYD ORDER NUMBER.		MATERIAL		230M07 OR EQUIVALENT		05/02/16		1 OF 1		A3	
LINEAR TOLERANCES UNLESS OTHERWISE STATED		MACHINE N° ALL OVER UNLESS OTHERWISE STATED.		DESCRIPTION		GRINDING FIXTURE FOR WORKPIECE							
0 to 6	> 6 to 30	> 30 to 120	> 120 to 400	> 400 to 1000	PART No		PWH001		SHEET		1 OF 1		
±0.10	±0.15	±0.20	±0.25	±0.50									
±1.0	±1.0	±1.0	±1.0	±1.0									

# Appendix Q - Workpiece Design

ALTERATION	REV
ORIGINAL ISSUE	1
REDRAWN FROM 2D CAD. 4 OFF M4 HOLES ADDED 26/10/16 PWH	2
DISTANCE WAS 6MM NOW 4MM 28/7/17 PWH	3

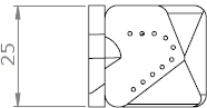
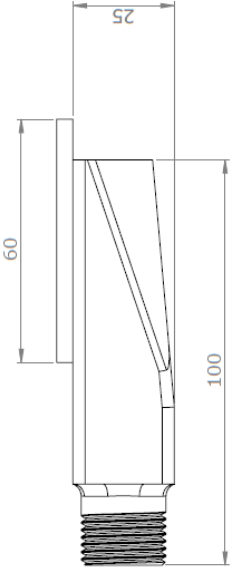
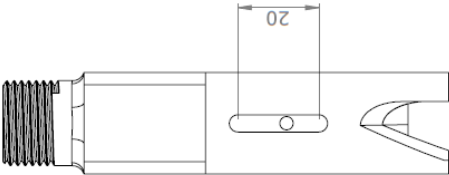
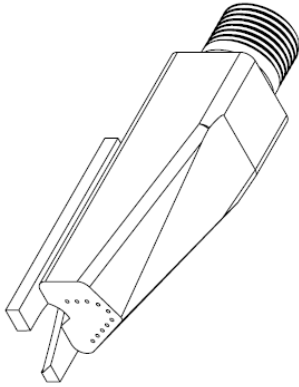
  
  

NOTE:  
FORM MILLING CUTTER TO BE SUPPLIED FOR CUTTING THE FORM GROOVE

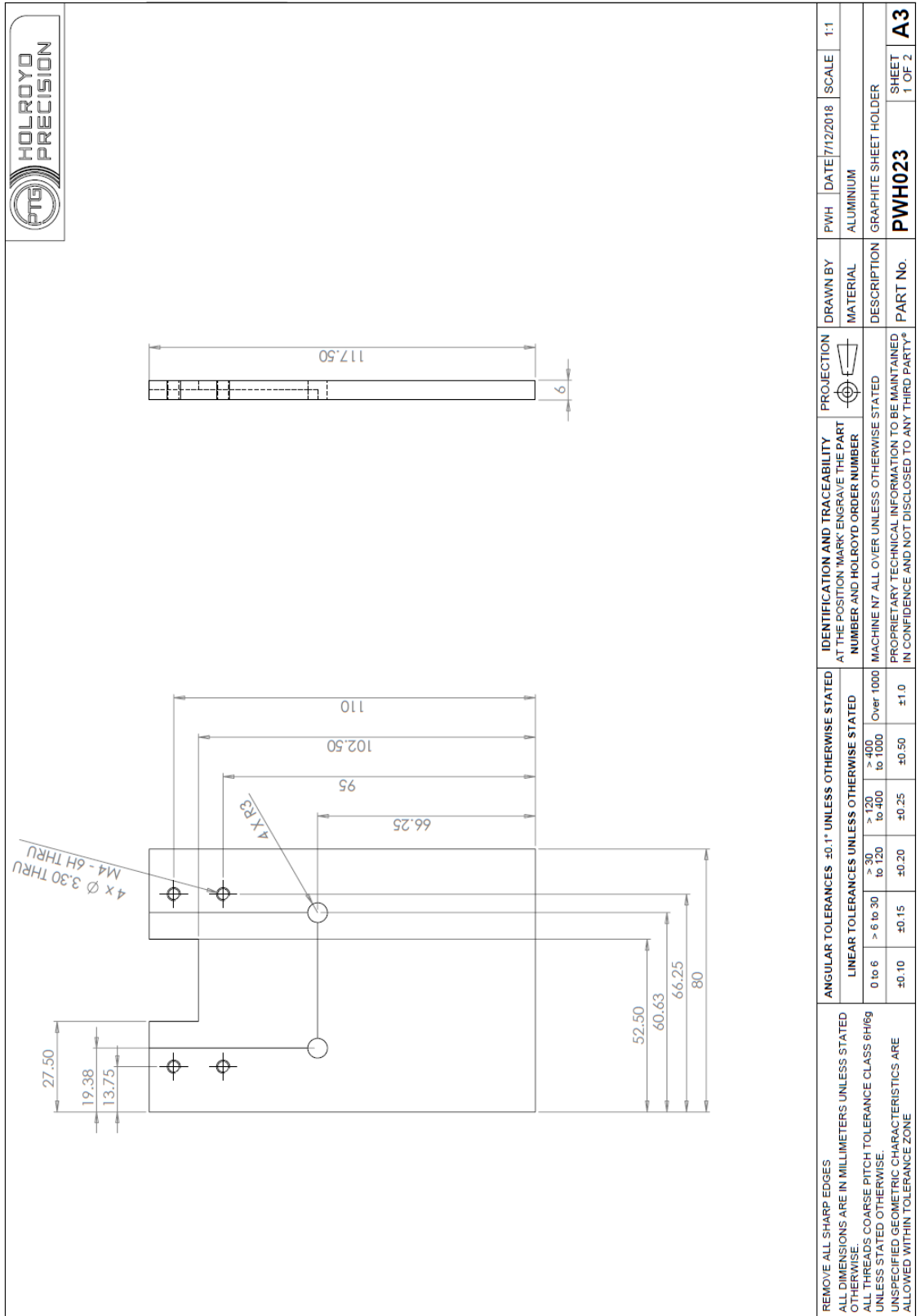
  

REMOVE ALL SHARP EDGES ALL DIMENSIONS ARE IN MILLIMETERS UNLESS STATED OTHERWISE. ALL THREADS COARSE PITCH TOLERANCE CLASS 6H/6g UNLESS STATED OTHERWISE. UNSPECIFIED GEOMETRIC CHARACTERISTICS ARE ALLOWED WITHIN TOLERANCE ZONE	ANGULAR TOLERANCES ±0.1° UNLESS OTHERWISE STATED	IDENTIFICATION AND TRACEABILITY AT THE POSITION 'MARK' ENGRAVE THE PART NUMBER AND HOLROYD ORDER NUMBER	PROJECTION 
	LINEAR TOLERANCES UNLESS OTHERWISE STATED	MACHINE N7 ALL OVER UNLESS OTHERWISE STATED	
	0 to 6 ±0.10	Over 1000 ±1.0	
	> 6 to 30 ±0.15	to 400 ±0.50	
	> 30 to 120 ±0.20	to 1000 ±0.25	
	> 120 to 400 ±0.25		
	> 400 to 1000 ±0.50		
		PROPRIETARY TECHNICAL INFORMATION TO BE MAINTAINED IN CONFIDENCE AND NOT DISCLOSED TO ANY THIRD PARTY®	
		DESCRIPTION PARALLELOGRAM WORKPIECE	
		DRAWN BY MATERIAL	
		PWH FREE ISSUE MATERIAL	
		DATE 30/03/2015	
		SCALE 2:1	
		PART No. PWH003	
		SHEET 1 OF 1	
			<b>A3</b>

# Appendix R - Coolant nozzle drawing

		<table border="1" style="width: 100%; border-collapse: collapse;"> <tr> <th colspan="2" style="text-align: center;">REVISIONS</th> </tr> <tr> <th style="width: 50%;">REV.</th> <th style="width: 50%;">DATE</th> </tr> <tr> <td style="text-align: center;">1</td> <td style="text-align: center;">APR</td> </tr> <tr> <td style="text-align: center;">First Issue</td> <td></td> </tr> </table>		REVISIONS		REV.	DATE	1	APR	First Issue							
REVISIONS																	
REV.	DATE																
1	APR																
First Issue																	
																	
<p>REMOVE ALL SHARP EDGES          ALL DIMENSIONS ARE IN MILLIMETERS UNLESS STATED OTHERWISE.          ALL THREADS COARSE PITCH TOLERANCE CLASS 6H/6g UNLESS STATED OTHERWISE.          UNSPECIFIED GEOMETRIC CHARACTERISTICS ARE ALLOWED WITHIN TOLERANCE ZONE</p>		<p><b>ANGULAR TOLERANCES</b> ±0.1° UNLESS OTHERWISE STATED</p> <table border="1" style="width: 100%; border-collapse: collapse;"> <tr> <th colspan="2" style="text-align: center;">LINEAR TOLERANCES UNLESS OTHERWISE STATED</th> </tr> <tr> <th style="width: 33%;">0 to 6</th> <th style="width: 33%;">&gt; 6 to 30</th> </tr> <tr> <td style="text-align: center;">±0.10</td> <td style="text-align: center;">±0.15</td> </tr> <tr> <th style="width: 33%;">&gt; 30 to 120</th> <th style="width: 33%;">&gt; 120 to 400</th> </tr> <tr> <td style="text-align: center;">±0.20</td> <td style="text-align: center;">±0.25</td> </tr> <tr> <th style="width: 33%;">&gt; 400 to 1000</th> <th style="width: 33%;">Over 1000</th> </tr> <tr> <td style="text-align: center;">±0.50</td> <td style="text-align: center;">±1.0</td> </tr> </table>		LINEAR TOLERANCES UNLESS OTHERWISE STATED		0 to 6	> 6 to 30	±0.10	±0.15	> 30 to 120	> 120 to 400	±0.20	±0.25	> 400 to 1000	Over 1000	±0.50	±1.0
LINEAR TOLERANCES UNLESS OTHERWISE STATED																	
0 to 6	> 6 to 30																
±0.10	±0.15																
> 30 to 120	> 120 to 400																
±0.20	±0.25																
> 400 to 1000	Over 1000																
±0.50	±1.0																
<p><b>IDENTIFICATION AND TRACEABILITY</b>          AT THE POSITION 'MARK' ENGRAVE THE PART NUMBER AND HOLROYD ORDER NUMBER</p>		<p><b>PROJECTION</b></p> <div style="text-align: center;">  </div> <p>MACHINE NOT ALL OVER UNLESS OTHERWISE STATED          PROPRIETARY TECHNICAL INFORMATION TO BE MAINTAINED IN CONFIDENCE AND NOT DISCLOSED TO ANY THIRD PARTY*</p>															
<p><b>DRAWN BY</b></p>		<p><b>DATE</b> 08/12/2018</p>															
<p><b>MATERIAL</b></p>		<p><b>SCALE</b> 1:1</p>															
<p><b>DESCRIPTION</b></p>		<p><b>PART No.</b></p>															
<p><b>COOLANT NOZZLE</b></p>		<p><b>PWH024</b></p>															
<p><b>SHEET</b></p>		<p><b>1 OF 1</b></p>															
<p><b>A3</b></p>		<p><b>1 OF 1</b></p>															

# Appendix S - Graphite sheet holder



<p>REMOVE ALL SHARP EDGES ALL DIMENSIONS ARE IN MILLIMETERS UNLESS STATED OTHERWISE. ALL THREADS COARSE PITCH TOLERANCE CLASS 6H/6g UNLESS STATED OTHERWISE. UNSPECIFIED GEOMETRIC CHARACTERISTICS ARE ALLOWED WITHIN TOLERANCE ZONE</p>		<p>ANGULAR TOLERANCES ±0.1° UNLESS OTHERWISE STATED</p> <p>LINEAR TOLERANCES UNLESS OTHERWISE STATED</p> <table border="1"> <tr> <td>0 to 6</td> <td>&gt; 6 to 30</td> <td>&gt; 30 to 120</td> <td>&gt; 120 to 400</td> <td>&gt; 400 to 1000</td> <td>Over 1000</td> </tr> <tr> <td>±0.10</td> <td>±0.15</td> <td>±0.20</td> <td>±0.25</td> <td>±0.50</td> <td>±1.0</td> </tr> </table>		0 to 6	> 6 to 30	> 30 to 120	> 120 to 400	> 400 to 1000	Over 1000	±0.10	±0.15	±0.20	±0.25	±0.50	±1.0	<p>IDENTIFICATION AND TRACEABILITY AT THE POSITION 'MARK' ENGRAVE THE PART NUMBER AND HOLROYD ORDER NUMBER</p> <p>MACHINENT ALL OVER UNLESS OTHERWISE STATED PROPRIETARY TECHNICAL INFORMATION TO BE MAINTAINED IN CONFIDENCE AND NOT DISCLOSED TO ANY THIRD PARTY*</p>		<p>PROJECTION</p>	<p>DRAWN BY</p> <p>MATERIAL</p> <p>DESCRIPTION</p> <p>PART No.</p>	<p>PWH</p> <p>ALUMINIUM</p> <p>GRAPHITE SHEET HOLDER</p> <p><b>PWH023</b></p>	<p>DATE/7/12/2018</p> <p>SCALE</p> <p>1:1</p>	<p>SHEET</p> <p>1 OF 2</p> <p><b>A3</b></p>
0 to 6	> 6 to 30	> 30 to 120	> 120 to 400	> 400 to 1000	Over 1000																	
±0.10	±0.15	±0.20	±0.25	±0.50	±1.0																	

# Appendix T - Graphite sheet holder clamp plate

